technische universität
dortmund

Dissertation

Instabilities and shape analyses of elastic shells

by
Sebastian Knoche
from Arnsberg

submitted for the degree of
Doctor rerum naturalium (Dr. rer. nat.)
of the Faculty of Physics, TU Dortmund University

Dortmund, October 2014

Contact to the author: sebastian.knoche@tu-dortmund.de

Abstract

This thesis presents research results on the deformation of elastic shells, especially concerning buckling and wrinkling instabilities. The theoretical description of such deformations is used to develop methods of shape analysis, which serve to infer material properties from simple experimental observations of deformed shells.

When an initially spherical shell is deflated, two successive instabilities can typically be observed. In a first buckling transition, an axisymmetric dimple appears. It grows with proceeding deflation and acquires a polygonal shape in a secondary buckling transition. The onset of the first instability is well known. Here, we draw a complete picture of axisymmetric buckled shapes from the onset to a fully collapsed state, where opposite sides of the shell are in contact. Furthermore, it is shown that the stability of buckled shapes with respect to further spontaneous deflation depends decisively on whether the interior shell volume is prescribed (buckled shapes are stable), the pressure difference is fixed (shapes are unstable and collapse immediately after the onset) or the deflation is controlled by osmosis (intermediate between the former cases). For the description of axisymmetric buckled shapes, we use two approaches: firstly non-linear shell theory and secondly a simple analytic model proposed originally by Pogorelov. The secondary buckling instability has so far only been observed in simulations and experiments. Here, we provide a theoretical explanation and analyse its onset quantitatively. A compressive circumferential stress in the vicinity of the dimple edge is identified as the driving force of the secondary buckling transition. Using the stability equations for shallow shells, we derive a critical circumferential stress which leads to wrinkles along the dimple edge, similar to the Euler buckling of straight rods.

Subsequently, we introduce a model for capsules that are created from liquid drops by an interfacial reaction and hang from a capillary. The interior liquid can be removed by suction through the capillary, which usually leads to wrinkling of the capsule membrane. The theoretical model is applied to completely characterise the elastic moduli of the membrane by an analysis of the capsule contour and wrinkle wavelength detected in experimental images. A test on two different capsule systems, polymerised polysiloxane capsules and bubbles coated with a layer of the protein hydrophobin, proves the concept of the proposed elastometry method. In the analysis of the hydrophobin capsule, we find an interesting non-linear elastic response which can be attributed to the molecular structure of the proteins consisting of a hard core and a softer shell. This motivates the development of a custom elasticity model based on the microscopic view of a bead-spring model including steric repulsions and can in part explain the experimental results of the hydrophobin capsule.

Kurze Zusammenfassung

Die vorliegende Arbeit präsentiert Forschungsergebnisse zur Deformation elastischer Schalen, insbesondere zu Instabilitäten wie Einbeulung und Faltenbildung. Die theoretische Beschreibung solcher Deformationen wird benutzt um Methoden der Formanalyse zu entwickeln, welche dazu dienen aus einfachen experimentellen Beobachtungen deformierter Schalen deren Materialeigenschaften abzuleiten.

Wird das innere Volumen einer ursprünglich runden Schale reduziert, so können typischerweise zwei Instabilitäten nacheinander beobachtet werden. In einem ersten Übergang bildet sich eine achsensymmetrische Beule. Im weiteren Verlauf wächst diese an und nimmt nach einem zweiten Übergang eine polygonale Form an. Das Einsetzen der ersten Instabilität ist wohl bekannt. Wir zeichnen hier ein vollständiges Bild achsensymmetrisch eingebeulter Formen vom anfänglichen Einbeulen bis zum völlig kollabierten Zustand, in welchem sich die gegenüberliegenden Seiten der Schale berühren. Außerdem wird gezeigt, dass die Stabilität der eingebeulten Form bezüglich weiterer spontaner Volumenreduktion sehr davon abhängt, ob das Volumen der Schale vorgegeben ist (gebeulte Formen sind stabil), die Druckdifferenz fest ist (Formen sind instabil und kollabieren sofort nach der Einbeulung) oder ob die Deformation durch Osmose gesteuert wird (Verhalten liegt zwischen den vorigen Fällen). Zur Beschreibung der achsensymmetrisch eingebeulten Form werden zwei Modelle verwendet: zum einen nicht-lineare Schalentheorie, zum anderen ein einfaches analytisches Modell welches ursprünglich von Pogorelov vorgeschlagen wurde. Die zweite Instabilität wurde bisher nur in Simulationen und Experimenten beobachtet. Hier liefern wir eine theoretische Erklärung und analysieren quantitativ ihr Einsetzen. Eine kompressive Spannung in der Umgebung des Beulenrandes wird als die treibende Kraft hinter der zweiten Instabilität identifiziert. Unter Verwendung der Stabilitätsgleichungen flacher Schalen leiten wir eine kritische Spannung her bei welcher sich entlang des Beulenrandes Falten ausbilden, ähnlich zur Eulerschen Knicklast gerader Stäbe.

Anschließend wird ein Modell für elastische Kapseln eingeführt, welche durch eine Grenzflächenreaktion aus einem Flüssigkeitstropfen erzeugt werden und an einer Kapillare hängen. Durch die Kapillare kann die innere Flüssigkeit abgesaugt werden, was üblicherweise zu Faltenbildung auf der Kapselmembran führt. Das theoretische Modell wird benutzt, um durch eine Analyse der Kapselkontur und der Wellenlänge der Falten die elastischen Moduln der Membran vollständig aus experimentellen Bildern zu bestimmen. Ein Test an zwei unterschiedlichen Kapselsystemen, polymerisierte Polysiloxan Kapseln sowie Bläschen die mit einer Lage des Proteins Hydrophobin ummantelt sind, belegt die prinzipielle Funktionsweise der vorgestellten Elastometrie-Methode. Bei der Analyse der Hydrophobin-Kapseln finden wir ein interessantes nicht-linear elastisches Verhalten, welches der molekularen Struktur bestehend aus einem harten Kern und einer weicheren Schale zugeschrieben werden kann. Dies motiviert die Entwicklung eines eignen Elastizitätsmodells auf Basis eines Federmodells, welches die sterischen Wechselwirkungen der Kerne mit berücksichtigt und die experimentellen Ergebnisse der Hydrophobin-Kapsel teilweise erklären kann.

Contents

List of figures

List of tables

List of symbols and abbreviations

Variants of the symbols listed below with an index "0" refer to the undeformed configuration. Variants with a tilde, overbar or hat denote reduced (dimensionless) quantities.

α	opening angle of the dimple, page 18
$\tilde{\alpha}, \tilde{\beta}, \tilde{\gamma}$	rescaled parameters for buckling under a parabolic stress profile, page 58
$\Delta\rho$	density difference of inner and outer fluid, page 83
Δl_s	length change of a fibre in s direction, page 89
$\delta u, \delta v$	normal and tangential variation, respectively, page 11
ΔV	volume difference with respect to the initial volume, page 18
$\mathrm{d}\bar{\boldsymbol{s}}$	deformed line element of a shallow shell, page 48
$\mathrm{d}\boldsymbol{s}$	undeformed line element of a shallow shell, page 48
$\mathrm{d}A$	surface area element of the midsurface, page 11
$\mathrm{D}_{ss}, \mathrm{D}_{\varphi\varphi}$	derivative operators in polar coordinates, page 73
ε	arc length at which the displacements in the Pogorelov model have decayed, page 19
$\varepsilon_x, \varepsilon_y$	Green-Lagrange strains of a shallow shell in x- and y-direction, page 47
ε_{xy}	Green-Lagrange shear strain component of a shallow shell, page 47
$\varepsilon_i^{(1)}$	linearised strain component $i \in \{x, y, xy\}$, page 53
η, ξ	principal directions for pure shear, page 48
γ	interfacial tension, page 83
γ	shear angle, page 48
γ_{FvK}	Föppl-von-Kármán-number, page 15
$\hat{H}$	matrix operator of the symmetrised second variation, page 53
κ_{edge}	meridional curvature at the dimple edge, page 26
κ_s, κ_φ	meridional and circumferential curvature of the midsurface, page 8
κ_x, κ_y	curvatures of an undeformed shallow shell in x- and y-direction, page 47
κ_{xy}	twist of an undeformed shallow shell, page 47
Λ	wrinkle wavelength for pendant capsules, page 89
λ	wavelength of the wrinkling pattern, page 55
$\lambda_s, \lambda_\varphi$	meridional and circumferential stretch, respectively, page 8
λ_x, λ_y	stretches in x- and y-direction, page 48
$\lambda_x^{(\mathrm{b})}$	boundary of the admissible region in the stretch space, page 99
$\bar{\lambda}_\varphi$	circumferential stretch of the pseudo-surface, page 87
Δ	Laplace operator, $\Delta = \partial_x^2 + \partial_y^2$ in Cartesian coordinates, page 53
ν	surface Poisson ratio, page 9
ν_{3D}	three-dimensional Poisson ratio, page 10
Φ	y-dependent part of the Airy stress function, page 62
ϕ	Airy stress function, page 53

φ_i	angle of orientation $i \in \{-1, 0, 1\}$, page 98
ψ	slope angle of the midsurface, page 8
ρ, θ	polar coordinates, page 89
σ	interval boundary for Pogorelov's piecewise defined solution, optimal value $\sigma_{\min} = 1.24667$, page 21
τ_0	amplitude of the parabolic stress profile, page 58
$\tau_{\min}$	minimum value of the hoop stress in the compressive region, page 70
τ_s, τ_φ	meridional and circumferential stress, respectively, page 10
$\bar{\tau}_s$	meridional stress, measured per unit length of the pseudo surface, page 87
τ_x, τ_y	stresses in x- and y- direction in a shallow shell, page 49
τ_{xy}	shear stress component in a shallow shell, page 49
$\tau_i^{(1)}$	linearised stress component $i \in \{x, y, xy\}$, page 53
$\tau_i^{(\mathrm{c})}$	hard-core contributions to the stress in direction $i \in \{x, y\}$ or $i \in \{s, \varphi\}$, page 99
$\tau_i^{(\mathrm{s})}$	spring contribution to the stress in direction $i \in \{x, y\}$ or $i \in \{s, \varphi\}$, page 98
$\boldsymbol{\varepsilon}$	Green-Lagrange strain tensor of a shallow shell, page 47
$\boldsymbol{\tau}$	stress tensor of a shallow shell, page 49
$\boldsymbol{K}$	bending strain tensor of a shallow shell, page 47
$\boldsymbol{m}$	bending moment tensor of a shallow shell, page 49
$\boldsymbol{F}$	force vector, page 49
$\boldsymbol{n}$	unit normal vector, page 49
$\boldsymbol{x}_i$	sampling points representing a capsule contour, page 90
ξ	length scale in the Pogorelov model, page 20
a	inner capillary diameter, page 83
a_c	curvature parameter in the curved plate model, page 62
a_p	coefficient in the parabolic stress profile describing its width, page 58
C	wrinkle amplitude, page 89
d	shell depth in the buckled state, page 41
d_i	deformed length of a spring along orientation $i \in \{-1, 0, 1\}$, page 98
E	three-dimensional Young modulus, page 10
$E_{2\mathrm{D}}$	surface Young modulus, page 9
E_{Gibbs}	Gibbs elasticity modulus, page 91
E_B	bending stiffness, page 9
e_s, e_φ	Cauchy strain in meridional and circumferential direction, respectively, page 9
F	stress integrated over the compressive region, page 69
F_{os}	osmotic free energy of the solutions, page 37
G	total enthalpy functional for osmotic buckling, page 37
g	acceleration of gravity, $g = 9.81\,\mathrm{m/s^2}$, page 83
G_1, G_2	undeformed and mirror-inverted regions of a buckled spherical shell, page 18
$G_{2\mathrm{D}}$	surface shear modulus, page 51
$G_{\mathrm{i}}, G_{\mathrm{o}}$	inner and outer neighbourhood of the dimple edge, page 18
H	elastic enthalpy functional, page 30
h	depth of the dimple, page 18

H_0	shell thickness, page 10
H_{barr}	enthalpy barrier for buckling under pressure control, page 34
J	rescaled energy functional in the Pogorelov model, minimised value $J_{\min} = 1.15092$, page 21
k	wave number $k = 2\pi/\lambda$, page 56
$K_{2\mathrm{D}}$	area compression modulus, page 51
k_B	Boltzmann constant, $k_B = 1.3806 \cdot 10^{-23}\,\mathrm{J/K}$, page 37
K_s, K_φ	bending strain in meridional and circumferential direction, respectively, page 9
K_x, K_y	bending strains of a shallow shell in x- and y-direction, page 47
K_{xy}	twist strain of a shallow shell, page 47
L	diameter of the hard cores, in units of the lattice constant, page 98
L_0	contour length of the undeformed midsurface, page 8
L_{eff}	effective width of the wrinkles, page 60
L_w	wrinkle length, page 86
L_x, L_y	length and width of a rectangular plate, page 55
m_s, m_φ	meridional and circumferential bending moment, respectively, page 10
m_x, m_y	bending moments in x- and y- direction in a shallow shell, page 49
m_{xy}	twisting moment in a shallow shell, page 49
n	number of wrinkles, page 70
N_{ex}	number of exterior osmotically active particles, page 37
N_{in}	number of interior osmotically active particles, page 37
P	load potential, page 11
p	normal pressure, negative for deflation, page 11
p_c	critical pressure for buckling under pressure control, page 31
p_{cb}	classical buckling pressure, page 19
p_{ex}	external osmotic pressure, page 37
$p_{\mathrm{ex,c}}$	critical pressure for osmotic buckling, page 38
$p_{\mathrm{ex,cb}}$	classical threshold for osmotic buckling, page 38
p_{os}	osmotic pressure difference, page 37
p_T	buckling pressure at finite temperature, page 35
p_u	upper critical pressure for buckling under pressure control, page 34
q	transverse shear stress, page 12
r, z, φ	polar cylindrical coordinates for the midsurface, page 8
$\bar{r}$	radial coordinate of the pseudo-surface, page 87
R_0	initial radius of a spherical shell, page 8
r_D	radius of the dimple, page 18
s	arc-length coordinate, page 8
s_c	arc-length coordinate where the meridional curvature vanishes, page 69
s_D	arc-length coordinate of the dimple edge, page 22
T	temperature, page 37
t	another arc-length coordinate, page 89
U	elastic energy functional, page 11

u, v	radial and vertical displacements in the Pogorelov model, page 18
u, v, w	displacements of a shallow shell in x, y, z direction, page 47
U_{Pog}	elastic energy of a buckled spherical shell in the Pogorelov model., page 22
U_{sph}	elastic energy of a uniformly compressed spherical shell, page 24
U_ξ	energy scale in the Pogorelov model, page 20
V	enclosed volume of the shell, page 11
$V_{1\mathrm{st}}$	critical volume for buckling under volume control, page 25
$V_{2\mathrm{nd}}$	critical volume for secondary buckling, page 72
V_{cb}	classical buckling volume, page 25
V_{ex}	volume outside the shell, page 37
$W(y)$	amplitude profile of the wrinkling pattern, page 56
W_0	amplitude of the wrinkling pattern, page 55
$\bar{w}$	rescaled derivative of the vertical displacement in the Pogorelov model, page 20
w_{bend}	surface energy density of bending, page 52
w_{ext}	surface energy density of the external potential, page 52
w_{stretch}	surface energy density of stretching, page 52
w_S	surface energy density, page 9
$z(x,y)$	height profile of a shallow shell over the x-y-plane, page 47
AFM	atomic force microscopy, page 82
DMV	Donnel-Mushtari-Vlasov (shell theory), page 47
FFT	far from threshold regime, page 46
HFBII	class II hydrophobin, page 82
NaOH	sodium hydroxide, page 96
NT	near threshold regime, page 46
OTS	octadecyltrichlorosilane, page 82
PSS	poly(styrene sulfonate, sodium salt), page 41

Chapter 1

Introduction

1.1. Elastic shells ...

An *elastic shell* is a sheet of elastic material or a thin-walled elastic structure which is curved in its undeformed state. To have a simple picture in mind, one could think of a rubber balloon as a paradigmatic example for an elastic shell. Because of its small thickness, the shell can be regarded as a quasi two-dimensional surface, which facilitates its mathematical description. Often, shells are closed and contain some medium. They are then also termed *elastic capsules*.

Being *elastic* means that a body can be deformed by external loads, but will restore its initial state (the so called reference state) if the loads are released. The larger the loads, the larger will be the deformation in most cases. This elastic behaviour can be contrasted to *viscous* behaviour: Viscous media can also be deformed by external loads – the larger the load, the quicker the configuration change – and will keep a deformed shape if the loads are released. A third class of material behaviour is *plasticity*. An ideal plastic material does not deform when the loads are small, but when a certain yield stress is exceeded it begins to deform irreversibly. Elementary examples are rubber for an elastic material, water or honey for viscous media and modelling clay for a plastic material.

In a continuum mechanics perspective, the internal *stress* in an elastic body depends on the *strain* (which is a measure of the local deformation, stretch or compression) [83]. We can consider a body being composed of individual particles, which are cross-linked in the elastic case: The "neighbourhoods" of the particles are fixed, two particles next to each other are also next to each other in the deformed body. In viscous media, however, the stresses depend on the *strain rate*, that is, the temporal derivative of the strains [84]. The neighbourhoods between the particles are not fixed, they can flow. In general media, the stresses depend on both strain and strain rate [53]. These media can be either solid-like (restoring their initial state) or fluid-like (staying in a deformed state). Shells can be constructed from both solid and fluid materials. Vesicles, for example, are composed of lipid bilayer membranes that are two-dimensional fluids and have received a lot of attention [117]. In this thesis, however, we will deal only with solid-like, elastic shell materials whose viscosity can be neglected.

The second distinctive property of elastic shells is that they are *curved* in their reference configuration, which is different from elastic plates which are planar in their reference state. This has an important impact on the deformability of shells and plates: Curved shells are often harder to deform than flat plates, a phenomenon called *geometry-induced rigidity* [85, 131]. To understand this effect we must take into account that thin sheets can be bent much easier than stretched. This can be quantified in terms of an elastic energy: Stretch and compression involve a large amount of elastic energy that scales linearly with the shell thickness H_0, while the bending energy scales with H_0^3 and is thus very small for thin shells. Since elastic bodies

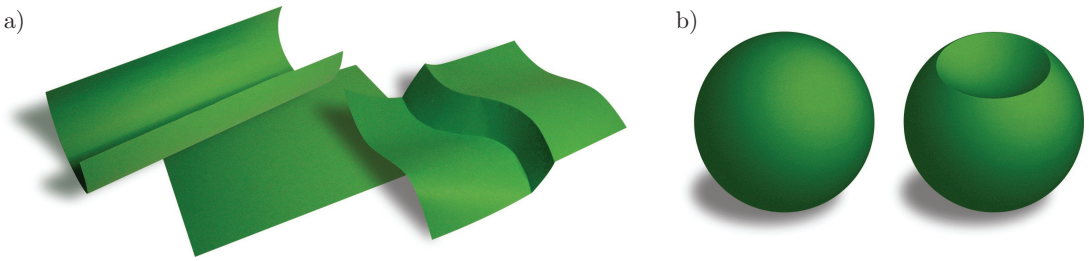

Figure 1.1.: Deformations of a) a paper sheet and b) a paper sphere. The sheet can be deformed isometrically in a smooth way by rolling it, or non-smoothly by creasing it. However, the sphere cannot be deformed isometrically in a smooth way because of its geometry-induced rigidity: All possible isometric deformations of the sphere contain creases.

tend to minimise their stored elastic energy, they prefer configurations in which they are less stretched and compressed, but they do not refuse to bend. Infinitely thin bodies are therefore preferably deformed *isometrically*, i.e. without any compression and stretching at all. An isometric deformation conserves the metric of the surface: Any curve drawn on the surface keeps its length during the deformation. As a consequence of Gauss' Theorema egregium, an isometric deformation implies that the Gaussian curvature of the surface does not change [4].

Such isometric deformations are possible for planar sheets; however, no general result is known when a curved surface can be deformed isometrically [4]. There are surfaces, such as spheres or ellipsoids, which cannot be deformed isometrically in a smooth way. Shells of these shapes are rigid because of their geometry: As no isometric deformations are possible, any deformation involves a costly stretch/compression contribution to the elastic energy.

We can get an intuitive feeling for isometric deformations by imagining that the body is made of paper, which cannot really be stretched without tearing. A planar sheet of paper, see fig. 1.1 a), can be smoothly rolled to a cylinder, which is a deformation that involves only bending, but no stretching. More complex isometric deformations arise when we are allowed to crease the paper [39] or to crumple it [137]. Creases are singularities with infinitely large curvature, and would imply an infinitely large bending energy. In reality the infinite energy is avoided by breakage of the paper fibres at the creases or by allowing the sheet to stretch in the vicinity of the crease [141, 142]. However, when we try to deform a paper sphere isometrically, we will find that it is not possible to do this in a smooth way. We need to introduce creases, for example a circular crease limiting a region that is mirror-inverted, see fig. 1.1 b).

This strong coupling between geometry and mechanics makes shells particularly interesting. Two elastic shells with the same thickness and material properties can behave very differently under external loads, just because they are differently shaped.

1.2. . . . and where to find them

Elastic shells are ubiquitous in our environment. On the macroscale we can find them in architecture and engineering, for example as roof structures, where they are preferably used because of their geometry-induced rigidity: Domes and arches are more stable than flat structures. Other examples from everyday life are egg shells, beach balls, beverage cans, tyres, plastic packages, . . . the list could grow arbitrarily long. On the microscale, there are natural shells like red blood cells [40], virus capsids [20, 94] or pollen grains [72] whose mechanical properties have gained a lot of attention in recent years. Artificial microcapsules have numerous

applications in today's industries, for example in food technologies, chemical industry and pharmacy [52, 148]. They can be used to encapsulate a substance that is to be released later on: In carbon-less copy paper, for example, dye-filled microcapsules get crushed by the mechanical force of a pencil and release the dye, perfume-filled capsules can be used in detergents to make the laundry smell nice over a long time span, and in delivery-and-release systems capsules are used to administer drugs. These are only some of the abundant applications of microcapsules, which are present in many products, but often not in the awareness of the customers.

Synthetic capsules can be produced by various methods [93, 147]. A common approach starts with droplets or bubbles which are embedded in another fluid phase. These droplets or bubbles are coated with an elastic membrane by an interfacial reaction: There are surfactants that can be added to the ambient fluid phase, which adsorb to the droplet's or bubble's surface and can form crosslinked networks, for example by polycondensation reactions or by radical reactions induced by irradiation of ultraviolet light [114]. Instead of droplets and bubbles, solid colloidal particles can also be used as templates for the capsule production. Charged colloids can be coated with a layer of oppositely charged polyelectrolytes (polymers with many charged groups). Interestingly, a charge reversal of the coated colloid can be achieved, which gives rise to a layer-by-layer technique: Further layers of polyelectrolytes, with alternating charges, can be deposited on the template until a desired shell thickness is reached. Finally, the template particle is dissolved [41].

1.3. Deformations of shells

Elastic shells can be deformed by external loads. For example, they can be stretched with optical tweezers, compressed between plates or indented by point forces [46]. Closed shells can be inflated and deflated, for example by osmosis, or deformed in shear flow or by centrifugal forces in a spinning drop apparatus [9,12]. Any deformation can be used to probe the mechanical properties of the shell. When there are theoretical calculations of the deformation available, a comparison between experiments and theory can be used to infer the elastic properties (measured by the *elastic moduli*) of the shell. This is the basic idea of a *shape analysis*, and we will encounter several examples in this thesis.

We will look mainly at deformations which follow from compressive loads. This kind of deformation is typically much more interesting than simple tensional loads because there are many possible deformation paths, and instabilities like *buckling* and *wrinkling* can occur. A simple example is the deformation of a thin elastic rod or spring: When tensional loads are applied to its ends, it simply stretches. But when compressive loads are exerted, the rod first contracts longitudinally and buckles into an arched configuration when a critical compression is reached. This buckling instability is well known since Leonhard Euler's mathematical treatment [43] and is easy to test by disassembling the nearest available ballpoint pen to obtain its spring and compress it between one's fingers.

The physics governing this phenomenon has already been mentioned above: It is the fact that thin structures are much easier to bend than to stretch or compress. By assuming an arched shape, the compressed rod can (nearly) restore its original length, thus reducing the compression energy at the expense of acquiring some additional bending energy.

Similar buckling instabilities can be observed when shells and plates are compressed. Buckling instabilities are interesting for physicists, especially theorists, because they can lead to a rich bifurcation behaviour, for example in the deflation of spherical shells as investigated in the author's diploma thesis [151]. The shape bifurcations and metastable shapes can explain the polymorphism often seen in soft matter systems, amongst others in gel-phase vesicles that

Figure 1.2.: The first and second buckling transition of a spherical shell can be observed on the macro- and microscale: a) a deflated plastic ball of diameter 5 cm, b) two microcapsules of diameter 2.5 µm (left, image taken from ref. [116]) and 5 µm (right, image taken from ref. [113]).

buckle into specific shapes [111]. For engineers, however, buckling is mostly undesirable because it represents a failure path by which a structure loses its stability. Shell buckling is especially "catastrophic" because the buckled shape typically supports significantly less load than the unbuckled one [135]. As a result, the shell collapses completely in a loud bang when the external load is increased beyond the critical load at which buckling sets in.

1.4. Outline of this thesis

In this thesis, we investigate several shells that are exposed to compressive stresses. The first example is a spherical shell that is deflated and goes through various shapes until it is completely empty. Two distinct buckling phenomena will be discussed in chapters 2 and 4: In the first buckling transition, a uniformly compressed shell changes to a buckled configuration, which has essentially the shape of a sphere with mirror-inverted spherical cap. This "dimple" acquires a polygonal shape in a secondary buckling transition, see fig. 1.2. Both transitions are examples of *stress focusing* [141], where an elastic structure concentrates its deformation energy along lines or in points instead of spreading it uniformly over its surface.

Between these two chapters on spherical shells there is chapter 3 focusing on the compression of flat plates and shallow shells. Originally, this research was meant to be auxiliary to explain the secondary buckling of spherical shells. However, two questions were encountered which have an importance on their own: Firstly, how does a plate buckle when it is compressed only over a small localised region (and not over its whole area), and secondly, how is wrinkling of thin sheets related to buckling?

Finally, in chapter 5, we discuss capsules that are produced by interfacial reactions from pendant drops or rising bubbles attached to a capillary. This setup is frequently used by physical chemists who are working on new shell materials [1, 42, 68, 119]. In order to facilitate the determination of the elastic properties of the newly synthesised capsule membrane, we develop a shape analysis based on the deflation of the capsules by suction through the capillary. We provide a proof-of-concept study that this shape analysis, in combination with an analysis of the wrinkles that generically form in the course of the deflation, can be used to infer all elastic moduli of the enclosing membrane. Motivated by the results on a capsule consisting of a protein layer, we develop an elasticity model based on the microscopic view of beads with hard cores and spring interactions and analyse its impact on the capsule deflation.

All these problems are solved using shell theory. The equations of shell theory seem to be best handled with finite element methods when they are applied in general. Here, however, we only consider special cases with simple geometry that allow some analytic treatment or lead to one-dimensional problems in which an ordinary differential equation must be solved numerically.

Chapter 2

Axisymmetric buckling of spherical shells

Abstract – In this chapter we present the basics of non-linear shell theory for axisymmetric shells. Shape equations are derived from an elastic energy functional, which are then used to compute the deflated shapes of spherical shells, including buckled shapes that are completely collapsed and have opposite sides in contact. The buckled shapes which exhibit an axisymmetric dimple can also be approximated by an analytic model proposed by Pogorelov, which is reviewed here and compared to the exact numerical results. A detailed analysis of the geometry shows that the curvature of the dimple edge can be used as an indicator for the bending stiffness in experiments. We conclude this chapter by a discussion of the stability of the buckled shapes with respect to further growth of the dimple. Striking differences are found between the three load cases where either the volume difference of the shell is fixed, the pressure difference between the inside and outside is fixed or the shell is deflated by osmosis.
Published material – Parts of this chapter are reproduced with modifications from the author's publications [152], © 2011 by the American Physical Society, [155], © 2014 by IOPscience, [156], with kind permission of The European Physical Journal (EPJ), and [157], reproduced by permission of The Royal Society of Chemistry. Parts of the theoretical background in sections 2.2.1 to 2.2.4 have already been presented in the author's Diploma thesis [151].

2.1. Introduction

The elastic deformation of spherical shells has been analysed for various deformation means using different shell theories. Soft microcapsules can be deformed by shear flow [8–10, 12, 47, 48, 73, 139], rotation [106], point forces [55, 102, 128, 130, 132, 150] or interactions with flat plates [23, 55, 56, 80, 101, 102, 128]. A comparison of experimental results with the appropriate theoretical models allows for a characterisation of the capsule materials in terms of the elastic moduli, see ref. [46] for a recent review.

Here we will discuss the deformation that occurs upon volume reduction or an applied pressure difference. In microcapsule experiments, the volume reduction can be achieved by osmosis through a semipermeable capsule membrane, drying, or chemical reactions [18, 45, 51, 97, 98, 100, 113, 116, 127, 150], while experiments on macroscopic shells necessitate an outlet incorporated in the shell wall [15, 24].

When a spherical shell is deflated, it first contracts uniformly at small pressure differences. A stability analysis shows that this prebuckled shape becomes unstable at a critical pressure p_{cb}. The stability analysis can be conducted for the full spherical shape [79] or for a shallow

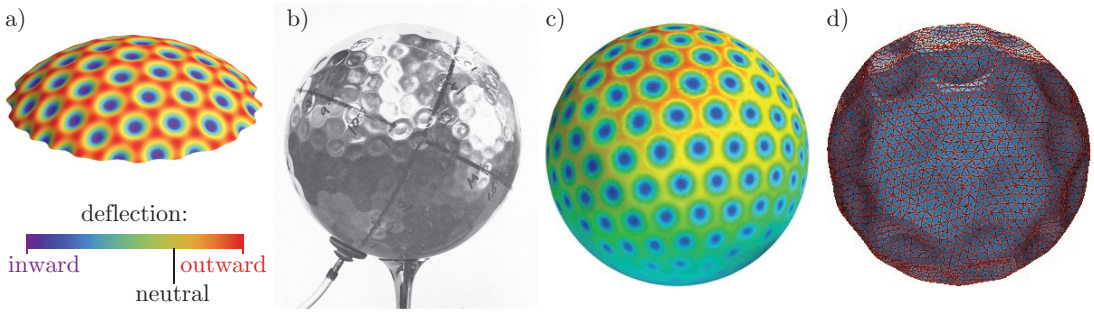

Figure 2.1.: Initial postbuckling shapes of spherical shells under normal pressure. Differences in the wavelength of the buckling pattern are due to different elastic moduli: Smaller bending stiffnesses result in smaller wavelengths. a) Plot of the normal deflection of Hutchinson's result for a shallow segment [69, 79]. b) Experimental observation by Carlson et al. using a wax mandrel inside the shell to limit the maximum indentation of the dimples, image taken from ref. [24]. c) Numerical simulation of the same setup, image taken from ref. [103]. d) Monte Carlo simulation (at practically vanishing temperature) with a large compression rate in which the shell is trapped in a metastable state, image taken from ref. [138].

segment of the shell [69, 103], with identical results for p_{cb}. The buckling mode has the shape of an oscillatory normal deflection – in fact, there exist many degenerate modes, all of them with wavelengths small compared to the shell radius [103]. The existence of a multitude of degenerate modes complicates the discussion of the initial post-buckling behaviour, because the modes interact with each other when the critical pressure is exceeded. The actual energy minimum is a linear combination of the critical modes, which was calculated by Hutchinson for shallow segments [69] and Koiter for full spheres [79] and is plotted in fig. 2.1 a). It consists of small dimples, arranged in a hexagonal mesh.

This buckling mode is unstable, which means that the dimples grow spontaneously if the pressure is prescribed [69, 79]. In experiments, the buckling mode can only be observed when it is stabilised against an endless growth of the dimples. This was achieved in ref. [24] by placing a solid sphere (termed "wax mandrel") inside the shell, with a small gap between shell and wax mandrel, thus limiting the depth of the dimples. The observation is in qualitative agreement with Koiter's and Hutchinson's theoretical results, see fig. 2.1 b). In simulations, similar shapes can be observed, for example by including a repulsive potential in the simulations mimicking the wax mandrel [103], or when the simulation is trapped in a metastable state with many dimples [113, 138, 140]. In the latter case, the shell can leave the metastable state by additional iterations or manually added perturbations, and finally ends up in a shape with only a single dimple.

In the conclusions of his extensive investigations of the buckling of spherical shells [79], Koiter reckoned that the shapes with many small dimples "play a vital role in the triggering of the buckling phenomenon, and that the shell returns to a configuration of rotational symmetry in a slightly more advanced post-buckling stage". This hypothesis is confirmed by the aforementioned simulations and by experiments, in which shapes with a single dimple are usually observed [45, 113, 116, 150].

In the following sections we will therefore concentrate on axisymmetric buckled shapes, which seem to be most relevant in practice. They are modelled in two different approaches. The first model is based on finite strain shell theory, from which equations for the deformed shape can be derived. Shape equations of similar non-linear shell theories have been analysed by

numerical methods, and were shown to have a large solution space which is usually presented in bifurcation diagrams [14, 62, 78]. The shape equations used in this thesis have already been described in the author's diploma thesis [151] and a subsequent publication [152], where rich bifurcation diagrams have been obtained. Here, we focus on the most relevant shapes with a single dimple and extend the investigations to bowl-like shapes with opposite sides in contact.

The second model for axisymmetric buckled shapes is an approximate analytic model proposed by Pogorelov [107]. Linear shell theory can be used to describe buckled shapes which are close to an isometric deformation of the sphere, where a spherical cap is mirror-inverted. Upon this basis, Pogorelov constructed an energy functional for the buckled shape and minimised it with calculus of variations. We summarise his derivation of the resulting shape and compare his analytic results to our numerical solutions of the shape equations.

The two models provide a numerical and an approximate analytic description of axisymmetric buckled shapes with one dimple. The curvature of the dimple edge is a good indicator of the shell's bending stiffness, and we provide scaling laws that can be used to interpret the results of microcapsule experiments and eventually determine the bending stiffness from a shape analysis. Furthermore, the stability of the buckled shapes will be discussed, which is very different depending on whether the volume or pressure is prescribed. Apart from that, the accurate descriptions of the axisymmetric buckled shapes are essential for the discussion of the secondary buckling transition in chapter 4, where the dimple loses its axisymmetry. Analysing the numerical and analytic solutions, we get a hint for the physical mechanism of the secondary buckling transition: We observe a region of compressive hoop stress, which is located in the inner neighbourhood of the dimple edge, just in the place where the secondary buckling occurs in experiments and simulations.

2.2. Shape equations for shells of revolution

The first model of axisymmetric shells is based on finite strain shell theory [89, 108]. A set of shape equations, whose solutions describe deformed axisymmetric shapes, shall be briefly derived in the present section. We consider shells with very thin walls, so that the shell is virtually two-dimensional, and in the following we will model it as a two-dimensional continuum. This approach differs from most textbooks on the theory of plates and shells [89, 96, 124, 125, 135], which derive the equations for the truly two-dimensional midsurface of a shell by descending from three-dimensional elasticity. While being general, deductive and mathematically precise, the descend from three dimensions necessitates prior knowledge of the whole three-dimensional elasticity theory. Our approach is less complete, but considerably faster and we can get a good overview over all the "ingredients" of the theory.

We will work with a fully non-linear shell theory. The only approximation comes with the elastic strain-energy function, which will have a simple quadratic form. This Hookean law is restricted to small strains; many other strain-energy functions have been proposed, like the Mooney-Rivlin law for rubber, which are suitable for larger strains [11, 49, 50, 58, 89]. However, the strains in the deformed shapes will remain quite small even after buckling, which justifies that we prefer the generic Hookean elasticity to a specialised large-strain elasticity.

Our discussion is valid for general shells of revolution, subjected to a normal pressure. Shells with spherical reference shape are a special case. The restriction to axisymmetric and torsionless deformations simplifies the analysis, because the principal directions of curvatures and stress are obvious from the geometry. This spares us the discussion of shear terms.

2.2.1. Geometry and deformation

Let us start with a description of the geometrical setup. In elasticity theory, we have to distinguish between the reference configuration and the deformed configuration of the elastic body. In this section, the reference configuration is free of stresses; this condition will be relaxed in the subsequent chapters.

The midsurface of the reference shape is parametrised in polar cylindrical coordinates (r_0, z_0) with an arc length coordinate s_0 ranging from 0 to L_0 and a circumferential angle $\varphi_0 \in [0, 2\pi)$, see fig. 2.2 a). We define a slope angle ψ_0 by the two relations

$$\frac{\mathrm{d}r_0}{\mathrm{d}s_0} = \cos\psi_0 \quad \text{and} \quad \frac{\mathrm{d}z_0}{\mathrm{d}s_0} = \sin\psi_0, \tag{2.1}$$

see fig. 2.2 b), which permits simple calculation of the principal curvatures of the midsurface. These are found in meridional (s_0-) and circumferential (φ_0-) direction, respectively, and read

$$\kappa_{s_0} = \frac{\mathrm{d}\psi_0}{\mathrm{d}s_0} \quad \text{and} \quad \kappa_{\varphi_0} = \frac{\sin\psi_0}{r_0}. \tag{2.2}$$

In the example of a spherical reference configuration with radius R_0, the parametrisation is explicitly given by $r_0(s_0) = R_0 \sin(s_0/R_0)$ and $z_0(s_0) = -R_0 \cos(s_0/R_0)$, where the arc length s_0 ranges from 0 to $L_0 = \pi R_0$. The slope angle then reads $\psi_0 = s_0/R_0$, and the principal curvatures reduce to $\kappa_{s_0} = \kappa_{\varphi_0} = 1/R_0$.

The index 0 of the symbols introduced so far indicates that they describe the reference configuration. The midsurface of the deformed configuration is described analogously without the indices 0. Specifically, its shape is determined by the functions $r(s)$, $z(s)$ which are to be determined. The geometrical relations (2.1) and (2.2) also hold for the deformed midsurface when all indices 0 are omitted, i.e.

$$\frac{\mathrm{d}r}{\mathrm{d}s} = \cos\psi, \quad \frac{\mathrm{d}z}{\mathrm{d}s} = \sin\psi, \quad \kappa_s = \frac{\mathrm{d}\psi}{\mathrm{d}s} \quad \text{and} \quad \kappa_\varphi = \frac{\sin\psi}{r}. \tag{2.3}$$

Upon deformation, the midsurface undergoes stretching and bending. We define the stretches in meridional and circumferential direction as

$$\lambda_s = \mathrm{d}s/\mathrm{d}s_0 \quad \text{and} \quad \lambda_\varphi = r/r_0, \tag{2.4}$$

respectively. The function $s(s_0)$ defined in this context determines the position s at which a shell element originally located at s_0 can be found after deformation; it must be determined as a part of the solution. These stretches measure the ratio of deformed length to undeformed length of material fibres oriented along the meridional and circumferential direction, respectively. With "material fibres" we do not imply that the elastic material is composed of individual fibres; we still consider it as a two-dimensional continuum. But it is a useful conception to imagine virtual

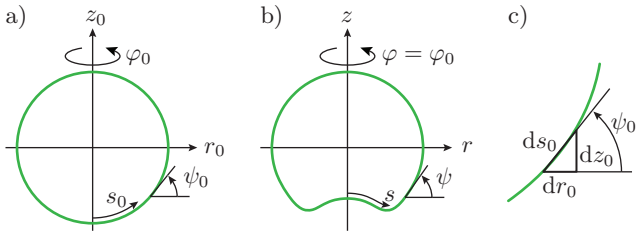

Figure 2.2.: Parametrisation of the axisymmetric midsurface in the a) reference configuration and b) deformed configuration. c) Definition of the slope angle in the reference configuration.

fibres in the material, like pencil lines that are drawn on the shell. The strains that correspond to the stretches are centred around 0 and are defined as

$$e_s = \lambda_s - 1 \quad \text{and} \quad e_\varphi = \lambda_\varphi - 1. \tag{2.5}$$

To measure the change in curvature, the bending strains

$$K_s = \lambda_s \, \kappa_s - \kappa_{s_0} \quad \text{and} \quad K_\varphi = \lambda_\varphi \, \kappa_\varphi - \kappa_{\varphi_0} \tag{2.6}$$

are defined [89, 108]. They are more suited for the use in shell theory than simple curvature differences $\Delta\kappa_s = \kappa_s - \kappa_{s_0}$ because they are, in a sense, energy conjugate to the bending moments, see eq. (2.10) below. For example, consider a uniform expansion of the spherical shell, where we do not expect any bending energy or bending moments: The curvature difference $\Delta\kappa_s = 1/R - 1/R_0$ does not vanish in this case, but the correct strains K_s and K_φ do. This is, however, a very subtle difference. In ref. [4] it is argued that it can be neglected, because the calculation of the bending energy needs to be accurate only for deformations with very small stretching, i.e. if $\lambda_s \approx \lambda_\varphi \approx 1$. Otherwise, the much larger stretching energy conceals the small mistakes in the anyway small bending energy. Here, however, we keep the full form (2.6) of the bending strains.

2.2.2. Finite strain elasticity

To deform an elastic shell, a certain amount of work is required. For hyperelastic materials, this work is stored in the deformed shape as an elastic energy, and so we have energy conservation. There exists a *surface energy density* $w_S(e_s, e_\varphi, K_s, K_\varphi)$ which measures the elastic energy that is stored in an infinitesimal patch of the membrane divided by the area that this patch takes in the *undeformed* configuration.

Several functions for the surface energy density w_S have been proposed to model various membrane materials [11, 49, 50, 58, 89], which show different large-strain behaviour. For small strains, they all can be reduced to *Hooke's law* [89],

$$w_S(e_s, e_\varphi, K_s, K_\varphi) = \underbrace{\frac{1}{2}\frac{E_{2\mathrm{D}}}{1-\nu^2}\left(e_s^2 + 2\nu e_s e_\varphi + e_\varphi^2\right)}_{w_{\text{stretch}}} + \underbrace{\frac{1}{2}E_B\left(K_s^2 + 2\nu K_s K_\varphi + K_\varphi^2\right)}_{w_{\text{bend}}}. \tag{2.7}$$

The two-dimensional Young modulus $E_{2\mathrm{D}}$, the two-dimensional Poisson ratio[1] ν and the bending stiffness E_B are material constants. Their physical interpretation will be discussed below in section 3.2 in the framework of linear elasticity theory.

Our motivation to write down the energy density (2.7) is that it is the simplest form which satisfies several conditions. The energy function should be symmetric with respect to interchanging the indices s and φ, so that the described material is isotropic (in its two dimensions). It must have a minimum at $e_s = e_\varphi = K_s = K_\varphi = 0$, so that the elastic tensions will always tend to restore the undeformed state. The simplest function to realise these requirements is a positive definite quadratic form like (2.7). We explicitly check that it is positive definite, because this limits the admissible range of the Poisson ratio ν. The stretching part of the energy density, for example, can be written as

$$w_{\text{stretch}} = (e_s, e_\varphi) \begin{pmatrix} \frac{1}{2}\frac{E_{2\mathrm{D}}}{1-\nu^2} & \frac{1}{2}\nu\frac{E_{2\mathrm{D}}}{1-\nu^2} \\ \frac{1}{2}\nu\frac{E_{2\mathrm{D}}}{1-\nu^2} & \frac{1}{2}\frac{E_{2\mathrm{D}}}{1-\nu^2} \end{pmatrix} \begin{pmatrix} e_s \\ e_\varphi \end{pmatrix} \tag{2.8}$$

[1] The two-dimensional Poisson ratio has different properties than the Poisson ratio from three-dimensional elasticity, which we denote as $\nu_{3\mathrm{D}}$ to avoid ambiguity.

and is positive definite if the eigenvalues of the matrix are positive. It is a standard calculation which shows that the eigenvalues are $\mu_1 = E_{2D}/2(1-\nu)$ and $\mu_2 = E_{2D}/2(1+\nu)$. They are both positive if the two-dimensional Poisson ratio is limited to $-1 < \nu < 1$. This coincides with the result of ref. [11] which is based on the investigation of isotropic tension, and is in contrast to the admissible range for the three-dimensional Poisson ratio $-1 \leq \nu_{3D} \leq 1/2$, see ref. [83].

In classical shell theory it is assumed that the shell consists of a (three-dimensional) elastic material that is homogeneous and isotropic. In the three-dimensional Hookean law, its elasticity is described by the Young modulus E and Poisson ratio ν_{3D} [83]. Then, the two-dimensional elastic moduli, which are to be used in the energy density (2.7), can be expressed in terms of E, ν_{3D} and the shell thickness H_0 [135]:

$$E_{2D} = EH_0, \quad \nu = \nu_{3D} \quad \text{and} \quad E_B = \frac{EH_0^3}{12(1-\nu^2)}. \tag{2.9}$$

Of course, ν inherits the allowable range $(-1, 1/2)$ from ν_{3D} in this case. The two-dimensional Hookean law introduced in (2.7), where $\nu \in (-1, 1)$, is thus more general; but values of ν larger than $1/2$ can only be realised with elastic materials that are not isotropic (in three dimensions) but have different elastic properties in normal direction. In such a more general case, the bending stiffness E_B is an autonomous parameter. The Poisson ratio for bending, which appears in the bending part w_{bend} of w_S, can then differ from the Poisson ratio for stretching used in the stretching part w_{stretch}. An example would be the Helfrich bending energy for vesicles [149], which corresponds to w_{bend} from (2.7) with $\nu = 1$ and simple curvature differences $\Delta\kappa_s$ and $\Delta\kappa_\varphi$ in place of the bending strains K_s and K_φ. However, we do not consider such models here.

From considerations of virtual displacements [151] or by descend from three-dimensional elasticity [89], it can be shown that the meridional stress and bending moment derive from the energy density via the *constitutive relations*

$$\tau_s = \frac{1}{\lambda_\varphi}\frac{\partial w_S}{\partial e_s} = \frac{E_{2D}}{1-\nu^2}\frac{1}{\lambda_\varphi}\left(e_s + \nu e_\varphi\right) \quad \text{and} \quad m_s = \frac{1}{\lambda_\varphi}\frac{\partial w_S}{\partial K_s} = E_B\frac{1}{\lambda_\varphi}\left(K_s + \nu K_\varphi\right), \tag{2.10}$$

and analogous for the circumferential (or hoop) stress and moment, τ_φ and m_φ, when all indices s and φ are interchanged. In our formalism that is based on the minimisation of an elastic energy functional, the stresses and moments are simply defined in terms of derivatives of the surface energy density. One could say that they are just abbreviations for these derivatives that occur in the calculus of variations below. But they have also a mechanical interpretation, as shown in fig. 2.4 below.

Stresses are forces per length. The factors $1/\lambda_\varphi$ in (2.10) occur because w_S is measured per unit area of the undeformed configuration, and $\partial w_S/\partial e_s$ is then a force per unit length of the undeformed configuration. Since the perimeter changes by the factor λ_φ upon deformation, τ_s as defined above is measured per unit length of the deformed configuration. This is the correct definition for the Cauchy stresses.

It is a legitimate question why we retain all the non-linearities in the shell theory, but use a simple Hookean energy density. When the energy density (2.7) is interpreted as a series expansion up to order $\mathcal{O}(\varepsilon^2)$ (where the strains are of order $e_i = \mathcal{O}(\varepsilon)$), then the Hookean constitutive relations (2.10) are accurate only to linear order in ε, and the prefactors $1/\lambda_i = 1 + \mathcal{O}(\varepsilon)$ in (2.10) could be neglected (shorthand notation with $i \in \{s, \varphi\}$). However, we want to have an energy functional at hand from which the shell theory and the shape equations follow by calculus of variations, because this allows us to discuss the stability of the shapes. When we retain all the non-linearities, our shape equations are fully consistent with the energy functional.

2.2.3. Derivation of equilibrium equations

The deformed configuration of the shell must satisfy equilibrium conditions, which can be derived by minimising the potential and elastic energy. The "ingredients" for the calculus of variations are just geometrical relations from section 2.2.1 and the constitutive relations in the form $\partial w_S/\partial e_s = \lambda_\varphi \tau_s$ and $\partial w_S/\partial K_s = \lambda_\varphi m_s$ (and analogous in φ-direction).

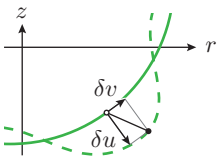

Figure 2.3.: Variation of the deformed shape

We consider a variation of the deformed shape $(r(s), z(s))$ by normal and tangential displacements δu and δv, see fig. 2.3,

$$\begin{pmatrix}\delta r\\ \delta z\end{pmatrix} = \begin{pmatrix}\sin\psi\\ -\cos\psi\end{pmatrix}\delta u + \begin{pmatrix}\cos\psi\\ \sin\psi\end{pmatrix}\delta v. \tag{2.11}$$

This leads to a variation of the elastic energy $U = \int w_S \,\mathrm{d}A_0$ (note that the energy density is measured per undeformed surface area element $\mathrm{d}A_0 = 2\pi r_0 \,\mathrm{d}s_0$),

$$\delta U = \int_0^{L_0} \mathrm{d}s_0\, 2\pi r_0 \left\{ \frac{\partial w_S}{\partial e_s}\,\delta e_s + \frac{\partial w_S}{\partial e_\varphi}\,\delta e_\varphi + \frac{\partial w_S}{\partial K_s}\,\delta K_s + \frac{\partial w_S}{\partial K_\varphi}\,\delta K_\varphi \right\}. \tag{2.12}$$

Furthermore, we assume that the normal pressure difference $p(s)$ that is applied to the shell (with $p > 0$ corresponding to an internal overpressure) is generated by a reservoir which has a potential energy P, the so-called load potential [89]. The variation of the load potential is obviously $\delta P = \int -p\,\delta u \,\mathrm{d}A$ since the normal displacement δu must work against the force $-p\,\mathrm{d}A$. The surface element of the deformed surface is given by $\mathrm{d}A = 2\pi r\,\mathrm{d}s = 2\pi r \lambda_s \,\mathrm{d}s_0$, and we obtain

$$\delta P = \int_0^{L_0} \mathrm{d}s_0 \left\{ -2\pi r \lambda_s\, p\, \delta u \right\}. \tag{2.13}$$

If the pressure p is constant over the whole shell surface, then the load potential is explicitly given by

$$P = -pV \quad \text{with the volume} \quad V = \int \pi r^2 \,\mathrm{d}z = \int_0^{L_0} \pi r^2 z'(s_0)\,\mathrm{d}s_0 \tag{2.14}$$

(a prime denotes from now on a derivative with respect to s_0). In appendix A.1 it is shown that this choice reproduces the variation (2.13); and the pressure p can be interpreted as a Lagrange multiplier that controls the shell volume V. The existence of a load potential is not essential to the derivation of the equilibrium equations. If the external forces on the shell are not conservative, a load potential does not exist. In this case, equation (2.13) is the amount of virtual work done by the variations and can still be used in the following steps. This covers, for example, the case of viscous traction when the shell is suspended in hydrodynamic flow, where in addition to $p\,\delta u$ a term $p_s\,\delta v$ must be included in (2.13), with p_s being the tangential force density exerted on the shell surface.

The variations must be written in terms of δu and δv to deduce the equilibrium equations. In appendix A.1 it is shown how the variations of the strains δe_i and δK_i are expressed in terms of δu and δv. With the geometric relations from section 2.2.1 and integration by parts, the total variation of the energy reduces to

$$\delta(U+P) = \int_0^{L_0} \mathrm{d}s_0\, 2\pi r \lambda_s \left\{ \delta u \left[\tau_s\kappa_s + \tau_\varphi\kappa_\varphi - p + \frac{1}{r}\frac{\mathrm{d}(rq)}{\mathrm{d}s} \right] + \delta v \left[\frac{\cos\psi}{r}\tau_\varphi + \kappa_s q - \frac{1}{r}\frac{\mathrm{d}(r\tau_s)}{\mathrm{d}s} \right] \right\} \tag{2.15}$$

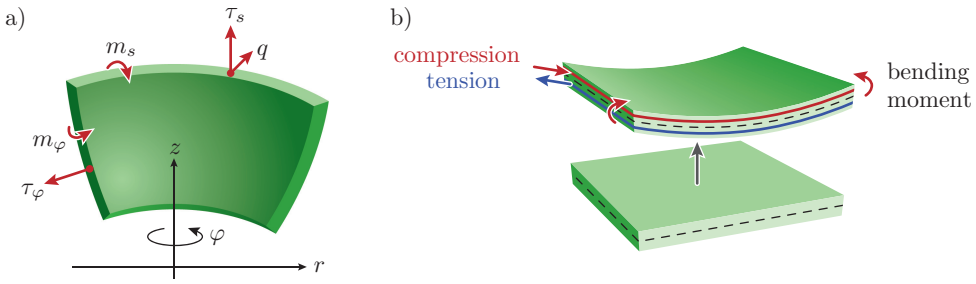

Figure 2.4.: a) Stresses and moments acting on a section of a shell. At the opposite faces, they point in opposite direction. The stresses τ_s and τ_φ act normal to the cross-section (i.e. tangential to the midsurface); the transverse shear stress q acts tangential to the cross-section but for symmetry reasons only on faces normal to the s-direction. The bending moments are trying to rotate the faces. b) The origin of the bending moments, here at the simpler example of a bent plate: When a plate is bent (without stretching the midsurface), inner layers (red) are compressed and outer layers (blue) are stretched. This stress couple gives the bending moment.

where the *transverse shear stress* q was introduced by $rq \equiv m_\varphi \cos\psi - \mathrm{d}(rm_s)/\mathrm{d}s$. The boundary terms from the integration by parts vanish for spherical shells, see appendix A.1.

For the equilibrium configuration, the first variation of the total energy must vanish for arbitrary δu and δv, and so we have the *equilibrium equations*

$$\begin{aligned} 0 &= \tau_s\kappa_s + \tau_\varphi\kappa_\varphi - p + \frac{1}{r}\frac{\mathrm{d}(rq)}{\mathrm{d}s} \\ 0 &= \frac{\cos\psi}{r}\tau_\varphi + \kappa_s q - \frac{1}{r}\frac{\mathrm{d}(r\tau_s)}{\mathrm{d}s} \\ 0 &= q + \frac{1}{r}\frac{\mathrm{d}(rm_s)}{\mathrm{d}s} - \frac{\cos\psi}{r}m_\varphi. \end{aligned} \tag{2.16}$$

They coincide with those presented in ref. [108] except for the sign convention of q; and they are equivalent to equations (L.12) - (L.15) of ref. [89] if the traction force p_T, the external stress couple l and the non-classical terms g and M_n are set to zero there.[2]

Instead of calculus of variations, force and torque balances can also be used to derive the equilibrium equations [89, 108]. In that approach, the physical interpretation of the stresses and bending moments becomes clearer; figure 2.4 a) shows on which sides the stresses and bending moments are pulling and twisting. If one considers the finite thickness of a bent plate or shell, one finds a stress variation across the thickness of the shell, where "stress" now refers to the components of the three-dimensional stress tensor [83]. This originates in the different compression and stretch of inner and outer layers, see fig. 2.4 b). Our two-dimensional stresses τ_s, τ_φ and q are simply the averages of the corresponding components of the three-dimensional stress over the shell thickness. The bending moments m_s and m_φ, on the other hand, are the first moments of the stress distribution across the thickness with respect to the midsurface.

2.2.4. Shape equations and their numerical solution

There are three groups of equations that determine the deformed shape of a shell: geometric relations from section 2.2.1, constitutive relations (2.10) and equilibrium equations (2.16).

[2] When comparing, note that in ref. [89] all quantities are referred to the reference shape, for example stresses are measured per unit length of the undeformed shape.

Among them are differential equations, which can be rearranged to form the *shape equations*

$$\begin{aligned} r'(s_0) &= \lambda_s \cos\psi, & \tau_s'(s_0) &= \lambda_s \left(\frac{\tau_\varphi - \tau_s}{r} \cos\psi + \kappa_s q \right), \\ z'(s_0) &= \lambda_s \sin\psi, & m_s'(s_0) &= \lambda_s \left(\frac{m_\varphi - m_s}{r} \cos\psi - q \right), \\ \psi'(s_0) &= \lambda_s \kappa_s, & q'(s_0) &= \lambda_s \left(-\kappa_s \tau_s - \kappa_\varphi \tau_\varphi - \frac{q}{r} \cos\psi + p \right). \end{aligned} \tag{2.17}$$

The equations in the left column follow from (2.3), the others from (2.16) when the derivatives with respect to s are replaced by derivatives with respect to s_0 by $\mathrm{d}/\mathrm{d}s_0 = \lambda_s \, \mathrm{d}/\mathrm{d}s$, see (2.4). Using s_0 as the independent variable has the advantage that its integration interval $[0, L_0]$ is known, whereas the arc length coordinate s runs up to an unknown deformed contour length L.

In order to close the system of shape equations, all functions appearing on the right-hand side must be expressed in terms of the basic functions r, z, ψ, τ_s, m_s and q. This is achieved by the geometric and constitutive relations that have not already been used for (2.17), rearranged in the set

$$\begin{aligned} \lambda_s &= (1-\nu^2)\, \lambda_\varphi \frac{\tau_s}{E_{2\mathrm{D}}} - \nu(\lambda_\varphi - 1) + 1, & \lambda_\varphi &= \frac{r}{r_0}, \\ K_s &= \frac{1}{E_B}\, \lambda_\varphi\, m_s - \nu\, K_\varphi, & K_\varphi &= \frac{\sin\psi - \sin\psi_0}{r_0}, \\ \kappa_s &= \frac{K_s + \kappa_{s_0}}{\lambda_s}, & \kappa_\varphi &= \frac{\sin\psi}{r}, \\ \tau_\varphi &= \frac{E_{2\mathrm{D}}}{1-\nu^2}\, \frac{1}{\lambda_s} \big((\lambda_\varphi - 1) + \nu\, (\lambda_s - 1) \big), & m_\varphi &= E_B\, \frac{1}{\lambda_s} \big(K_\varphi + \nu\, K_s \big). \end{aligned} \tag{2.18}$$

A problem arises when the right hand sides of (2.17) and (2.18) must be evaluated at the poles $s_0 = 0$ or $s_0 = L_0$ of a closed shell, where $r = r_0 = 0$ and some terms are ill-defined as ratios of two vanishing quantities. We can evaluate those terms analytically using L'Hôpital's rule and symmetry arguments, see appendix A.2, which gives

$$\begin{aligned} \lambda_s = \lambda_\varphi &= \frac{E_{2\mathrm{D}}}{E_{2\mathrm{D}} - \tau_s(1-\nu)}, & q' &= \lambda_s \left(\frac{p}{2} - \kappa_s\, \tau_s \right), \\ \kappa_s = \kappa_\varphi &= \frac{m_s}{E_B\, (1+\nu)} + \frac{\kappa_{s_0}}{\lambda_s}, & \tau_s' &= m_s' = 0 \end{aligned} \tag{2.19}$$

at $s_0 = 0$ and $s_0 = L_0$. With these expressions, the right-hand side of the shape equations can be evaluated numerically at $s_0 = 0$ and $s_0 = L_0$ without problems.

Next, boundary conditions for the shape equations must be defined. From the geometry of spherical shells, it is obvious that $r(0) = r(L_0) = 0$, otherwise the shell would have a gap. The z coordinate does not appear on the right hand side of the shape equations; thus the system is invariant with respect to a movement along the z axis. For simplicity, we choose $z(0) = 0$ in the numerical routines; the value $z(L_0)$ is then unknown a priori. The slope angle must satisfy $\psi(0) = 0$ and $\psi(L_0) = \pi$, so that the shell has no kinks at the poles, which would result in an infinite curvature and an infinite bending energy. The last boundary conditions concern the transverse shear stress, $q(0) = q(L_0) = 0$. These conditions are necessary so that the term q/r in the last of the shape equations does not diverge at the poles, see also appendix A.2. The case of a transverse shear stress diverging at the poles corresponds to an applied external point force [151] and will not be discussed here. To summarise, the boundary conditions are

$$\begin{aligned} &r(0) = 0, \quad z(0) = 0, \quad \psi(0) = 0, \quad q(0) = 0 && \text{at the south pole} \\ &\text{and} \quad r(L_0) = 0, \quad \psi(L_0) = \pi, \quad q(L_0) = 0 && \text{at the north pole.} \end{aligned} \tag{2.20}$$

There are *seven* boundary conditions to a system of *six* first-order differential equations, which produces some complications. To see why this is a problem, we must discuss how the shape equations will be solved numerically on the interval $s_0 \in [0, L_0]$. The technique employed here is called *parallel shooting* or *shooting to a fitting point* [14, 109]. We have seen that there are removable singularities in the shape equations at the end points of this interval. It is numerically impracticable to integrate *into* a removable singularity; therefore we split the integration interval in two, $I_1 = [0, L_0/2]$ and $I_2 = [L_0/2, L_0]$. The first interval will be integrated in forward direction, from 0 to $L_0/2$, and the second one in backward direction, from L_0 to $L_0/2$, so that we integrate in both intervals *away from* the singularity (see fig. 2.5).

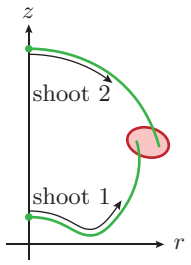

Figure 2.5.: Parallel shooting method

At both starting points of integration, 0 and L_0, initial values for the six basic functions r, z, ψ, τ_s, m_s and q must be specified so that the numerical integrator, e.g. a Runge-Kutta method, can start. The boundary conditions (2.20) provide some of these values; the other values must be guessed, they are free and are called the *shooting parameters*. In total, there are five shooting parameters: $\tau_s(0)$, $m_s(0)$, $z(L_0)$, $\tau_s(L_0)$ and $m_s(L_0)$.

At $L_0/2$, where the two solutions meet, we must enforce continuity conditions for the six basic functions $\boldsymbol{f} = (r, z, \psi, \tau_s, m_s, q)$ of the shape equations. We denote the two solutions as $\boldsymbol{f}_1(s_0)$ on the interval I_1 and $\boldsymbol{f}_2(s_0)$ on I_2. The residual $\boldsymbol{R} = \boldsymbol{f}_1(L_0/2) - \boldsymbol{f}_2(L_0/2)$ measures how much the continuity conditions are violated. It is a function of the shooting parameters, and its root must be searched by varying the shooting parameters. But since the residual has *six* components and there are only *five* shooting parameters, the system is overdetermined. This is the problem caused by the surplus boundary condition.

Astonishingly, we find that the overdetermined system does have a solution, i.e. all six components of the residual can be made zero by adjusting the five shooting parameters. An explanation of this phenomenological result was offered in the author's diploma thesis [151], and also published in [152]. There, the calculus of variations differs from our formulation here in that the variations δr and $\delta\psi$ of the radial coordinate and slope angle were used instead of δu and δv. This results in equilibrium equations that reproduce the first two of (2.16), but the last equilibrium equation is replaced by an algebraic relation for the transverse shear stress,

$$q = -\tau_s \tan\psi + \frac{1}{2}\, p\, \frac{r}{\cos\psi}. \tag{2.21}$$

lengths, volumes and curvatures	pressure and energy
$\tilde{r} = r/R_0, \quad \tilde{z} = z/R_0$	$\tilde{p} = R_0\, p/E_{2\mathrm{D}}$
$\tilde{V} = V/R_0^3, \quad \tilde{\kappa}_i = R_0\, \kappa_i$	$\tilde{U} = U/E_{2\mathrm{D}}\, R_0^2$
tensions	**bending moments**
$\tilde{\tau}_i = \tau_i/E_{2\mathrm{D}}, \quad \tilde{q} = q/E_{2\mathrm{D}}$	$\tilde{m}_i = m_i/R_0\, E_{2\mathrm{D}}$
elastic moduli	**bending strains**
$\tilde{E}_{2\mathrm{D}} = 1, \quad \tilde{E}_B = E_B/R_0^2\, E_{2\mathrm{D}}$	$\tilde{K}_i = R_0\, K_i$

Table 2.1.: Overview of reduced variables for spherical shells (indices $i \in \{s, \varphi\}$). Adapted from the author's diploma thesis [151].

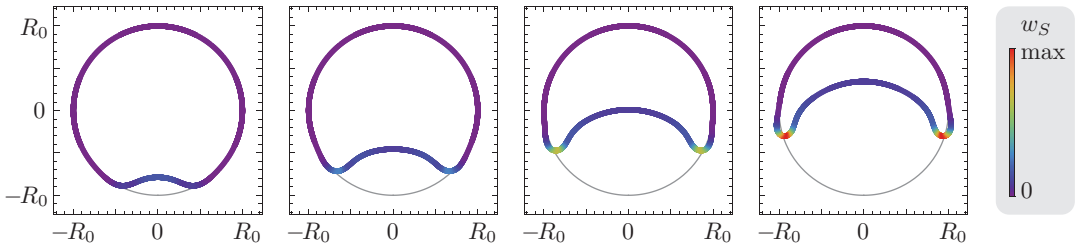

Figure 2.6.: Buckled shapes of a spherical shell. Shown are parametric plots of the shell contour $(r(s_0), z(s_0))$, which are coloured according to the energy density w_S. The pressure was adjusted so that the deflated shells have a volume of $V/V_0 = 0.98, 0.9, 0.7, 0.5$ (from left to right) and the elastic moduli are $\tilde{E}_B = 0.0001$ and $\nu = 1/3$.

It can be easily verified that this expression satisfies the differential equilibrium equations (2.16). Let us assume that we have adjusted the shooting parameters so that the first five components of the residual vanish. The algebraic relation (2.21) then asserts that also the last component of the residual vanishes, because q is expressed in terms of continuous functions and must be continuous, too. So the continuity condition for q (or the last component of the residual) may be dropped, and we finally arrive at five continuity conditions which can be satisfied by adjusting five shooting parameters. In principle, the differential equation for q could be dropped from the shape equations (2.17), because q can be calculated from (2.21) in each integration step. This, however, would lead to numerical problems due to the (removable) singularity in (2.21) at points where $\psi = \pi/2$.

For a numerical solution of the shape equations, it is advantageous to introduce dimensionless quantities. To this end, we choose R_0 as the length unit and E_{2D} as the tension unit, which results in the reduced quantities summarised in table 2.1. In the shape equations, all dimensional quantities can then be replaced by the dimensionless ones, and R_0 and E_{2D} are set to 1. Of special importance is the reduced bending stiffness. For thin shells of isotropic three-dimensional material, see (2.9), it reads

$$\tilde{E}_B = \frac{E_B}{R_0^2\, E_{2D}} = \frac{H_0^2}{12(1-\nu^2)R_0^2} = \frac{1}{\gamma_{FvK}} \tag{2.22}$$

and is the inverse of the *Föppl-von-Kármán-number* γ_{FvK}. It is independent of the Young modulus; in fact, the value of the Young modulus does not enter the non-dimensional shape equations at all. The reduced bending stiffness and the Poisson ratio are the only material properties in the shape equations and completely govern the shape of the shell.

Now, the system (2.17) can be solved numerically. The parallel shooting method can be improved by using a multiple shooting method [122] for both shoots 1 and 2 in fig. 2.5, which enhances the convergence. The numerical code calculates shapes for successively changed pressure $p < 0$ using parameter tracing. Figure 2.6 presents some typical solutions of the shape equations. The largest strains occurring in the plotted shapes are around $\lambda_\varphi \approx 0.05$. This justifies the usage of Hookean elasticity, which is valid only for small strains.

2.2.5. Shape equations for self-contacting shapes

For very large deflation, the original shape equations (2.17) predict self-intersecting shapes, see fig. 2.7 on the left, which is clearly unacceptable. We want to replace these self-intersecting shapes by configurations where the opposite sides of the shell are in contact with each other. An

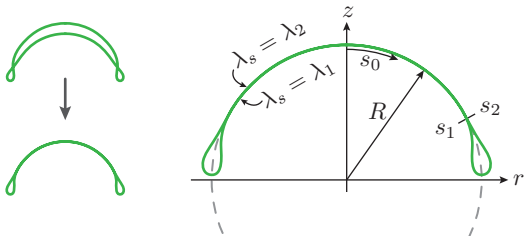

Figure 2.7.: Shell configurations with opposite sides in contact, to replace self-intersecting shapes. The region of self-contact is assumed to be a spherical cap of radius R, limited by the coordinates $s_0 = s_1$ and s_2. The two sides meeting there are allowed to have constant meridional stretches λ_1 and λ_2, respectively.

exact solution to this problem seems very hard to find, because the constraint of no intersection is difficult to handle in the variational analysis of the elastic energy functional. However, an approximate model can easily be constructed and yields plausible results.

In this approach, see fig. 2.7, the complete shape consists of a region of self-contact which is connected to a free region. In the free region, the only external force is the pressure p, and its shape is therefore determined by the usual shape equations (2.17). Additional contact forces may act on the self-contacting region, and so its shape is not a solution of the shape equations. Motivated by the shape of the self-intersecting configurations, we assume that the contact region can be modelled as a spherical cap, see fig. 2.7. This is a reasonable approach because the parts that are in contact are then deformed nearly isometrically, which is energetically favourable.

In the spherical cap of radius R, a region $s_0 \in [0, s_1]$ (termed region 1) around the south pole meets a region $s_0 \in [s_2, L_0]$ (region 2) around the north pole. In addition, the two regions may suffer an in-plane deformation described by constant meridional stretches $\lambda_s(s_0) = \lambda_1$ in region 1 and $\lambda_s(s_0) = \lambda_2$ in region 2. These two stretches may be different, but they are not independent. They must satisfy the constraint $\lambda_1 s_1 = \lambda_2(L_0 - s_2)$ which ensures that the deformed arc lengths of regions 1 and 2 are equal (see fig. 2.7 for the positions of s_1 and s_2). Thus, the deformation of regions 1 and 2 is completely described by the four parameters R, s_1, s_2 and λ_1 in this simplified model.

To derive an explicit parametrisation of the shape in the region of self-contact, we notice that the deformed arc length s is given by $s(s_0) = \lambda_1 s_0$ in region 1. The spherical cap with radius R is then parametrised by

$$r(s_0) = R \sin\left(\frac{s_0\lambda_1}{R}\right), \quad z(s_0) = R\cos\left(\frac{s_0\lambda_1}{R}\right) \quad \text{and} \quad \psi(s_0) = -\frac{s_0\lambda_1}{R} \tag{2.23}$$

on $0 \le s_0 \le s_1$. We eventually choose s_0 instead of s as the coordinate because this facilitates the connection with the free region. The strains are then given by

$$\lambda_s = \lambda_1, \quad \text{and} \quad \lambda_\varphi = \frac{r}{r_0} = \frac{R}{R_0}\frac{\sin(s_0\lambda_1/R)}{\sin(s_0/R_0)}. \tag{2.24}$$

Since the curvature of region 1 is nearly inverted, $\kappa_s = \kappa_\varphi = -1/R$, the bending strains read

$$K_s = \lambda_s\kappa_s - \kappa_{s_0} = -\lambda_1/R - 1/R_0 \quad \text{and} \quad K_\varphi = -\lambda_\varphi(s_0)/R - 1/R_0. \tag{2.25}$$

From Hooke's law (2.10) the stresses and moments in region 1 can now be evaluated.

The shape, strains and stresses of region 2 can be derived analogously, based on the arc length $s(s_0) = [L_0 - s_0]\lambda_2$ that is now measured from the north pole on. The final parametrisation is then

$$r(s_0) = R\sin\left(\frac{[L_0 - s_0]\lambda_2}{R}\right), \quad z(s_0) = R\cos\left(\frac{[L_0 - s_0]\lambda_2}{R}\right), \quad \psi(s_0) = -\frac{[L_0 - s_0]\lambda_2}{R} + \pi,$$

$$\begin{aligned} \lambda_s &= \lambda_1, & \lambda_\varphi &= \frac{R}{R_0}\frac{\sin([L_0 - s_0]\lambda_2/R)}{\sin(s_0/R_0)}, \\ K_s &= \lambda_2/R - 1/R_0, & K_\varphi &= \lambda_\varphi(s_0)/R - 1/R_0 \end{aligned} \tag{2.26}$$

on $s_2 \le s_0 \le L_0$. It should be noted that there is a sign change in the first terms of the bending strains, because the curvature of region 2 is not inverted; it only changes from $1/R_0$ to $1/R$.

The free part of the shell is governed by the force balance with the pressure p as the only external force. Therefore, the original system of shape equations (2.17) can be used to calculate the shape of the free part when appropriate boundary conditions are used. The shape equations are six coupled first-order differential equations, which are integrated from $s_0 = s_1$ to s_2 with a shooting method. There are, thus, six initial conditions at the starting point of integration, plus the four parameters R, s_1, s_2 and λ_1 of the self-contacting region. That are, in total, ten shooting parameters which can be chosen to enforce continuity conditions at the junction of the free and self-contacting region. We select the functions r, z, ψ, τ_s and m_s for which continuity conditions are imposed at the end points s_1 and s_2 of the integration interval, which are ten conditions in total,

$$\begin{aligned} r(s_1) &= R\sin(s_1\lambda_1/R), & r(s_2) &= R\sin(s_1\lambda_1/R), \\ z(s_1) &= R\cos(s_1\lambda_1/R), & z(s_2) &= R\cos(s_1\lambda_1/R), \\ \psi(s_1) &= -s_1\lambda_1/R, & \psi(s_2) &= -s_1\lambda_1/R + \pi, \\ \tau_s(s_1) &= \frac{E_{2D}}{(1-\nu^2)}\frac{\lambda_1 - 1 + \nu(\lambda_{\varphi 1} - 1)}{\lambda_{\varphi 1}}, & \tau_s(s_2) &= \frac{E_{2D}}{(1-\nu^2)}\frac{\lambda_2 - 1 + \nu(\lambda_{\varphi 2} - 1)}{\lambda_{\varphi 2}}, \\ m_s(s_1) &= \frac{E_B}{\lambda_{\varphi 1}}\left(-\frac{\lambda_1 + \nu\lambda_{\varphi 1}}{R} - \frac{1+\nu}{R_0}\right), & m_s(s_2) &= \frac{E_B}{\lambda_{\varphi 2}}\left(\frac{\lambda_2 + \nu\lambda_{\varphi 2}}{R} - \frac{1+\nu}{R_0}\right) \\ \text{with} \quad \lambda_{\varphi 1} &= R\sin(s_1\lambda_1/R)/R_0\sin(s_1/R_0), & \lambda_{\varphi 2} &= R\sin(s_1\lambda_1/R)/R_0\sin(s_2/R_0). \end{aligned} \tag{2.27}$$

Thus, the only quantity for which no continuity condition is imposed is the transverse shear stress q. In our current formulation, we have no expression for q in the self-contacting region. In principle, the equilibrium equations (A.10) can be used to determine the transverse shear stress $q(s_0)$, along with the tangential and normal force densities $p_s(s_0)$ and $p_n(s_0)$ (which may be non-constant in the contacting region since the simple hydrostatic pressure is supplemented by contact forces exerted from region 1 onto region 2 and vice versa). We do not carry out this analysis here, but there is some evidence that q will indeed have a discontinuity at s_1 and s_2: In the numerical solutions it can be observed that the derivative $m_s'(s_0)$ is discontinuous at s_1 and s_2, and this results according to the last of the stability equations (2.16) in a discontinuity in q. This is a very typical behaviour for shells which are in contact with an obstacle, for example with a rigid wall, see ref. [4] section 14.6. A discontinuity in the transverse shear stress is, by virtue of the first of the equilibrium equations (2.16), related to an external normal pressure p_n that contains a Dirac δ-function. This divergence is smoothed out over a length scale of the shell's thickness when a refined shell theory, which considers effects from the finite shell thickness, is used [4].

Numerical solutions of the proposed model for self-contacting shapes can be obtained with the parallel shooting method described above. The same nondimensionalisation as before can be used, see table 2.1. Solutions for the same elastic parameters as used in fig. 2.6 show that the strains stay relatively small, even when the shell is heavily deflated with $V/V_0 \approx 0.002$: Then the maximum strain is around $\lambda_s \approx 0.008$.

2.3. Analytic model for buckled spherical shells

Before discussing the behaviour of spherical shells upon deflation in detail in section 2.4, we will first develop an approximate, analytic model for buckled shapes. This approach was proposed by Pogorelov [107], we summarise his reasoning here and analyse his results. The approximations that will be introduced in the mathematical formulation are satisfied if the dimple has a small but finite size, and for small reduced bending stiffnesses $\tilde{E}_B \ll 1$.

The basic idea is that for small bending stiffness, the shape of the axisymmetric dimple will be close to an *isometric deformation* of the sphere: a shape where a spherical cap is mirror inverted (see fig. 2.8, grey lines). As it is isometric to the sphere, this shape is free of stretching. For vanishing bending stiffness, $E_B = 0$, this shape has therefore vanishing elastic energy. However, the bending strain at the edge of the inverted cap is infinitely large, which gives rise to infinitely large bending energy for $E_B > 0$. Thus, switching from $E_B = 0$ to $E_B > 0$, the sharp edge of the dimple has to be smoothed out.

In order to describe the deformation from the isometric shape to the final smooth shape, we follow the ideas of Pogorelov and introduce displacements $u(s_0)$ and $v(s_0)$ in r- and z-direction, respectively, see fig. 2.8. Assuming that u and v are small, we use linear shell theory to calculate the bending and stretching energies in the final shape. This technique is quite remarkable because it enables us to describe large deformations with linear shell theory by choosing not the undeformed shape as reference state, but the isometric buckled shape.

First, there are geometric relations for isometric deformations of spheres, which are obtained by mirror reflection of a spherical cap, see fig. 2.8 a). The resulting dimple is characterised by its opening angle α, from which we can calculate the dimple radius r_D, depth h and volume difference $\Delta V = V_0 - V$. For later use, we already introduce a first order approximation in α, since we will assume that the dimple is small compared to R_0. The exact and approximated relations then read

$$\begin{aligned} r_D &= R_0 \sin\alpha \approx \alpha R_0, \quad h = R_0 - R_0\cos\alpha \approx \alpha^2 R_0/2 \quad \text{and} \\ \Delta V &= 2h^2\pi(3R_0 - h)/3 \approx \pi\alpha^4 R_0^3/2. \end{aligned} \tag{2.28}$$

In order to evaluate the elastic energies in the final shape, we split it into different regions which are investigated separately. We define the inner neighbourhood G_i and outer neighbourhood G_o of the dimple edge (see fig. 2.8) as the regions in which the displacements (u, v) are significant. This is only the case in a narrow strip to both sides of the dimple edge, see (2.35) below. Outside these regions, the displacements are negligible; these regions are referred to as G_2 (for the rest of the dimple) and G_1 (for the rest of the undeformed part).

The elastic energies that we have to evaluate consist of the bending needed to invert the curvature in G_2, and the bending and stretching due to the displacements in G_i and G_o. The uniform compressive strains in G_1 and G_2, which result from the negative inner pressure and which are already present in the spherical (prebuckled) shape, are neglected. This is justified if

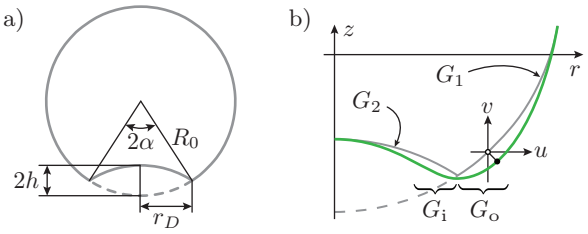

Figure 2.8.: Midsurface geometry in the analytic model. a) Isometric deformation, where a spherical cap of radius r_D and depth h is mirror inverted. b) The final shape (green line) differs from the isometric shape by small displacements (u, v).

the pressure is small. The pressure in a buckled shell is of the order of the classical buckling pressure [83, 135] $p_{\mathrm{cb}} = -4\sqrt{E_{2\mathrm{D}}E_B}/R_0^2$, which can be written according to table 2.1 in the dimensionless form $\tilde{p}_{\mathrm{cb}} = -4\sqrt{\tilde{E}_B}$. Conclusively, the assumption is satisfied for small reduced bending stiffnesses $\tilde{E}_B$.

The bending energy in G_2 is readily written down. From the spherical shape to the isometric deformed shape, the curvatures change from $1/R_0$ to $-1/R_0$, thus giving bending strains $K_s = K_\varphi = -2/R_0$, where the stretches in the definition (2.6) are neglected. The energy density (2.7) is integrated over the area of the inverted spherical cap. We neglect that the area of the dimple should be reduced by the area of G_{i} since we assume that G_{i} is much smaller than G_2, and hence the area of G_2 is $A(G_2) = 2\pi h R_0 \approx \pi\alpha^2 R_0^2$. Thus, the bending energy in G_2 reads

$$U_B(G_2) = \frac{1}{2}E_B \int_{G_2} \mathrm{d}A \left\{K_s^2 + 2\nu K_s K_\varphi + K_\varphi^2\right\} = 4\pi\alpha^2 E_B(1+\nu). \tag{2.29}$$

In the region G_{o}, the deformation energy is governed by the displacements $u(s_0)$ and $v(s_0)$ (where s_0 is the undeformed arc length). From "graphic considerations" [107] Pogorelov concludes that a meridian will not stretch or compress very much: $e_s \approx 0$. Using the nonlinear shape equations, it was checked that this assumption holds, even for quite large dimples, if the Poisson ratio is not too large and the reduced bending stiffness is small. However, this approximation is probably the most inaccurate one introduced in the Pogorelov model, but necessary to advance analytically. The stretching of circumferential fibres results in the strain $e_\varphi = u(s_0)/r_0(s_0) \approx u(s_0)/r_D$, see eq. (2.5), where the approximation holds if G_{o} is sufficiently narrow. The integration of the stretching energy is performed over the area element $\mathrm{d}A_0 \approx 2\pi r_D \mathrm{d}s_0$ with $s_0 \in [0, \varepsilon]$. Here the arc length coordinate was centred around the dimple edge and runs up to a point ε where the displacements have decayed sufficiently to be neglected. The stretching energy of the outer neighbourhood is thus given by[3]

$$U_S(G_{\mathrm{o}}) = \frac{1}{2}\frac{E_{2\mathrm{D}}}{1-\nu^2}\int_{G_{\mathrm{o}}} e_\varphi^2 \,\mathrm{d}A_0 = \frac{\pi E_{2\mathrm{D}}}{(1-\nu^2)r_D}\int_0^\varepsilon u(s_0)^2 \,\mathrm{d}s_0. \tag{2.30}$$

Pogorelov approximates the bending strains as $K_s = v''(s_0)$ and $K_\varphi = v'(s_0)/\alpha R_0$. In the integral of the bending energy, a term $v'(s_0)v''(s_0)$ occurs, which can be readily integrated to $v'(s_0)^2/2$, and we need to specify boundary conditions for the displacement v to proceed. We require the dimple to have a horizontal tangent at the dimple edge $s_0 = 0$, hence $-v'(0) = \sin\alpha \approx \alpha$. At the other end $s_0 = \varepsilon$, the displacement shall have decayed and we enforce $v(\varepsilon) = v'(\varepsilon) = 0$. The resulting expression for the bending energy is

$$U_B(G_{\mathrm{o}}) = \pi E_B r_D \int_0^\varepsilon v''(s_0)^2 \,\mathrm{d}s_0 - \pi\alpha E_B \nu r_D/R_0. \tag{2.31}$$

In total, the elastic energy of the outer neighbourhood G_{o} is therefore given by

$$U(G_{\mathrm{o}}) = \int_0^\varepsilon \mathrm{d}s_0 \left\{\pi E_B r_D v''(s_0)^2 + \frac{\pi E_{2\mathrm{D}} u(s_0)^2}{(1-\nu^2)r_D}\right\} - \pi\alpha E_B \nu \frac{r_D}{R_0}. \tag{2.32}$$

Analogously, the elastic energy of the inner neighbourhood G_{i} can be calculated. The stretching energy is the same as for the outer neighbourhood. The bending strains have to be modified because we have to take into account that the curvature of the inverted cap is already

[3] In ref. [107] the prefactor of the integral is wrong, but the results presented there are correct.

inverted, and we get $K_s = v''(s_0) - 2/R_0$ and $K_\varphi = -v'(s_0)/\alpha R_0 - 2/R_0$. The resulting elastic energy of the inner neighbourhood is given by

$$U(G_\mathrm{i}) = \int_{-\varepsilon}^{0} \mathrm{d}s_0 \left\{ \pi E_B r_D v''(s_0)^2 + \frac{\pi E_{2\mathrm{D}} u(s_0)^2}{(1-\nu^2) r_D} \right\} - 4\pi\alpha E_B (1+\nu) \frac{r_D}{R_0} + \pi\alpha E_B \nu \frac{r_D}{R_0}. \quad (2.33)$$

The integrand coincides with the result (2.32) for the outer neighbourhood; only the constant terms differ.

To find the functions $u(s_0)$ and $v(s_0)$ which represent the final shape, we have to minimise the functional of total elastic energy with respect to u and v. During the variation $u \to u + \delta u$ and $v \to v + \delta v$ we keep the parameters α, h, r_D and ΔV of the isometric shape constant. Since the volume change due to u and v can be neglected (compared to the large ΔV due to the isometric deformation), this corresponds to a variation at constant shell volume, and we do not need to introduce a Lagrange multiplier controlling the volume. As the integrals in the elastic energies of the inner and outer neighbourhood are identical, we expect a symmetric shape of the dimple, with an odd function $u(s_0)$ and an even function $v(s_0)$. It is thus sufficient to determine the solution on the interval $s_0 \in [0, \varepsilon]$ by minimising (2.32).

During the minimisation we have to impose a constraint on u and v, because the energy functional was set up under the assumption of vanishing (or negligible) meridional strain $e_s = 0$. The final solution must satisfy this condition, which can be written as

$$u'(s_0) + \alpha v'(s_0) + \frac{1}{2} v'(s_0)^2 = 0. \quad (2.34)$$

Furthermore, the variation has to respect the boundary conditions, which are evident from geometrical considerations: $u(0) = 0$ so that the shell is not ripped apart at the dimple edge, $v'(0) = -\alpha$ for a horizontal tangent at the dimple edge, and $u(\varepsilon) = v(\varepsilon) = v'(\varepsilon) = 0$ because the displacements must have decayed at $s_0 = \varepsilon$.

The number of parameters in the problem can be greatly reduced with a suitable nondimensionalisation by introducing characteristic length and energy scales. Inspection of the integrand in (2.32) and the constraint (2.34) shows that the substitutions

$$s_0 = \xi \bar{s}_0, \quad u = \xi \alpha^2 \bar{u}, \quad \frac{\mathrm{d}v}{\mathrm{d}s_0} = \alpha \bar{w} \quad \text{with} \quad \xi \equiv \left[\tilde{E}_B (1-\nu^2)\right]^{1/4} \left(\frac{R_0 r_D}{\alpha}\right)^{1/2} \quad (2.35)$$

with a typical arc length scale ξ prove useful. For small $\tilde{E}_B \ll 1$, the length scale $\xi \ll R_0$ is also small, which shows that the regions G_i and G_o are indeed narrow strips as announced when they were defined above. The substitutions lead to a dimensionless form of the energy (2.32),

$$U(G_\mathrm{o}) = U_\xi \int_0^{\bar{\varepsilon}} \mathrm{d}\bar{s}_0 \left\{ \bar{w}'(\bar{s}_0)^2 + \bar{u}(\bar{s}_0)^2 \right\} + C \quad \text{with} \quad U_\xi \equiv \pi \alpha^{5/2} r_D^{1/2} R_0^{3/2} \frac{E_{2\mathrm{D}} \tilde{E}_B^{3/4}}{(1-\nu^2)^{1/4}}, \quad (2.36)$$

where the constant terms are gathered in C and U_ξ is the energy scale. Using the geometric relations (2.28), the scaling parameters ξ, U_ξ, and α can be expressed as functions of the elastic moduli, the shell radius R_0, and the reduced volume difference $\Delta V/V_0$ (or alternatively the reduced volume V/V_0 with $V = V_0 - \Delta V$). Inverting the exact geometric relations is possible but quite elaborate, and is best handled with a computer algebra system. This results in the

scaling factors

$$\begin{aligned} \alpha &= \arccos\left(2\cos\left(\frac{1}{3}\left[\pi + \arctan\sqrt{(V_0/V)^2 - 1}\right]\right)\right), \\ \xi = R_0\sqrt{\frac{\sin\alpha}{\alpha}}\left[\tilde{E}_B(1-\nu^2)\right]^{1/4} \quad &\text{and} \quad U_\xi = \pi E_{2\mathrm{D}} R_0^2\sqrt{\alpha^5\sin\alpha}\,\frac{\tilde{E}_B^{3/4}}{(1-\nu^2)^{1/4}}. \end{aligned} \tag{2.37}$$

Starting from the the first-order approximations for the geometric relations, simpler scaling parameters are obtained,

$$\alpha \approx \left(\frac{8}{3}\frac{\Delta V}{V_0}\right)^{1/4}, \quad \xi \approx R_0\left[\tilde{E}_B\left(1-\nu^2\right)\right]^{1/4}, \quad U_\xi \approx \pi\frac{E_{2\mathrm{D}}\,R_0^2}{\left(1-\nu^2\right)^{1/4}}\left(\frac{8}{3}\tilde{E}_B\frac{\Delta V}{V_0}\right)^{3/4}, \tag{2.38}$$

which will be useful for further analytic calculations. We must keep in mind that they are only accurate for small dimples, i.e. for $\Delta V \ll V_0$.

Both the arc length scale ξ and the energy scale U_ξ emerge from the competition of stretching and bending energies in (2.32) (under the constraint (2.34)): ξ gives the typical arc length size of the neighbourhoods G_i and G_o, and U_ξ gives the typical energy of the buckled configuration. In the literature, this Föppl-von-Kármán length scale is often written as $\xi \sim \sqrt{R_0 H_0}$, the geometric average of shell radius and thickness [83]. The final result for the Pogorelov buckling energy, which is obtained after minimisation of the total energy with respect to u and v will differ from U_ξ only by a numerical prefactor, see eq. (2.44) below.

For the minimisation of the total energy, the integral in eq. (2.36) has to be minimised. Note that the limit $\bar{\varepsilon}$ of the integral has been rescaled, too, according to $\varepsilon = \xi\bar{\varepsilon}$. Following Pogorelov, we consider the case of small $\tilde{E}_B$, where $\bar{\varepsilon} \to \infty$ because $\xi \to 0$ according to (2.37) and (2.38). Thus our task for the calculus of variations is to minimise the functional

$$J[\bar{u},\bar{w}] = \int_0^\infty \mathrm{d}\bar{s}_0\left\{\bar{w}'^2 + \bar{u}^2\right\} \tag{2.39}$$

subjected to the constraint (2.34) which reads

$$\bar{u}' + \bar{w} + \frac{1}{2}\bar{w}^2 = 0 \tag{2.40}$$

in rescaled variables and with boundary conditions

$$\bar{u}(0) = 0, \quad \bar{w}(0) = -1, \quad \bar{u}(\infty) = 0, \quad \bar{w}(\infty) = 0. \tag{2.41}$$

Pogorelov solved the constrained variational problem analytically. His results for the minimising functions $\bar{u}(\bar{s}_0)$ and $\bar{w}(\bar{s}_0)$ are presented in appendix B. These functions are defined piecewise, due to some simplifications, on two intervals $\bar{s}_0 \in [0,\sigma)$ and $\bar{s}_0 \in [\sigma,\infty)$, where the optimal choice for σ is $\sigma_\mathrm{min} = 1.24667$. The minimal value of the functional is found to be $J_\mathrm{min} = 1.15092$.

Now we can switch back from the rescaled quantities to physical quantities in order to analyse the features of Pogorelov's model, plot solutions and compare them to our results from the nonlinear shape equations. The rescaling of the displacements u and v describing the shape is obviously given by (2.35). We also have to take into account that the origin of s_0 was shifted to the dimple edge. In the coordinate system of the nonlinear shape equations, the origin of s_0 starts at the south pole of the capsule, and the dimple edge (of the isometric deformation)

is located at $s_D = \alpha R_0$. When comparing these solutions, the functions from the Pogorelov model must be shifted.

The displacements $u(s_0)$ and $v(s_0)$ can be used to plot the deformed shape and to calculate further properties, like curvatures and tensions. With the strain definitions $e_s = 0$ and $e_\varphi = u/r_D$ we see that the maximum strain scales like $e_\varphi \sim (\tilde{E}_B \Delta V/V_0)^{1/4}$. This shows again that the strains remain small throughout the deformation if the reduced bending stiffness $\tilde{E}_B$ is small, see also fig. 2.9 a) where the reduced tension $\tau_\varphi/E_{2\mathrm{D}} \sim e_\varphi$ is plotted. From the strains we obtain the stresses with the Hookean law (2.10),

$$\tau_\varphi = \frac{E_{2\mathrm{D}}}{1-\nu^2}\frac{u(s_0-s_D)}{r_D} \quad \text{and} \quad \tau_s = \nu\,\tau_\varphi \tag{2.42}$$

in linearised form, i.e. the prefactors $1/\lambda_i$ have been omitted. The definitions of the bending strains imply curvatures

$$\kappa_s = \begin{cases} -1/R_0 + v''(s_0-s_D), & s_0 < s_D \\ 1/R_0 + v''(s_0-s_D), & s_0 \geq s_D \end{cases} \quad \text{and} \quad \kappa_\varphi = \begin{cases} -1/R_0 + v'(s_0-s_D)/\alpha R_0, & s_0 < s_D \\ 1/R_0 + v'(s_0-s_D)/\alpha R_0, & s_0 \geq s_D \end{cases} \tag{2.43}$$

The total elastic energy is obtained by adding $U(G_2) + U(G_\mathrm{o}) + U(G_\mathrm{i})$. We see that the constant terms cancel each other, and only the integral terms of $U(G_\mathrm{i})$ and $U(G_\mathrm{o})$ survive. Each integral gives $J_{\min} U_\xi$. Our final result for the elastic energy of an axisymmetric buckled shell with a given volume difference is

$$U_{\mathrm{Pog}} = 2J_{\min}U_\xi \approx 2\pi J_{\min}\left(\frac{8}{3}\right)^{3/4}\frac{E_{2\mathrm{D}}}{\left(1-\nu^2\right)^{1/4}}\left(\tilde{E}_B\frac{\Delta V}{V_0}\right)^{3/4} R_0^2. \tag{2.44}$$

Here, the simplified scaling factors (2.38) are used and so this result is valid only for small volume differences.

2.4. Buckled shapes of deflated spherical shells

With the shape equations and the Pogorelov model, we have two models at hand to calculate the shape of a deflated spherical shell. In the author's diploma thesis [151], the shape equations were analysed in detail, and a rich bifurcation behaviour was found, see also ref. [152]. Various solution branches with axisymmetric buckled and crumpled shapes were found and traced, but the shape with a single dimple was found to have the least elastic energy and therefore represents the ground state of the deflated shell. This is in accordance with experiments [15,45,97,98,113,116], simulations [112,113,138,140] and some analytic estimates [112,138] which are based on a short account of Pogorelov's model given by Landau and Lifshitz [83].

From eq. (2.44) it can be easily seen that shapes with one dimple are energetically favourable to shapes with several, say N, dimples. When we impose a volume difference ΔV, the elastic energy of a shape with one dimple is $\tilde{U}_1 \sim (\tilde{E}_B\,\Delta\tilde{V})^{3/4}$ in reduced units. If the volume is divided into N smaller dimples, each contributes $(\tilde{E}_B\,\Delta\tilde{V}/N)^{3/4}$ to the total elastic energy $\tilde{U}_N \sim N(\tilde{E}_B\,\Delta\tilde{V}/N)^{3/4} \sim N^{1/4}$. The smallest elastic energy is thus assumed by the shape with only $N = 1$ dimple.

Strictly speaking, this justification is only valid when the internal volume of the shell is prescribed, and not, for example, when the pressure exerted on the shell is prescribed and the shell volume adjusts itself. For this pressure-controlled case, however, it was shown in

the author's diploma thesis that shapes with a single dimple are still preferred to shapes with two dimples. For the case of osmotically induced buckling discussed below, where neither the internal shell volume nor the pressure difference is prescribed, we will provide an argument in section 2.5.4 asserting that shapes with a single dimple are the energetical ground state also for buckling under osmosis.

Therefore, we focus the discussion of the results in the following on the most relevant shape with one axisymmetric dimple.

2.4.1. Solutions of the shape equations and the analytic model

For the shape equations, solutions can be obtained numerically for given elastic moduli $\tilde{E}_B$ and ν, and the pressure p can be adjusted to meet a given shell volume. Solutions of the Pogorelov model are obtained by proper rescaling of the dimensionless functions $\bar{u}$ and $\bar{w}$; they depend on the shell volume and elastic moduli because the rescaling parameters do. In the Pogorelov model, the same length and tension units (R_0 and E_{2D}, respectively) as in the shape equations are used for the plots that are presented here.

Figure 2.9 compares typical solutions of the shape equations and analytic model. The circumferential stress τ_φ is quite consistent in both models, but there are considerable deviations in the meridional stress τ_s which can be attributed to Pogorelov's strong simplification of vanishing meridional strain $e_s = 0$. We see a characteristic region of strong circumferential compression that is located in the inner neighbourhood of the dimple edge, in which the models even agree quantitatively. In the outer neighbourhood of the dimple edge, a corresponding region of strong hoop stretch is present. A simple explanation why hoop compression arises in the inner neighbourhood and stretch in the outer neighbourhood of the dimple edge is evident from fig. 2.8 b): Upon smoothing of the dimple edge, the inner neighbourhood G_i is displaced horizontally to the left, and the outer neighbourhood G_o to the right. Thus, the circumferential fibres of the inner neighbourhood are compressed and those of the outer neighbourhood are stretched. The compressive peak of the hoop stress will form the basis for our explanation of the secondary buckling transition, where the dimple loses its axisymmetry by wrinkles appearing in this compressive region.

Both models also agree very well concerning the curvatures and the shape. Due to the piecewise definitions of the displacements in the Pogorelov model, the meridional curvature κ_s is discontinuous; but nevertheless it approximates the exact numerical result of the shape

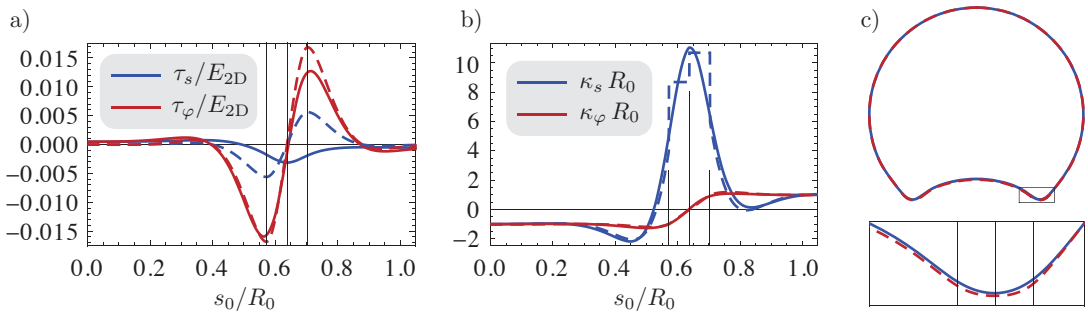

Figure 2.9.: Comparison of the shape equations and analytic model. The solutions for a) tensions, b) curvatures and c) the shape are plotted for the shape equations (continuous lines) and Pogorelov model (dashed lines), with parameter values $\Delta V/V_0 = 0.05$, $\tilde{E}_B = 10^{-5}$, $\nu = 1/3$. The vertical lines in a), b) and the close-up of c) indicate the position of the dimple edge s_D and $s_D \pm \sigma_{\min}\xi$.

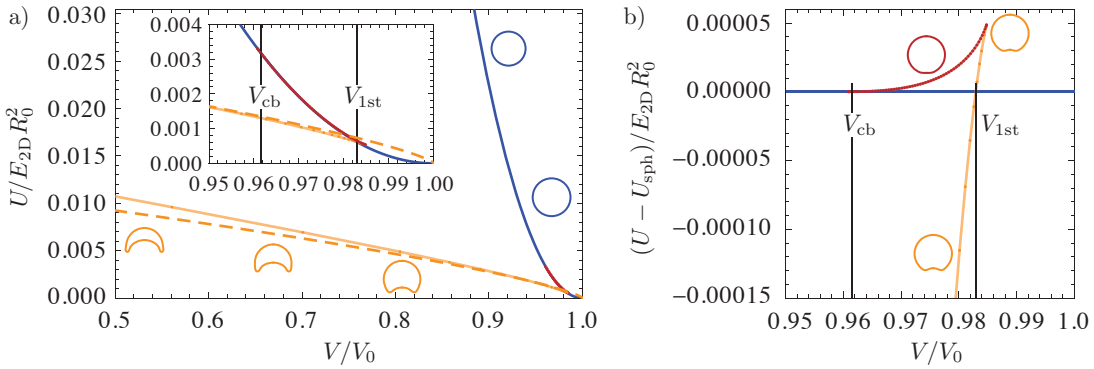

Figure 2.10.: a) Elastic energy $U(V)$ of the axisymmetric buckled shapes for the shape equations (red and orange points with light red and orange interpolation) and Pogorelov model (dashed line), and for the spherical shapes $U_{\mathrm{sph}}(V)$ (blue line). The elastic moduli are $\tilde{E}_B = 10^{-4}$ and $\nu = 1/3$. In the inset, the critical volume of classical buckling V_{cb} according to (2.49) and of the first buckling $V_{1\mathrm{st}}$ are marked. b) To resolve the beginning of the buckled solution branch better, the energy difference between buckled and spherical shapes is plotted. The pictograms included in the diagrams are plots of the shape according to the shape equations.

equations accurately. The agreement of the shape is even more striking. Only in the close-up, deviations between the two models can be recognised. The characteristic curvature peak at the dimple edge may serve as the foundation for a very rudimentary shape analysis, which will be further discussed in section 2.4.2.

Now, let us turn to the comparison of the elastic energies of the deformed shapes, from which the bifurcation behaviour can be deduced. First of all, there is the trivial (spherical) solution branch, which can be handled analytically. If the deformed shell is a sphere with radius R, the strains are uniform and homogeneous, $e_s = e_\varphi = R/R_0 - 1 = (V/V_0)^{1/3} - 1$, and the bending strains vanish. The elastic energy density (2.7) must be integrated over the undeformed surface with area $4\pi R_0^2$, which gives the elastic energy

$$U_{\mathrm{sph}} = 4\pi \frac{E_{2\mathrm{D}}}{1-\nu} R_0^2 \left[(V/V_0)^{1/3} - 1 \right]^2 . \tag{2.45}$$

This function of the reduced shell volume V/V_0 is plotted in fig. 2.10 a), blue line, and increases rapidly with decreasing volume.

The classical shell theory shows that the spherical shape becomes unstable at the classical buckling pressure $p_{\mathrm{cb}} = -4EH_0^2/R_0^2\sqrt{12(1-\nu^2)}$ (see, for example, refs. [124, 135]), which can be expressed in the two-dimensional elastic moduli via (2.9) as

$$p_{\mathrm{cb}} = -4\frac{\sqrt{E_{2\mathrm{D}}E_B}}{R_0^2} = -4\frac{E_{2\mathrm{D}}}{R_0}\sqrt{\tilde{E}_B}. \tag{2.46}$$

This pressure corresponds to a classical buckling volume V_{cb}, which can be obtained through the pressure-volume relation of the spherical solution branch,

$$p = \frac{\partial U_{\mathrm{sph}}}{\partial V} = 2\frac{E_{2\mathrm{D}}}{1-\nu}\frac{1}{R_0}\left[\left(\frac{V}{V_0}\right)^{1/3} - 1 \right] \left(\frac{V_0}{V}\right)^{2/3}, \tag{2.47}$$

see (2.56) below where we show that $p = \partial U/\partial V$, which is related to a Legendre transformation. Inverting this relation between p and V results in

$$\frac{V}{V_0} = \left(\frac{E_{2D}}{pR_0(1-\nu)}\right)^3 \cdot \left(1 \pm \sqrt{1 - 2pR_0\frac{1-\nu}{E_{2D}}}\right)^3 = 8\left(1 + \sqrt{1 - 2pR_0\frac{1-\nu}{E_{2D}}}\right)^{-3}, \quad (2.48)$$

where the minus sign in the first expression must be taken in order to ensure the limit $V \to V_0$ for $p \to 0$, and the simplification in the last step can be accomplished by multiplying the expression with $(1+\sqrt{\dots})^3/(1+\sqrt{\dots})^3$. Inserting $p = p_{cb}$ finally gives the classical buckling volume

$$\frac{V_{cb}}{V_0} = \left(\frac{1}{2} + \sqrt{\frac{1}{4} + 2(1-\nu)\sqrt{\tilde{E}_B}}\right)^{-3} \approx 1 - 6(1-\nu)\sqrt{\tilde{E}_B}, \quad (2.49)$$

where the approximation in the last step holds for small $\tilde{E}_B$, see also ref. [112]. This volume is marked in the energy diagram fig. 2.10.

The energy of a buckled solution of the shape equations can be calculated by numerical integration of the surface energy density, $U = \int 2\pi r w_S \, \mathrm{d}s_0$. The data points for numerical solutions of the shape equations are shown in fig. 2.10 a). As this solution branch is very close to the spherical solution branch at the beginning, fig. 2.10 b) contains a modified presentation, where the energy difference between buckled and spherical shapes is plotted as a function of the volume.

At the classical buckling volume V_{cb} the buckled solution branch separates from the spherical branch. At first, it runs to the right and lies at slightly higher energies than the spherical solution branch. These shapes correspond to unstable energy maxima and have the form of a sphere with a flattened pole, see the pictograms in fig. 2.10 b). After a turning point, the buckled branch crosses the spherical branch at a volume V_{1st}, where the dimple is well developed. From there on, the axisymmetric buckled configuration is energetically favourable to the spherical shape, representing the global energy minimum.

The spherical shape is still metastable between V_{1st} and V_{cb} and represents a local energy minimum. Koiter's stability analysis [79] suggests that the buckling transition of real (imperfect) shells occurs somewhere in this region, depending on the severity of the imperfections. For a perfect shell, an energy barrier must be overcome if the buckling shall occur before V_{cb}. It is not clear how the height of the barrier could be determined. If the shell is constrained to axisymmetric shapes all along the path from spherical to buckled, the energy barrier may be read off from fig. 2.10 b). But such a constraint is not very natural; and transition states that are non-axisymmetric as obtained in the post-buckling analysis of Koiter [79] and Hutchinson [69], see fig. 2.1, are likely to have a lower energy barrier and play a more important role. For $V \le V_{cb}$, the spherical branch is unstable and buckles spontaneously without energy barrier.

Note that there also exists a metastable region of the buckled solution branch, between V_{1st} and the turning point, see fig. 2.10 b). Bifurcation theory [92] assures that the solution branch represents local minima in this region, and changes into a maximum or saddle point at the turning point. The metastable region is relevant when a shell is re-inflated; the shell can stay on the buckled branch beyond V_{1st}, but has to fall back to the spherical branch when it reaches the turning point of the buckled one. This bifurcation scenario with metastable spherical and buckled branches below and above V_{1st}, respectively, is typical for a *discontinuous shape transition*.

The elastic energy U_{pog} derived in the Pogorelov model, eq. (2.44), is also plotted in the bifurcation diagram fig. 2.10 a). For volumes smaller than V_{1st}, it agrees well with the data points from the shape equations. Deviations start to develop for large deformations ($V < 0.8V_0$),

which is obviously due to the assumption of small dimples in the Pogorelov model. For shapes with too small dimples, $V > V_{1\mathrm{st}}$, the model is also inaccurate, for two reasons. Firstly, it was assumed that the neighbourhood of the dimple which is deformed, G_i and G_o, is narrow. For too small dimples, this condition is not satisfied since the size of the inner neighbourhood becomes as large as the dimple itself. Secondly, for shapes with small dimples, the pre-buckling deformation (that is, the uniform contraction due to the negative inner pressure) cannot be neglected as it has been done in the Pogorelov model. This is also the reason why the tensions τ_s and τ_φ do not reach the correct limits far away from the dimple edge, see fig. 2.9 a), but show a small offset.

However, the inset in fig. 2.10 suggests that the Pogorelov model can be successfully used to calculate the first buckling volume $V_{1\mathrm{st}}$ by setting $U_\mathrm{Pog} = U_\mathrm{sph}$. Doing so using (2.44) and (2.45), we obtain for small $\Delta V/V_0$ the critical volume difference for the first buckling,

$$\left.\frac{\Delta V_{1\mathrm{st}}}{V_0}\right|_\mathrm{Pog} = 6 J_\mathrm{min}^{4/5} \frac{(1-\nu)^{4/5}}{\left(1-\nu^2\right)^{1/5}} \tilde{E}_B^{3/5}. \tag{2.50}$$

The limitation to small $\Delta V/V_0$ allowed us to approximate the volume-dependent term of (2.45) as $(V/V_0)^{1/3} - 1 = (1 - \Delta V/V_0)^{1/3} - 1 \approx -\Delta V/3V_0$ in the derivation of this result. Thus, the volume difference of first buckling has a different scaling law than that of the classical buckling, $\Delta V_{1\mathrm{st}}/V_0 \sim \tilde{E}_B^{3/5}$ on the one hand and $\Delta V_\mathrm{cb}/V_0 \sim \tilde{E}_B^{1/2}$ on the other, cf. (2.49).

2.4.2. Edge curvature as an indicator for the bending stiffness

As smaller bending stiffnesses allow sharper bends in the elastic shell, we expect the meridional curvature at the dimple edge, $\kappa_\mathrm{edge} = \max_{s_0} \kappa_s$, to depend sensitively on $\tilde{E}_B$. Accordingly, this curvature represents an adequate observable to infer the reduced bending stiffness, e.g. from microscopy images in experiments on microcapsules.

The theoretical foundation for this very simple shape analysis can be derived from the analytic model or from the numerical results of the shape equations. Figure 2.9 b) shows that the meridional curvature of the Pogorelov model assumes its maximum at $s_0 = s_{D+}$ (that is the limit $s_0 \to s_D$ with $s_0 > s_D$). The curvature function is given by (2.43) with the exact rescalings (2.37) and the non-dimensional solution (B.1), and we obtain at s_{D+} the value

$$\kappa_\mathrm{edge} = \frac{1}{R_0} + v''(0_+) = \frac{1}{R_0} + \frac{1}{R_0\,\sigma_\mathrm{min}} \sqrt{\frac{\alpha^3}{\sin\alpha}} \left[\tilde{E}_B(1-\nu^2)\right]^{-1/4}, \tag{2.51}$$

where α is a function of the shell volume, see (2.37). For small reduced bending stiffnesses, which is equivalent to large edge curvatures, this is a power law $\kappa_\mathrm{edge} \sim \tilde{E}_B^{-1/4}/R_0$, as observed in ref. [138]. The leading order dependence on the volume difference can be obtained by using the simplified geometric relation $\alpha \sim (\Delta V/V_0)^{1/4}$, see (2.38), which results in

$$\kappa_\mathrm{edge} \sim \frac{1}{R_0} \left(\frac{\Delta V}{V_0}\right)^{1/4} \tilde{E}_B^{-1/4} \tag{2.52}$$

for small $\tilde{E}_B$ and small ΔV.

To verify these expressions for the edge curvature, the shape equations were solved for reduced volumes of $V/V_0 = 0.9, 0.8, 0.7, 0.6$ and 0.5 for a large range of bending stiffnesses $\tilde{E}_B$. From the solutions, the edge curvature was obtained by numerical maximisation of $\kappa_s(s_0)$. Figure 2.11 a) shows a comparison of the results from the shape equations (data points) and the Pogorelov

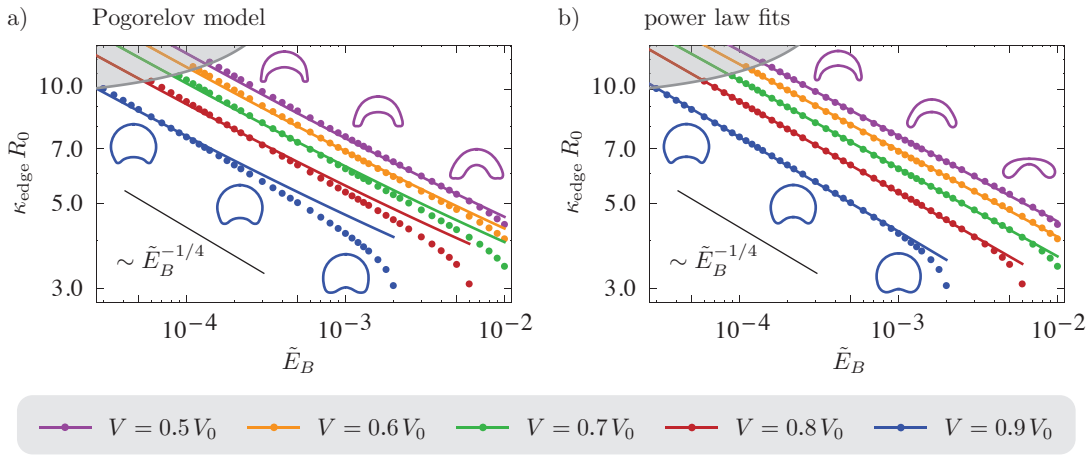

Figure 2.11.: Curvature of the dimple edge as a function of the reduced bending stiffness (double logarithmic), for different shell volumes. The dots are results from the shape equations, with $\nu = 1/3$. In a), the lines are the predictions (2.51) of the analytic model, and in b) the lines are power law fits to the data points from the shape equations, see tab. 2.2. The grey area in the upper left corner is not suitable for an analysis of the edge curvature because the dimple edge becomes polygonal here. The pictograms in a) show shapes of the Pogorelov model and in b) solutions of the shape equations.

model (2.51) (continuous lines). Surprisingly, the results match excellently for *large* volume differences over the whole range of $\tilde{E}_B$. This achievement is in part due to the exact scaling parameters (2.37) that are used in (2.51); if the simplified scaling parameters (2.38) are used, the results do not match satisfactorily. However, several simplifications have been introduced in the Pogorelov model which become inaccurate for large dimples, and the surprising match seems to be a matter of chance – the pictograms in fig. 2.11 indeed show considerable deviations in the shape at large dimples and large bending stiffnesses.

For small volume differences, the results of the analytic model and the shape equations match only for small reduced bending stiffnesses, see the blue line in fig. 2.11 a). The pictograms included in the diagram suggest a reason for the deviations at large $\tilde{E}_B$. For large bending stiffnesses, the dimple edge is not a sharp bend, but has a relatively small curvature. The deviations between the isometric shape and the final shape are then relatively large, so that the assumptions of small displacements u and v and narrow regions G_i and G_o become more and more inaccurate with increasing $\tilde{E}_B$.

For the shape analysis of experiments, it might be favourable to work with more accurate relations between κ_{edge} and $\tilde{E}_B$ than (2.51). These can be obtained from fitting the data points of the shape equations with power laws, see (2.52),

$$\kappa_{\mathrm{edge}} R_0 = c \left(\frac{\Delta V}{V_0} \right)^{1/4} \tilde{E}_B^b, \tag{2.53}$$

where the exponent b can be expected to be close to $-1/4$ and the prefactor c will be weakly volume dependent. By taking the logarithm on both sides of (2.53) we see that a simple linear regression can be used on the data points consisting of tuples $(\ln \tilde{E}_B,\ \ln \kappa_{\mathrm{edge}})$. The results for these fits are shown in fig. 2.11 b) and the numerical values of the fit parameters b and c are summarised in tab. 2.2. For the fits with $V \geq 0.7V_0$ not all available data points have been used, because points with large $\tilde{E}_B$ deviate too much from the power law behaviour. The data

reduced Volume V/V_0	prefactor c	exponent b	$\tilde{E}_B$-range used for the fit
0.9	1.355 ± 0.009	-0.2480 ± 0.0008	$3.0 \cdot 10^{-5}$ to $1 \cdot 10^{-3}$
0.8	1.517 ± 0.007	-0.2405 ± 0.0006	$6.0 \cdot 10^{-5}$ to $4 \cdot 10^{-3}$
0.7	1.691 ± 0.004	-0.2315 ± 0.0003	$9.0 \cdot 10^{-5}$ to $5 \cdot 10^{-3}$
0.6	1.808 ± 0.007	-0.2271 ± 0.0006	$1.1 \cdot 10^{-4}$ to $1 \cdot 10^{-2}$
0.5	1.898 ± 0.010	-0.2247 ± 0.0008	$1.4 \cdot 10^{-4}$ to $1 \cdot 10^{-2}$

Table 2.2.: Fit parameters (estimated value ± standard error) for different shell volumes according to the model (2.53). The last column indicates the data range used for the fits.

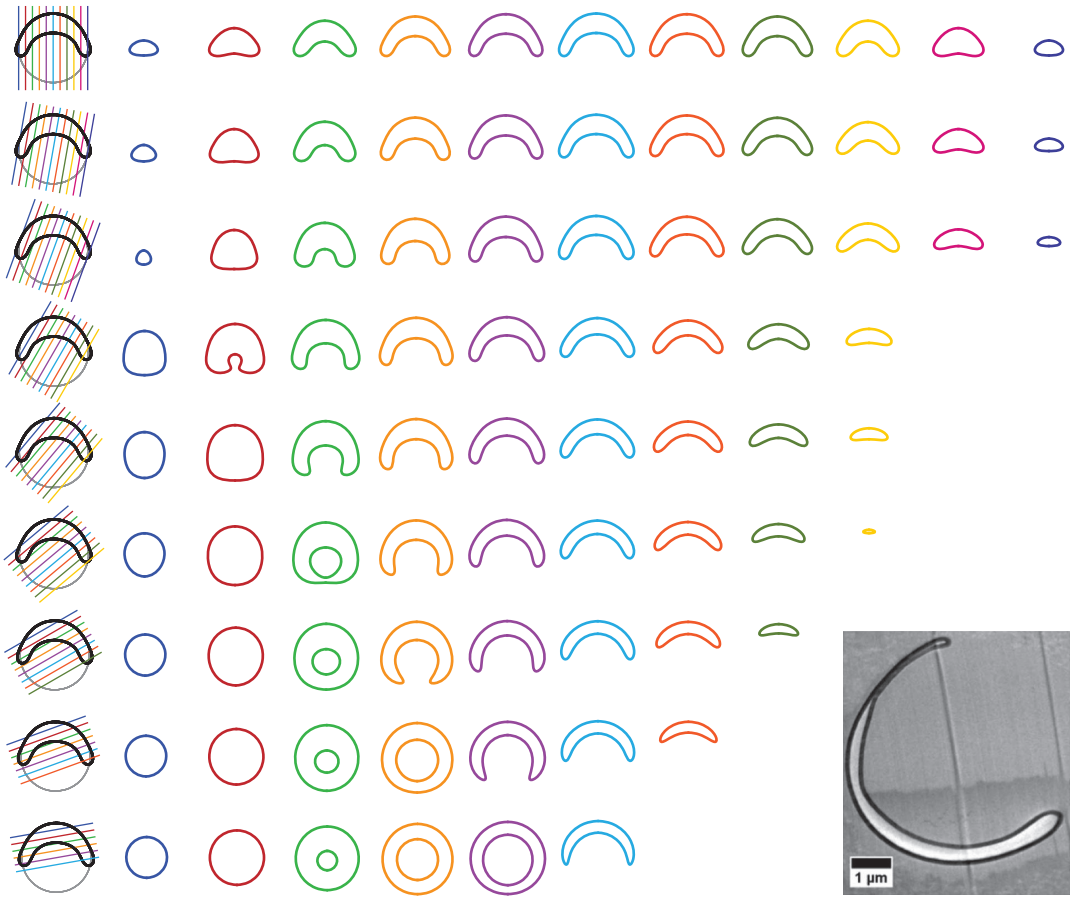

Figure 2.12.: Sections through a buckled shell at different angles and offsets from the axis of symmetry. The leftmost column shows in black the contour of a buckled shell (with $V = 0.5V_0$, $\tilde{E}_B = 10^{-3}$ and $\nu = 1/3$). The coloured shapes in the other columns are sections through the shell as indicated by the straight coloured lines. The image in the bottom right corner shows a section of an Epon-embedded aminoplast microcapsule (taken from [110]). An unambiguous assignment to one of the plotted sections (or other sections of capsules with less volume) is not possible.

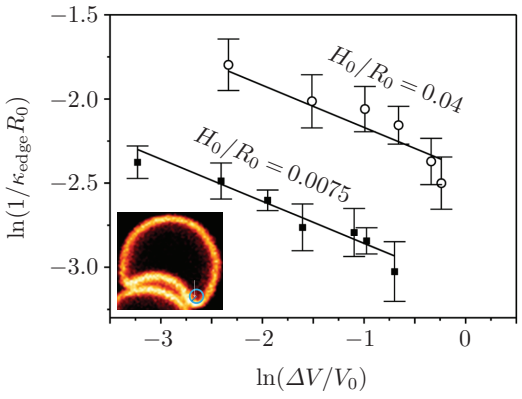

Figure 2.13.: Experimental verification of the edge curvature scaling. Jose et al. analysed two datasets of buckled siloxane microcapsules with different shell thicknesses with confocal microscopy (see the inset). The radius of curvature depends on the volume difference as expected from (2.52), and the data points have been fitted with a power law $1/\kappa_{\mathrm{edge}} \sim \Delta V^{-1/4}$ (straight lines). Images adapted from ref. [71].

points used for the fit are also indicated in tab. 2.2; and the fits are very accurate within these $\tilde{E}_B$-ranges. For small volume differences, the fitted exponent b agrees best with our expectation $-1/4$.

The range of admissible $\tilde{E}_B$ is also restricted by the results of chapter 4. There, it is shown that the dimple edge acquires a polygonal shape for very small reduced bending stiffnesses so that the curvature of the rim cannot be analysed any more. This is the case if $V/V_0 < 1 - 3706\tilde{E}_B$, see (4.9) below. The corresponding region in the $\kappa_{\mathrm{edge}}\left(\tilde{E}_B\right)$ diagram, obtained by inserting this threshold volume into (2.51), is shaded grey in fig. 2.11.

The results just presented can help researchers interpret their experiments and deduce the shell's reduced bending stiffness, if they are able to measure the radius of curvature at the dimple edge. This is a challenging task because it requires imaging the cross section of the buckled shell. It can be achieved, in the case of microcapsules, by confocal microscopy [45,51,95] or by cutting a microcapsule that is embedded in some elastic gel [110]. However, attention must be paid to the position and orientation of the (real or virtual) section through the shell, because this directly affects the measured edge curvature. As a guide for experimenters, fig. 2.12 shows the morphology of cross sections at different angles and offsets from the axis of symmetry for a buckled shell. A reconstruction of the reduced volume or the edge curvature based on one single section seems impossible. For example, if the rightmost shape in the bottom row is interpreted as a section along the axis of symmetry, one would conclude that the reduced volume is much smaller and the edge curvature much larger than the actual values (which can only be determined from the black shapes in the leftmost column).

Recently, a group of experimenters tested the proposed procedure [71] which the author had published in ref. [152]. High resolution confocal microscopy was used to measure the radius of curvature at the dimple edge. Their results confirm the $\kappa_{\mathrm{edge}} \sim \Delta V^{1/4}$ dependence of the edge curvature on the volume reduction, see fig. 2.13, and the values for $\tilde{E}_B$ determined from the power law fits are in reasonable agreement with those obtained directly from measuring the thickness-to-radius-ratio [71].

2.5. Stability discussion for different load cases

Already in the early investigations of shell buckling, evidence was found that buckled shapes are unstable with respect to further dimple growth when the load (i.e. the pressure difference) has a fixed value [79,83]. To see this, first recall our sign conventions: For deflation, $V < V_0$, the load parameter p is negative and corresponds to the internal underpressure in the shell;

$-p$ is consequently the value of the external overpressure. On the buckled solution branch, an anomalous pressure-volume-relation with $\mathrm{d}V/\mathrm{d}p < 0$ has been found [79, 83]. Upon further deflation ($\mathrm{d}V < 0$) it follows that $\mathrm{d}p > 0$, and so the shell can bear smaller loads $|p|$ for growing dimples. The classical buckling pressure p_{cb} is thus an upper bound for the load which a shell can withstand.

From this it can be concluded that "shell buckling is always disastrous" [135] in the sense that the stable state after buckling has a very large deformation. This behaviour is called *snap-through buckling*, and we will see that the final shape is so extremely deformed that the opposite sides of the shell (the regions around the two poles) are in contact.

This instability has also consequences for experiments because even small, unavoidable, imperfections have a large impact on the critical buckling load [69, 79]. For example, Carlson et al. report in ref. [24] buckling pressures of high quality, electropolished shells that are at maximum 86% of the theoretical value.

In the next sections we will discuss the stability of the buckled configurations in the cases (i) prescribed volume, (ii) prescribed pressure difference between inside and outside and (iii) osmotic pressure, which is equivalent to an externally pressurised shell that encloses a fixed amount of an ideal gas. Experimentally, these cases can be realised by different setups. For (i) volume control, we can fill a (non-permeable) shell with a given amount of an incompressible liquid. (ii) Pressure control corresponds to a shell that is empty inside and pressurised externally. In experiments with microcapsules, the case of (iii) osmotic pressure is frequently met; here, a shell material that is permeable for the solvent medium is required, and an osmotic pressure can be exerted by different osmolyte concentrations inside and outside the shell.

2.5.1. Stability of buckled shapes under pressure and volume control

The shape equations (2.17) have been derived from a variational analysis of an energy functional, and very general theorems about the stability of the solution branches exist [92]. A solution of the shape equations is only stable if it represents a local minimum of the energy functional (and not a maximum or saddle point). Mathematically, this is related to the second variation of the energy functional: If it has negative eigenvalues, the solution is unstable because there exists a deformation mode which lowers the elastic energy in second order.

The variational problem from which the shape equations have been derived admits two interpretations. On the one hand, it can be considered as an unconstrained minimisation of the *enthalpy* $H[\boldsymbol{r}, p] = U[\boldsymbol{r}] - pV[\boldsymbol{r}]$ (the functionals depend on the parametrisation $\boldsymbol{r}(s_0)$ of the deformed shape). This corresponds to a prescribed pressure difference p that acts on the shell, and we call it "mechanical pressure control". On the other hand, it can be interpreted as a constrained minimisation of the energy functional $U[\boldsymbol{r}]$ under the constraint that the volume functional $V[\boldsymbol{r}]$ equals some given value. This case is termed "volume control" and leads, by the theory of Lagrange multipliers, to the same shape equations. The parameter p is then just a Lagrange multiplier which controls the shell volume. In both interpretations, the same shapes are calculated as solutions of the shape equations, but the stability requirements differ.

In the unconstrained problem, solutions are stable (i.e. stable under mechanical pressure control) if all eigenvalues of the second variation of the enthalpy functional H are positive. In ref. [92], Maddocks discusses the stability of solution branches in a *distinguished bifurcation diagram* which uses the bifurcation parameter (p in our case) as the ordinate and the derivative $-\partial_p H$ as the abscissa. In our case, $-\partial_p H = V$, see (2.55) below, and this distinguished bifurcation diagram is just the $V(p)$ diagram of fig. 2.14 a). Maddocks rigorously shows that a stable solution branch has a positive slope $\partial V/\partial p \geq 0$ in the bifurcation diagram. So the branches A and C/C' in fig. 2.14 are possible candidates for branches that are stable under

mechanical pressure control. However, $\partial V/\partial p \geq 0$ is only a necessary criterion for stability under mechanical pressure control, not a sufficient one. The $H(p)$ diagram, see fig. 2.14 b), suggests that the branches C and C' are stable; C' seems to be the global enthalpy minimum over a large pressure range.

A further result from ref. [92] concerns the *principle of exchange of stability* at a simple fold, that is, a point with a vertical tangent in the $V(p)$ diagram like the point where branch B meets C. At such points, one eigenvalue of the second variation crosses zero. Maddocks even specifies the direction in which the eigenvalue crosses zero: In a fold that opens to the left, as in the case where branches B and C meet, the higher lying branch has one more negative eigenvalue than the lower branch. In our case, where we assume that branches C and C' are stable and have consequently no negative eigenvalues, we can conclude that branches B and A have precisely one negative eigenvalue, and are both unstable under mechanical pressure control.

The bifurcation behaviour under mechanical pressure control can thus be summarised as follows. When a spherical shell is loaded with a negative internal pressure it remains spherical for small magnitudes of the load, because the spherical branch is the global enthalpy minimum. At a critical pressure p_c, the branch C' (consisting of buckled shapes with self-contact) crosses the spherical branch in the $H(p)$ diagram. Beyond this pressure, branch C' is the global energy minimum. Although it is energetically preferable for the shell to change from the spherical into a fully buckled shape at p_c, this will not happen spontaneously because both branches are local energy minima, and an energy barrier must be overcome. The point where spontaneous buckling is possible is at p_{cb}, the classical buckling pressure. Here, the spherical solution branch becomes unstable, and the shell will "fall" from the spherical branch onto the branch C' where it is nearly completely collapsed (see pictograms in fig. 2.14 b). Remarkably, the absolute value of p_c is much smaller than that of p_{cb}, for the elastic moduli of fig. 2.14 approximately $p_c = 0.12 p_{\mathrm{cb}}$, see also (2.59) below. The buckling behaviour under mechanical pressure control is thus similar to that under volume control as discussed in section 2.4.1, with the important difference that the first stable states after buckling are completely collapsed with opposite sides in contact. The buckled shapes of branch B, with a dimple of small to medium size, are not accessible with mechanical pressure control; and the shapes of branch C with large dimples but without self-contact are only reachable by exploiting the metastability of this branch upon re-inflation. The same qualitative behaviour holds for all bending stiffnesses that were under consideration, from $\tilde{E}_B = 10^{-6}$ to 10^{-2}. This is a fairly large investigated range, and no indication was found that the behaviour would change for smaller or larger bending stiffnesses.

Maddocks also discusses the stability of the solution branches in the constrained problem. He calls branches that are stable in the constrained problem "c-stable", and in our case this means "stable under volume control". The stability under volume control is a weaker condition than stability under mechanical pressure control, because only for volume-preserving modes must be checked whether they lead to a second order energy decrease. Maddocks shows in [92] that (i) all "stable" (stable under mechanical pressure control) branches are also "c-stable" (stable under volume control), and (ii) the branches that are "c-stable" but not "stable" are those with precisely one negative eigenvalue and negative slope in the distinguished bifurcation diagram (the $V(p)$ diagram).

Since we have seen that branches A and B have precisely one negative eigenvalue of the second variation of the enthalpy functional and B has a negative slope $\partial_p V < 0$, we can conclude that branch B is stable under volume control, but A is not. C and C' are, of course, also stable under volume control. This coincides with our previous results in section 2.4.1 which have been drawn from the $U(V)$ diagram alone.

Branch B, which contains the buckled shapes with small to medium sized dimples that are frequently observed in microcapsule experiments, see fig. 1.2 b) for example and refs.

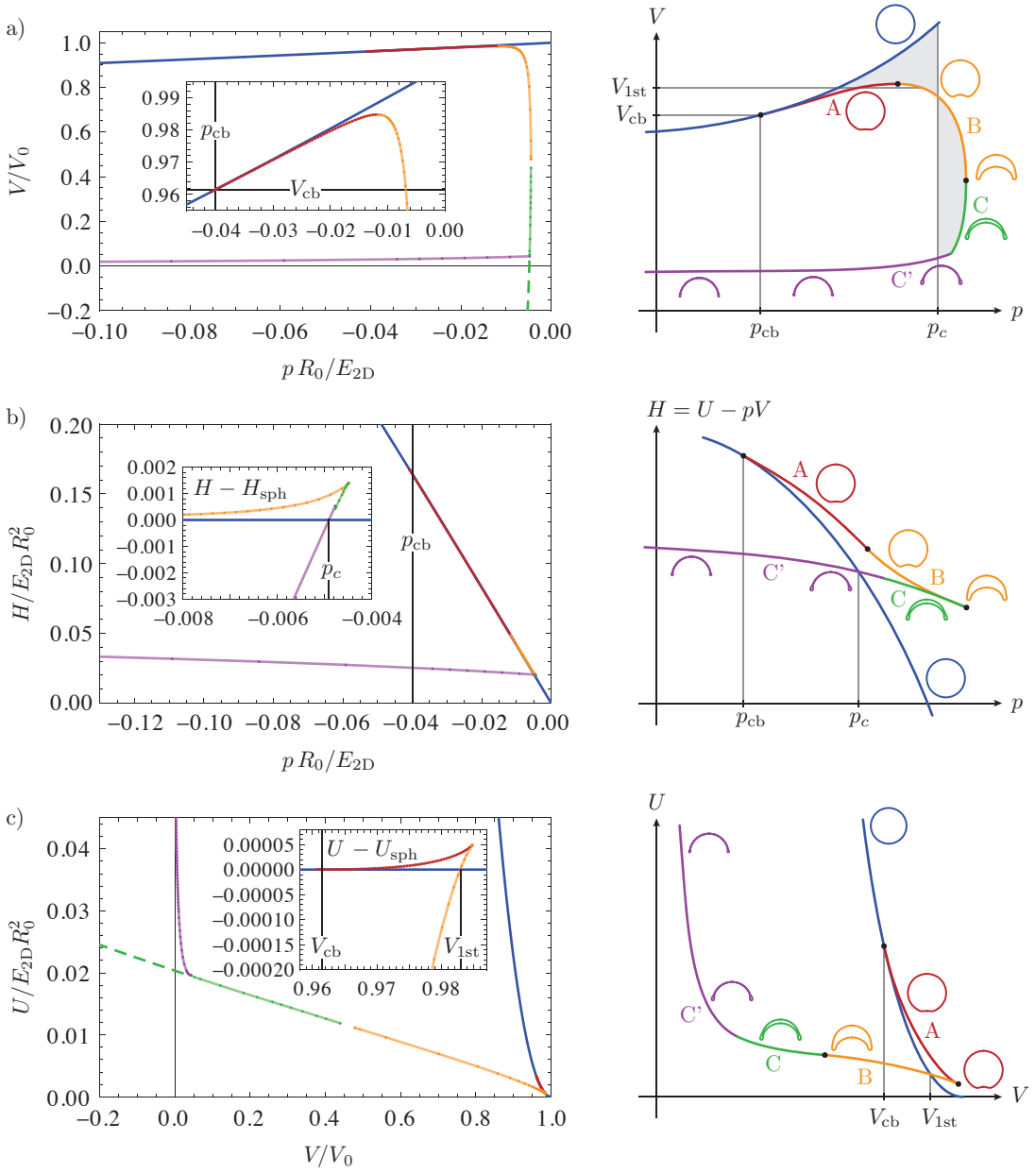

Figure 2.14.: Bifurcation diagrams: a) volume-pressure relation, b) enthalpy as a function of the pressure, c) elastic energy as a function of the volume. The continuous blue line represents the spherical solution branch, the other coloured lines represent buckled solution branches A, B, C and C' according to the pictograms, and the dashed green lines in a) and c) represent self-intersecting shapes. The insets of the energy diagrams show the differences between buckled and spherical branches. On the right, schematic diagrams clarify how the solution branches lie with respect to each other. The elastic moduli are $\tilde{E}_B = 10^{-4}$ and $\nu = 1/3$, but he same qualitative behaviour has been obtained for all bending stiffnesses under consideration, from $\tilde{E}_B = 10^{-6}$ to 10^{-2}, see also ref. [152]. The spherical solution branch has been plotted according to the analytic results (2.45) and (2.48).

[45, 97, 98, 113, 116], has thus a very interesting property: It changes from stable to unstable when the pressure is controlled instead of the volume. In real experiments, something between pressure and volume control is usually achieved, and then one part of branch B is stable, and the other part unstable. This will be discussed in the next section.

We conclude the discussion of stability under pressure and volume control by establishing a link (in form of a Legendre transformation) between the three bifurcation diagrams shown in fig. 2.14. The function $H(p)$ stems from the functional $H[\boldsymbol{r}, p] = U[\boldsymbol{r}] - pV[\boldsymbol{r}]$ by inserting the numerical solutions $\boldsymbol{r}(p)$ of the shape equations for a given pressure p, i.e.

$$H(p) = U[\boldsymbol{r}(p)] - pV[\boldsymbol{r}(p)]. \tag{2.54}$$

When we take the derivative with respect to p, we must consider that the shape changes by $\delta\boldsymbol{r}$ when the pressure is changed by $\mathrm{d}p$. We thus obtain

$$\frac{\mathrm{d}H}{\mathrm{d}p} = \frac{\delta U - p\,\delta V}{\mathrm{d}p} - V[\boldsymbol{r}(p)] = -V(p), \tag{2.55}$$

where we use $\delta U - p\,\delta V = 0$ because the shape equations were derived from this condition. This result connects the $V(p)$ diagram, fig. 2.14 a), to the $H(p)$ diagram, fig. 2.14 b). Now, the function $U(V)$ is obtained as $U = H + pV$, or more precisely as

$$U(V) = H(p(V)) + p(V)V, \tag{2.56}$$

where $p(V)$ is the inverse function of $V(p)$. We recognise that the energy $U(V)$ is the *Legendre transformation* of the enthalpy $H(p)$, just like in thermodynamics [22] from where our notation is adopted. Consequently, it follows that $\mathrm{d}U/\mathrm{d}V = p$ and that H is also the Legendre transform of U.

The *Maxwell construction* known from thermodynamics [22] can therefore be applied to the $V(p)$ and $p(V)$ diagram in order to construct the critical pressure p_c and volume $V_{1\mathrm{st}}$ of the buckling transition. They are defined as the points in the energy diagrams $H(p)$ and $U(V)$, respectively, where the buckled solution branch crosses the spherical one. In the $V(p)$ diagram, this means that the critical pressure p_c is positioned so that the shaded areas in fig. 2.14 a) have equal size. The critical volume $V_{1\mathrm{st}}$ can be constructed analogously, with equal enclosed areas between the horizontal line $V_{1\mathrm{st}}$ and the spherical and buckled branches.

2.5.2. Enthalpy landscape for mechanical pressure control

The instability of buckled shapes under mechanical pressure control can be explained by considering the energy landscape during the buckling process. The "reaction coordinate" that describes the progress of the buckling is $\Delta V = V_0 - V$, and for the model of the elastic energy of the buckled shapes we take the Pogorelov energy $U_{\mathrm{Pog}}(\Delta V) \sim \Delta V^{3/4}$, see (2.44). For mechanical pressure control, a term $-pV = -p(V_0 - \Delta V)$ must be added to obtain the total enthalpy

$$H(\Delta V) = U_{\mathrm{Pog}}(\Delta V) + p\Delta V + \mathrm{const.} \tag{2.57}$$

This results in a function $H(\Delta V) \sim \Delta V^{3/4} - |p|\Delta V$ (because p is negative, with const set to zero) as plotted in fig. 2.15. For sufficiently small internal pressure (red line in fig. 2.15), the shell tends to $\Delta V \to \infty$ in order to minimise its energy after an energy barrier has been overcome, for example by manually indenting the shell. This model is, of course, over-simplified because it relies on the Pogorelov model that is inaccurate for too large dimples. The shell cannot reach $\Delta V \geq V_0$, and even before there will be additional terms in the elastic energy

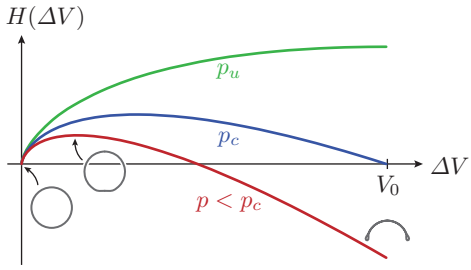

Figure 2.15.: Enthalpy landscape for buckling under mechanical pressure control for different values of the internal pressure. The shell can reside in the boundary minimum at $\Delta V = 0$ or $\Delta V = V_0$, corresponding to the spherical shape or the fully collapsed shape, respectively. The boundary minima are separated by an enthalpy maximum which represents the energy barrier that has to be overcome to induce buckling.

caused by the constraint of no self-intersection. However, we can conclude from the energy landscape that the shell collapses completely under mechanical pressure control, and takes its place in the boundary minimum at $\Delta V = V_0$ in the enthalpy landscape. Pogorelov's model is also inaccurate for too small dimples, see the discussion of fig. 2.10. For the energy landscape, this has the effect that the energy barrier is always present, even if p exceeds the critical buckling threshold p_{cb}, which should not be the case. Apart from that minor point, the enthalpy landscape is qualitatively correct for $|p| < |p_{\mathrm{cb}}|$, i.e. for all three lines plotted in fig. 2.15.

In the discussion of the bifurcation diagrams in the previous section, the critical pressure p_c was defined as the point where the spherical solution branch and the collapsed solution branch C' cross in the enthalpy diagram. This condition of equal enthalpies of the spherical and collapsed configuration corresponds in the picture of the enthalpy landscape to the condition that the two boundary minima at $\Delta V = 0$ and $\Delta V = V_0$ are on equal level, see the blue line in fig. 2.15. Thus, solving the equation $H(0) = H(V_0)$ for the pressure p gives the critical pressure

$$p_c = -2 \cdot 6^{1/4} J_{\min} \frac{E_{2\mathrm{D}} \tilde{E}_B^{3/4}}{R_0 (1-\nu^2)^{1/4}}. \tag{2.58}$$

Notably, this critical pressure $\tilde{p}_c \sim -\tilde{E}_B^{3/4}$ has a different scaling than the classical buckling pressure $\tilde{p}_{\mathrm{cb}} \sim -\tilde{E}_B^{1/2}$, see eq. (2.46), and is thus much smaller for small reduced bending stiffnesses.

Another critical pressure p_u is reached when the right boundary minimum vanishes. That happens when the maximum of the $H(\Delta V)$-function lies at $\Delta V = V_0$, that is, when $H'(V_0) = 0$. From this equation we obtain that p_u has the same scaling as p_c, but with a different prefactor: $p_u = p_c \cdot 3/4$. In the bifurcation diagrams of fig. 2.14 a) and b), this upper critical pressure corresponds to the point where the buckled branch turns around, i.e. where branches B and C meet. Between p_c and p_u, the spherical shape is the global energy minimum and the buckled shape is metastable, and above p_u, only the spherical equilibrium shapes exists.

From the simple model (2.57), we can also obtain the magnitude of the energy (or enthalpy) barrier, which can be of interest when considering fluctuating shells to see whether the fluctuations can drive the shell from the spherical into the buckled shape. The maximum value of the function $H(\Delta V)$ is pressure dependent, and of special interest is the energy barrier at the critical pressure p_c. The general and special result are

$$H_{\mathrm{barr}}(p) = \frac{27}{2} J_{\min}^4 \pi \frac{E_{2\mathrm{D}}^4 \tilde{E}_B^3}{(-p)^3 R_0 (1-\nu^2)} \quad \text{and} \quad H_{\mathrm{barr}}(p_c) = \frac{9}{16} \frac{3^{1/4}}{2^{3/4}} J_{\min} \pi \frac{E_{2\mathrm{D}} R_0^2 \tilde{E}_B^{3/4}}{(1-\nu^2)^{1/4}}, \tag{2.59}$$

respectively.

We checked with our numerical results the accuracy of p_c and $H_{\mathrm{barr}}(p_c)$ over a large range of bending stiffnesses, from $\tilde{E}_B = 2 \cdot 10^{-6}$ to 10^{-3}, and found that the scaling laws $\sim \tilde{E}_B^{3/4}$ are

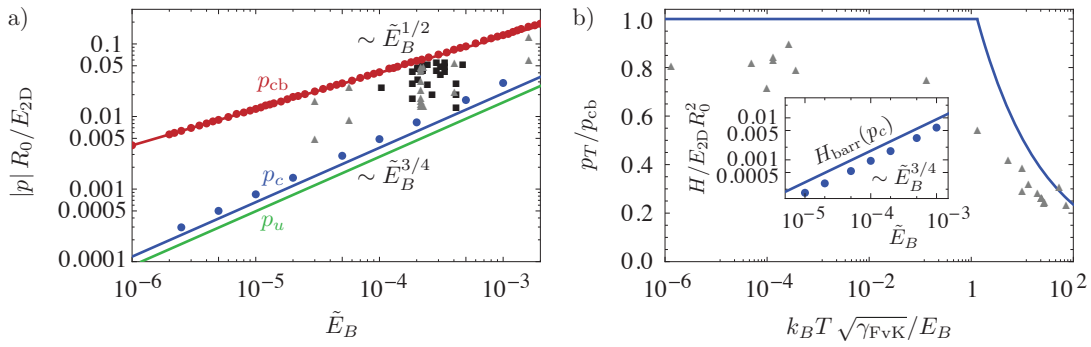

Figure 2.16.: Critical pressures and energy barrier derived from the enthalpy landscape. a) The analytic results for the critical pressures p_{cb}, p_c and p_u (lines) are in good agreement with numeric results from the shape equations (red and blue dots). Experimental results (black squares, from ref. [24]) and finite-temperature Monte Carlo simulations (grey triangles, from ref. [104]) for the buckling pressure lie between p_{cb} and p_u. b) Temperature dependence of the buckling pressure. Our analytic estimate (blue line) is an upper bound for the simulation results (grey triangles) from ref. [104]. The inset shows the energy barrier that has to be overcome by the thermal fluctuations according to the analytic approximation (2.59) (blue line) and numeric results from the shape equations (dots).

correct, see fig. 2.16 a) and inset in b). Even the prefactors are in reasonable agreement with the numerical results, despite the over-simplicity of the enthalpy landscape.

The energy barrier (2.59) can be overcome, for instance, by thermal fluctuations. As a consequence, the actual buckling pressure p_T at finite temperatures will be smaller in magnitude than the classical threshold p_{cb}, as observed in Monte Carlo simulations in ref. [104]. Ignoring the renormalisation of elastic constants at finite temperature discussed in this reference for the moment, we can estimate the condition for thermally activated buckling as $H_{barr}(p_T) = k_BT$. Solving this equation for the pressure p_T we find

$$\frac{p_T}{p_{cb}} = \frac{3}{4}\sqrt{\tilde{E}_B}\left(\frac{\pi J_{min}^4 E_{2D} R_0^2}{2k_BT(1-\nu^2)}\right)^{1/3} = \frac{3}{4}\left(\frac{\pi J_{min}^4}{2(1-\nu^2)}\,\frac{E_B}{k_BT\sqrt{\gamma_{FvK}}}\right)^{1/3}. \tag{2.60}$$

The latter form was obtained by using the definition (2.22) of $\tilde{E}_B$ and γ_{FvK}, and can be compared to the simulation results of ref. [104] where a dependence of the buckling pressure on the parameter $E_B/k_BT\sqrt{\gamma_{FvK}}$ is reported. The deficiency of the enthalpy landscape that the energy barrier does not vanish at $p = p_{cb}$ leads to the unphysical result that values of the thermal buckling pressure $|p_T| > |p_{cb}|$ are possible according to (2.60). If we assume that the energy barrier at the classical buckling pressure can be overcome spontaneously even at zero temperature, the final result for the thermal buckling pressure is

$$\frac{p_T}{p_{cb}} = \min\left[1,\ \frac{3}{4}\left(\frac{\pi J_{min}^4}{2(1-\nu^2)}\,\frac{E_B}{k_BT\sqrt{\gamma_{FvK}}}\right)^{1/3}\right]. \tag{2.61}$$

This function is plotted in fig. 2.16 b) in comparison with the Monte Carlo simulation results of ref. [104]. The assumption that the barrier at p_{cb} can be overcome spontaneously is equivalent to the assumption that dimples of depth $h \sim H_0$ can form spontaneously (at any temperature), which has also been used in the Landau-Lifshitz derivation of the classical buckling pressure [83].

2.5.3. Buckling under osmosis or with an enclosed ideal gas

Many deformation experiments with microcapsules are based on osmosis [45, 51, 116] or similar mechanisms [97, 98, 113]. In this approach, some of the enclosed medium diffuses through the semi-permeable capsule membrane because of a concentration gradient between the inside and outside. The osmosis tends to decrease the concentration gradient, and the deflation of the capsule stops when the concentrations in the inside and outside are sufficiently equalised. This is an important difference to mechanical pressure control, where the deflation only stops when the opposite sides of the capsule are in contact and the capsule volume is virtually zero. Osmotic pressure control rather resembles the case of volume control because the capsule has a preferred osmotic volume.

Dilute solutions of osmotically active particles can be treated like ideal gases [22], and we will see that the case of osmosis is mathematically equivalent to the case where a shell containing an ideal gas is deflated by means of an external pressure. In this example, which is perhaps intuitively more accessible than osmosis, we can anticipate the same effect: The shell will not collapse fully after buckling as in the case of mechanical pressure control without internal gas, because the internal gas requires the shell volume to remain finite. Or in other words: When the shell buckles under an external pressure, the decreasing volume available to the internal gas increases the internal pressure (according to the ideal gas equation), which eventually balances the external pressure.

The stability of buckled shapes for these two load scenarios can be analysed when we use adequate energy diagrams, where the energy contains not only the elastic energy stored in the shell, but also the free energy of the solutions of osmotically active particles or ideal gases. The shapes themselves must be the same as computed before, because the force density applied to the shell wall is again a spatially constant normal pressure p. So we do not have to solve the shape equations anew; the same data set of computed shapes as used for the bifurcation diagrams in fig. 2.14 can be used to draw the appropriate stability diagrams for osmotically induced buckling or buckling with an enclosed ideal gas.

Now, let us establish the appropriate energy functional that is to be minimised in the case of osmosis, which is depicted in fig. 2.17. The osmotic free energy of the inner and outer solution is given by [90]

$$F_{\mathrm{os}} = -k_B T N_{\mathrm{in}} \ln\left(\frac{e}{\lambda_B^3}\frac{V}{N_{\mathrm{in}}}\right) - k_B T N_{\mathrm{ex}} \ln\left(\frac{e}{\lambda_B^3}\frac{V_{\mathrm{ex}} - V}{N_{\mathrm{ex}}}\right). \tag{2.62}$$

In this expression, k_B is the Boltzmann constant, T the temperature of the solutions, $e = \exp(1)$ the Euler number, $\lambda_B = h/\sqrt{2\pi m k_B T}$ the thermal de Broglie wavelength with Planck constant h and particle mass m. N_{in} and N_{ex} are the numbers of osmotically active particles inside and outside the shell, respectively, V is the volume inside the shell and $V_{\mathrm{ex}} - V$ the volume outside the shell. It is assumed that the osmotically active particles cannot diffuse through the shell wall, so that N_{in} is fixed during the deflation. Furthermore, the temperature T is considered to

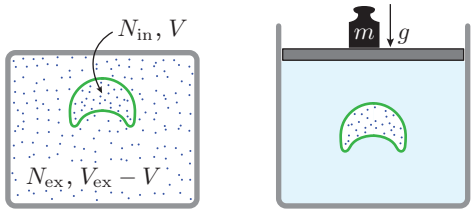

Figure 2.17.: Buckling by osmosis (left) or under pressure control with an internal gas (right). Both cases are mathematically equivalent and lead to the same results concerning the stability of buckled shapes.

affect only the ideal solutions; we do not incorporate fluctuations in the elastic shell that are due to a finite temperature [104].

If we assume $V \ll V_{\mathrm{ex}}$, the second logarithm in F_{os} can be expanded, $\ln(V_{\mathrm{ex}} - V) \approx \ln V_{\mathrm{ex}} - V/V_{\mathrm{ex}}$, and the expression simplifies to

$$F_{\mathrm{os}} = -k_B T N_{\mathrm{in}} \ln V + \frac{k_B T N_{\mathrm{ex}}}{V_{\mathrm{ex}}} V + \mathrm{const}(T, V_{\mathrm{ex}}, N_{\mathrm{in}}, N_{\mathrm{ex}}). \tag{2.63}$$

All terms that do not depend on V are gathered in const. They do not influence our analysis because they are fixed when we are minimising the total energy functional with respect to the shape of the shell, which only has an influence on V in (2.63). The osmotic pressure difference can be derived from this equation by $p_{\mathrm{os}} = -\partial F_{\mathrm{os}}/\partial V = k_B T(N_{\mathrm{in}}/V - N_{\mathrm{ex}}/V_{\mathrm{ex}})$. The first term in this expression represents the internal pressure, and $p_{\mathrm{ex}} \equiv k_B T N_{\mathrm{ex}}/V_{\mathrm{ex}}$ the external pressure which also occurs in (2.63) as the prefactor of the term linear in V.

Let us pretend for the moment that the shape of the shell can be changed without any elastic energy, so that F_{os} is the only free energy contribution of the system. Then we just have to minimise (2.63) with respect to V, which results in $V = N_{\mathrm{in}} V_{\mathrm{ex}}/N_{\mathrm{ex}}$. So the desired state of the system is that the concentration of osmotically active particles is identical in the inside and outside of the capsule. Thus, if the osmotic terms dominate the energy of the system, a precise volume control is possible by adjusting the external osmolyte concentration. Specifically, there are no problems with snap-through behaviour as in the case of mechanical pressure control with an empty capsule interior.

The total energy functional accounts for the elastic energy of the deformed shell and the free energies of the solutions, and reads

$$G = U + F_{\mathrm{os}} = U - k_B T N_{\mathrm{in}} \ln V + p_{\mathrm{ex}} V. \tag{2.64}$$

In this functional, U and V depend on the shape of the shell, and its variation is $\delta G = \delta U + (\partial F_{\mathrm{os}}/\partial V)\delta V = \delta U - p_{\mathrm{os}} \delta V$. Thus, the same equilibrium equations (2.16) are obtained, with $p = p_{\mathrm{os}} = k_B T N_{\mathrm{in}}/V - p_{\mathrm{ex}}$ as the pressure that is exerted on the shell.

In the case of a shell containing an ideal gas, fig. 2.17 on the right, the same energy functional is obtained. The internal gas has a free energy $F_{\mathrm{gas}} = -k_B T N_{\mathrm{in}} \ln V$, where N_{in} is now the number of gas atoms. According to the ideal gas equation $pV = N k_B T$, the prefactor can also be written as $k_B T N_{\mathrm{in}} = p_{\mathrm{in}} V$ with an internal gas pressure p_{in}. For isothermal processes, the left-hand side of the equation is constant during the deflation, and we may choose the initial state as the reference, where the shell volume is V_0 and the internal pressure equal to some ambient pressure p_a, and so we have $F_{\mathrm{gas}} = -p_a V_0 \ln V$. For the applied external pressure p_{ex}, an energy contribution $p_{\mathrm{ex}} V$ must be included, which corresponds in the simple setup of fig. 2.17 to the potential energy change of the weight that generates the pressure. The total energy functional is thus $G = U - p_a V_0 \ln V + p_{\mathrm{ex}} V$, which is of the same form as (2.64). Note that in the undeformed configuration, the force balance requires $p_{\mathrm{ex}} = p_a$. The buckling of spherical shells with an internal ideal gas has in part been studied numerically in ref. [91].

A large set of solutions of the shape equations has already been computed to generate the bifurcation diagrams in fig. 2.14, and these shapes can be used to plot the adequate bifurcation diagram for osmotically induced buckling. They are available as separate files that contain the pressure p for which they have been calculated, the parametrisation $\boldsymbol{r}(s_0)$ of the shape and the numerically integrated volume V and elastic energy U. The bifurcation parameter in the present case is the external (osmotic) pressure $p_{\mathrm{ex}} = k_B T N_{\mathrm{ex}}/V_{\mathrm{ex}}$, because this quantity can be changed in experiments by changing the concentration of osmotically active particles outside the shell, and its value can be obtained from the available data as $p_{\mathrm{ex}} = k_B T N_{\mathrm{in}}/V - p$ when a value for $k_B T N_{\mathrm{in}}$ is chosen.

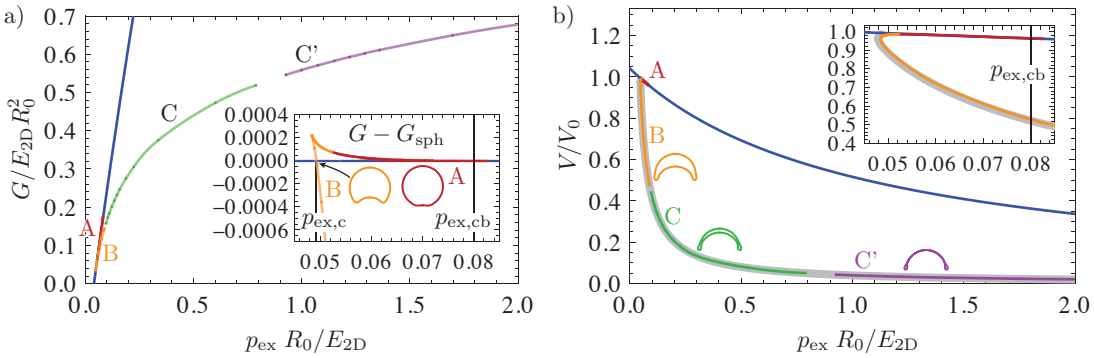

Figure 2.18.: Bifurcation diagrams for osmotically induced buckling or buckling under pressure control with an internal gas. The diagrams were created from the same data set used for fig. 2.14 (with $\tilde{E}_B = 10^{-4}$, $\nu = 1/3$ and $k_BTN_{in} = -p_{cb}V_0$), and the colour code of the different branches is also the same. In comparison with fig. 2.14 a) and b) it should be noted that p and p_{ex} have different signs, and that a part of the orange branch B is stable now. The thick grey line in the background of subfigure b) represents the analytic result (2.69) derived below.

Figure 2.18 shows the resulting bifurcation diagrams; in a) the energy diagram $G(p_{ex})$ and in b) the reduced volume $V(p_{ex})/V_0$. The latter one is related to Maddock's distinguished bifurcation diagram, since $-\partial_{p_{ex}}G = -V$, and his stability discussion can be applied to the $V(p_{ex})$ diagram when the minus sign is kept in mind. From both bifurcation diagrams it is evident that, compared to mechanical pressure control without internal gas, some of the buckled shapes are stabilised. To illustrate this, the same colour code for the different branches as in fig. 2.14 is used, i.e. a data point that is orange in fig. 2.14 is also orange in fig. 2.18. Specifically, the buckled shape at the critical external pressure $p_{ex,c}$ is now an orange one, with a medium large dimple, and not one with opposite sides in contact.

There are two critical external pressures: $p_{ex,c}$ corresponding to the point where the buckled and spherical branches cross in the energy diagram and $p_{ex,cb}$ corresponding to the classical buckling threshold where the buckled branch separates from the spherical one. Again, the threshold $p_{ex,c}$ where buckling becomes energetically favourable (but is only accessible by overcoming an energy barrier, see the inset in fig. 2.18 b) is much smaller than the classical threshold $p_{ex,cb}$ where the spherical branch loses its stability. The latter value can be calculated as

$$p_{ex,cb} = \frac{k_BTN_{in}}{V_{cb}} - p_{cb} \approx \frac{k_BTN_{in}}{V_0} + \left(4\frac{E_{2D}}{R_0} + 6(1-\nu)\frac{k_BTN_{in}}{V_0}\right)\sqrt{\tilde{E}_B}, \tag{2.65}$$

see (2.46) and (2.49), where the approximation holds for small $\tilde{E}_B$.

The amount how much of the orange branch B is stabilised depends on the choice of k_BTN_{in}. Our numerical investigations have shown that the larger this value, the larger is the stabilised part when p_{ex} is the control parameter. In the limit $N_{in} \to 0$, where there are no osmotically active particles (or gas particles) enclosed in the shell, the original behaviour for mechanical pressure control is recovered in which the whole branch B is unstable and the first buckled shape after the instability is a self-contacting one. In the limit $E_{2D} \to 0$ on the other hand, where the osmotic terms dominate the enthalpy (2.64), we obtain a precise volume control with $V = N_{in}V_{ex}/N_{ex}$ as shown above. Then, the whole branch B is stable. Therefore, buckling under osmotic pressure interpolates between buckling under volume control and buckling under mechanical pressure.

2.5.4. Enthalpy landscape for osmosis

The stabilising effect of an internal medium or osmolyte concentration on shapes with medium large dimples can be explained with an enthalpy landscape similar to the case of mechanical pressure control discussed in section 2.5.2. When we consider the appropriate energy functional for osmosis or pressure control with an internal gas, a term $\sim -\ln V$ must be added to the enthalpy landscape (2.57) of mechanical pressure control. It penalises small volumes and therefore prevents the shell from going to $\Delta V \to V_0$ by replacing the boundary minimum at $\Delta V = V_0$ by a divergence. The total (free) enthalpy reads

$$G(\Delta V) = U_{\mathrm{Pog}}(\Delta V) - p_{\mathrm{ex}}\Delta V - k_B T N_{\mathrm{in}} \ln(V_0 - \Delta V) \tag{2.66}$$

and has the qualitative shape as plotted in fig. 2.19, continuous line. The global enthalpy minimum is assumed at a finite ΔV that depends on the elastic moduli, the external pressure p_{ex} and the internal particles $k_B T N_{\mathrm{in}}$. This qualitatively explains why an internal gas or internal osmotically active particles prevent the full collapse of the shell and stabilise buckled shapes with medium volume reduction (parts of branch B).

Based on this simple model, we can also justify why buckled shapes with a single dimple are usually observed in osmosis based buckling experiments, and not shapes with multiple indentations. As argued before in the introduction of section 2.4, buckled shapes with a single dimple are favourable if the internal volume of the shell is fixed. When we consider shapes with two dimples, the volume reduction ΔV of the shell is divided between the two dimples which have $\Delta V/2$ each. According to the Pogorelov model, the elastic energy of a double buckled shell is thus $U_{\mathrm{Pog}\,2}(\Delta V) = 2\,U_{\mathrm{Pog}}(\Delta V/2) = 2^{1/4} \cdot U_{\mathrm{Pog}}(\Delta V)$, where the last equation holds because $U_{\mathrm{Pog}} \sim \Delta V^{3/4}$. Thus, for given volume difference it is energetically unfavourable to create multiple dimples [112].

Now we have to clarify how this translates to the free enthalpy $G(p_{\mathrm{ex}})$ for osmotic pressure control where a change of variables from ΔV to p_{ex} is necessary. The branch with a single dimple has a free enthalpy

$$G(p_{\mathrm{ex}}) = \min_{\Delta V} \left[U_{\mathrm{Pog}}(\Delta V) - p_{\mathrm{ex}}\Delta V - k_B T N_{\mathrm{in}} \ln(V_0 - \Delta V)\right] \equiv \min_{\Delta V} \left[f(\Delta V,\, p_{\mathrm{ex}})\right] \tag{2.67}$$

for osmosis. A function $f(\Delta V, p_{\mathrm{ex}})$ was defined here to simplify the notation. To obtain the enthalpy of the symmetrically buckled branch we just change U_{Pog} to $U_{\mathrm{Pog}\,2}$ in this expression,

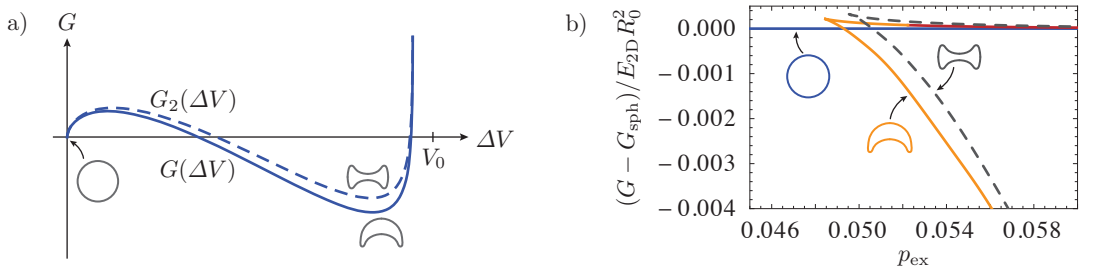

Figure 2.19.: a) Free enthalpy landscape for buckling under osmosis. The enthalpy minimum lies at finite ΔV, hence the shell does not collapse completely. For shapes with two dimples (dashed curve), the enthalpy is larger, and thus two dimples are energetically less favourable. b) The numerical solutions of the shape equations confirm that the solution branch with two dimples (dashed grey) lies at higher energies than the branch with a single dimple (orange).

which results in

$$G_2(p_{\mathrm{ex}}) = \min_{\Delta V} \Big[f(\Delta V,\, p_{\mathrm{ex}}) + \big(2^{1/4}-1\big) U_{\mathrm{Pog}}(\Delta V) \Big] \tag{2.68}$$

The additional term $\big(2^{1/4}-1\big)U_{\mathrm{Pog}}(\Delta V)$ is positive for all ΔV. The volume-dependent enthalpy function whose minimum we are searching is thus shifted to higher values, see fig. 2.19 a), dashed line. As a consequence, the stationary shape that resides in the minimum is shifted to a higher enthalpy when there are two dimples on the shell instead of one; and also the transition states at the enthalpy maximum lie at higher enthalpy. This result is confirmed by the enthalpy diagram fig. 2.19 b) that was generated from the shape equations.

Let us find the enthalpy minimum analytically so that we can give recommendations to experimenters how they should choose the concentrations of osmotically active particles inside and outside the shell in order to stabilise buckled shapes of a desired volume reduction. The condition for an extremum of the free enthalpy is

$$\begin{aligned} 0 = G'(\Delta V) &= U'_{\mathrm{Pog}}(\Delta V) - p_{\mathrm{ex}} + \frac{k_B T N_{\mathrm{in}}}{V_0 - \Delta V} \\ \Rightarrow \quad p_{\mathrm{ex}} &= \frac{k_B T N_{\mathrm{in}}}{V_0 - \Delta V} + \frac{3}{2} 6^{1/4} J_{\min} \frac{E_{2\mathrm{D}} \tilde{E}_B^{3/4}}{R_0 (1-\nu^2)^{1/4}} \left(\frac{\Delta V}{V_0} \right)^{-1/4}. \end{aligned} \tag{2.69}$$

This relation matches the numerical results with a striking accuracy, see the bifurcation diagram fig. 2.18 b), grey line. Because the free enthalpy landscape is based on the approximate Pogorelov model, which is inaccurate for large dimples, we would expect our analytic estimate also to become inaccurate for large ΔV. But this is not the case. For large ΔV, the position of the free enthalpy minimum is primarily determined by the competition of the terms $-p_{\mathrm{ex}}\Delta V$ and $-k_B T N_{\mathrm{in}} \ln(V_0 - \Delta V)$ in (2.66); the elastic energy U_{Pog} plays a subordinate role. Indeed, the approximation $p_{\mathrm{ex}} = k_B T N_{\mathrm{in}}/(V_0 - \Delta V)$, where the elastic contribution is completely neglected, is in good agreement with the numerical pressure-volume-relation for $\Delta V \gtrsim 0.5$. Neglecting the elastic contribution in (2.69) is justified for small $\tilde{E}_B$ (and not too small ΔV) because $k_B T N_{\mathrm{in}}/V_0 = \mathcal{O}(p_{\mathrm{cb}}) \sim \tilde{E}_B^{1/2}$ and the elastic term is $\sim \tilde{E}_B^{3/4}$.

To obtain buckled capsules, we must ensure that the external osmotic pressure is close to the classical threshold (2.65), $p_{\mathrm{ex}} = p_{\mathrm{ex,cb}}$, so that the shell can buckle spontaneously. Inserting this into (2.69) and solving for the interior osmolyte concentration yields

$$k_B T \frac{N_{\mathrm{in}}}{V_0} = \frac{\frac{9}{8} J_{\min} \left(\frac{8}{3}\right)^{3/4} \frac{E_{2\mathrm{D}}}{R_0} \frac{\tilde{E}_B^{3/4}}{(1-\nu^2)^{1/4}} \left(\frac{V_0}{\Delta V}\right)^{1/4} - 4 \frac{E_{2\mathrm{D}}}{R_0} \sqrt{\tilde{E}_B}}{1 + 6(1-\nu)\sqrt{\tilde{E}_B} - V_0/(V_0 - \Delta V)}. \tag{2.70}$$

This expression simplifies considerably when only the leading order in $\tilde{E}_B$ is retained. The value of $k_B T N_{\mathrm{in}}$ influences the external pressure $p_{\mathrm{ex,cb}}$ needed to induce buckling, see (2.65). For both values, the simplified results in leading order are

$$k_B T \frac{N_{\mathrm{in}}}{V_0} \approx 4 \left(\frac{V_0}{\Delta V} - 1 \right) \frac{E_{2\mathrm{D}}}{R_0} \sqrt{\tilde{E}_B} \qquad \text{and} \qquad p_{\mathrm{ex,cb}} \approx 4 \frac{V_0}{\Delta V} \frac{E_{2\mathrm{D}}}{R_0} \sqrt{\tilde{E}_B}. \tag{2.71}$$

The external osmotic pressure has been introduced as $p_{\mathrm{ex}} = k_B T N_{\mathrm{ex}}/V_{\mathrm{ex}}$, and so both results can be directly translated into concentrations of osmotically active particles inside and outside the shell. The classical buckling pressure $p_{\mathrm{cb}} = -4\sqrt{\tilde{E}_B} E_{2\mathrm{D}}/R_0$ occurs as the relevant scale in (2.71). If we want to get buckled shapes with $\Delta V = V_0/2$, for example, we should choose $k_B T N_{\mathrm{in}}/V_0 = -p_{\mathrm{cb}}$ and $k_B T N_{\mathrm{ex}}/V_{\mathrm{ex}} = -2p_{\mathrm{cb}}$ in osmosis based experiments. These are exactly the values used to draw fig. 2.18, and the inset in fig. 2.18 b) confirms that the buckling at the classical threshold indeed results in a shape close to $V = V_0/2$.

2.5.5. Applications of the results on osmotic buckling

Equation (2.69) can form the basis for measurements of the external osmotic pressure by using elastic capsules as pressure sensors. The capsules must be "calibrated" in the sense that their elastic properties, size and internal osmolyte concentration are known. If they are embedded in a bath with a larger, unknown osmolyte concentration and buckle consequently, their volume difference can be measured and inserted into (2.69) to obtain p_{ex} or the external osmolyte concentration $N_{\mathrm{ex}}/V_{\mathrm{ex}} = p_{\mathrm{ex}}/k_BT$. The volume measurement could be achieved through a microscopy image analysis, in the simplest version by measuring the shell depth d and original radius R_0 (see fig. 2.20) and using the geometrical relations (2.28) of the isometric buckled shapes to obtain $\Delta V/V_0 = (1 - d/2R_0)^2(2 + d/2R_0)/2$. While the $p_{\mathrm{ex}}(\Delta V)$ relation (2.69) is very precise, this $\Delta V(d)$ relation introduces some errors, but figure 2.20 shows that these errors are only significant for $d \lesssim R_0/2$.

Vice versa, eq. (2.69) or the resulting relation for p_{ex} as a function of d/R_0, see fig. 2.20, can be used to determine the capsule's material parameters by fitting experimental data for d/R_0 at different external osmotic pressures p_{ex}. Specifically, eq. (2.69) can be used to determine the parameter combination $E_{2\mathrm{D}}\tilde{E}_B^{3/4}/R_0$ and the number N_{in} of enclosed osmotically active particles. In combination with the analysis of the maximal edge curvature of buckled shapes proposed in section 2.4.2, which allows to determine the reduced bending modulus $\tilde{E}_B$, both elastic moduli and the internal osmotic pressure can be obtained from relatively simple shape analyses of osmotically pressurised shells. To this end, accurate measurements of the external osmotic pressure and images of cross-sections along the axis of symmetry of the shells must be provided.

A test of such an analysis was performed using the data published in ref. [51] for polyelectrolyte capsules with radius $R_0 = 2 \cdot 10^{-6}\,\mathrm{m}$ and wall thickness $H_0 = 2 \cdot 10^{-8}\,\mathrm{m}$. The polyelectrolyte capsules were deflated osmotically, by adding poly(styrene sulfonate, sodium salt) (PSS) to the exterior solution. The osmotically active particles are the counter-ions surrounding the PSS molecules, and they exert an external osmotic pressure p_{ex} on the capsules. In the experiments, the values of p_{ex} were measured with a vapour pressure osmometer. In view of the few available data points which can be obtained from the confocal microscopy capsule images in ref. [51], we use the value for the shear modulus of the shell material $G = 500\,\mathrm{MPa}$ given in ref. [51], which corresponds to a Young modulus of $E = 1500\,\mathrm{MPa}$ if $\nu = 0.5$. Using also the measured values for capsule radius and thickness this leads to $E_{2\mathrm{D}} = 30\,\mathrm{N/m}$ and $\tilde{E}_B = 1.11 \cdot 10^{-5}$. Inside the capsule we also expect a certain concentration of ions, because the capsule was fabricated from polyelectrolytes. This gives rise to a nonzero but unknown value of k_BTN_{in} which serves as the only fitting parameter in (2.69).

The value for G obtained in ref. [51] might be questionable because its determination relied on a measurement of the buckling pressure using the classical buckling pressure $|p_{\mathrm{cb}}|$, see eq. (2.46). This determination assumes a vanishing internal osmolyte concentration, i.e. $k_BTN_{\mathrm{in}} \approx 0$ in eq. (2.65) and, moreover, the classical buckling pressure (2.65) only represents an upper bound for the buckling pressure. In fig. 2.16 a) it is shown that real imperfect shells buckle already at considerably weaker pressures. As already pointed out, values for $E_{2\mathrm{D}}$ and $\tilde{E}_B$ could also be obtained from a shape analysis, in principle, if shape images for more external osmotic pressures p_{ex} were available.

From five confocal microscopy images, figs. 2 (b) and (c) in ref. [51], the ratio d/R_0 was measured. An uncertainty arises because one cannot be sure if the cross-sections imaged by the confocal microscopy cut through the centre of the capsules and if they are oriented along the axis of symmetry of the capsules. For each image, the external osmotic pressure was given in ref. [51]. The resulting data points are plotted in fig. 2.20 b), together with the fit using

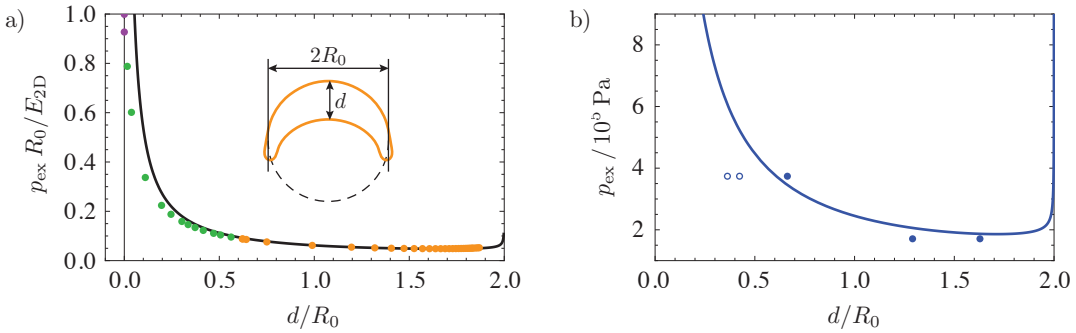

Figure 2.20.: Using a buckled shell as an osmotic pressure sensor: From a measurement of the depth d and original shell radius R_0, the external osmotic pressure p_{ex} can be determined. a) The data points are generated from the data set already used in figs. 2.14 and 2.18, with $\tilde{E}_B = 10^{-4}$, $\nu = 1/3$ and $k_BTN_{in} = -p_{cb}V_0$, and the solid line represents the analytic approximation (2.69). b) Analysis of experimental results published in ref. [51]. The data points from the experiments are fitted using eq. (2.69) with k_BTN_{in} as fitting parameter. The open points were excluded from the fit because the experimental images looked conspicuous that they may not represent centred cross-sections.

eq. (2.69). For the fit parameter we obtained $k_BTN_{in} = 5.4 \cdot 10^{-12}\,\mathrm{J}$, which corresponds to an internal osmotic pressure (in the undeformed state) of $p_{in,0} = k_BTN_{in}/V_0 = 1.6 \cdot 10^5\,\mathrm{Pa}$ and to a concentration of $N_{in}/V_0 = 65\,\mathrm{mol/m^3}$. Equation (2.69) describes the experimental results with reasonable accuracy.

Recently, a group of experimenters also suggested to use microcapsules as osmotic pressure sensors [74]. In their approach, capsules with different interior osmolyte concentrations $c_1, c_2, c_3, \ldots$ are prepared using a microfluidic device and immersed in a solution whose osmolyte concentration c_{ex} is to be determined. When very thin shells are used, those with $c_i < c_{ex}$ are deflated and buckle consequently. The external osmolyte concentration can thus be estimated to lie between two values $c_i < c_{ex} < c_j$ if type i capsules are found to buckle and type j capsules are found to be undeformed (or slightly inflated). Based on the presented theoretical description, their procedure could be extended and could possibly work with less different internal osmolyte concentrations c_i when an analysis of the volume according to (2.69) is incorporated.

Chapter 3

Buckling and wrinkling of plates and shallow shells

Abstract – The following chapter focuses on instabilities of flat plates and plates with a weak initial curvature upon in-plane compression. These instabilities involve out-of-plane deflections and are termed buckling (if the wavelength of the deflection pattern is large) or wrinkling (if the wavelength is small). The calculation of such instabilities is based on the small strain elasticity of shallow shells, which is introduced first. In contrast to the large-strain shell theory of the last chapter, we now include shear components and formulate the theory with Cartesian tensors. The derived stability equations are then applied to three setups: (i) a narrow, infinitely long rectangular plate with simply supported edges under a compression τ_x and tension τ_y which wrinkles over its whole width, (ii) an infinitely large plate subject to a uniform tension τ_y and a parabolic stress τ_x that is locally compressive, on which localised wrinkles form, and (iii) the previous setup with the difference that the plate has an initial weak curvature in y direction. The ultimate goal is to use the buckling criterion of the third setup to explain the secondary buckling of spherical shells, where the dimple loses its axisymmetry by wrinkles developing under a locally compressive stress.

Published material – Parts of sections 3.3.2 and 3.3.3 are reproduced with modifications from the author's publications [155], © 2014 by IOPscience and [156], with kind permission of The European Physical Journal (EPJ).

3.1. Introduction and motivation

The axisymmetric buckling transition of spherical shells, which we investigated in the previous chapter, is one example of an instability that is driven by a trade-off between compression and bending energy. The uniformly contracted configuration of a deflated spherical shell stores a large amount of compression energy, which can be released by buckling out of the symmetric shape. The small dimensionless bending stiffness $\tilde{E}_B \sim H_0^2/R_0^2$, see (2.22), causes the amount of bending energy stored in the buckled shape to be much less than the amount of compression energy that could be released. So the total elastic energy that is stored in the deformed configuration can be lowered by buckling. This is the basic mechanism behind all buckling and wrinkling phenomena.

An even simpler, quasi one-dimensional example is the buckling of a slender rod under axial compression, which was considered two-and-a-half centuries ago by Leonard Euler [43]. If the compressive axial force exceeds a critical force, the initially straight rod of length L buckles [83], i.e. it assumes a curved configuration with a sinusoidal transverse deflection with wavelength

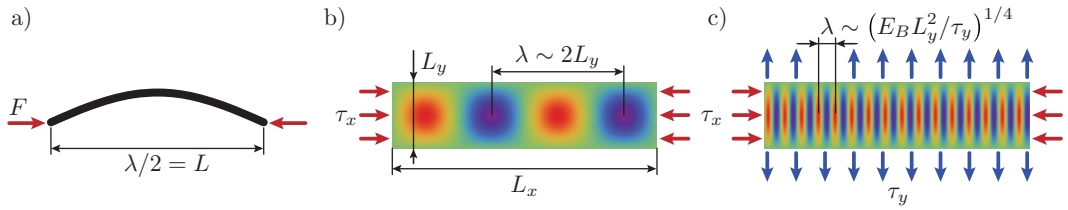

Figure 3.1.: From buckling to wrinkling: a) Euler-Buckling of a bar under axial compression with longest possible wavelength (side view). b) Top view of a buckled rectangular plate with simply supported edges under compression in x-direction, with a wavelength comparable to the width L_y of the plate [124]. c) Wrinkling of a plate under compression in x-direction and tension in y-direction with shorter wavelength λ depending on the bending stiffness E_B, width L_y and tension τ_y [26]. In the colour plots, red indicates an upward deflection and blue a downward deflection; green is neutral.

$\lambda = 2L$, see fig. 3.1 a). The critical force can be calculated as $F_c = \pi^2 EI/L^2$, where I is the second moment of area of the rod's cross section.

Things get more involved, compared to the Euler buckling of rods, when the elastic bodies are (quasi) two-dimensional plates and shells because then the geometry plays a very important role. In the books of Timoshenko [124,125], the buckling of plates under compressive in-plane stresses with various geometries and boundary conditions is investigated. An important difference to the Euler buckling of rods is the wavelength of the buckling pattern. Whereas rods buckle in a mode with largest possible wavelength, plates with simply supported edges typically buckle in a wavelength comparable to the width of the plate, see fig. 3.1 b).

More recently, the wrinkling of surfaces has received a lot of attention, which is essentially the same as buckling but with relatively short wavelengths, see fig. 3.1 c), although the distinction between the terms buckling and wrinkling is vage and not clearly defined in the literature. It has been observed and analysed in many different geometries, for example for rectangular strips being stretched [26, 27], sheared [143–145], compressed [30] or subjected to inhomogeneous growth like in plant leafs [88], circular sheets [33,34] which are placed on water drops [64,65,75] or pressed into hemispherical moulds [67], pressurised shells that are indented [129,130,132], elastic tubes that are bent [121] and for many more setups, see [86] for a recent review.

The mechanism behind wrinkling is the same as for buckling: Compressive strains can be traded for energetically more favourable bending strains. However, the wavelength in the case of wrinkling is much shorter than for buckling, which can be achieved in three different ways: (i) applying a tensional stress in the direction perpendicular to the compressive stress [26,27,33,34,130], (ii) attaching the elastic membrane to a liquid or soft elastic substrate [35,59,75,87] and (iii) by using curved elastic membranes instead of flat ones [47,48]. The overall explanation is that high wrinkle amplitudes are rendered energetically unfavourable by these three effects. Thus, the excess length of the material that was deposited in the buckling pattern must then be deposited in a pattern with smaller amplitude. This is a purely geometrical problem, and can be achieved by using smaller wavelengths, thus turning the buckling pattern into a wrinkling pattern.

Interestingly, there are several setups where elastic membranes do wrinkle, although the applied external loads are not compressive, but tensional or shearing. The term *tensional wrinkles* appearing occasionally in this context is a bit misleading, since a compression in one direction is still the responsible stress for wrinkling; the tension in the other direction rather controls the wrinkle wavelength and compression threshold. Figure 3.2 shows three examples that can be observed in everyday life, for example when handling cloths or foils, but which

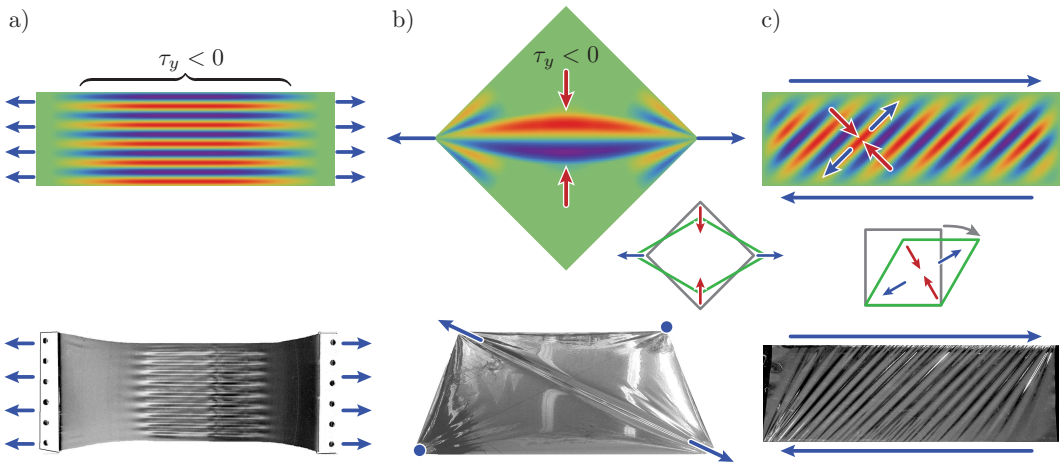

Figure 3.2.: Three examples of wrinkling under external tension or shear. a) Rectangular strip with clamped short edges and free long edges under uniaxial stretch [26], b) a square with free edges under diagonal tension applied to two corners (in the experimental image, the other two corners are fixed and also under slight tension) [143], c) rectangular strip with simply supported edges under shear stress [143]. The experimental images are taken from the cited references.

are quite challenging for the physical intuition. In fig. 3.2 a), a rectangular strip is under a tension $\tau_x > 0$ and the long edges are free. Near the short edges, there is a tension $\tau_y > 0$ because the membrane "wants to contract" according to the Poisson effect, but is hindered from contraction because the short edges are clamped. An analysis of the stress field then shows that there is a compression $\tau_y < 0$ far away from the short edges [27], which leads to the observed wrinkling. The setup of fig. 3.2 b) is perhaps more intuitive to understand. Here, a quadratic membrane is stretched along the diagonals, which leads to a compression along the other diagonal near the centre. The occurrence of compression can be understood by imagining that a large hole is in the centre the square, so that the membrane only consists of four narrow strips along the sides of the original square. When this square is stretched along one diagonal it will deform into a rhombus, see the inset in fig. 3.2 b), and the two free corners will move to the centre. In the complete square, the free corners will thus push the interior material, leading to compression and consequently wrinkling. Figure 3.2 c) shows that a shear stress exerted on a rectangular membrane also leads to wrinkling. The reason is that the pure shear stress can be expressed as compression and tension if the coordinate system is rotated by 45° as we will see below. Intuitively, this becomes clear by considering a small quadratic part of the membrane. Upon shearing, the square will deform into a rhombus, as in the previous case, with one diagonal stretched and the other compressed. The wrinkles are oriented along the direction of the tensional stress, i.e. in a 45° angle as shown in fig. 3.2 c).

So far, buckling and wrinkling are mostly handled separately from a theoretical point of view. Whereas a buckling analysis usually involves a stability analysis of the Föppl-von-Kármán equations (for planar membranes) or the shallow shell equations (for curved membranes) to obtain the critical load and the complete buckling pattern [124, 135], many investigations of wrinkling rely on energy considerations with an ansatz for a sinusoidal wrinkling pattern whose wavelength can then be determined [26, 144]. A recent attempt to model the crossover between buckling and wrinkling has been presented in refs. [33, 34] for the Lamé setup (an annular sheet under axisymmetric tensile loads), where a distinction between a near-threshold (NT) regime

and a far-from-threshold (FFT) regime has been drawn. In the NT regime, the critical buckling load is only slightly exceeded so that a stability analysis of the Föppl-von-Kármán equations is appropriate, but in the FFT regime it is assumed that the compressive stress has been fully released by the well developed wrinkles.

Below, we will present a very simple study of a rectangular strip that explains the transition from buckling (with large wavelength) to wrinkling (with small wavelength). The whole analysis is based on a stability analysis of the Föppl-von-Kármán equations and the transition from buckling to wrinkling is driven completely by the magnitude of the tensional stress along the wrinkles (perpendicular to the compressive stress that cause the wrinkles).

In many real cases, the wrinkled region is not limited by the boundaries of the membrane, see fig. 3.2 a) and b) for example, leading to *partly wrinkled membranes* [121]. Such behaviour is seen when a membrane is compressed only locally and not over its whole width. In classical tension field theory [121, 144], the stress field for planar deformation is calculated, and then it is assumed that regions with compressive stresses wrinkle and the compressive stresses are released to zero. We will approach this problem by using a parabolic stress profile that is locally compressive and conduct a stability analysis without the above mentioned assumptions. Our analysis shows that the wrinkles indeed limit themselves to the compressive region (with a slight overhang to the sides), and that the same scaling laws for the critical compression and wavelength as obtained for membranes with clamped edges hold.

Apart from the purely theoretical interest evoked above, this chapter also fulfils a practical purpose. In the previous chapter we saw that in a buckled shell a region of strong hoop compression exists along the inner side of the dimple edge, see fig. 2.9. In numerical simulations and in experiments with microcapsules, it has been observed that wrinkles develop in this region upon sufficient deflation, so that the dimple loses its axisymmetry and acquires a polygonal shape. The threshold for this *secondary buckling* will be calculated from the simple model with a parabolic, locally compressive stress mentioned above.

3.2. Small strain elasticity theory for shallow shells

In this chapter we consider the stability of elastic plates and shallow shells which are compressed (at least in one direction). A *plate* is by definition a sheet of elastic material which is flat in its reference configuration. It can be conveniently parametrised with Cartesian coordinates (x, y) for the plane of the plate, and its deformed image by a height profile $w(x, y)$. A *shallow shell*, on the other hand, is a curved plate, i.e. its reference configuration already has a small curvature. A shallow shell above the x-y-plane is also parametrised by the plane Cartesian coordinates. As long as the shell is shallow, we can neglect the complication that x and y are no arc length coordinates [135], or in other words, the metric of the shallow shell is approximately flat. The formulations of plate theory and shallow shell theory are thus very similar to each other and will be presented below.

According to the conventions of the finite strain shell theory used in chapter 2, the coordinates for the reference shape should rather read (x_0, y_0), but we omit the indices "0" for two reasons. Firstly, we are mainly concerned with linear elasticity theory in this chapter and describe the deformation with displacement fields, as usual in linear theory, rather than a function $\boldsymbol{x}(\boldsymbol{x}_0)$ as typical for non-linear theory [126]. Secondly, we apply the results to cases where the reference configuration of the plate or shell is an approximation to an already deformed configuration.

In the small strain theory of shallow shells, there are two important differences to the large strain shell theory of chapter 2. On the one hand, there are some simplifications due to the smallness of the strains, e.g. the $1/\lambda_i$ factors in the constitutive law (2.10) can be neglected.

On the other hand, the principal axes of deformation are not along the directions of the parametrisation, so that we get additional shear and twist terms. The theory will therefore be presented in terms of 2×2 Cartesian tensors.

3.2.1. Tensors of strain and bending

We consider a shallow shell with a reference shape described by the height profile $z(x, y)$, whose initial curvatures can be approximated by

$$\kappa_x = \frac{\partial^2 z}{\partial x^2}, \qquad \kappa_y = \frac{\partial^2 z}{\partial y^2}, \quad \text{and} \quad \kappa_{xy} = \frac{\partial^2 z}{\partial x \partial y}. \tag{3.1}$$

This reference state is deformed by small displacements u, v, w (in x, y and z direction, respectively). According to the Donnel-Mushtari-Vlasov (DMV) shell theory [96], the strains and bending strains induced by the displacement field are given by

$$\begin{aligned} \varepsilon_x &= \frac{\partial u}{\partial x} - \kappa_x w + \frac{1}{2}\left(\frac{\partial w}{\partial x}\right)^2 & K_x &= \frac{\partial^2 w}{\partial x^2} \\ \varepsilon_y &= \frac{\partial v}{\partial y} - \kappa_y w + \frac{1}{2}\left(\frac{\partial w}{\partial y}\right)^2 & K_y &= \frac{\partial^2 w}{\partial y^2} \\ \varepsilon_{xy} &= \frac{1}{2}\left(\frac{\partial u}{\partial y} + \frac{\partial v}{\partial x}\right) - \kappa_{xy} w + \frac{1}{2}\frac{\partial w}{\partial x}\frac{\partial w}{\partial y} & K_{xy} &= \frac{\partial^2 w}{\partial x \partial y}. \end{aligned} \tag{3.2}$$

These strain-displacement relations are approximate, because only three selected non-linear terms are included and others have been omitted. They are justified if the displacements are approximately perpendicular to the midsurface of the shell, which is the case for shallow shells [96, 135].

We can arrange these components in tensor form,

$$\boldsymbol{\varepsilon} = \begin{pmatrix} \varepsilon_x & \varepsilon_{xy} \\ \varepsilon_{xy} & \varepsilon_y \end{pmatrix} \quad \text{and} \quad \boldsymbol{K} = \begin{pmatrix} K_x & K_{xy} \\ K_{xy} & K_y \end{pmatrix}, \tag{3.3}$$

to define the *strain tensor* and *bending tensor*, respectively. Both tensors are symmetric and since they are Cartesian tensors, we do not have to distinguish between co- and contravariant components.

From the definition of the bending strains in (3.2), it is clear that they measure the curvature change of the shallow shell, see fig. 3.3. The principal components K_x and K_y are therefore

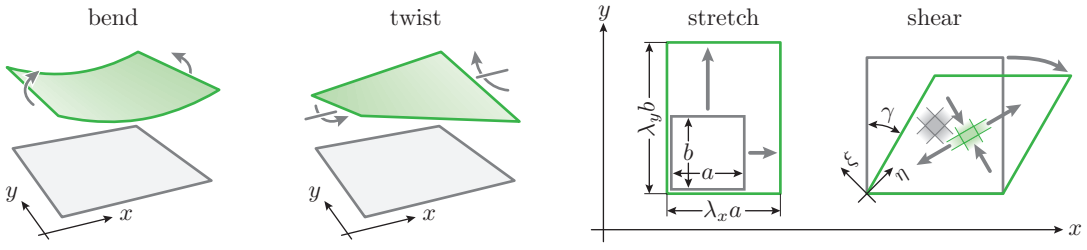

Figure 3.3.: The basic deformations of a shallow shell, illustrated for a plate. The grey shape is the reference configuration, the green shape the deformed configuration. For the shear deformation, a new coordinate system (η, ξ), the principal axes system, is introduced along the diagonals.

very similar to the non-linear bending strains (2.6). The new component K_{xy} measures the "twist" of the shallow shell.

The strain tensor describes the change of the metric of the shell's midsurface, that is, the length change of a line element $\mathrm{d}\boldsymbol{s}$ that is deformed to $\mathrm{d}\bar{\boldsymbol{s}}$. This information is obtained from the strain tensor by multiplying it with the undeformed line element $\mathrm{d}\boldsymbol{s} = (\mathrm{d}x, \mathrm{d}y)^\intercal$ from the left and the right:

$$\mathrm{d}\boldsymbol{s}^\intercal \, \boldsymbol{\varepsilon} \, \mathrm{d}\boldsymbol{s} = \frac{1}{2} \left(\mathrm{d}\bar{\boldsymbol{s}}^2 - \mathrm{d}\boldsymbol{s}^2 \right) . \tag{3.4}$$

In ref. [4], this relation is called the *fundamental property* of the strain tensor.

To get a feeling for the different components of the strain tensor, let us consider some simple cases of strain at the example of a plate under in-plane deformation. Since the strain tensor is symmetric, it can be diagonalised at any point by a principal axis transformation. In the general case, the principal axes will vary from point to point. After rotating the coordinate system so that the strain tensor is diagonal at one specific material point, it is not diagonal at the other material points. For now we will pick special deformations where the strain tensor is constant over the whole membrane, which can also be interpreted as zooming in so close that we cannot see the variations of the strain tensor across the membrane anymore.

When a plate is stretched in x- and y-direction, the strain tensor is diagonal,

$$\boldsymbol{\varepsilon} = \begin{pmatrix} \varepsilon_x & 0 \\ 0 & \varepsilon_y \end{pmatrix} . \tag{3.5}$$

A line element $\mathrm{d}\boldsymbol{s} = (\mathrm{d}x, 0)$ changes its quadratic length according to (3.4) to $\mathrm{d}\bar{\boldsymbol{s}}^2 = (2\varepsilon_x + 1)\mathrm{d}\boldsymbol{s}^2$. Thus, the material fibres oriented in x-direction get stretched by a factor $\lambda_x = \sqrt{2\varepsilon_x + 1}$ (and analogously in y-direction). The rather cumbersome relation between strains and stretches, $\varepsilon_i = (\lambda_i^2 - 1)/2$ and $\lambda_i = \sqrt{2\varepsilon_i + 1}$, simplifies for small strains $\varepsilon_i \ll 1$: Then we simply get $\varepsilon_i = \lambda_i - 1$ in leading order (with $i \in \{x, y\}$). In the finite strain shell theory of chapter 2, we worked mainly with the stretches λ_i, but also introduced the *engineering strains* $e_i = \lambda_i - 1$ in (2.5). The strains ε_i introduced here are called the *Green-Lagrange strains*, and they are identical to the engineering strains within the accuracy of the small-strain theory discussed here.

The off-diagonal elements of the strain tensor are also called the shear components. A shear deformation which produces a strain tensor with vanishing diagonal elements is shown in fig. 3.3 and is described by the displacement fields $u = \gamma\, y$ and $v = 0$. This gives a strain tensor of

$$\boldsymbol{\varepsilon} = \begin{pmatrix} 0 & \gamma/2 \\ \gamma/2 & 0 \end{pmatrix} . \tag{3.6}$$

With (3.4), we see that line elements along the x- and y-axes are unchanged in length. The principal axes of the shear strain tensor are along the vectors $\boldsymbol{e}_\eta = (1, 1)^\intercal/\sqrt{2}$ and $\boldsymbol{e}_\xi = (-1, 1)^\intercal/\sqrt{2}$. A rotation of the coordinate system by $\pi/4$ therefore diagonalises the strain tensor,

$$\boldsymbol{\varepsilon}^{\mathrm{diag}} = \boldsymbol{Q}^\intercal \boldsymbol{\varepsilon} \boldsymbol{Q} = \begin{pmatrix} \varepsilon_\eta & 0 \\ 0 & \varepsilon_\xi \end{pmatrix} = \begin{pmatrix} \gamma/2 & 0 \\ 0 & -\gamma/2 \end{pmatrix} \quad \text{with} \quad \boldsymbol{Q} = \frac{1}{\sqrt{2}} \begin{pmatrix} 1 & -1 \\ 1 & 1 \end{pmatrix} . \tag{3.7}$$

This means that the membrane is stretched in η-direction by $\lambda_\eta = \sqrt{1 + \gamma}$ and compressed in ξ-direction by $\lambda_\xi = \sqrt{1 - \gamma}$, which is visualised in fig. 3.3 by the deformed image (green) of a diagonal square (grey) in the reference state. That demonstrates that a shear deformation can be described by tension and compression in a suitable coordinate system, and explains the shear wrinkles presented in fig. 3.2 c).

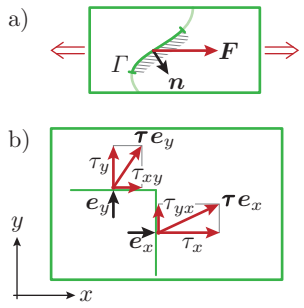

Figure 3.4.: Interpretation of the stress tensor. a) The force $\boldsymbol{F}$ exerted on a curve Γ by the neighbouring material (shaded) is determined by the integral over the stress tensor, see eq. (3.8), here in the case of a horizontally stretched membrane. b) The force density on a vertical line element is $\boldsymbol{\tau e}_x = (\tau_x, \tau_{yx})$, with a *shear stress* τ_{yx} and a *normal stress* τ_x. For a horizontal line element we have $\boldsymbol{\tau e}_y = (\tau_{xy}, \tau_y)$.

3.2.2. Stresses and bending moments

In the finite strain shell theory of chapter 2 we introduced stresses and bending moments as derivatives of a surface energy density. To understand the concept of stresses a bit better, we will now explain their mechanical relevance as force densities.

The fundamental relation for the (two-dimensional) stress tensor $\boldsymbol{\tau}$ is that the force $\boldsymbol{F}$ which acts on a curve Γ is given by the line integral

$$\boldsymbol{F} = \int_\Gamma \boldsymbol{\tau}\,\boldsymbol{n}\,\mathrm{d}s \quad \text{with} \quad \boldsymbol{\tau} = \begin{pmatrix} \tau_x & \tau_{xy} \\ \tau_{yx} & \tau_y \end{pmatrix}, \tag{3.8}$$

where $\boldsymbol{n}$ is the (unit) normal to the curve Γ. To be precise, the material lying in $\boldsymbol{n}$-direction next to the curve exerts this force on the material lying on the opposite side of the curve, see fig. 3.4.

Unlike the stress-tensor in three-dimensional elasticity, the two-dimensional stress tensor is not necessarily symmetric [96, 135]. However, in this thesis we are only concerned with special and approximate cases where $\boldsymbol{\tau}$ is symmetric, i.e. $\tau_{yx} = \tau_{xy}$. This is guaranteed for shells with vanishing bending stiffness, spherical shells, shells with a flat reference state (plates), approximately for shallow shells, and for deformations without shearing (e.g. axisymmetric deformations of axisymmetric shells as in chapter 2).

The bending moments already introduced in the finite strain shell theory are now also written in tensor form, including an off-diagonal element,

$$\boldsymbol{m} = \begin{pmatrix} m_x & m_{xy} \\ m_{yx} & m_y \end{pmatrix}. \tag{3.9}$$

In our shallow shell theory, $\boldsymbol{m}$ is also symmetric. The off-diagonal element is associated to the twist (see fig. 3.3) of the shell. As explained before, the bending moments arise because of variations of the (three-dimensional) stress across the thickness of the shell. However, we skip this discussion because it necessitates the knowledge of three-dimensional elasticity theory.

3.2.3. Small strain elasticity theory

As in the finite strain shell theory, the stresses and bending moments can be related to the strains and bending strains by an elastic energy density $w_S(\boldsymbol{\varepsilon}, \boldsymbol{\tau})$. The centrepiece of this argument is the principle of virtual work [96, 135]. Let us assume that the shallow shell is in a configuration with strain tensor $\boldsymbol{\varepsilon}$, bending strain tensor $\boldsymbol{K}$, stress tensor $\boldsymbol{\tau}$ and moment tensor $\boldsymbol{m}$. When the strains and bending strains are now altered by virtual displacements $\delta\boldsymbol{\varepsilon}$ and $\delta\boldsymbol{m}$, this additional deformation has to work against the stresses and bending moments that are present in the shell, thus increasing the stored elastic energy.

For a diagonalised stress tensor, the change of the stretching energy density is $\delta w_{\text{stretch}} = \tau_\eta\,\delta\varepsilon_\eta + \tau_\xi\,\delta\varepsilon_\xi$, where we denote the principal axes with η and ξ. This equation is just the continuum version of the basic law "work equals force times distance". It can be transferred to non-diagonal stress tensors by writing it in a manifestly invariant form, $\delta w_{\text{stretch}} = \mathrm{Tr}\,(\boldsymbol{\tau}\,\delta\boldsymbol{\varepsilon})$. Similarly, the change of the energy density due to the bending moments and virtual bending strains is $\mathrm{Tr}\,(\boldsymbol{m}\,\delta\boldsymbol{K})$, which can be derived by taking the thickness of the shell into account [151]. Thus, the total energy change due to the virtual displacements is

$$\delta w_S = \tau_x\delta\varepsilon_x + 2\tau_{xy}\delta\varepsilon_{xy} + \tau_y\delta\varepsilon_y + m_x\delta K_x + 2m_{xy}\delta K_{xy} + m_y\delta K_y \tag{3.10}$$

in component notation for non-diagonal tensors.

In order to derive the general constitutive relations it remains to specify an explicit form of the strain-energy-function w_S. The Hookean energy density (2.7) in the principal axes system can be generalised to non-diagonal strain tensors by the observation that terms like $\varepsilon_\eta^2 + 2\nu\varepsilon_\eta\varepsilon_\xi + \varepsilon_\xi^2$ in the principal axes system can be written as $\mathrm{Tr}\left(\boldsymbol{\varepsilon}^2\right) + 2\nu\,\mathrm{Det}\,\boldsymbol{\varepsilon}$, which expands to $\varepsilon_x^2 + 2\nu\varepsilon_x\varepsilon_y + \varepsilon_y^2 + 2(1-\nu)\varepsilon_{xy}^2$ for non-diagonal tensors. The complete Hookean energy density function thus reads

$$\begin{aligned} w_S = {} & \frac{1}{2}\frac{E_{2\mathrm{D}}}{1-\nu^2}\left(\varepsilon_x^2 + 2\nu\varepsilon_x\varepsilon_y + \varepsilon_y^2 + 2(1-\nu)\varepsilon_{xy}^2\right) \\ & + \frac{1}{2}E_B\left(K_x^2 + 2\nu K_xK_y + \varepsilon_y^2 + 2(1-\nu)K_{xy}^2\right) \end{aligned} \tag{3.11}$$

which reproduces the literature result, see for example ref. [135], p. 341.

From (3.10) and (3.11), the general constitutive relations of small strain elasticity can be deduced,

$$\begin{aligned} \tau_x &= \frac{\partial w_S}{\partial\varepsilon_x} = \frac{E_{2\mathrm{D}}}{1-\nu^2}(\varepsilon_x + \nu\varepsilon_y), & m_x &= \frac{\partial w_S}{\partial K_x} = E_B(K_x + \nu K_y), \\ \tau_y &= \frac{\partial w_S}{\partial\varepsilon_y} = \frac{E_{2\mathrm{D}}}{1-\nu^2}(\varepsilon_y + \nu\varepsilon_x), & m_y &= \frac{\partial w_S}{\partial K_y} = E_B(K_y + \nu K_x), \\ \tau_{xy} &= \frac{1}{2}\frac{\partial w_S}{\partial\varepsilon_{xy}} = \frac{E_{2\mathrm{D}}}{1+\nu}\varepsilon_{xy}, & m_{xy} &= \frac{1}{2}\frac{\partial w_S}{\partial K_{xy}} = E_B(1-\nu)K_{xy}. \end{aligned} \tag{3.12}$$

In contrast to the finite strain constitutive relations (2.10), these equations do not contain the $1/\lambda_i$ prefactors anymore since they represent order effects, $1/\lambda_i = 1 + \mathcal{O}(\varepsilon_i)$.

3.2.4. Examples and further elastic moduli

Now we will explore the behaviour of an elastic plate in different deformation modes: Uniaxial stress, isotropic stress and shear stress, see fig. 3.5. This allows us to interpret the role of the Young modulus and Poisson ratio. We will define the shear modulus and area compression modulus, which are frequently met in the literature.

For uniaxial stress, see fig. 3.5 a), the only non-vanishing stress component is τ_x. In small strain elasticity (3.12), it follows from $\tau_y = 0$ that $\varepsilon_y = -\nu\varepsilon_x$, i.e. the membrane contracts in y-direction when it stretches in x-direction, and the ratio of the strains is $\varepsilon_y/\varepsilon_x = -\nu$. If $\nu = 1$, the area of the membrane is preserved upon deformation. Negative Poisson ratios characterise *auxetic materials*, which were believed not to exist for a long time[1] but have been found, e.g. in

[1] Landau and Lifshitz write "There are no substances known for which $\nu < 0$, i.e. which would expand transversely when stretched longitudinally." [83]

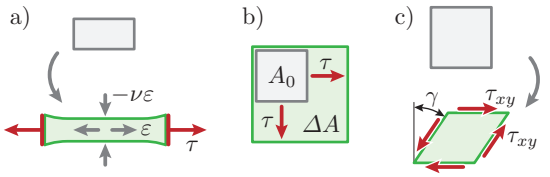

Figure 3.5.: Three states of membrane stress: a) Uniaxial stress, where the membrane elongates in one direction and contracts in the other, b) isotropic stress with uniform expansion of the membrane, c) shear stress inducing a shear deformation.

folded structures and re-entrant foams, see ref. [57] for a recent review. We can further see from the linear Hookean law that

$$\tau_x = \frac{E_{2D}}{1-\nu^2}\left(\varepsilon_x - \nu^2\varepsilon_x\right) = E_{2D}\,\varepsilon_x, \tag{3.13}$$

so that the Young modulus is the proportionality constant between stress and strain for uniaxial stress.

Isotropic stress, see fig. 3.5 b), is characterised by equal normal stresses in x- and y-direction, $\tau_x = \tau_y = \tau$, and results in a uniform stretch (or compression), $\varepsilon_x = \varepsilon_y = \varepsilon$. The plate changes its surface area from A_0 in the reference state to $A = \lambda_x\lambda_y A_0 \approx (1+2\varepsilon)A_0$ in the deformed state. Thus, the area change is $\Delta A = 2\varepsilon A_0$, and the relation between stress and strain reads

$$\tau = \frac{E_{2D}}{1-\nu}\varepsilon = K_{2D}\frac{\Delta A}{A_0} \quad \text{with} \quad K_{2D} = \frac{E_{2D}}{2(1-\nu)}, \tag{3.14}$$

where the *area compression modulus* or *area dilatation modulus* K_{2D} was defined, which serves as the proportionality constant between stress and normalised area difference for isotropic stress.

Finally, a pure shear stress τ_{xy} with $\tau_x = \tau_y = 0$ induces a shear deformation, see fig. 3.5 c). In our discussion of shear deformations, we saw with (3.6) that the shear component of the strain tensor equals half the shear angle, $\varepsilon_{xy} = \gamma/2$. With Hooke's law (3.12) we get

$$\tau_{xy} = G_{2D}\,\gamma \quad \text{with} \quad G_{2D} = \frac{E_{2D}}{2(1+\nu)}, \tag{3.15}$$

where G_{2D} is called the *surface shear modulus*.

3.2.5. Stability equations for plates and shallow shells

In the previous sections we covered the basis to examine the equilibrium and stability of shallow shells. These investigations are based on an energy functional, whose first and second variation produces equilibrium and stability equations, and the third and fourth variation give information about the behaviour after the onset of instability.

As in the previous sections, we consider a shallow shell with a reference shape described by the height profile $z(x, y)$. This reference state is, however, not the undeformed or unstressed state: We assume that the shell is subjected to in-plane stresses (τ_x, τ_y and τ_{xy}), bending moments (m_x, m_y and m_{xy}) and a normal pressure p. We do not make any assumptions on the origin of these stresses, they may be produced by a preceding elastic deformation (linear or non-linear), thermal expansion, inhomogeneous growth [88] or swelling [77], residual stresses after plastic deformation [88], or anything that satisfies the equilibrium conditions presented below. This general framework is necessary in order to capture the specific case analysed in sections 3.3.2 and 3.3.3, because the parabolic stress state analysed there does not satisfy the compatibility conditions of plate theory [135].

To analyse the stability of this reference state, we perturb it by small displacements u, v, w (in x, y and z direction, respectively), which are all of order $\mathcal{O}(\delta)$. The elastic energy of the shell will change due to this perturbation. If a displacement field which lowers the elastic energy exists, the given state is unstable.

According to (3.2), these displacements lead to strains and bending strains. The strains are non-linear only in the field w, which is justified because shallow shells are close to flat plates and are therefore much easier to deflect perpendicular to its surface than in-plane [135], so that $|w| > |u|, |v|$.

The total energy variation can be written as a surface integral

$$\Delta U = \int \mathrm{d}A \left\{ w_{\text{stretch}} + w_{\text{bend}} + w_{\text{ext}} \right\} \tag{3.16}$$

over the energy densities

$$\begin{aligned} w_{\text{stretch}} &= \tau_x \varepsilon_x + 2\tau_{xy}\varepsilon_{xy} + \tau_y \varepsilon_y + \frac{1}{2}\frac{E_{2\text{D}}}{1-\nu^2}\left(\varepsilon_x^2 + 2\nu\varepsilon_x\varepsilon_y + \varepsilon_y^2 + 2(1-\nu)\varepsilon_{xy}^2\right) \\ w_{\text{bend}} &= m_x K_x + 2m_{xy}K_{xy} + m_y K_y + \frac{1}{2}E_B\left(K_x^2 + 2\nu K_x K_y + 2(1-\nu)K_{xy}^2\right) \\ w_{\text{ext}} &= pw. \end{aligned} \tag{3.17}$$

The terms in w_{stretch} and w_{bend} which are linear in the strains ($\tau_x\varepsilon_x$, m_xK_x, etc.) account for the presence of stresses and moments in the reference configuration: It is the work (density) required to create the perturbation u, v, w against the present stresses and moments, cf. (3.10). The quadratic terms measure the work done on the shell due to the additional stresses and moments that develop upon the perturbation, cf. (3.11), and w_{ext} is the work done on the external system that provides the pressure p.

We sort the energy functional by different orders of the displacement fields, $\Delta U = \Delta U^{(1)} + \Delta U^{(2)} + \Delta U^{(3)} + \Delta U^{(4)}$ where $\Delta U^{(n)} = \mathcal{O}(\delta^n)$. Analysis of the variations of different order then yields equilibrium equations, stability equations and information about post-buckling behaviour, i.e. the evolution of the amplitude of the buckling or wrinkling pattern after the loss of stability.

In the *first variation* we collect all terms linear in u, v and w. It reads

$$\begin{aligned} \Delta U^{(1)} = \int \mathrm{d}A \Big\{ & u\left[-\partial_x\tau_x - \partial_y\tau_{xy}\right] + v\left[-\partial_y\tau_y - \partial_x\tau_{xy}\right] \\ & + w\left[-\kappa_x\tau_x - 2\kappa_{xy}\tau_{xy} - \kappa_y\tau_y + \partial_x^2 m_x + 2\partial_x\partial_y m_{xy} + \partial_y^2 m_y + p\right] \Big\} \end{aligned} \tag{3.18}$$

after integration by parts has been used. Boundary terms of the integration by parts are omitted since they only contribute to the boundary conditions, not to the differential equations themselves. Linear stability requires the contents of the three square brackets to vanish,

$$\begin{gathered} \frac{\partial\tau_x}{\partial x} + \frac{\partial\tau_{xy}}{\partial y} = 0, \quad \frac{\partial\tau_y}{\partial y} + \frac{\partial\tau_{xy}}{\partial x} = 0, \quad \text{and} \\ -\kappa_x\tau_x - 2\kappa_{xy}\tau_{xy} - \kappa_y\tau_y + \frac{\partial^2 m_x}{\partial x^2} + 2\frac{\partial^2 m_{xy}}{\partial x\partial y} + \frac{\partial^2 m_y}{\partial y^2} + p = 0, \end{gathered} \tag{3.19}$$

which reproduces the ordinary equilibrium equations for shallow shells (see ref. [96], p. 360, or ref. [135], p. 526; only the sign conventions differ).

The *second variation* contains all quadratic terms, including terms mixing different fields. Integration by parts can be used to write the integrand in a symmetric form. This results in

$$\Delta U^{(2)} = \int \mathrm{d}A \left\{ (u,v,w) \begin{pmatrix} \hat{H}_{uu} & \hat{H}_{uv} & \hat{H}_{uw} \\ \hat{H}_{uv} & \hat{H}_{vv} & \hat{H}_{vw} \\ \hat{H}_{wu} & \hat{H}_{wv} & \hat{H}_{ww} \end{pmatrix} \begin{pmatrix} u \\ v \\ w \end{pmatrix} \right\} \qquad \text{with} \tag{3.20}$$

$$\hat{H}_{uu} = -\frac{1}{2}\frac{E_{2D}}{1-\nu^2}\left(\partial_x^2 + \frac{1-\nu}{2}\partial_y^2\right), \quad \hat{H}_{vv} = -\frac{1}{2}\frac{E_{2D}}{1-\nu^2}\left(\partial_y^2 + \frac{1-\nu}{2}\partial_x^2\right), \quad \hat{H}_{uv} = -\frac{1}{4}\frac{E_{2D}}{1-\nu}\partial_x\partial_y,$$
$$\hat{H}_{uw} = \frac{1}{2}\frac{E_{2D}}{1-\nu^2}\left[\partial_x(\kappa_x + \nu\kappa_y) + (1-\nu)\partial_x\kappa_{xy}\right], \quad \hat{H}_{wu} = -\frac{1}{2}\frac{E_{2D}}{1-\nu^2}\left[(\kappa_x + \nu\kappa_y)\partial_x + (1-\nu)\kappa_{xy}\partial_y\right],$$
$$\hat{H}_{vw} = \frac{1}{2}\frac{E_{2D}}{1-\nu^2}\left[\partial_y(\kappa_y + \nu\kappa_x) + (1-\nu)\partial_x\kappa_{xy}\right], \quad \hat{H}_{wv} = -\frac{1}{2}\frac{E_{2D}}{1-\nu^2}\left[(\kappa_y + \nu\kappa_x)\partial_y + (1-\nu)\kappa_{xy}\partial_x\right],$$
$$\hat{H}_{ww} = \frac{1}{2}E_B\Delta^2 - \frac{1}{2}\left(\tau_x\partial_x^2 + 2\tau_{xy}\partial_x\partial_y + \tau_y\partial_y^2\right) + \frac{1}{2}\frac{E_{2D}}{1-\nu^2}\left(\kappa_x^2 + 2\nu\kappa_x\kappa_y + \kappa_y^2 + 2(1-\nu)\kappa_{xy}^2\right).$$

Note that terms like $\partial_x\kappa_{xy}w$ are to be understood as $\partial_x[\kappa_{xy}w]$, so that the derivative operator acts also on the function w to which the operator is applied; $\Delta = \partial_x^2 + \partial_y^2$ is the Laplace operator. It can be shown with integration by parts that the 3×3 matrix operator $\hat{H}$ is self-adjoint. Therefore, it has an eigenbasis and is positive definite if all its eigenvalues are positive. When the lowest eigenvalue falls below zero, $\hat{H}$ is not positive definite and, thus, a deformation mode exists which lowers the elastic energy. This is exactly the critical point where buckling or wrinkling can occur. We can thus find the critical point by setting $\hat{H}(u,v,w)^T = (0,0,0)^T$. These three equations are equivalent to

$$0 = \frac{\partial\tau_x^{(1)}}{\partial x} + \frac{\partial\tau_{xy}^{(1)}}{\partial y}, \qquad 0 = \frac{\partial\tau_y^{(1)}}{\partial y} + \frac{\partial\tau_{xy}^{(1)}}{\partial x} \qquad \text{and} \tag{3.21}$$

$$E_B\Delta^2 w = \tau_x\frac{\partial^2 w}{\partial x^2} + 2\tau_{xy}\frac{\partial w}{\partial xy} + \tau_y\frac{\partial^2 w}{\partial y^2} + \kappa_x\tau_x^{(1)} + 2\kappa_{xy}\tau_{xy}^{(1)} + \kappa_y\tau_y^{(1)}. \tag{3.22}$$

We introduced the additional stresses, which are of the same form as Hooke's law,

$$\tau_x^{(1)} = \frac{E_{2D}}{1-\nu^2}\left(\varepsilon_x^{(1)} + \nu\varepsilon_y^{(1)}\right), \quad \tau_y^{(1)} = \frac{E_{2D}}{1-\nu^2}\left(\varepsilon_y^{(1)} + \nu\varepsilon_x^{(1)}\right), \quad \tau_{xy}^{(1)} = \frac{E_{2D}}{1+\nu}\varepsilon_{xy}^{(1)}, \tag{3.23}$$

and depend on the strains $\varepsilon_x^{(1)} = \partial_x u - \kappa_x w$, $\varepsilon_y^{(1)} = \partial_y v - \kappa_y w$ and $\varepsilon_{xy}^{(1)} = (\partial_y u + \partial_x v)/2 - \kappa_{xy}w$ which are the linearised versions of (3.2).

The in-plane stability equations (3.21) are of the same form as the in-plane equilibrium equations. Their general solution is

$$\tau_x^{(1)} = \frac{\partial^2\phi}{\partial y^2}, \qquad \tau_y^{(1)} = \frac{\partial^2\phi}{\partial x^2}, \qquad \tau_{xy}^{(1)} = -\frac{\partial^2\phi}{\partial x\partial y} \tag{3.24}$$

with an arbitrary function $\phi(x,y)$ which is called the *Airy stress function* or *stress potential* [83, 96, 135]. With any choice of $\phi(x,y)$, the in-plane stability equations are satisfied, but there are additional conditions on ϕ because the stresses must be compatible with Hooke's law (3.23). The strains can be expressed in terms of the stress function and in terms of the displacements,

$$\begin{aligned} \frac{1}{E_{2D}}\left(\frac{\partial^2\phi}{\partial y^2} - \nu\frac{\partial^2\phi}{\partial x^2}\right) &= \varepsilon_x^{(1)} = \frac{\partial u}{\partial x} - \kappa_x w \\ \frac{1}{E_{2D}}\left(\frac{\partial^2\phi}{\partial x^2} - \nu\frac{\partial^2\phi}{\partial y^2}\right) &= \varepsilon_y^{(1)} = \frac{\partial v}{\partial y} - \kappa_y w \\ -\frac{1+\nu}{E_{2D}}\frac{\partial^2\phi}{\partial x\partial y} &= \varepsilon_{xy}^{(1)} = \frac{1}{2}\left(\frac{\partial u}{\partial y} + \frac{\partial v}{\partial x}\right) - \kappa_{xy}w. \end{aligned} \tag{3.25}$$

As the strains are derivatives of the displacements, they must satisfy certain integrability conditions. We can find these conditions, also known as *compatibility conditions* [135], by eliminating the in-plane displacements u and v from (3.25) using the combination $\partial_y^2\varepsilon_x^{(1)}+\partial_x^2\varepsilon_y^{(1)}-2\partial_x\partial_x\varepsilon_{xy}^{(1)}$. Simplifying this term with the left hand sides of (3.25) results in $\Delta^2\phi/E_{2\mathrm{D}}$. Using the right hand sides of (3.25), we see that the term equals $-\partial_y^2(\kappa_x w)-\partial_x^2(\kappa_y w)+2\partial_x\partial_y(\kappa_{xy}w)$, which can be further simplified by inserting the curvature definitions (3.1). So eventually we have derived $\Delta^2\phi = -E_{2\mathrm{D}}\left(\kappa_x\partial_y^2 w - 2\kappa_{xy}\partial_x\partial_y w+\kappa_y\partial_x^2 w\right)$. This equation and eq. (3.22) determine the fields $w(x,y)$ and $\phi(x,y)$. Introducing the stress potential in (3.22) gives the complete set of stability equations,

$$\begin{aligned}\frac{1}{E_{2\mathrm{D}}}\Delta^2\phi &= -\kappa_x\frac{\partial^2 w}{\partial y^2}+2\kappa_{xy}\frac{\partial^2 w}{\partial x\partial y}-\kappa_y\frac{\partial^2 w}{\partial x^2}\\ E_B\Delta^2 w &= \tau_x\frac{\partial^2 w}{\partial x^2}+2\tau_{xy}\frac{\partial^2 w}{\partial x\partial y}+\tau_y\frac{\partial^2 w}{\partial y^2}+\kappa_x\frac{\partial^2\phi}{\partial y^2}-2\kappa_{xy}\frac{\partial^2\phi}{\partial x\partial y}+\kappa_y\frac{\partial^2\phi}{\partial x^2}.\end{aligned} \tag{3.26}$$

In ref. [135], similar stability equations are given on p. 570, with the only difference that the reference shape there is assumed to have principal curvatures along the x and y coordinate lines. Our equations are a bit more general; however, we will apply them only to simple cases where $\kappa_{xy}=0$ anyway.

The stability equations are a set of partial differential equations which are linear and homogeneous. The curvatures κ_i and stresses τ_i are known functions of x and y at the time we want to solve the stability equations; they characterise the reference state whose stability is investigated. Boundary conditions must be specified for w and ϕ. In section 3.3 it turns out that the boundary value problem has a solution only for special choices of the functions κ_i and τ_i. Let us assume that at least one of these functions depends on a parameter q, with the interpretation that for increasing q the load on the shallow shell increases. At a critical value q_c, a solution of (3.26) exists; this is the point where the shell loses its stability. The solution and the actual value q_c can, in most cases, only be found numerically.

The solution of the stability equations determines the shape of the buckling or wrinkling pattern when the instability sets in. Once it is found, it can be desirable to evaluate the energy functional (3.20) in order to check that $\Delta U^{(2)}<0$ for $q>q_c$. For this purpose we re-write (3.20) in terms of w and ϕ which results in

$$\Delta U^{(2)} = \int \mathrm{d}A\,\frac{w}{2}\left\{E_B\Delta^2 w-\tau_x\frac{\partial^2 w}{\partial x^2}-2\tau_{xy}\frac{\partial^2 w}{\partial x\partial y}-\tau_y\frac{\partial^2 w}{\partial y^2}-\kappa_x\frac{\partial^2\phi}{\partial y^2}+2\kappa_{xy}\frac{\partial^2\phi}{\partial x\partial y}-\kappa_y\frac{\partial^2\phi}{\partial x^2}\right\}. \tag{3.27}$$

Evaluating the integrand for $q>q_c$ with solutions (w,ϕ) found for $q=q_c$ is an approximation, analogous to the first-order perturbation theory of quantum mechanics.

As the stability equations are homogeneous, the amplitude of the buckling pattern is arbitrary, in a mathematical sense. In practice, we have to take into account higher order terms in the elastic energy for large amplitudes. From these higher order terms, we may also obtain the bifurcation behaviour. The higher order energy contributions are evaluated for a deformation mode (w,ϕ) which is a solution of the stability equations (3.26).

The *third variation* vanishes due to symmetry restrictions in our applications. For completeness, however, it is given here:

$$\Delta U^{(3)} = \frac{1}{2}\int \mathrm{d}A\; w\cdot\left\{-\frac{\partial^2 w}{\partial x^2}\frac{\partial^2\phi}{\partial y^2}+2\frac{\partial^2 w}{\partial x\partial y}\frac{\partial^2\phi}{\partial x\partial y}-\frac{\partial^2 w}{\partial y^2}\frac{\partial^2\phi}{\partial x^2}\right\}. \tag{3.28}$$

It is obtained from the $\mathcal{O}\left(\delta^3\right)$ terms in (3.16) and has been simplified with integration by parts, introduction of the Airy stress function and by using (3.21). The third variation vanishes if

the stability problem has the following symmetry. From (3.26) it is clear that if (w, ϕ) is a solution of the stability equations, then $(-w, -\phi)$ also is. If the shallow shell has a symmetry so that the (w, ϕ) and $(-w, -\phi)$ patterns are equivalent, we can expect $\Delta U(w, \phi) = \Delta U(-w, -\phi)$. Since $\Delta U^{(3)}(-w, -\phi) = -\Delta U^{(3)}(w, \phi)$ we can conclude that the third variation (and all odd variations) vanish: $\Delta U^{(3)} = 0$. This is the case for many plate buckling problems (with $p = 0$), since a buckling in $+z$-direction is essentially the same as a buckling in $-z$-direction, and typically results in a pitchfork bifurcation as shown in section 3.3.3. For a spherical cap, on the other hand, it is a great difference if the dimple buckles inward or outward; and the third variation cannot vanish. Eventually, this leads to a more catastrophic buckling behaviour, see ref. [135], p. 565 for a general discussion.

For the *fourth variation* of the energy we obtain

$$\Delta U^{(4)} = \frac{1}{8} \frac{E_{2D}}{1 - \nu^2} \int \mathrm{d}A \left[\left(\frac{\partial w}{\partial x} \right)^2 + \left(\frac{\partial w}{\partial y} \right)^2 \right]^2 . \tag{3.29}$$

Evidently, this term is positive and will limit the amplitude of the buckling (or wrinkling) pattern.

3.3. Applications to the buckling and wrinkling of plates and shallow shells

3.3.1. Rectangular plate with simply supported edges

As a first example we consider the buckling and wrinkling of an initially flat plate, see fig. 3.6. It shall have a rectangular geometry with a width L_y and a length $L_x \gg L_y$, for simplicity we only consider the limit $L_x \to \infty$ so that the wavelength of the buckling pattern can take any value and is not quantised by boundary conditions in x-direction. Along the edges $y = 0$ and $y = L_y$ of the plate, we impose the boundary conditions that these edges shall be simply supported, that is, the displacements must vanish at the boundary. The plate is in a stressed state with a compression $\tau_x < 0$ and a tension τ_y. There shall be no shear stress, bending moment or external pressure.

We will see that the buckling wavelength is considerably affected by the tension τ_y, which is confirmed by a simple scaling law. Let us assume that the buckling pattern is a periodic normal deflection with amplitude W_0, wavelength λ in x-direction and wavelength $2L_y$ in y-direction, so that the boundary conditions are met and one bulge spans the whole width L_y. This buckling pattern leads to the following energy densities:

- Bending occurs mainly in x-direction and costs $w_{\text{bend}} \sim E_B K_x^2 \sim E_B (W_0/\lambda^2)^2$.
- In x-direction, compression is released and brings the energy reduction $w_{\text{compress}} \sim \tau_x \varepsilon_x \sim \tau_x (W_0/\lambda)^2$, which is negative because $\tau_x < 0$.
- In y-direction, the plate stretches against τ_y, which costs $w_{\text{stretch}} \sim \tau_y \varepsilon_y \sim \tau_y (W_0/L_y)^2$.

By the onset of the buckling, the elastic energy (per area) of the plate therefore changes by

$$\Delta w_S \sim E_B \frac{W_0^2}{\lambda^4} + \tau_x \frac{W_0^2}{\lambda^2} + \tau_y \frac{W_0^2}{L_y^2}, \tag{3.30}$$

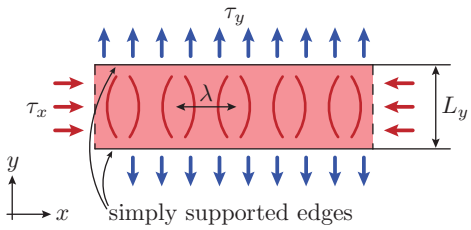

Figure 3.6.: Rectangular plate under compression and tension. The plate has a width of L_y and is infinitely large in x-direction. A compression $\tau_x < 0$ and a tension τ_y are applied, which lead to a buckling or wrinkling pattern of wavelength λ, indicated by the dark red curves.

which must be negative in case of an energetically favourable buckling. This is equivalent to demanding a minimum magnitude of the compression τ_x,

$$\Delta w_S \leq 0 \quad \Leftrightarrow \quad \tau_x \leq -\left(\frac{E_B}{\lambda^2} + \tau_y \frac{\lambda^2}{L_y^2}\right). \tag{3.31}$$

When the compression is gradually increased, the mode for which $-\tau_x$ is minimal buckles first. The condition $\partial\tau_x/\partial\lambda = 0$ determines the critical wavelength λ_c and critical stress $\tau_c = \tau_x(\lambda_c)$,

$$\lambda_c \sim \left(\frac{E_B L_y^2}{\tau_y}\right)^{1/4} \quad \text{and} \quad \tau_c \sim -2\frac{\sqrt{E_B \tau_y}}{L_y}. \tag{3.32}$$

We see that the wrinkle wavelength gets smaller for increasing τ_y. In refs. [26, 27], similar estimates of the energy contributions were presented, and the same critical wavelength was derived.

In the following, the problem just presented shall be solved properly by means of the stability equations of shallow shells. First of all, we note that the imposed stress satisfies the equilibrium equations (3.19), and so the problem is well-posed. The stability equations (3.26) simplify considerably for flat plates, where all curvatures κ_i vanish: In this case, the two partial differential equations for w and ϕ decouple. As we are primarily interested in the shape $w(x,y)$ of the wrinkling pattern and not in the stress potential $\phi(x,y)$, it is sufficient to solve the single equation

$$E_B \Delta^2 w = \tau_x \frac{\partial^2 w}{\partial x^2} + \tau_y \frac{\partial^2 w}{\partial y^2}, \tag{3.33}$$

i.e. the second stability equation of (3.26) with $\kappa_i = 0$ and $\tau_{xy} = 0$. It must be solved with the boundary conditions for simply supported edges, $0 = w(x, y_0) = \partial_y^2 w(x, y_0)$ at $y_0 = 0$ and $y_0 = L_y$, which state that the edge is not deflected and moment free [83, 135].

A separation ansatz $w(x,y) = W(y)\sin(kx)$ with wavenumber $k = 2\pi/\lambda$ leads to an ordinary differential equation for the amplitude function $W(y)$,

$$W''''(y) - \left(\frac{\tau_y}{E_B} + 2k^2\right) W''(y) + \left(k^4 + \frac{\tau_x}{E_B} k^2\right) W(y) = 0. \tag{3.34}$$

We choose $W(y) \sim \sin(\pi y/L_y)$ as an ansatz that conforms the boundary conditions. This corresponds to one bulge in y-direction, and it can be shown that this mode becomes unstable first (in comparison to several oscillations in y-direction). Inserting the ansatz into (3.34) shows that it satisfies the differential equation if

$$\tau_x = -\frac{1}{k^2}\left(E_B \frac{\pi^4}{L_y^4} + \frac{\pi^2 \tau_y}{L_y^2}\right) - 2E_B \frac{\pi^2}{L_y^2} - E_B k^2. \tag{3.35}$$

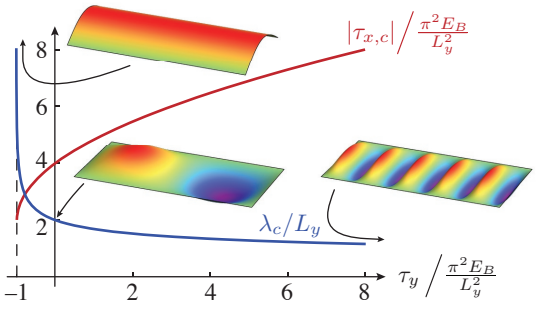

Figure 3.7.: Behaviour of a plate under compression in x-direction and tension in y-direction, according to the results (3.36). Shown are the critical compression $|\tau_{x,c}|$ (red line) and the wavelength λ_c of the buckling pattern (blue line) as a function of the transversal tension τ_y. The insets show three-dimensional views of the buckled plate for $\tau_y \to -\pi^2 E_B / L_y^2$, $\tau_y = 0$ and $\tau_y \gg \pi^2 E_B / L_y^2$.

This is the critical value of τ_x for which a solution of the stability equations exists; and the second variation of the energy functional has an eigenvalue that becomes negative at this τ_x. We are interested in the mode that becomes unstable first, hence we must minimise $-\tau_x$ with respect to k. The condition $\partial_k \tau_x = 0$ is met for $k = (1 + \tau_y L_y^2 / \pi^2 E_B)^{1/4} \pi / L_y$, which yields a critical wavelength and associated critical tension

$$\lambda_c = 2L_y \left(1 + \frac{\tau_y L_y^2}{\pi^2 E_B}\right)^{-1/4} \quad \text{and} \quad \tau_{x,c} = -\frac{2\pi^2 E_B}{L_y^2} \left(1 + \sqrt{1 + \frac{\tau_y L_y^2}{\pi^2 E_B}}\right). \tag{3.36}$$

These results are plotted in fig. 3.7, and there are several limits that are relevant. First of all, we see that both functions are only defined for $\tau_y > -\pi^2 E_B / L_y^2$. If τ_y is negative, i.e. compressive, and approaches this limit, the wavelength $\lambda_c \to \infty$ diverges. This value for τ_y is the critical value for Euler-buckling in y-direction, where the plate buckles only in y-direction (see the inset in fig. 3.7). Secondly, the buckling pattern at $\tau_y = 0$ has $\lambda = 2L_y$, so that the bulges have a quadratic base area. This case is discussed in more detail in ref. [124]. Finally, we can investigate the limit $\tau_y \gg \pi^2 E_B / L_y^2$, which is equivalent to very small bending stiffnesses $E_B \to 0$. The results (3.36) then simplify to

$$\lambda_c \approx \left(\frac{16\pi^2 E_B L_y^2}{\tau_y}\right)^{1/4} \quad \text{and} \quad \tau_{x,c} \approx \sqrt{\frac{4\pi^2 E_B \tau_y}{L_y^2}}. \tag{3.37}$$

These are the same scaling laws as estimated above, and this version of λ_c coincides exactly with the results of Cerda and Mahadevan [26].

In addition to the literature results [26], we were able to derive the critical compressive stress and have retraced the transition from *buckling* (at small transversal tension) to *wrinkling* (at large transversal tension). The basic mechanism is the same in both cases: The compressive stress is reduced by deforming the plate out of plane.

3.3.2. Infinite plate under local compression

In many systems, the wrinkled regions of a membrane are not limited by clamped or supported borders, but arise from the circumstance that only certain regions of the membrane exhibit compressive stresses. In classical tension field theory [121, 144] it is assumed that the wrinkles end at the boundaries of the compressed regions and that the compressive stress in these regions is collapsed to zero (or a small value according to the Euler buckling load) as a consequence of the wrinkling.

Here, we develop an alternative model for such localised wrinkling and buckling, which is comparable to the model of the previous section. This time, the plate shall be infinitely large

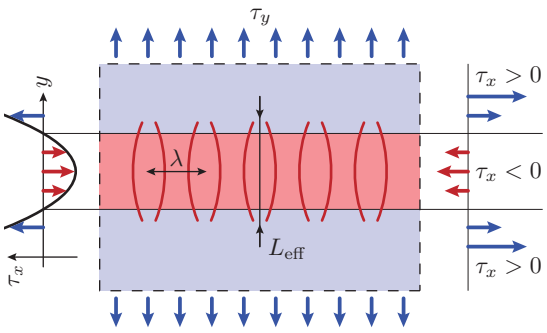

Figure 3.8.: Infinite plate under a parabolic stress profile $\tau_x(y)$ and tension τ_y. The stress in x-direction is locally compressive (in the light red region) and will lead, beyond a threshold, to wrinkles of wavelength λ and effective width L_{eff}.

in both x and y direction. In y-direction, a spatially constant tension and in x-direction a parabolic stress profile is applied:

$$\tau_x(x,y) = -\tau_0(1 - a_p y^2), \quad \tau_y = \text{const} \quad \text{and} \quad \tau_{xy} = 0 \tag{3.38}$$

with $\tau_0 > 0$. First of all, we confirm with the equilibrium equations (3.19) that the plate is in a linearly stable state. However, the stress state violates the compatibility equations [135], i.e. it cannot be the result of a preceding in-plane deformation within Hookean elasticity. This renders the problem somewhat artificial, but this model is nevertheless of academic interest.

The stress distribution is compressive in the region $-1/\sqrt{a_p} < y < 1/\sqrt{a_p}$ and tensional for larger values of $|y|$, see fig. 3.8. Beyond a threshold, which is to be determined, the plate will buckle in order to release the compressive stress. Outside the compressed region, however, buckling would be energetically unfavourable, and so we expect the wrinkles to confine themselves to the region $-1/\sqrt{a_p} < y < 1/\sqrt{a_p}$.

To verify the expectations, the plate equation (3.33) must be solved; now with a spatially varying τ_x which requires a numerical solution. Again we choose the separation ansatz $w(x,y) = W(y)\sin(kx)$ to transform the partial differential equation into an ordinary differential equation for the amplitude function $W(y)$,

$$W''''(y) - \left(2k^2 + \frac{\tau_y}{E_B}\right) W''(y) + \left(k^4 - \frac{k^2}{E_B}\tau_0\left(1 - a_p y^2\right)\right) W(y) = 0. \tag{3.39}$$

For a numerical treatment it is beneficial to reduce the number of parameters as much as possible, which can be achieved by the rescaling $y = \tilde{y}/\sqrt{2k^2 + \tau_y/E_B}$, which leads to

$$\begin{gathered} W''''(\tilde{y}) - W''(\tilde{y}) + \left(-\tilde{\beta} + \tilde{\alpha}\tilde{y}^2\right) W(\tilde{y}) = 0 \\ \text{with} \quad \tilde{\alpha} = \frac{a_p \tau_0 k^2/E_B}{\left(2k^2 + \tau_y/E_B\right)^3} \quad \text{and} \quad \tilde{\beta} = \frac{-k^4 + \tau_0 k^2/E_B}{\left(2k^2 + \tau_y/E_B\right)^2}. \end{gathered} \tag{3.40}$$

A shooting method [109, 122] can be applied to solve this differential equation numerically if boundary conditions are provided. Since a numerical solution can be expected to be symmetrical, it is sufficient to solve the equation for $\tilde{y} > 0$. We require the displacements and bending moments to vanish at infinity, that is, $W(\infty) = W''(\infty) = 0$. In practice, we end the integration at a point $\tilde{y}_{\max}$ that is sufficiently large (so that the results do not change anymore when $\tilde{y}_{\max}$ is further increased) and enforce these boundary conditions there. The boundary conditions at the starting point of integration are chosen appropriately for an even function, $W(0) = 1$, $W''(0) = -\tilde{\gamma}$ and $W'(0) = W'''(0) = 0$. The choice $W(0) = 1$ is arbitrary, since the differential equation is homogeneous, and $\tilde{\gamma}$ serves as a shooting parameter. To satisfy the two boundary

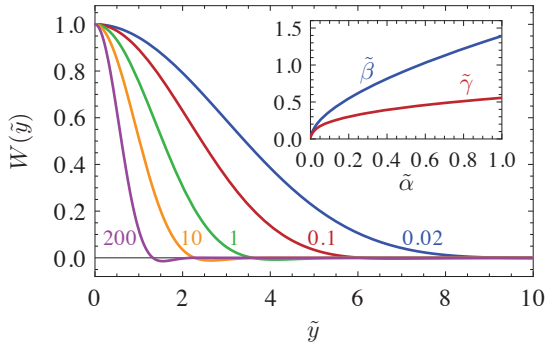

Figure 3.9.: Numerical results of the rescaled differential equation. The main plot shows the wrinkle amplitude function for different values of $\tilde{\alpha}$ as indicated by the coloured numbers, and the inset shows the final values of the shooting parameters as a function of $\tilde{\alpha}$.

conditions at the endpoint of integration $\tilde{y}_{\max}$, a second shooting parameter is required. This second shooting parameter is one of the parameters occurring in the differential equation; here we take $\tilde{\beta}$ as a shooting parameter, and consider $\tilde{\alpha}$ as fixed for the moment. The differential equation can be interpreted as an *eigenvalue problem*, where $\tilde{\beta}$ plays the role of an "eigenvalue" and must be chosen so that the boundary value problem has a non-trivial solution.

As a result of the numerical analysis one obtains the two functions $\tilde{\beta}(\tilde{\alpha})$ and $\tilde{\gamma}(\tilde{\alpha})$, plus the shape $W(\tilde{y})$ of the wrinkles for any given $\tilde{\alpha}$, see fig. 3.9. For small $\tilde{\alpha}$, the amplitude function resembles a Gaussian function. An inspection of the differential equation shows that

$$W(\tilde{y}) \approx \exp\left(-\frac{1}{2}\sqrt{\tilde{\alpha}}\tilde{y}^2\right) \quad \text{and} \quad \tilde{\beta} \approx \sqrt{\tilde{\alpha}} \quad \text{for} \quad \tilde{\alpha} \ll 1 \tag{3.41}$$

is an approximate solution of the eigenvalue problem.

For the further analytic and numerical analysis, we must switch to different rescaled quantities because the length unit introduced in $\tilde{y}$ contains the wavenumber k which is not known a priori. To this end we choose $1/\sqrt{a_p}$ as the length unit (which is the root of the stress parabola), and E_B as the energy unit. With the dimensionless length, wavenumber and stresses

$$y = \hat{y}/\sqrt{a_p}, \qquad k = \hat{k}\sqrt{a_p}, \qquad \tau_i = \hat{\tau}_i a_p E_B, \tag{3.42}$$

the parameters of the rescaled differential equation read

$$\tilde{\alpha} = \frac{\hat{\tau}_0 \hat{k}^2}{\left(2\hat{k}^2 + \hat{\tau}_y\right)^3} \quad \text{and} \quad \tilde{\beta} = \frac{-\hat{k}^4 + \hat{\tau}_0 \hat{k}^2}{\left(2\hat{k}^2 + \hat{\tau}_y\right)^2}. \tag{3.43}$$

From the numerical analysis, the function $\tilde{\beta}(\tilde{\alpha})$ is known. This relation corresponds to choosing $\hat{\tau}_0$ for given transversal tension $\hat{\tau}_y$ and given wavenumber $\hat{k}$ in such a way that the eigenvalue problem has a solution. Since both $\tilde{\alpha}$ and $\tilde{\beta}$ depend on $\hat{\tau}_0$, the equation

$$\tilde{\beta}(\tilde{\alpha}(\hat{\tau}_0)) = \frac{-\hat{k}^4 + \hat{\tau}_0 \hat{k}^2}{\left(2\hat{k}^2 + \hat{\tau}_y\right)^2} \tag{3.44}$$

can only be solved numerically for $\hat{\tau}_0(\hat{k}, \hat{\tau}_y)$. Once this function is determined, it can be minimised with respect to $\hat{k}$ – this corresponds to the question, which mode with critical wavenumber $\hat{k}_c(\hat{\tau}_y)$ or critical wavelength $\hat{\lambda}_c = 2\pi/\hat{k}_c$ becomes unstable first when the compressive stress $\hat{\tau}_0$ is ramped up. By this minimisation, we also obtain the critical compressive stress $\hat{\tau}_{0,c}$ at which the first mode becomes unstable,

$$\hat{\tau}_{0,c}(\hat{\tau}_y) = \min_{\hat{k}} \hat{\tau}_0\left(\hat{k}, \hat{\tau}_y\right) = \hat{\tau}_0\left(\hat{k}_c\left(\hat{\tau}_y\right), \hat{\tau}_y\right). \tag{3.45}$$

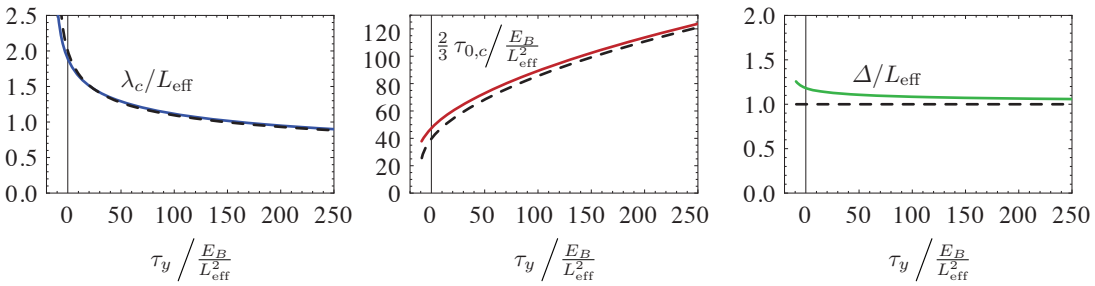

Figure 3.10.: Buckling under locally compressive stress compared to buckling with fixed edges. The solid lines represent the numerical results for buckling of an infinite plate under a parabolic stress profile and the dashed lines are the previous results for a simply supported plate of corresponding width L_{eff}. In the three plots, the critical wavelength, critical compressive tension and effective width of the wrinkles are shown.

The minimisation proceeds numerically and the results are presented in fig. 3.10. In the units used in these plots, the results are very close to the previous results from eq. (3.36) and fig. 3.7 for a simply supported plate of width L_{eff}.

We can derive the value of L_{eff} that lets the results match so closely by investigating the limit of large $\hat{\tau}_y$. The numerical analysis shows that this limit corresponds to $\tilde{\alpha} \ll 1$, so that the approximate solution (3.41) of the rescaled differential equation can be used. Using $\tilde{\beta}(\tilde{\alpha}) = \sqrt{\tilde{\alpha}}$ in (3.44) gives

$$\hat{\tau}_0(\hat{k}, \hat{\tau}_y) = 1 + \hat{k}^2 + \frac{\hat{\tau}_y}{2\hat{k}^2} + \sqrt{\left(1 + \frac{\hat{\tau}_y}{2\hat{k}^2}\right)\left(1 + 2\hat{k}^2 + \frac{\hat{\tau}_y}{2\hat{k}^2}\right)}. \tag{3.46}$$

The minimisation of this function with respect to $\hat{k}$ is rather tedious and was performed with a computer algebra system. To simplify the results for $\hat{\tau}_c$ and $\hat{\lambda}_c$, they can be expanded about $\hat{\tau}_y = \infty$, which yields

$$\hat{\tau}_{0,c} = \frac{9}{4} + \sqrt{\frac{27}{4}\,\hat{\tau}_y} + \mathcal{O}\left(\hat{\tau}_y^{-1/2}\right) \quad \text{and} \quad \hat{\lambda}_c = \left(\frac{64\,\pi^4}{3\,\hat{\tau}_y}\right)^{1/4} + \mathcal{O}\left(\hat{\tau}_y^{-3/4}\right). \tag{3.47}$$

In this result, the dimensionless quantities can be re-substituted by real physical quantities, giving $\lambda_c = \left(64\pi^4 E_B / 3 a_p \tau_y\right)^{1/4}$ and $\tau_{0,c} = \frac{9}{4} a_p E_B (1 + \sqrt{4\tau_y / 3 a_p E_B})$. In this form, the wavelength and critical tension are very similar to the results (3.36) for fixed plate edges if $\tau_y \gg E_B / L_y^2$, i.e. if the transversal tension is very large or the bending stiffness very small. In fact, the results for fixed plate edges can be recovered by introducing the *effective length* of the wrinkles

$$L_{\text{eff}} = \frac{2\,\pi}{\sqrt{3\,a_p}} \approx 3.63 \cdot \sqrt{1/a_p}\,. \tag{3.48}$$

With this length unit, we can write the critical wavelength and critical stress as

$$\lambda_c = \left(\frac{16\pi^2 E_B L_{\text{eff}}^2}{\tau_y}\right)^{1/4} \quad \text{and} \quad \tau_{0,c} = \frac{3}{2} \cdot \frac{2\pi^2 E_B}{L_{\text{eff}}^2} \left(1 + \sqrt{\frac{\tau_y L_{\text{eff}}^2}{\pi^2 E_B}}\right) \tag{3.49}$$

for large τ_y in the same form as in the case of fixed plate edges. Only the factor $3/2$ in $\tau_{0,c}$ is new. It arises because the tension τ_0 is the maximum compressive stress (in the middle of

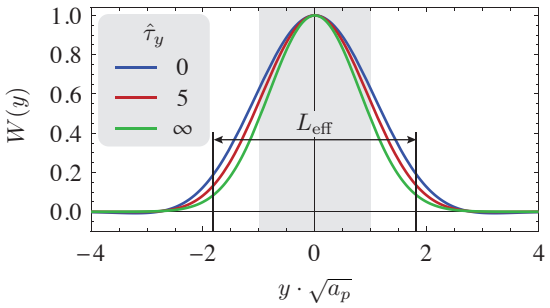

Figure 3.11.: Plot of the amplitude function for different values of $\hat{\tau}_y$, with $\hat{\tau}_y = \infty$ corresponding to the analytic solution (3.50). The parabolic stress profile τ_x is compressive in the region between $|y| < 1/\sqrt{a_p}$ (shaded grey), and the effective wrinkle length L_{eff} is larger than the compressive region.

the compressive region). The average compressive stress $\langle \tau_x \rangle$ is smaller: Averaging the stress distribution $\tau_x = -\tau_0(1 - a_p y^2)$ over the compressive region gives precisely $\langle \tau_x \rangle = \frac{2}{3}\tau_0$. Thus, the average compressive stress has the same critical value as the constant compressive stress in the case of fixed edges.

The effective wrinkle length L_{eff} roughly corresponds to the actual length of the wrinkles: At $y = L_{\text{eff}}/2$, the function $W(y)$ has decayed to a large extent. Figure 3.11 shows some amplitude functions, which are all very similar, irrespective of the value $\hat{\tau}_y$ of the transversal tension. The analytic solution (3.41) for the limit $\hat{\tau}_y \to \infty$ is also shown. It can be written as

$$W(y) \approx \exp\left(-\frac{3}{4} a_p y^2\right) = \exp\left(-\pi^2 \frac{y^2}{L_{\text{eff}}^2}\right) \quad \text{for} \quad \tau_y \gg a_p E_B \tag{3.50}$$

and has decayed to $\exp(-\pi^2/4) \approx 0.084$ at $y = L_{\text{eff}}/2$. The amplitude functions for smaller $\hat{\tau}_y$ have decayed to $\exp(-\pi^2/4)$ at $y = \Delta(\hat{\tau}_y)/2$. The function $\Delta(\hat{\tau}_y)$ is obtained from the numerical results, and figure 3.10 shows that Δ is always close to L_{eff}.

It is surprising that the effective wrinkle length is clearly larger than the width of the compressive region. They reach into the region of the membrane that is under tension in x-direction, which is energetically unfavourable when one considers the stretching energy in x-direction. However, the stretching energy in y-direction can be held smaller this way (compared to the case where the wrinkle length is confined to a smaller region).

3.3.3. Curved plate under local compression

Now we discuss the influence of an initial plate curvature on the buckling instability, i.e. we investigate the buckling of a shallow shell that is subject to a parabolic stress distribution in x-direction. This is motivated by the results of chapter 2 and the phenomenological result [112, 113, 138] that buckled spherical shells undergo a second instability: The dimple acquires a polygonal shape due to wrinkles developing on the inner side of the dimple edge. Our results have shown that the hoop stress τ_φ exhibits a negative peak in this region, which can be approximated locally by a parabolic stress distribution, see fig. 2.9 a). The secondary buckling is thus comparable to the case discussed in the previous section. In order to obtain quantitative results that can be used to predict the secondary buckling threshold, we refine the analysis by including curvature effects. In the region where wrinkles occur, the buckled shape has a curvature that increases approximately linear, see fig. 2.9 b), which corresponds to a height profile in the form of a cubic parabola (because the curvature is the second derivative of the height profile in the shallow shell approximation).

Therefore, we investigate the buckling of a shallow shell with a reference height profile

$$z(x, y) = \frac{1}{6} a_c y^3 \quad \text{with curvatures} \quad \kappa_y = a_c y, \quad \kappa_x = \kappa_{xy} = 0 \tag{3.51}$$

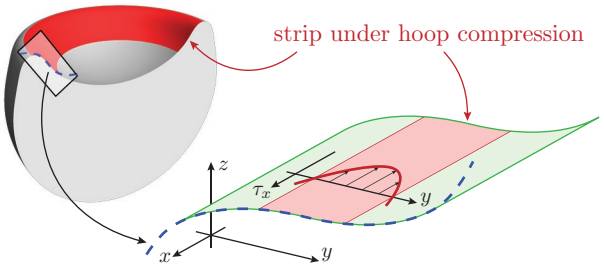

Figure 3.12.: The simplified stability problem: A plate with a height profile of a cubic parabola is a local approximation to the compressive region in the section through the buckled shell (dashed blue lines). The stress is compressive in the red strips.

under a stress state

$$\tau_x(x,y) = -\tau_0(1 - a_p y^2), \quad \text{and} \quad \tau_y = \tau_{xy} = 0, \tag{3.52}$$

see fig. 3.12. A discussion how the parameters a_p and a_c of the parabola and cubic parabola are related to the buckled axisymmetric shape and why τ_y and the curvature κ_y are set to zero will follow in chapter 4. Here, we will just analyse the posed problem, which proceeds analogously to the previous section. Again, we start by noticing that the geometry and stress state satisfy the equilibrium equations (3.19) and now continue to the stability equations.

In contrast to the investigation of plate buckling, we now have to solve the full coupled system (3.26) of stability equations for the normal deflection $w(x,y)$ and stress potential $\phi(x,y)$. Again, we use an ansatz that is harmonic in x-direction, $w(x,y) = W(y)\sin(kx)$ and $\phi(x,y) = \Phi(y)\sin(kx)$. Inserting this ansatz and the given expressions for the curvatures and stresses in the reference configuration of the shallow shell into (3.26) results in two coupled linear ordinary differential equations for the amplitude functions

$$\begin{aligned} 0 &= \left(\partial_y^4 - 2k^2\partial_y^2 + k^4 - \frac{k^2}{E_B}\tau_0\left(1 - a_p y^2\right)\right) W + \frac{a_c k^2 y}{E_B}\Phi \\ 0 &= \left(\partial_y^4 - 2k^2\partial_y^2 + k^4\right)\Phi - \left(a_c k^2 E_{2D} y\right) W. \end{aligned} \tag{3.53}$$

For a numerical solution, it is necessary to nondimensionalise the equations, which gives useful information on the relevant parameters. As before, we choose a length unit $1/\sqrt{a_p}$. Substituting $y = \hat{y}/\sqrt{a_p}$ and $\partial_y = \sqrt{a_p}\,\partial_{\hat{y}}$ in (3.53) induces further substitutions for the parameters of the differential equations such that they can finally be written in the form

$$\begin{aligned} 0 &= \left(\partial_{\hat{y}}^4 - 2\hat{k}^2\partial_{\hat{y}}^2 + \hat{k}^4 - \hat{k}^2\hat{\tau}_0\left(1 - \hat{y}^2\right)\right)\hat{W} + \left(\hat{a}_c\hat{k}^2\hat{y}\right)\hat{\Phi} \\ 0 &= \left(\partial_{\hat{y}}^4 - 2\hat{k}^2\partial_{\hat{y}}^2 + \hat{k}^4\right)\hat{\Phi} - \left(\hat{a}_c\hat{k}^2\hat{y}\right)\hat{W}. \end{aligned} \tag{3.54}$$

The substitutions included here are

$$\hat{y} = \sqrt{a_p}y, \quad \hat{k} = \frac{k}{\sqrt{a_p}}, \quad \hat{a}_c = \sqrt{\frac{E_{2D}}{E_B}}\frac{a_c}{a_p^{3/2}}, \quad \hat{\tau}_0 = \frac{\tau_0}{a_p E_B}, \quad \hat{\Phi} = \frac{\Phi}{E_B}, \quad \text{and} \quad \hat{W} = \sqrt{\frac{E_{2D}}{E_B}}W. \tag{3.55}$$

Because of the symmetry of the problem, we expect $\hat{W}(\hat{y})$ to be an even function. From eq. (3.54) then follows that $\hat{\Phi}(\hat{y})$ is an odd function, and it is sufficient to solve the differential equations on an interval $0 \le \hat{y} \le \hat{y}_{\max}$. The boundary conditions at the left end of this interval, the starting point of integration, follow from the symmetry conditions, $\hat{\Phi}(0) = \hat{\Phi}''(0) = 0$, $\hat{W}'(0) = \hat{W}'''(0) = 0$ and $\hat{W}(0) = 1$. The latter choice is arbitrary, since the differential equations are homogeneous. We imagine the plate to be infinitely large, so that the wrinkles

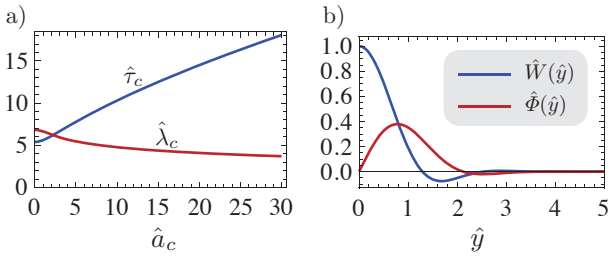

Figure 3.13.: Results for the buckling of curved plates under local compression. a) The dimensionless critical stress $\hat{\tau}_c = \tau_c/E_B a_p$ and wavelength $\hat{\lambda}_c = \lambda_c\sqrt{a_p}$ as a function of the curvature parameter $\hat{a}_c = \sqrt{E_{2D}/E_B}a_c/a_p^{3/2}$. b) Numerical solution for the amplitude functions for $\hat{a}_c = 20$.

are confined by the local nature of the compression rather than plate edges. For $\hat{y} \to \infty$, the wrinkle amplitude $\hat{W}$ has to approach 0 as well as the slope $\hat{\Phi}'$ of the stress potential because the additional tension derived from Φ shall approach 0. In practice, we integrate up to a sufficiently large $\hat{y}_{\max}$ and impose the boundary conditions $\hat{W}(\hat{y}_{\max}) = \hat{W}'(\hat{y}_{\max}) = 0$ and $\hat{\Phi}'(\hat{y}_{\max}) = \hat{\Phi}''(\hat{y}_{\max}) = 0$. When the shooting method must satisfy four boundary conditions at the endpoint of integration, it needs to vary four independent shooting parameters. In the present case, due to the homogeneity of the differential equations, there are only three free starting conditions, $\hat{W}''(0)$, $\hat{\Phi}'(0)$ and $\hat{\Phi}'''(0)$; the choice of $W(0)$ is arbitrary and cannot serve as a shooting parameter. Thus, the shooting method must be allowed to vary one of the additional parameters of the differential equations, $\hat{k}$, $\hat{a}_c$ or $\hat{\tau}_0$.

Exactly as in the previous section, we can interpret the differential equations as an eigenvalue problem, where one of the three parameters $\hat{k}$, $\hat{a}_c$ or $\hat{\tau}_0$ plays the role of an "eigenvalue" and must be chosen so that the equations do have a non-trivial solution. In our case, we choose $\hat{\tau}_0$ as the eigenvalue, because this has the simplest physical interpretation: We increase the stress on the curved plate until a non-trivial solution in form of wrinkles exists. This value is then the critical stress $\hat{\tau}_0$ which the plate can resist; for larger loads it will wrinkle. Obviously, the critical stress will depend on the other two parameters, $\hat{\tau}_0 = \hat{\tau}_0(\hat{a}_c, \hat{k})$. We consider the value of $\hat{a}_c$ to be given; the wavenumber $\hat{k}$, however, is unknown. The critical wrinkling mode, that becomes unstable first when the compressive stress is gradually increased, is obtained by minimising $\hat{\tau}_0$ with respect to $\hat{k}$,

$$\hat{\tau}_c(\hat{a}_c) = \min_{\hat{k}} \hat{\tau}_0(\hat{a}_c, \hat{k}) = \hat{\tau}_0(\hat{a}_c, \hat{k}_c). \tag{3.56}$$

Thus, the dimensionless critical stress only depends on $\hat{a}_c$, and so does the critical wavenumber $\hat{k}_c$ or wavelength $\hat{\lambda}_c = 2\pi/\hat{k}_c$. The procedure just outlined is carried out numerically.

Figure 3.13 shows the results of the numerical analysis. The critical tension $\hat{\tau}_c$ increases with increasing curvature parameter $\hat{a}_c$. This reflects the well known fact that bent surfaces (like corrugated cardboard) are harder to bend in the perpendicular direction than flat surfaces. The critical wavelength, on the other hand, is only weakly dependent on $\hat{a}_c$. In addition to the functions $\hat{\tau}_c(\hat{a}_c)$ and $\hat{\lambda}_c(\hat{a}_c)$, our numerical procedures return the shape of the wrinkles, that is, the amplitude function $\hat{W}(\hat{y})$. As shown in fig. 3.13 b), the amplitude decays rapidly outside the compressive region, i.e. for $|\hat{y}| > 1$.

The main result of this section is the formula for the critical compressive stress on which a curved plate starts to wrinkle,

$$\tau_c = a_p E_B \hat{\tau}_c(\hat{a}_c) \quad \text{with} \quad \hat{a}_c = \sqrt{\frac{E_{2D}}{E_B}}\frac{a_c}{a_p^{3/2}}, \tag{3.57}$$

where the function $\hat{\tau}_c(\hat{a}_c)$ is known numerically, see fig. 3.13 a), blue line. If the minimum value $\tau_x|_{y=0} = -\tau_0$ of the parabolic stress falls below $-\tau_c$, an instability sets in which has the

wavelength

$$\lambda_c = \frac{1}{\sqrt{a_p}}\,\hat{\lambda}_c(\hat{a}_c), \tag{3.58}$$

where the function $\lambda_c(\hat{a}_c)$ is also known numerically, see fig. 3.13 a), red line. In the special case $\hat{a}_c = 0$ corresponding to a flat plate, these results coincide with the results of the previous section if $\tau_y = 0$ is chosen and the formulation is changed to have $L_{\text{eff}} = 2\pi/\sqrt{3a_p}$ as the length unit.

In the remainder of this section, we will discuss the bifurcation behaviour of the wrinkling transition, and show that it is continuous. This discussion is based on the second and fourth order energy changes $\Delta U^{(2)}$ and $\Delta U^{(4)}$, see eqs. (3.27) and (3.29), respectively (the third order energy change (3.28) vanishes due to symmetry).

The second order energy change (3.27) reads

$$\Delta U^{(2)} = \frac{1}{2}\int \mathrm{d}A\; w\left\{E_B\Delta^2 w + \tau_0(1-a_p y^2)\,\partial_x^2 w - a_c y\,\partial_x^2\phi\right\} \tag{3.59}$$

in the present case, which can be simplified by the replacement $\partial_x^2 \to -k^2$ because all functions have an x-dependence $\sim \sin(kx)$. We checked with our numerical solutions (w, ϕ) that this integral vanishes at the critical point $\tau_0 = \tau_c$. To calculate the energy decrease for $\tau_0 > \tau_c$, we use the same functions (w, ϕ) which were calculated at the critical point. This is analogous to the first order perturbation theory used in quantum mechanics. Writing $\tau_0 = \tau_c + (\tau_0 - \tau_c)$ and using that the integral vanishes at τ_c, we obtain

$$\Delta U^{(2)} = \frac{1}{2}\int \mathrm{d}A\; w\left\{-k^2(\tau_0-\tau_c)(1-a_p y^2)\right\} w \tag{3.60}$$

Since our plate is infinitely long in x-direction, it is appropriate to discuss the energy decrease per length, and so the integral in x-direction over the trigonometric function is replaced by its average, $\int_0^{L_x}\sin^2(kx)/L_x = 1/2$. Furthermore, we switch to the reduced units introduced in (3.55), and finally obtain

$$\frac{\Delta\hat{U}^{(2)}}{L_x} = \frac{1}{2}(\hat{\tau}_0-\hat{\tau}_c)\hat{W}_0^2\int_0^{\hat{y}_{\max}}\mathrm{d}\hat{y}\;\hat{W}(\hat{y})\left\{-\hat{k}^2\left(1-\hat{y}^2\right)\right\}\hat{W}(\hat{y}). \tag{3.61}$$

In this equation, the function $\hat{W}$ has a fixed amplitude of $\hat{W}(0) = 1$, and $\hat{W}_0$ denotes the actual wrinkle amplitude (in reduced units). The integral is negative since $\hat{W}(\hat{y})$ decays rapidly for $\hat{y} > 1$. For $\hat{a}_c = 20$, for example, the integral has a numerical value of $-b_2 = -1.0188$.

The fourth order energy change caused by the wrinkling pattern can be calculated analogously, with $\int_0^{L_x}\sin^4(kx)/L_x = 3/8$ and $\int_0^{L_x}\cos^2(kx)\sin^2(kx)/L_x = 1/8$,

$$\frac{\Delta\hat{U}^{(4)}}{L_x} = \frac{1}{32}\frac{1}{1-\nu^2}\hat{W}_0^4\int_0^{\hat{y}_{\max}}\mathrm{d}\hat{y}\;\left[3\big(\hat{k}\hat{W}\big)^4 + \big(\hat{k}\hat{W}\partial_{\hat{y}}\hat{W}\big)^2 + 3\big(\partial_{\hat{y}}\hat{W}\big)^4\right], \tag{3.62}$$

where the integral evaluates to $b_4 = 9.34$ for $\hat{a}_c = 20$.

In total we have an elastic energy

$$\frac{\Delta\hat{U}}{L_x} = -\frac{1}{2}b_2(\hat{\tau}_0-\hat{\tau}_c)\hat{W}_0^2 + \frac{1}{32}b_4\frac{1}{1-\nu^2}\hat{W}_0^4. \tag{3.63}$$

The optimal wrinkle amplitude is obtained by minimising this function with respect to $\hat{W}_0$, which gives

$$\hat{W}_0 = \pm\sqrt{\frac{8b_2}{b_4}(1-\nu^2)(\hat{\tau}_0-\hat{\tau}_c)} \tag{3.64}$$

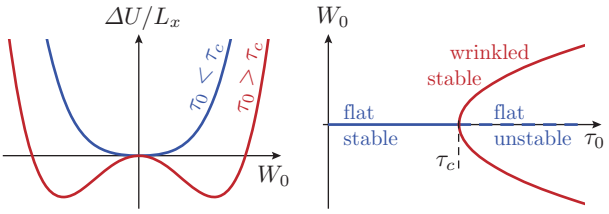

Figure 3.14.: Bifurcation behaviour for the compressed shallow shell. The energy landscape shown on the left gives rise to a pitchfork bifurcation, where the wrinkle amplitude grows like $\hat{W}_0 \sim \sqrt{\hat{\tau}_0 - \hat{\tau}_c}$ when the critical point $\hat{\tau}_c$ is exceeded.

for $\hat{\tau}_0 > \hat{\tau}_c$. The energy function and the position of the (un)stable extrema can nicely be visualised, see fig. 3.14. The elastic energy $\Delta\hat{U}/L_x$ shows, as a function of the wrinkle amplitude $\hat{W}_0$, either one minimum at $\hat{W}_0 = 0$ (for $\hat{\tau}_0 \leq \hat{\tau}_c$) or two minima and one maximum (for $\hat{\tau}_0 > \hat{\tau}_c$). For the equilibrium configuration, which resides in one of the minima, we get a behaviour that changes at $\hat{\tau}_c$: The flat solution ($\hat{W}_0 = 0$) splits at $\hat{\tau}_c$ into two stable wrinkled solutions that are equivalent by symmetry, and the flat solution becomes unstable. The wrinkling of the shallow shell thus represents a *supercritical pitchfork bifurcation.*

3.4. Comparison and application to other setups

In the last three sections we investigated different models for the buckling and wrinkling of plates and shallow shells. In each setup, the critical compressive stress τ_c, where the instability sets in, and the wavelength λ_c of the unstable mode have been calculated. The "reference model" is the long rectangular plate with simply supported long edges, subjected to a uniform compression τ_x and lateral tension τ_y. Already in this simple model, useful information about the transition from buckling to wrinkling has been obtained. The other two models are focused on the confinement of the wrinkles by a parabolic stress profile that is only locally compressive: We investigated a flat plate under parabolic stress in x-direction and uniform tension τ_y, and a curved plate with linearly increasing curvature $\kappa_y \sim y$ under parabolic stress in x-direction with $\tau_y = 0$.

The two models of localised wrinkling can be mapped on the reference model by choosing an effective wrinkle length L_{eff}. Even the curvature effects influence only the numerical prefactors. In all models, the following scaling laws describe the critical compressive stress and critical wavelength:

$$\tau_c \sim -\frac{E_B}{\lambda_c^2} \quad \text{with} \quad \begin{cases} \lambda_c \sim L_{\text{eff}} & \text{for buckling } (\tau_y = 0) \\ \lambda_c \sim \left(\dfrac{E_B L_{\text{eff}}^2}{\tau_y}\right)^{1/4} & \text{for wrinkling } (\tau_y \gg E_B/L_{\text{eff}}^2). \end{cases} \tag{3.65}$$

The scaling law of the critical stress is exactly the same as for Euler buckling of bars [83].

Considering the agreement of all the different models, we are encouraged to transfer these results to other cases like the shear wrinkles shown in fig. 3.2 c). In contrast to the fixed plate, where we have varied τ_x and τ_y independently, we now have only one control parameter: the shear angle γ. It leads to shear strains $\varepsilon_{xy} = \gamma/2$ and shear stresses $\tau_{xy} = G_{2\text{D}}\gamma$, see (3.6) and (3.15) respectively. In the principal axes system, this shear stress corresponds to the components $\tau_\eta = G_{2\text{D}}\gamma$ and $\tau_\xi = -G_{2\text{D}}\gamma$, which are equal in magnitude but have opposite signs. The shear wrinkles are oriented in a 45° angle and have, therefore, an effective length $L_{\text{eff}} = \sqrt{2}L_y$. To find the critical compressive stress $\tau_\xi = \tau_c$, we use the relation (3.36) from the fixed plate model

(with the replacements $\tau_{x,c} \to \tau_c$, $\tau_y \to -\tau_c$ and $L_y \to L_{\text{eff}}$),

$$\tau_c = -\frac{2\pi^2 E_B}{L_{\text{eff}}^2}\left(1+\sqrt{1-\frac{\tau_c L_{\text{eff}}^2}{\pi^2 E_B}}\right) \quad \Rightarrow \quad \tau_c = -8\pi^2\frac{E_B}{L_{\text{eff}}^2} = -4\pi^2\frac{E_B}{L_y^2}. \tag{3.66}$$

This is close to the exact result, $\tau_c = -5.35\,\pi^2 E_B/L_y^2$, see ref. [124]. According to (3.36), the critical wavelength is of the order of the plate width,

$$\lambda_c = \frac{2}{\sqrt{3}}\,L_{\text{eff}} = 2\sqrt{\frac{2}{3}}\,L_y \approx 1.63\,L_y, \tag{3.67}$$

which is also in reasonable agreement with the results of ref. [124]. The deviations to the exact results can be attributed to the crude simplification of the buckling pattern: Two neighbouring shear wrinkles are not exactly side by side as the wrinkles in our models, they are shifted in the 45° direction, see fig. 3.2 c).

We can go beyond this near-threshold regime describing the onset of shear buckling to the far-from-threshold regime by assuming that a further increase of the shear angle γ will increase the tensional stress τ_η, but not the compressive stress τ_ξ because it is absorbed by the wrinkles. This will soon result in $\tau_\eta \gg |\tau_\xi|$, so that the scaling laws for large lateral tension (3.37) must be used. The critical compression is of minor interest because it is exceeded anyway in the far-from-threshold regime. The wavelength of the wrinkles depends on the shear angle,

$$\lambda = \left(\frac{16\pi^2 E_B L_{\text{eff}}^2}{\tau_\eta}\right)^{1/4} = \left(\frac{8\pi^2 L_y^2 H_0^2}{3(1-\nu^2)\gamma}\right)^{1/4} \tag{3.68}$$

where we assumed $\tau_\eta = E_{2\text{D}}\gamma/2$ because the wrinkled membrane is approximately under uniaxial stress. Our result coincides with that of ref. [144] and shows that the wavelength decreases with increasing shear angle, so that we can again observe a transition from buckling (wavelength of the order of the plate width) in the near-threshold regime to wrinkling (short wavelength) in the far-from-threshold regime.

It should be noted that our approach always uses an analysis of the stability equations, which implies that we consider small displacements. Thus, the essential difference between buckling and wrinkling is not that wrinkles are well developed and have a large amplitude, but that wrinkles are under strong tension in the direction perpendicular to the compression. The condition of "strong tension", $\tau_y \gg E_B/L_{\text{eff}}^2$, should not be taken too literally because it can also be fulfilled with small (but positive) τ_y if the bending stiffness E_B is small and/or the wrinkle length L_{eff} is large. In the Lamé geometry as discussed in ref. [34], for example, the transition from the NT to the FFT regime is mainly controlled by an increasing wrinkle length.

A key point in our analysis of plate buckling is that we control the compression τ_x and tension τ_y independently. This gives us very general scaling laws (3.65) for the critical compression and critical wavelength as a function of τ_y, E_B and L_{eff}. When setups such as shear wrinkling or wrinkling in the Lamé geometry are studied, the whole deformation is controlled by a single parameter. This parameter influences both the compression τ_x and the tension τ_y (and in the Lamé geometry also the length L_{eff}) simultaneously, and so these models offer only limited views on the scaling behaviour of wrinkle characteristics like the wavelength or compressive stress. For this reason, the authors of ref. [34] report a FFT scaling for the wavelength that is "in sharp contrast to the NT scaling" – however, if their scalings are re-written in terms of τ_y, E_B and L_{eff} they are exactly the same for NT and FFT and coincide with (3.65).

Chapter 4

Secondary buckling of spherical shells

Abstract – In the following, we combine the results of the last two chapters to explain and quantify the secondary buckling phenomenon, that is, the transition in which the axisymmetric dimple of a buckled spherical shell loses its axisymmetry. We first present a simplified analysis based on the wrinkling criterion for shallow shells under localised compression. This approach identifies the physical mechanism underlying the secondary buckling and already yields useful quantitative predictions for the critical volume of the secondary buckling that agree with numerical simulation results available from the literature. A stability analysis of the axisymmetric buckled shape in the framework of DMV shell theory confirms these findings. Eventually, a phase diagram for deflated spherical shells is presented, which summarises many of the results obtained for spherical shells in this thesis.
Published material – Large parts of this chapter are reproduced with modifications from the author's publications [155], © 2014 by IOPscience and [156], with kind permission of The European Physical Journal (EPJ).

4.1. Introduction

In chapter 2 we have seen that spherical shells buckle upon deflation and assume an axisymmetric shape with a round dimple. We discussed the stability of those shapes with respect to further growth of the dimple, but not the stability with respect to non-axisymmetric modes. This important and very relevant subject is examined in the present chapter.

There is evidence that the dimple can lose its axisymmetry when it exceeds a certain size if the shell's bending stiffness is sufficiently small: The dimple can acquire a polygonal shape as shown in fig. 4.1. This phenomenon, termed *secondary buckling*, has been observed in experiments on microcapsules [97, 98, 113] and in numerical simulations based on triangulated surfaces [112, 113, 138]. The secondary buckling also occurs when the dimple is formed in other ways than deflation by uniform pressure, for example by indenting the capsule with a point force [102, 128–130], when the capsule is pressed between rigid plates [128] or when the capsule adheres to a substrate [80]. Also other shells than perfectly spherical and homogeneous shells show this behaviour, for example shells with softer regions [31, 103] and models for pollen grains [72]. It is, thus, a very generic behaviour.

Previous research on the secondary buckling has remained mostly on a phenomenological level and was concentrated on the reconstruction of experimental results with numerical simulations of shells, which allowed to determine important characteristics like the critical volume at the onset of the secondary buckling and the number of wrinkles [112, 113]. In the regime far

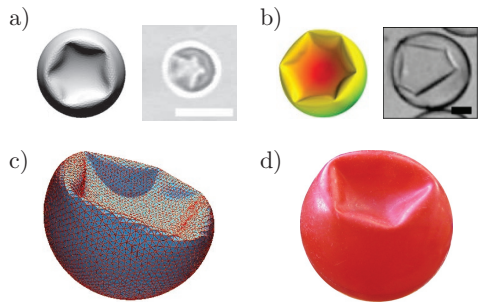

Figure 4.1.: Experimental and simulated shapes of spherical shells beyond the secondary buckling. a) Surface Evolver simulation [112] and buckled organo-silica shell [113] (scale bar 5 µm), b) simulation and experimental result for a shell with inhomogeneous thickness [31] (scale bar 35 µm), c) Monte Carlo simulation [138], d) deflated plastic ball which the author found on the campus. Images a)–c) are taken from the cited references.

beyond the onset of secondary buckling, some results from the theory of *stress focusing* in elastic sheets [141, 142] can be applied to shells. In this approach the shape is modelled by straight ridges joined by d-cones [102], and the appropriate scaling laws show that the polygonal structure has less elastic energy than the axisymmetric buckled shape with a "ring ridge" [141].

However, a theory rationalising the mechanics of the *onset* of the secondary buckling is still lacking. Here we will offer an explanation within continuum elasticity theory. This also demonstrates that polygonal capsule shapes can occur in the absence of any discretisation effects. For crystalline elastic capsules, defects in the triangulation give rise to additional faceting effects upon deflation [146].

Our explanation is based on the results of the previous chapter, where a buckling criterion for shallow shells under locally compressive stress has been derived. As seen in chapter 2, fig. 2.9, the inner neighbourhood of the dimple edge is under compressive hoop stress. Wrinkles develop in this region to release this compression when it exceeds a certain threshold. The critical stress τ_c obtained in the curved plate model with a parabolic stress profile, section 3.3.3, can be used to make quantitative predictions at which volume difference the axisymmetric shapes will start to form wrinkles. To this end, the parameters of the geometry and stress field of the curved plate model must be adjusted so that the curved plate locally approximates the compressive region of the buckled axisymmetric shape. When the onset of secondary buckling is found, the critical wavelength λ_c of the curved plate model can be used to estimate the number of wrinkles that will form.

The results of this approach are verified with a more involved stability analysis of the full axisymmetric shape, which confirms the results for the critical volume difference at secondary buckling. The prediction of consistent results for the number of wrinkles is more difficult. A comparison of our results to experiments and simulations is furthermore complicated by the fact that our calculations are only valid at the onset; but wrinkles in experiments and simulations can be counted best when they are well developed. We show with scaling arguments that the number of wrinkles changes with further deflation.

4.2. Simplified analysis based on the curved plate criterion

4.2.1. Simplification of geometry and stress state

In order to apply the critical stress (3.57) and wavelength (3.58) of the curved plate model to the secondary buckling, we must first justify that the setup of this simplified model is a reasonable approximation to the real geometry and stress distribution in an axisymmetric, buckled shape of a deflated spherical shell. Let us recall the results of the axisymmetric shape equations and Pogorelov model presented in fig. 2.9.

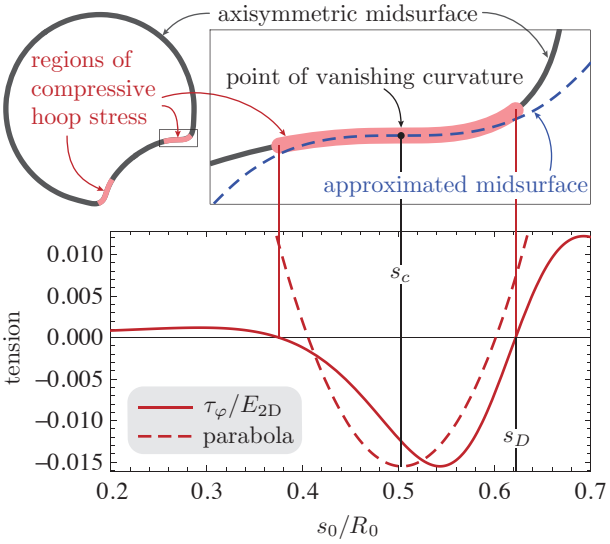

Figure 4.2.: Approximation of the shape and stress distribution for a numerical solution of the shape equations at $\tilde{E}_B = 10^{-5}$, $\nu = 1/3$ and $\Delta V/V_0 = 0.05$. The hoop tension τ_φ is compressive (negative) in a narrow strip along the inner side of the dimple edge, marked light red, where we can expect wrinkles to occur. The dashed lines show the simplifications made in the curved plate model, namely a parabolic stress profile and a cubic parabola for the approximated midsurface. The arc length coordinates s_c of the point of vanishing curvature and s_D of the dimple edge are indicated.

The region of interest is the s_0-range where the hoop stress τ_φ has its compressive (negative) peak. Around its minimum, the peak can be fitted well with a parabola; therefore, the φ-direction of the deflated shell is mapped onto the x-direction of the curved plate model, where a stress $\tau_x = -\tau_0(1 - a_p y^2)$ is applied. Consequently, the s-direction is mapped onto the y-direction; and as the meridional tension τ_s is much smaller than τ_φ in the region of interest and the axisymmetric shape is guaranteed to be free of shear stresses, the choices $\tau_y = \tau_{xy} = 0$ of the curved plate model are also justified, see (3.52). Secondly, the geometrical setup must be checked for accuracy. Fig. 2.9 b) shows that the meridional curvature κ_s has a root near the point of maximal compression and increases approximately linearly in its vicinity. The curvature κ_φ remains small, around $|\kappa_\varphi| = 1/R_0$, and can be neglected if the wrinkles have a wavelength (in x-direction) that is considerably smaller than R_0. This justifies the geometrical setup (3.51) with $\kappa_y = a_c y$ and $\kappa_x = \kappa_{xy} = 0$.

The values of the parameters a_p and a_c of the stress parabola and curvature are obtained as follows. The cubic parabola is fitted to the point $s_0 = s_c$ where the exact midsurface has vanishing meridional curvature, $\kappa_s(s_c) = 0$, see fig. 4.2. Since the relevant portion of the shell is shallow, differences in the metric for the description with s_0 or y as a coordinate can be neglected [135]. So we can calculate a_c by simple differentiation of $\kappa_s(s_0)$ with respect to s_0, which can be done numerically for a given axisymmetric solution,

$$a_c = \partial_{s_0} \kappa_s \big|_{s_c} . \tag{4.1}$$

The parabola to approximate the hoop tension is chosen to have the same minimum value $-\tau_0$ and the same integral $\int \tau_\varphi \, \mathrm{d}s_0$ over the compressive part as the exact numerical function $\tau_\varphi(s_0)$. Let $F = \int_{s_1}^{s_2} \tau_\varphi(s_0) \, \mathrm{d}s_0$ denote the exact numerical integral, which has the physical interpretation of the net force in the compressive region $s_0 \in [s_1, s_2]$. We can evaluate it by numerical integration for a given solution of the shape equations. A parabola of the form $\tau_x = -\tau_0 \left(1 - a_p y^2\right)$ has the roots $y = \pm 1/\sqrt{a_p}$. The integral over the parabola between its roots is $-4\tau_0/3\sqrt{a_p}$ and must equal F. Thus we have

$$a_p = (4\tau_0/3F)^2 \quad \text{with} \quad F = \int_{s_1}^{s_2} \tau_\varphi(s_0) \, \mathrm{d}s_0 \tag{4.2}$$

to determine the parameter of the parabola from a given axisymmetric shape. Note that the parabola is centred at $y = 0$, corresponding to the point $s_0 = s_c$ of vanishing meridional curvature. This point does not agree exactly with the minimum of the exact hoop tension $\tau_\varphi(s_0)$, but is very close (see fig. 4.2).

Figure 4.2 shows that the approximations are not perfect, and that there are considerable deviations especially far away from the point $y = 0$ (corresponding to $s_0 = s_c$). However, these deviations are acceptable since they are in regions where no wrinkles develop.

4.2.2. Results for the secondary buckling threshold

We can apply the buckling criterion of the curved plate to both the numerical solutions of the shape equations and the analytic Pogorelov model. Before presenting the detailed results, we start with considering the scaling laws of the involved quantities. According to all plate buckling models of chapter 3, the critical compressive stress is $\tau_c \sim E_B/\lambda_c^2$. For small τ_s, the wavelength λ_c is of the same order as the effective wrinkle width W_{eff}, which is determined by the width of the compressive region. In the Pogorelov model, eq. (2.38), we saw that the relevant length scale for this width is $\xi \sim R_0 \tilde{E}_B^{1/4}$. Thus, the critical compressive stress is $\tau_c \sim E_B/R_0^2 \tilde{E}_B^{1/2} \sim E_{2\text{D}} \tilde{E}_B^{1/2}$. The actual hoop stress in the Pogorelov model is obtained from (2.42), (2.35) and (2.28), $\tau_\varphi \sim E_{2\text{D}} \tilde{E}_B^{1/4} (\Delta V/V_0)^{1/4}$. It reaches the threshold, $\tau_\varphi \sim \tau_c$, when $\Delta V/V_0 \sim \tilde{E}_B$. This gives the correct parameter dependence of the secondary buckling volume, see (4.3) and (4.9) below.

The wrinkles of wavelength $\lambda \sim R_0 \tilde{E}_B^{1/4}$ are distributed over the perimeter $2\pi r_D \sim R_0 (\Delta V/V_0)^{1/4}$ of the dimple edge, see (2.28). With $\Delta V/V_0 \sim \tilde{E}_B$ at the secondary buckling threshold, we thus see that the number of wrinkles $n = 2\pi r_D/\lambda \sim \mathcal{O}(1)$ does not scale with the reduced bending stiffness at the onset of secondary buckling. This result is a bit surprising: One might have expected that shells with smaller bending stiffness have more wrinkles, because they are easier to bend. And indeed, the wavelength decreases with decreasing bending stiffness; however, the perimeter on which the wrinkles are distributed also decreases: The secondary buckling happens earlier for smaller bending stiffnesses. Both effects cancel out, so that the number of wrinkles at the onset of secondary buckling is quite robust against changes in the bending stiffness.

We discuss the application of the curved plate buckling criterion to the numerical solutions exemplary for a capsule with $\tilde{E}_B = 10^{-5}$ and $\nu = 1/3$. For a numerical solution of the shape equations, the parameters a_c and a_p, eqs. (4.1) and (4.2), are calculated to obtain the critical compressive stress τ_c from the curved plate model (3.57). Then the shape can be judged if it is beyond the secondary buckling: If the minimum value $\tau_{\min} = \min_{s_0} \tau_\varphi(s_0)$ in the compressive region exceeds the critical stress, i.e. if $|\tau_{\min}| > \tau_c$, the final shape will be non-axisymmetric. For the given elastic parameters, this happens first at a critical volume difference $\Delta V/V_0 = 0.048$. At this volume, the dimensionless curvature parameter is $\hat{a}_c = 20.86$, and the wrinkle wavelength (3.58) evaluates to $\lambda_c = 0.396 R_0$. Since the wrinkles are centred at s_c where the radius of the axisymmetric midsurface is $r(s_c) = 0.476 R_0$, the number of wrinkles is given by $n = 2\pi r(s_c)/\lambda_c = 7.55$, so either $n = 7$ or $n = 8$. These results are illustrated in fig. 4.3 in a meridional section and in a three-dimensional view. The amplitude of the wrinkles is undefined (since the governing differential equations are homogeneous) and is chosen arbitrarily in the plot. The results show that the wrinkle amplitude decays rapidly outside the compressive region (compare with fig. 4.2), and that the approximated midsurface is quite accurate in the region of large wrinkle amplitude. This indicates that our approximations are justified, because their inaccuracies lie in regions where the wrinkles do not develop.

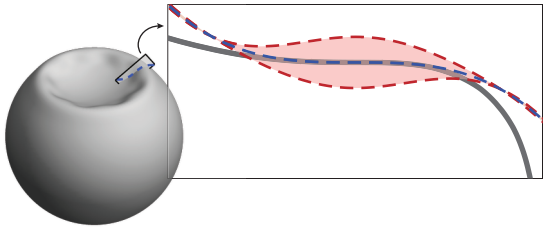

Figure 4.3.: Wrinkle shape according to the curved plate model for $\tilde{E}_B = 10^{-5}$ and $\nu = 1/3$ at the onset of secondary buckling. The cross section shows the axisymmetric mid-surface (grey), cubic parabola (dashed blue), and wrinkle profile W (red). In the three-dimensional view, the frame indicates the position and orientation of the cross section.

This analysis was applied to a whole range of reduced bending stiffnesses $\tilde{E}_B$, and the critical volume difference where the secondary buckling sets in depends by a power law on the bending stiffness,

$$\left.\frac{\Delta V_{\text{2nd}}}{V_0}\right|_{\text{shape eqs.}} = 2552\,\tilde{E}_B^{0.95} \tag{4.3}$$

as a fit shows. This dependency is illustrated in the phase diagram in the discussion at the end of this chapter, see fig. 4.5 below.

Now we apply the curved plate buckling criterion to the axisymmetric shapes of the Pogorelov model. This way we obtain an analytic result for the secondary buckling threshold. At first, the parameters a_p and a_c must be determined. In the Pogorelov model, the hoop stress τ_φ is given by (2.42). Its minimum value $-\tau_0$ and the integral F between its roots can be calculated as

$$\tau_0 = \frac{\sigma_{\min}}{3}\frac{E_{\text{2D}}}{1-\nu^2}\frac{\xi\alpha}{R_0} \quad \text{and} \quad F = \frac{E_{\text{2D}}}{1-\nu^2}\frac{\xi^2\alpha}{R_0}\left[\frac{5}{24}\sigma_{\min}^2 + \frac{\sigma_{\min}}{3}\left(e^{-3\pi/4}+\sqrt{2}\right)\right]. \tag{4.4}$$

Evaluating the parameter a_p of the stress parabola (4.2) leads to

$$a_p = \frac{\bar{a}_p}{R_0^2\left[\tilde{E}_B(1-\nu^2)\right]^{1/2}} \quad \text{with} \quad \bar{a}_p \approx 0.33955 \tag{4.5}$$

where, for convenience, the numerical constants have been reduced to $\bar{a}_p$ and the linearised scaling parameters (2.38) were used.

Calculating the curvature parameter a_c is a bit more difficult and cannot be done explicitly. The problem is that the root of the meridional curvature $\kappa_s(s_0)$ according to (2.43) cannot be found analytically. It is implicitly determined by the equation

$$\frac{\alpha}{\xi}\bar{w}'(\bar{s}_c) - \frac{1}{R_0} = 0 \quad \Rightarrow \quad \bar{w}'(\bar{s}_c) = \left(\frac{3}{8}(1-\nu^2)\frac{\tilde{E}_B}{\Delta V/V_0}\right)^{1/4} = \left(\frac{3}{8}(1-\nu^2)\right)^{1/4}\frac{1}{X} \tag{4.6}$$

where the simplified scaling parameters (2.38) were used for α and ξ and a substitution $X = (\Delta V/V_0\tilde{E}_B)^{1/4}$ was defined. The function $\bar{w}(\bar{s}_0)$ is known, see (B.7) in appendix B, and thus this equation can be solved (numerically) for $\bar{s}_c$ and implicitly defines a function $\bar{s}_c(X)$. With this numerical function $\bar{s}_c(X)$, the curvature parameter a_c can be evaluated numerically with (4.1) and (2.43) for any given X,

$$a_c(X) = \frac{\alpha}{\xi^2}\bar{w}''(\bar{s}_c(X)). \tag{4.7}$$

After these steps, a_p and $a_c(X)$ can be plugged into the critical buckling stress τ_c (3.57) of the curved plate. The onset of secondary buckling requires $\tau_c = \tau_0$ with τ_0 from (4.4), which is

equivalent to

$$\hat{\tau}_c(\hat{a}_c(X)) = \frac{\sigma_{\min}}{3\bar{a}_p}\left(\frac{8}{3}\right)^{1/4}\left(1-\nu^2\right)^{-1/4}X \quad \text{with} \quad \hat{a}_c(X) = \left(\frac{8}{3}\left(1-\nu^2\right)\right)^{1/4}\frac{X}{\bar{a}_p^{3/2}}\,\bar{w}''(\bar{s}_c(X)). \tag{4.8}$$

Solving this equation numerically results, for $\nu = 1/3$, in $X = 7.8024$. Thus, with the original definition $X = (\Delta V/V_0\tilde{E}_B)^{1/4}$, we have derived the secondary buckling volume

$$\left.\frac{\Delta V_{\text{2nd}}}{V_0}\right|_{\text{Pog}} = 3706\,\tilde{E}_B \tag{4.9}$$

for the Pogorelov model with the curved plate buckling criterion. The prefactor is still weakly ν-dependent, but the exponent 1 is exact and fixed in this model. This result is similar to the result (4.3) of the curved plate model applied to the shape equations. Both lines are shown in the phase diagram below.

The wrinkle number can also be calculated in the Pogorelov model. At $X = 7.8024$, we have (for $\nu = 1/3$) a curvature parameter of $\hat{a}_c(X) = 15.14$ and a non-dimensional wavelength of $\hat{\lambda}_c(\hat{a}_c) = 4.366$ (see fig. 3.13). This results in a real wavelength of

$$\lambda_c = \frac{\hat{\lambda}_c}{\sqrt{a_p}} = R_0\left[\tilde{E}_B\left(1-\nu^2\right)\right]^{1/4}\frac{\hat{\lambda}_c}{\sqrt{\bar{a}_p}}. \tag{4.10}$$

The perimeter on which the wrinkles are distributed is $2\pi r_D \approx 2\pi(8\Delta V/3V_0)^{1/4}R_0$, see (2.28) and (2.38). Inserting the volume difference (4.9) at the onset of secondary buckling and dividing by λ_c gives the number of wrinkles,

$$n = \frac{2\pi r_D}{\lambda_c} = 2\pi\left(\frac{8}{3}\right)^{1/4}\frac{X\sqrt{\bar{a}_p}}{\hat{\lambda}_c\left(1-\nu^2\right)^{1/4}} \approx 8.6 \tag{4.11}$$

Thus, in this combination of simplified models (Pogorelov model for the axisymmetric shape and buckling criterion from the curved plate model), the number of wrinkles at the onset of secondary buckling seems fixed at 8 or 9 over the whole range of $\tilde{E}_B$.

4.3. Stability analysis of the full axisymmetric buckled shape

The results of the previous section are based on the very simple curved plate model for the buckling threshold, which only incorporates the key features of the geometry and stress state of the axisymmetric buckled shape. While the reduction to these key features helps understanding the underlying mechanics, it is questionable if the results are quantitatively correct. In the following, we present a more rigorous approach, in which stability equations are applied to the full axisymmetric shape. In comparison with the curved plate model, this is an improvement because also the less prominent features like the meridional tension $\tau_s \neq 0$ and circumferential curvature $\kappa_\varphi \neq 0$ are contained in the stability analysis. However, it might be problematic that the dimple is not shallow for large volume differences. In the curved plate model, this problem was avoided because we only looked at a small section of the shell, which was even for large dimples quite shallow.

4.3.1. Stability equations of shells of revolution

The stability equations for shallow shells that can be found in the literature are formulated in Cartesian coordinates, like our eq. (3.26). For the treatment of shells that are axisymmetric before the onset of instability, a polar coordinate system is more appropriate and easier to handle from a numerical point of view, because it allows a separation ansatz to model the buckling pattern. We can derive these stability equations for shells of revolution analogously to section 3.2.5. The basis for this derivation are the strain-displacements relations of the nonlinear DMV shell theory, which are given in ref. [96] in general coordinates. In appendix C.1 it is shown that the stability equations can be formulated again in the normal displacement w and stress potential ϕ and are formally very similar to the Cartesian case,

$$\begin{aligned} E_B\Delta^2 w &= (\kappa_s \mathrm{D}_{\varphi\varphi} + \kappa_\varphi \mathrm{D}_{ss})\phi + (\tau_s \mathrm{D}_{ss} + \tau_\varphi \mathrm{D}_{\varphi\varphi})w \\ \frac{1}{E_{2\mathrm{D}}}\Delta^2\phi &= -(\kappa_s \mathrm{D}_{\varphi\varphi} + \kappa_\varphi \mathrm{D}_{ss})w. \end{aligned} \tag{4.12}$$

Only the derivative operators must be re-defined according to

$$\mathrm{D}_{ss} \equiv \partial_s^2, \quad \mathrm{D}_{\varphi\varphi} \equiv \frac{\cos\psi}{r}\,\partial_s + \frac{1}{r^2}\,\partial_\varphi^2 \quad \text{and} \quad \Delta = \mathrm{D}_{ss} + \mathrm{D}_{\varphi\varphi}. \tag{4.13}$$

The functions for curvature (κ_s, κ_φ), tension (τ_s, τ_φ) and geometric properties (ψ, r) occurring in the stability equations are properties of the axisymmetric buckled configuration that is to be tested for its stability with respect to non-axisymmetric deflections. They are, thus, known numerically when (4.12) is solved.

Because the DMV theory is an approximate shell theory, these stability equations are also only approximate. They are applicable under the conditions that (i) the typical length scale of the deformation is much smaller than the smallest radius of curvature of the reference shape, (ii) the displacements are predominantly normal to the surface and (iii) the stresses due to bending are smaller than the stresses due to stretching [96]. These prerequisites are met when the shell is shallow, but also for shells which are closed and, therefore, essentially non-shallow as long as the "relevant" part of the shell, which is subjected to the largest deformation, is shallow. In the derivation of the stability equations in appendix C.1, we explicitly assume that the slope angle ψ (recall fig. 2.2 for its definition) varies slowly with the arc length. This assumption is violated at the dimple edge, but we can expect that the wrinkles are repelled from this region anyway, because bent surfaces (like corrugated cardboard) are hard to bend in the perpendicular direction. However, this is probably the most inaccurate point in this approach.

In the following, we are searching for non-axisymmetric solutions in the form of wrinkles. They are modelled by an ansatz

$$w(s,\varphi) = W(s)\cos(n\varphi), \qquad \phi(s,\varphi) = \Phi(s)\cos(n\varphi), \tag{4.14}$$

where n is the number of wrinkles in circumferential direction and W and Φ are amplitude functions as in section 3.3. Inserting this ansatz into (4.12) results in ordinary differential equations for the amplitude functions; the only change in the equations is $\partial_\varphi^2 \to -n^2$.

The boundary conditions for the amplitude functions are similar to the ones used for the infinite plates in section 3.3: The normal displacement and the additional stresses shall approach 0 far outside the deformed region. In the present case, this means that we choose a sufficiently large $s_{\max}$, where we require $W(s_{\max}) = W'(s_{\max}) = 0$ and $\Phi(s_{\max}) = \Phi'(s_{\max}) = 0$. At the point $s = 0$, there are, in principle, no boundary conditions at all, since this is not a point on

a boundary. However, the point $s = 0$ causes problems, since some terms in the differential equations diverge here, for example the $1/r$ terms in (4.13). This problem is circumvented by choosing a suitable discretisation scheme (see appendix C.2) that is borrowed from the numerical methods for the Poisson equation in polar coordinates, where the same problems concerning divergences at $s = 0$ are encountered [81, 82, 123].

4.3.2. Results for the secondary buckling threshold

The discretisation that we use to transform the differential equations into a linear system is documented in appendix C.2. The solution is then represented by the values $W^{(i)} = W\big(s^{(i)}\big)$ and $\Phi^{(i)} = \Phi\big(s^{(i)}\big)$ of the amplitude functions evaluated on the grid $s^{(i)} = i \cdot h$, with $0 \leq i \leq N$ and a step size $h = s_{\max}/N$.

Since the linear system is homogeneous, see eq. (C.23) in the appendix, a non-trivial solution only exists if the determinant of the coefficient matrix vanishes. Thus, the stability equations turn out to be similar to an eigenvalue problem, as in the curved plate model, where the eigenvalue is "hidden" in the axisymmetric buckled shape. Plotting the determinant along the axisymmetric buckled branch, for example as a function of the pressure p, the determinant has a root at a critical pressure which is the onset of the wrinkling instability, see fig. 4.4 a). A similar procedure has been successfully applied to the unsymmetrical buckling of shallow shells [21, 66]. We use the pressure as the parameter to run through the branch of deflated shapes, because it directly enters the shape equations as a Lagrange multiplier. The branch consists of shapes which are unstable in experiments with prescribed pressure; however, these shapes are accessible in volume controlled experiments. The first root of the determinant functions occurs, in the example of fig. 4.4, for a wrinkle number $n = 6$ at approximately $p = -0.00107 E_{2\mathrm{D}}/R_0$, which corresponds to a volume reduction of $\Delta V/V_0 = 0.055$. These are the results for the critical wrinkle number, critical pressure and critical volume difference for the secondary buckling for the specific capsule of fig. 4.4.

At the critical volume, the stability equations have a non-trivial solution, which can easily be found by standard methods for linear systems. The resulting wrinkle amplitude $W(s)$, as the interpolation of the $W^{(i)}$ points, is plotted in fig. 4.4 b). We find qualitative agreement with the curved plate model (cf. figs. 3.13 and 4.3): The wrinkle amplitude has a prominent peak which is centred in the region of compressive hoop stress, and decays rapidly outside this region. In contrast to the curved plate model, the wrinkle amplitude is not symmetric with respect to its maximum; instead we observe an overshoot only in the outer region, and not towards the centre of the dimple. The most obvious difference in the three-dimensional views is the different wrinkle number, which will be discussed later.

Repeating the above procedure to calculate the critical volume of the secondary buckling for different $\tilde{E}_B$, we obtain a further line for the phase diagram fig. 4.5. For sufficiently small bending stiffness, $\tilde{E}_B < 10^{-5}$ in the present case, the data points can be fitted with a power law

$$\left.\frac{\Delta V_{2\mathrm{nd}}}{V_0}\right|_{\mathrm{DMV}} = 19000\, \tilde{E}_B^{1.11} \tag{4.15}$$

and are close to the previously generated secondary buckling line according to the curved plate model, see fig. 4.5. Only for too large bending stiffnesses, the data points deviate from the power law fit and the previous lines. This is due to the violation of the assumption that the characteristic length of the deformation is small compared to the radius of curvature, on which the DMV theory is based, but which is not justified for large dimples.

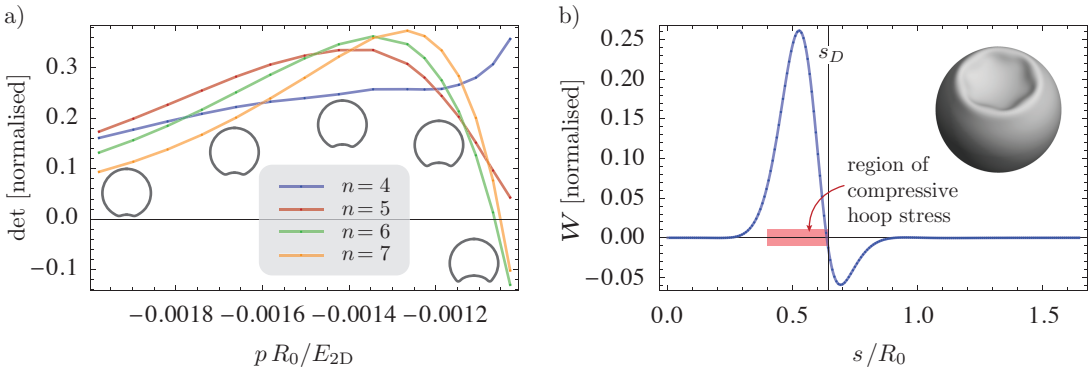

Figure 4.4.: Solution of the discretised stability equations for a shell with $\tilde{E}_B = 10^{-5}$ and $\nu = 1/3$. a) Normalised determinant of the coefficient matrix for different wrinkle numbers n for successively deflated, axisymmetric buckled shapes. b) Solution for the wrinkle amplitude W at the secondary buckling transition. The vertical line marks s_D, the position of the dimple edge where the curvature κ_s is at its maximum. The inset shows a three-dimensional view when this wrinkle profile is added as a normal displacement to the axisymmetric buckled shape.

4.4. Discussion of results

4.4.1. Complete phase diagram of deflated spherical shells

In the preceding chapters we have developed a fairly complete picture of the deflation of spherical shells. Our theory contains three phases of deflation: For small volume changes, the shell remains in a spherical shape, then jumps to an axisymmetric buckled configuration in a primary buckling transition, and finally undergoes a secondary buckling transition where the dimple loses its axisymmetry. We have obtained quantitative results for the critical volumes of both buckling transitions using different approaches, which are summarised in the "phase diagram" fig. 4.5. In addition, literature results for the secondary buckling transition, which are all based on numerical simulations, are shown [63, 112, 113]. For completeness, the line of auto-contact, where opposite sides of extremely deflated shells touch each other, is also shown [63].

The phase diagram fig. 4.5 is set up in the ΔV-$\tilde{E}_B$-plane and is valid for buckling under volume control. The Poisson ratio is an additional parameter, which is expected to have only a weak influence on the phase diagram, see ref. [112] for a discussion of this influence. In all calculations contributing to the phase diagram, it has been fixed to $\nu = 1/3$.

We will discuss the deflation behaviour of a spherical shell under volume control by following an imaginary vertical line in this phase diagram. Starting at the bottom, at small volume difference, there is only one possible shape for the shell: It is spherical, with a radius smaller than the initial radius. This trivial solution of the shape equations can be easily handled analytically, see section 2.4.1.

Upon deflation, the shell will cross the critical volume of first buckling, ΔV_{1st} (blue in fig. 4.5). From there on, there are two possible shell configurations: A spherical shape and an axisymmetric buckled shape. Of these shapes, the buckled one is stable and the spherical one metastable; or in other words, the buckled one stores less deformation energy than the spherical one as shown by the energy diagrams 2.10 in section 2.4.1. Thus, without external perturbations, the shell will remain spherical. However, it is also possible to indent the shell

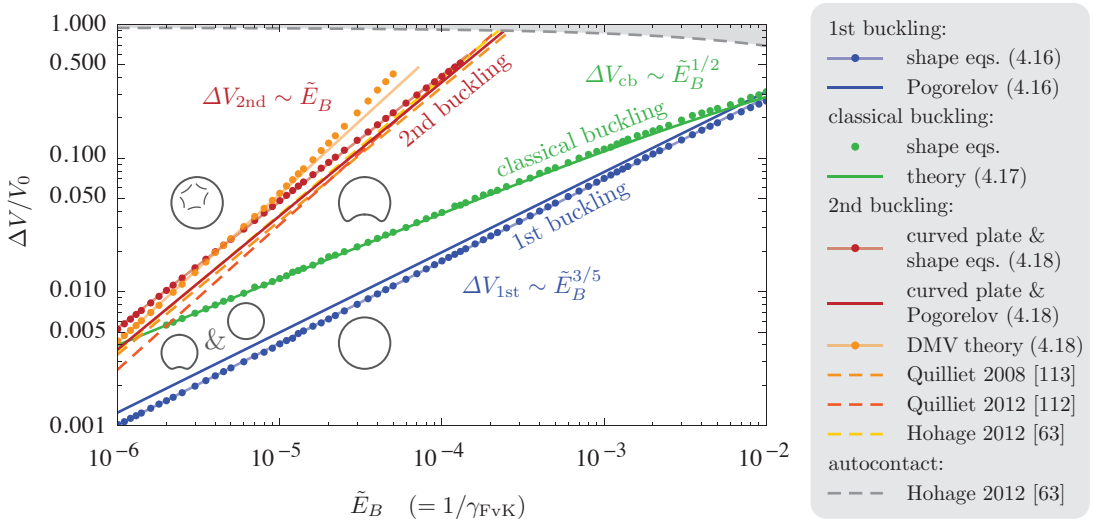

Figure 4.5.: Phase diagram of deflated spherical shells with Poisson ratio $\nu = 1/3$ and varying bending stiffness $\tilde{E}_B$ (which is related to the Föppl-von-Kármán-number $\gamma_{\mathrm{FvK}} = 1/\tilde{E}_B$). Dots represent results derived from numerical solutions of the axisymmetric shape equations, continuous semi-transparent lines (blue, red, orange) fits to those data points, solid lines (blue, green, red) analytic results, and dashed lines results from numerical simulations. The legend to the right indicates the appropriate equation numbers or literature references.

manually, and the dimple will remain on the shell. Thermal fluctuations or imperfections in the geometry or material, as they are inherent to real shells, may also cause a sudden transition to the dimpled shape, although the spherical shape is theoretically (meta)stable. The critical volume difference $\Delta V_{1\mathrm{st}}$ of the first buckling has been calculated analytically for the Pogorelov model, see eq. (2.50) and the blue solid line in the phase diagram. The blue data points from the shape equations can be fitted with a power law (semi-transparent blue line). Both results coincide very well,

$$\left.\frac{\Delta V_{1\mathrm{st}}}{V_0}\right|_{\mathrm{Pog}} = 6 J_{\mathrm{min}}^{4/5} \frac{(1-\nu)^{4/5}}{(1-\nu^2)^{1/5}} \tilde{E}_B^{3/5} \qquad \text{and} \qquad \left.\frac{\Delta V_{1\mathrm{st}}}{V_0}\right|_{\text{shape eqs.}} = 4.78\, \tilde{E}_B^{0.61} \tag{4.16}$$

(the numerical prefactor of the Pogorelov result evaluates to 4.97 for $\nu = 1/3$).

Deflating the shell further, we will cross the line of classical buckling (green in fig. 4.5). At this critical volume difference ΔV_{cb}, the spherical configuration becomes unstable, and thus the shell must buckle. In eq. (2.49) we derived the classical buckling volume,

$$\frac{\Delta V_{\mathrm{cb}}}{V_0} = 1 - \left(\frac{1}{2} + \sqrt{\frac{1}{4} + 2(1-\nu)\sqrt{\tilde{E}_B}}\right)^{-3} \approx 6(1-\nu)\sqrt{\tilde{E}_B}. \tag{4.17}$$

The exact version of this result is plotted as the solid green line in the phase diagram.

The transition from the spherical to the axisymmetric buckled shape is a discontinuous transition as our considerations in section 2.4.1 have shown: The dimple will have a finite size when it is formed; shapes with infinitesimal dimples are energy maxima lying above the energy of the spherical branch and represent a possible transition state at the discontinuous transition [152].

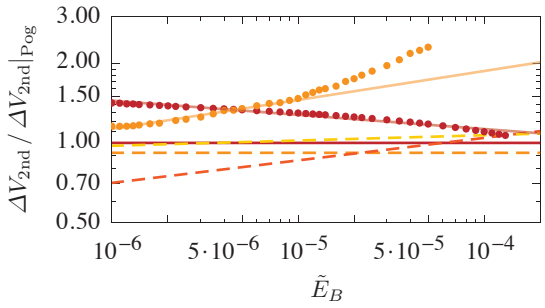

Figure 4.6.: The secondary buckling lines, normalised by the secondary buckling volume of the Pogorelov model. For the legend, see fig. 4.5.

When we cross the line of secondary buckling at ΔV_{2nd}, the axisymmetric buckled shape will lose its stability with respect to non-axisymmetric deformations. Due to a region of strong hoop compression in the inner neighbourhood of the dimple edge, circumferential wrinkles will appear in this region and the dimple acquires a polygonal shape. In the range of $\tilde{E}_B$ investigated here, the buckled shape is axisymmetric at first; but extrapolating the lines to smaller $\tilde{E}_B$ suggests that this will not be the case for very small $\tilde{E}_B$.

We calculated the line of this secondary buckling transition via three different routes: (i) Deriving a wrinkling criterion for a curved rectangular plate and applying this criterion to the numerical results of the axisymmetric shape equations, (ii) applying the same criterion to the approximate analytical results in the framework of the Pogorelov model, and (iii) by a linear stability analysis of the full form in the framework of the DMV shell theory. Variants (i) and (iii) are plotted in the phase diagram as red and orange data points, respectively, with fitted power laws (4.3) and (4.15) as semi-transparent lines. Variant (ii) led to the analytic result (4.9) and is plotted as a solid red line. For convenience, we repeat the results (i) - (iii) here,

$$\left.\frac{\Delta V_{2nd}}{V_0}\right|_{\text{shape eqs.}} = 2552\,\tilde{E}_B^{0.95}, \quad \left.\frac{\Delta V_{2nd}}{V_0}\right|_{\text{Pog}} = 3706\,\tilde{E}_B, \quad \text{and} \quad \left.\frac{\Delta V_{2nd}}{V_0}\right|_{\text{DMV}} = 19000\,\tilde{E}_B^{1.11}. \tag{4.18}$$

The apparent mismatch of the numerical prefactors is compensated by the slightly different exponents, so that all three approaches agree well within the regimes of their respective validity, see fig. 4.5. Literature results for the secondary buckling line, based on simulations with the program Surface Evolver [112, 113] or a bead-spring model for a triangulated sphere [63], are also in good agreement with our findings. They are plotted in the phase diagram as dashed lines by their power laws

$$\Delta V_{2nd}/V_0 = 3400\,\tilde{E}_B \qquad \text{from ref. [113]} \tag{4.19}$$

$$\Delta V_{2nd}/V_0 = 8470\,\tilde{E}_B^{1.085} \qquad \text{from ref. [112]} \tag{4.20}$$

$$\Delta V_{2nd}/V_0 = 4764\,\tilde{E}_B^{1.020} \qquad \text{from ref. [63],} \tag{4.21}$$

as obtained from fitting the simulation results.

In fact, the different secondary buckling lines are so close that some of them cannot be distinguished. To resolve the differences, we "normalise" the secondary buckling lines by the line of the Pogorelov model in the sense of plotting

$$\frac{\Delta V_{2nd}|_i}{\Delta V_{2nd}|_{\text{Pog}}} \tag{4.22}$$

for each line i as a function of $\tilde{E}_B$ in fig. 4.6. This plot shows that the secondary buckling volume differences obtained in numerical simulations (dashed lines) are typically smaller than

our results, which might be due to the fact that the simulated shells are imperfect because of the triangulation. Furthermore, this plot illustrates that the stability analysis of the full form in DMV theory (orange data points and fit) is in very good agreement with the linear $\tilde{E}_B$ dependence from the Pogorelov model for small $\tilde{E}_B$, but deviates for larger $\tilde{E}_B$. The reason is, as mentioned before, that for large $\tilde{E}_B$ the dimple grows too large before the secondary buckling, so that the DMV theory is inaccurate. Indeed, fitting only the seven data points with smallest bending stiffness $\tilde{E}_B < 2 \cdot 10^{-6}$ results in $\Delta V_{2\mathrm{nd}}|_{\mathrm{DMV}} \sim \tilde{E}_B^{1.05}$ with an exponent very close to the analytic exponent 1.

4.4.2. Number of wrinkles in secondary buckling

The most eye-catching feature of shells beyond the secondary buckling transition is the number of wrinkles, or the number of edges in the polygonal dimple. Although the different approaches agree fairly well concerning the critical volume of secondary buckling, their predictions of the number of wrinkles at the onset of secondary buckling show substantial differences, see fig. 4.7.

In applying the critical wavelength (3.58) of the curved plate model to the axisymmetric shapes of the Pogorelov model, we have seen in (4.11) that the wrinkle number seems to be fixed at $n \approx 8.6$, independently of the bending stiffness (see red line in fig. 4.7). Applying the curved plate result (3.58) to the shape equations (red data points), we observe a slight decrease in the wrinkle number for increasing bending stiffness. In contrast, the wrinkle number in the DMV theory (orange data points) slightly increases with increasing bending stiffness.

The question whether the wrinkle number *at the onset* of the secondary buckling should depend on $\tilde{E}_B$ is difficult to answer from intuition, because there are two opposing effects at work: On the one hand, we expect the wrinkle wavelength λ to become smaller for smaller bending stiffness; but on the other hand, the dimple size r_D at the onset of the secondary buckling also becomes smaller (see the phase diagram, fig. 4.5). The number of wrinkles is $n = 2\pi r_D/\lambda$, and we have seen by the scaling laws at the beginning of section 4.2.2 that both effects cancel out. If there are significant variations of the wrinkle number at the onset, the dependence on $\tilde{E}_B$ comes from subtle effects, e.g. the detailed geometry. This possibly explains why our different approximate models, which all have their flaws, predict slightly different results.

Comparison with previous simulation results is difficult since most results are given for highly deflated shells, and not at the onset of secondary buckling. In ref. [113], four different deflation trajectories are reported, from $\tilde{E}_B \approx 9 \cdot 10^{-6}$ to 10^{-4}. They all exhibit 5 wrinkles at the onset, except the one with smallest $\tilde{E}_B$, which starts to wrinkle with 6 wrinkles. This affirms that the wrinkle number at the onset is quite unaffected by the bending stiffness.

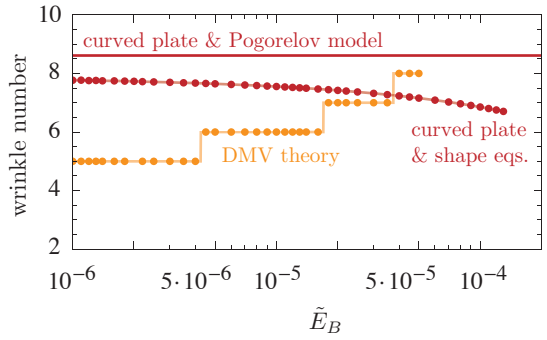

Figure 4.7.: Number of wrinkles at the onset of secondary buckling. The red data points represent the result (3.58) from the curved plate model applied to the shape equations, the red line shows the constant wrinkle number $n = 8.6$ as obtained in (4.11), and the orange data points represent the results from the DMV theory.

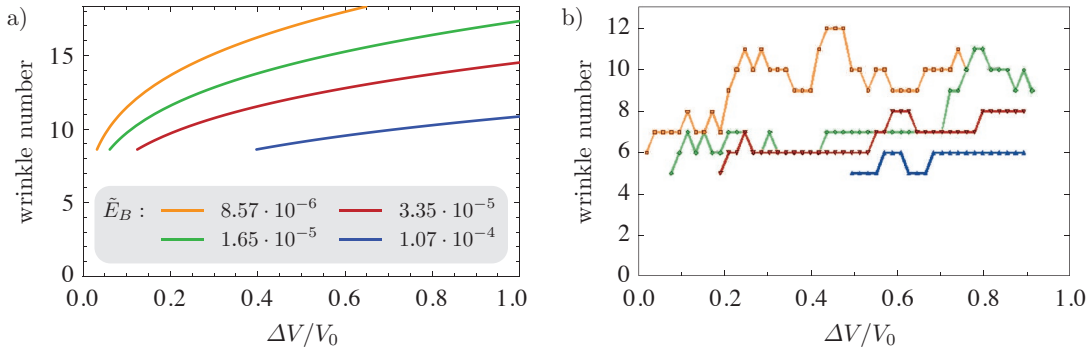

Figure 4.8.: Volume dependence of the wrinkle number. a) Our analytic result (4.24) from the Pogorelov model and curved plate criterion, plotted for different bending stiffnesses as indicated. b) Surface Evolver simulations with the same bending stiffnesses; image adapted from ref. [113].

We can get a first idea of the volume dependence of the wrinkle number by considering the Pogorelov model and the curved plate criterion for wrinkling. In the analysis of the Pogorelov model we have seen that the parameter a_p is independent of the volume, see (4.5). Since $1/\sqrt{a_p}$ determines the width of the compressive region, and the wavelength is of the same order as this width, we can expect that the wavelength of the wrinkles stays approximately constant when the shell volume is further decreased. Therefore, the change of the wrinkle number with further deflation can primarily be attributed to the change of the perimeter $2\pi r_D$ along which the wrinkles are distributed. The change of r_D with ΔV is of purely geometric nature, according to (2.28) and (2.38)

$$r_D \approx \left(\frac{8}{3}\right)^{1/4} \left(\frac{\Delta V}{V_0}\right)^{1/4} R_0. \tag{4.23}$$

Together with the critical wavelength λ_c from (4.10) we thus obtain the volume-dependent wrinkle number

$$n(\Delta V) = \frac{2\pi r_D}{\lambda_c} = 2\pi \left(\frac{8}{3}\right)^{1/4} \frac{\sqrt{\bar{a}_p}}{\hat{\lambda}_c} \left(\frac{\Delta V}{V_0} \frac{1}{\tilde{E}_B(1-\nu^2)}\right)^{1/4} \approx 1.1 \cdot \left(\frac{\Delta V}{V_0} \frac{1}{\tilde{E}_B}\right)^{1/4}. \tag{4.24}$$

In the last step, all numerical constants (with $\nu = 1/3$) have been reduced to the single numerical prefactor. This relation is, of course, only valid beyond the secondary buckling threshold, i.e. for $\Delta V/V_0 \geq \Delta V_{2\mathrm{nd}}/V_0 = 3706\tilde{E}_B$.

Figure 4.8 a) shows the volume dependence of the wrinkle number for different values of the reduced bending stiffness. After the onset with $n = 8.6$, the wrinkle number increases with increasing deflation. This is in qualitative agreement with the simulation results presented in ref. [113] which are shown in fig. 4.8 b) for comparison. There are quantitative differences concerning the wrinkle number at the onset (5 to 6 in the simulations, and 8 to 9 in our prediction) and how fast the wrinkle number increases after the onset.

Of course, the deviations could be attributed to the crude approximations made in our calculation, but there is also some dubiety about the simulations. The oscillations, especially in the orange curve in fig. 4.8 b), are very peculiar and probably artifacts caused by the energy minimisation algorithm being trapped in local minima. Later reports of similar Surface Evolver simulations [112] show a slightly different behaviour than depicted above: There, the wrinkle number initially decreases before increasing again with proceeding deflation. Furthermore, in

simulations carried out in our group [63, 140] we observed that the number of wrinkles depends sensitively on the triangulation, specifically on the position and type of disclinations.

We can conclude that neither our theory nor the numerical simulations from the literature are able to produce consistent results concerning the wrinkle number. It seems that this most striking feature of the secondary buckled shapes is governed by subtle effects and prone to perturbances.

Chapter 5

Deflation of pendant and rising capsules

Abstract – Elastic capsules that are prepared from droplets or bubbles attached to a capillary can be deflated by suction through the capillary. In the following chapter we study this deflation and show that a combined analysis of the shape and wrinkling characteristics can find the elastic properties of the capsule membrane. For the shape analysis, an elastic model based on the previously introduced theory of shells of revolution is developed which incorporates the wrinkles that typically form upon deflation. Fitting the solutions of these shape equations to the experimental images gives the surface Young modulus and surface Poisson ratio of the membrane. Analysing the wavelength of the wrinkles then gives its bending stiffness. This concept is first tested with theoretically generated shapes to fit, and then applied to two experiments with polysiloxane capsules and hydrophobin coated bubbles.
Published material – Large parts of this chapter are reproduced with modifications from the author's publication [154], with permission of Langmuir, © 2013 American Chemical Society. The theory of sections 5.2.1 and 5.2.2 is already contained in the author's diploma thesis [151].

5.1. Introduction

So far, we have mainly considered spherical shells in this thesis. In the forthcoming chapter we turn to a setup that is less trivial, but frequently used by researchers that synthesise elastic membranes by interfacial reactions: pendant drops or rather pendant capsules. The typical experiment in this setup is sketched in fig. 5.1. It starts with a liquid drop hanging in another fluid, for example a water drop in oil. Alternatively, if the drop has a smaller density than the bulk liquid, the experiment can be performed upside down using a J-shaped needle, resulting in a rising capsule, for example an air bubble in water. By adding appropriate chemicals to the bulk phase, an interfacial reaction can enclose the droplet with an elastic membrane, thus producing a pendant capsule with the shape of the drop. The elastic properties of the shell can be probed by provoking a deformation, for example by suction of the inner liquid through the capillary.

The instrumentation to perform and monitor this type of experiments is well developed and commercially available. Pendant drop apparatuses come with an electronic control of the syringe that allows precise control of the droplet's volume, and they contain a digital camera to image the shape of the pendant capsule. They are usually used for pendant drop tensiometry, a method to determine the interfacial tension between the two liquids by analysing the shape of the drop.

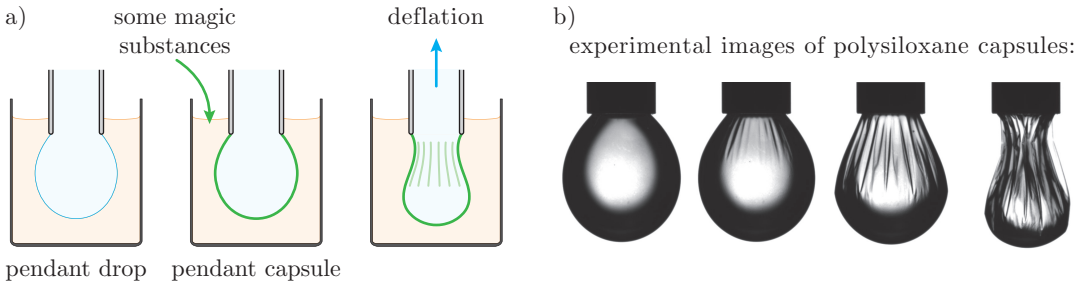

Figure 5.1.: A typical pendant capsule experiment. a) From a drop hanging from a capillary, a pendant capsule is created by an interfacial reaction. This elastic capsule can be deformed to probe its elastic properties, for example by suction through the capillary. In this case, it typically wrinkles, as indicated by the lines. b) Experimental realisation with polysiloxane capsules.

Because of the simplicity of this procedure, various membrane materials have been studied in this geometry [1, 36, 37, 42, 68, 119]. So far, the analysis of those experiments was based on the pendant drop tensiometry [2, 38, 115, 120], which is, however, only valid for liquid/liquid-interfaces. This technique neglects the elastic stresses within the capsule membrane [25, 44], and is therefore not valid for the analysis of pendant capsules. We show below that conclusions about the elastic moduli of the membrane derived from this kind of analysis are more erroneous than intuitively expected.

Inspired by the pendant drop tensiometry, our aim for this chapter is to develop a method of *pendant capsule elastometry*: an analysis tool to infer the elastic properties of a pendant capsule by analysing its shape upon deflation. To this end, a theoretical model based on the shape equations for shells of revolution is developed. Since the membranes in these experiments are typically very thin [114], the influence of the bending stiffness on the shape is negligible, which leads to simpler shape equations than those of section 2.2. However, we must take into account that wrinkles appear upon deflation as a consequence of compressive hoop stresses. Solutions of this elastic model can then be fitted to contours extracted from experimental images, with the surface Young modulus E_{2D} and surface Poisson ratio ν as fit parameters. As the bending modulus E_B has negligible influence on the capsule shape, its value cannot be determined from the fit of the contour. Instead, we can analyse the wavelength of the wrinkles which depends on E_B as seen in eq. (3.36) for example.

This combined approach enables us to determine all elastic constants of individual capsules from an image analysis, thus offering a valuable alternative to other methods that have been developed for the mechanical characterisation of single capsules, see refs. [46, 86] for recent reviews. Most often, these methods involve contact between the capsule and a probe such as an AFM (atomic force microscope) tip [3, 54, 132]. There are other methods, like interfacial shear rheometry [17, 68] and Langmuir troughs [105, 119, 136], that work with planar films instead of capsules. Our approach is a non-contact method that works with capsules that have a geometry similar to those used in applications in pharmacy or industry. Conceptually, it is comparable to methods like shape analysis in shear flow [8, 28, 139] and spinning drop rheometry [106] developed by Barthès-Biesel.

In a proof of concept study, this new method is applied to two very different capsule materials: polymerised octadecyltrichlorosilane (OTS) capsules and hydrophobin (HFBII) coated bubbles. The results for HFBII indicate a very non-linear elastic behaviour. To model this non-linear elasticity, a new material model is developed, based on the microscopic view of hard-core beads that are connected with soft springs.

5.2. Elastic model for pendant capsules

5.2.1. The Laplace-Young equation for the reference shape

A capsule that is synthesised in the experiment sketched in fig. 5.1 has the shape of a pendant drop in its undeformed state. If the interior and exterior liquids are not density matched, the shape of the drop is not exactly spherical but elongated by gravity, and can be described by the Laplace-Young equation [84], which expresses a balance between gravity and the interfacial tension γ between the two liquids.

The interfacial tension is a parameter which describes how much energy $\mathrm{d}U$ is required to enlarge the interface between the two liquids by an area $\mathrm{d}A$; it is defined as $\gamma = \mathrm{d}U/\mathrm{d}A$. Its value depends on the two fluids that are in contact at the interface, for an air/water-interface, for example, the interfacial tension is 72.5 mN/m at room temperature [84]. As a physical system tries to minimise its energy, the surface tension tends to contract the interface to the smallest possible shape compatible with the boundary conditions or volume constraints. For this reason, droplets are spherical in the absence of gravity: Of all geometric bodies, the sphere has the least surface area for given volume. The tendency to contract the droplet surface also leads to a higher internal pressure, in the same fashion as if the droplet was enclosed with a uniformly stretched rubber membrane. The important difference between an elastic sheet and a liquid interface is that in an elastic membrane, neighbouring molecules are linked and have to stay neighbours during the deformation, whereas the liquid interface can be reorganised easily, i.e. the molecules can flow past each other. Elastic tensions develop as a consequence of strain that alters the distance between neighbouring molecules, but the liquid-liquid surface tension is independent of local strains. Furthermore, there cannot be shear stresses in the liquid/liquid-interface because the molecules in the interface are free to flow and change neighbourhoods. The stress tensor of the fluid interface is thus diagonal, and both principal stresses equal γ.

To determine the shape of a pendant drop, we use the same notation for the geometry and parametrisation of the axisymmetric surface as introduced in section 2.2.1, with an index 0 indicating that we are currently dealing with the reference shape of the capsule to-be, see fig. 5.2 a). Then the Laplace-Young equation reads

$$\gamma\,(\kappa_{s_0} + \kappa_{\varphi_0}) = p_0 - \Delta\rho\, g\, z_0, \tag{5.1}$$

where $\Delta\rho$ is the density difference of inner and outer fluid, $g = 9.81\,\mathrm{m/s^2}$ the acceleration of gravity and p_0 the pressure inside the drop at the position $z_0 = 0$. It can be obtained from the general equilibrium equation of the normal forces for shells of revolution, first of eqs. (2.16), by setting $\tau_s = \tau_\varphi = \gamma$, $q = 0$ and $p = p_0 - \Delta\rho\, g\, z_0$.

With the geometric relations for the axisymmetric surface, see sec. 2.2.1, the Laplace-Young equation is a differential equation and can also be written in the first-order system

$$\begin{aligned} r_0'(s_0) &= \cos\psi_0 \\ z_0'(s_0) &= \sin\psi_0 \\ \psi_0'(s_0) &= \frac{1}{\gamma}(p_0 - \Delta\rho\, g\, z_0) - \frac{\sin\psi_0}{r_0}\,. \end{aligned} \tag{5.2}$$

For the numerical solution, boundary conditions must be specified. The arc length coordinate s_0 runs from the apex ($s_0 = 0$) to the capillary ($s_0 = L_0$ with a not yet specified contour length L_0). From the geometry of the drop, it is clear that $r_0(0) = z_0(0) = \psi_0(0) = 0$ and $r_0(L_0) = a/2$, where a is the capillary diameter on which the upper rim of the droplet is fixed. The choice $z_0 = 0$ is arbitrary, because the system (5.2) exhibits a translational symmetry along

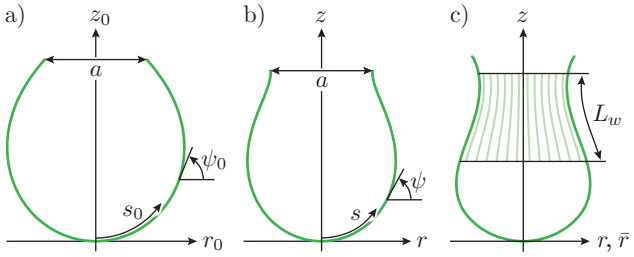

Figure 5.2.: Arc-length parametrisations in cylindrical coordinates of the undeformed $(r_0(s_0), z_0(s_0))$, deformed $(r(s), z(s))$ and the wrinkled midsurface. The wrinkled region of length L_w is described by an axisymmetric pseudo-surface around which the real midsurface oscillates.

the z_0-axis: It is invariant under the substitutions $z_0 = z_0^* + c$ and $p_0 = p_0^* + \Delta\rho\, g\, c$. Using a shooting method, the system (5.2) can be solved in order to obtain the drop shape. The shooting parameter that can be adjusted to satisfy the boundary condition at the upper rim of the drop is the contour length L_0. For a liquid drop, this length is not fixed a priori.

Similar to the elastic shape equations for spherical shells, the system is ill-defined at $s_0 = 0$: The fraction $\sin\psi_0/r_0$ is of the type "0/0". It can be evaluated using L'Hôpital's rule,

$$\lim_{s_0\to 0} \frac{\sin\psi_0}{r_0} = \lim_{s_0\to 0} \frac{\psi_0'(s_0)\cos\psi_0}{\cos\psi_0} = \psi_0'(0). \tag{5.3}$$

The last equation of the system (5.2) thus simplifies to $\psi_0'(0) = p_0/2\gamma$ at the starting point of integration.

We introduce dimensionless quantities for the numerics by choosing the surface tension γ as the tension unit and the capillary diameter a as the length unit. The resulting dimensionless variables and parameters, indicated by a tilde, are summarised in table 5.1 below. The dimensionless system of shape equations then reads $\tilde{r}_0'(\tilde{s}_0) = \cos\psi_0$, $\tilde{z}_0'(\tilde{s}_0) = \sin\psi_0$ and $\psi_0'(\tilde{s}_0) = \tilde{p}_0 - \tilde{\rho}\,\tilde{z}_0 - \sin\psi_0/\tilde{r}_0$. The only two parameters occurring in this system are the reduced pressure $\tilde{p}_0 = a\,p_0/\gamma$ and the reduced density difference $\tilde{\rho} = a^2\,\Delta\rho\, g/\gamma$. While the density parameter determines if the drop is rather spherical (small $\tilde{\rho}$) or elongated (large $\tilde{\rho}$), the pressure influences the volume of the resulting drop, which can be calculated by numerical integration (see (2.14)) as

$$V = \int \pi\, r_0^2\, \mathrm{d}z_0 = \int_0^{L_0} \pi\, r_0^2\, \sin\psi_0\, \mathrm{d}s_0. \tag{5.4}$$

5.2.2. Elastic shape equations

With a solution of the Laplace-Young equation, we have a parametrisation $(r_0(s_0), z_0(s_0))$ of the reference configuration, which is assumed to be free of elastic stresses because the membrane has been synthesised in this shape. We neglect the weight of the membrane because it is very thin, so that only the density difference between inner and outer fluid gives rise to gravitational effects in form of a hydrostatic pressure $p - \Delta\rho\, g\, z$ that is exerted on the capsule membrane. In the reference configuration, this pressure is still $p_0 - \Delta\rho\, g\, z_0$ as in the case of the pendant drop; and it must be balanced so that the capsule can keep its reference shape. We therefore assume that the interfacial tension γ continues to act in the interfacial layer, although the two liquids are now separated by the elastic membrane. The reason for this is that there are now two solid/liquid-interfaces which also give rise to an interfacial tension. During the creation process of the elastic membrane, it is often observed that the measured interfacial tension of the drop decreases as a function of time, because the molecules that attach to the interface in order to

build up a membrane act as surfactants, but eventually approaches a steady value [1, 5, 68, 119]. We can interpret this decrease of the interfacial tension as the crossover between the liquid-liquid interfacial tension before the reaction and the liquid-solid interfacial tension after the capsule creation is completed.

Therefore, the stress-strain relations (2.10) of the elasticity theory of axisymmetric shells must be extended to account for an additional, constant surface tension γ. At the same time, we can neglect the bending stiffness because the capsule walls are very thin [151]. This approximation of shell theory is also called membrane theory [89], and can be applied if the deformation of the capsule is not close to an isometric deformation as in the case of buckled spherical shells, but dominated by stretching. The resulting surface energy density for our capsule model thus reads

$$w_S(\lambda_s, \lambda_\varphi) = \frac{1}{2}\frac{E_{2D}}{1-\nu^2}\left[(\lambda_s-1)^2 + 2\nu(\lambda_s-1)(\lambda_\varphi-1) + (\lambda_\varphi-1)^2\right] + \lambda_s\lambda_\varphi\gamma. \tag{5.5}$$

Recall from section 2.2.1 that the meridional and circumferential stretches are defined as $\lambda_s = \mathrm{d}s/\mathrm{d}s_0$ and $\lambda_\varphi = r/r_0$ for a deformation from (r_0, z_0) to (r, z), see fig. 5.2 a) and b). The term $\lambda_s\lambda_\varphi\gamma$ accounts for the energy change according to the basic definition of the surface tension, $\gamma = \mathrm{d}U/\mathrm{d}A$. With eq. (5.5), the energy change of a small membrane element can be calculated as $\mathrm{d}U = w_S\,\mathrm{d}A_0 = \gamma\,\mathrm{d}A + \text{elastic terms}$ because $\mathrm{d}A = \lambda_s\lambda_\varphi\,\mathrm{d}A_0$.

According to the constitutive relations (2.10) we now obtain

$$\tau_s = \frac{1}{\lambda_\varphi}\frac{\partial w_S}{\partial \lambda_s} = \frac{E_{2D}}{1-\nu^2}\frac{1}{\lambda_\varphi}\left[(\lambda_s-1) + \nu(\lambda_\varphi-1)\right] + \gamma \tag{5.6}$$

for the meridional stress, and the same with indices s and φ interchanged for the circumferential stress τ_φ. In the undeformed configuration, where $\lambda_s = \lambda_\varphi = 1$, the membrane is in the same stress state as the liquid drop has been before, $\tau_s = \tau_\varphi = \gamma$, as required for equilibrium. The approach of incorporating the interfacial tension γ into the stress-strain relations has been developed in the author's diploma thesis from 2011 [151], and independently from this by Carvajal et. al. [25] in 2011 and Ferri et. al. [44] in 2012.

Due to the vanishing bending stiffness and bending moments, the equilibrium equations for shells of revolution (2.16) simplify considerably. By the last of eqs. (2.16), the vanishing bending moments imply that the transverse shear tension q also vanishes. Hence the shape equations (2.17) reduce to only four first order differential equations,

$$\begin{aligned} r'(s_0) &= \lambda_s\cos\psi, & \psi'(s_0) &= \frac{\lambda_s}{\tau_s}(p - \Delta\rho\, g\, z - \kappa_\varphi\tau_\varphi), \\ z'(s_0) &= \lambda_s\sin\psi, & \tau_s'(s_0) &= \lambda_s\frac{\tau_\varphi - \tau_s}{r}\cos\psi. \end{aligned} \tag{5.7}$$

Analogous to section 2.2, all quantities appearing on the right hand sides must be expressed in terms of the basic functions r, z, ψ and τ_s with the help of geometric relations, see sec. 2.2.1, and the constitutive relations (5.6). The equations

$$\begin{aligned} \lambda_\varphi &= \frac{r}{r_0}, & \lambda_s &= \frac{1-\nu^2}{E_{2D}}\lambda_\varphi\left(\tau_s - \gamma\right) - \nu(\lambda_\varphi - 1) + 1, \\ \kappa_\varphi &= \frac{\sin\psi}{r}, & \tau_\varphi &= \frac{E_{2D}}{1-\nu^2}\frac{1}{\lambda_s}\big((\lambda_\varphi - 1) + \nu\left(\lambda_s - 1\right)\big) + \gamma \end{aligned} \tag{5.8}$$

close the system (5.7) of shape equations.

lengths, volumes and curvatures	pressure, density and energy
$\tilde{r} = r/a, \quad \tilde{z} = z/a$ $\tilde{V} = V/a^3, \quad \tilde{\kappa}_i = a\,\kappa_i$	$\tilde{p} = a\,p/\gamma, \quad \tilde{\rho} = a^2\,\Delta\rho\,g/\gamma$ $\tilde{U} = U/\gamma\,a^2$
tensions	elastic modulus
$\tilde{\tau}_i = \tau_i/\gamma, \quad \tilde{\gamma} = 1$	$\tilde{E}_{2\mathrm{D}} = E_{2\mathrm{D}}/\gamma$

Table 5.1.: Overview of reduced variables for pendant capsules (indices $i \in \{s, \varphi\}$). Adapted from the author's diploma thesis [151].

The boundary conditions for the system of differential equations are obvious from geometry: At the upper rim they must fix the capsule radius to the radius $a/2$ of the capillary, and at the apex they must ensure that the capsule is closed and smooth. These conditions read

$$r(0) = z(0) = \psi(0) = 0 \quad \text{and} \quad r(L_0) = a/2, \tag{5.9}$$

where the choice $z(0) = 0$ is justified by the same argument as for the Laplace-Young equation. We thus have four boundary conditions for four first-order differential equations, which is appropriate.

There are again problems with ill-defined terms at the start point $s_0 = 0$ of integration, which can be solved by L'Hôpital's rule and symmetry arguments as for the shape equations of spherical shells, see appendix A.2. The results can be easily transferred from the spherical shells to pendant capsules, and we get at $s_0 = 0$

$$\lambda_s = \lambda_\varphi = \frac{E_{2\mathrm{D}}}{E_{2\mathrm{D}} - (\tau_s - \gamma)(1-\nu)}, \quad \psi' = \frac{1}{2} p \frac{\lambda_s}{\tau_s} \quad \text{and} \quad \tau_s' = 0. \tag{5.10}$$

A shooting method as already used for spherical shells can solve the shape equations. For the nondimensionalisation we choose the equilibrium surface tension γ as the tension unit and the capillary diameter a as the length unit. Setting γ and a to 1 and replacing dimensional quantities by their dimensionless variants as summarised in table 5.1 leads to shape equations that are ready to be solved numerically.

5.2.3. Wrinkling and modified shape equations

The theory of pendant capsules presented so far has already been developed in the author's diploma thesis [151]. However, it is not suitable for the application to experiments, because wrinkles appear on the deflated capsule most often, see fig. 5.1 for example. The reason for the wrinkling is the same as discussed throughout chapter 3: A negative stress. Indeed, numerical solutions of the shape equations (5.7) show that there are regions of negative hoop stress $\tau_\varphi < 0$. Note that to obtain $\tau_\varphi < 0$, the compressive elastic contribution to the stress must be larger in magnitude than the isotropic surface tension γ, see eq. (5.6).

A membrane with small bending modulus cannot support compressive stresses, instead, it will wrinkle [13, 34, 75, 130]. As our membrane is modelled with vanishing bending stiffness, its critical compressive stress for wrinkling is $\tau_\varphi = 0$. This value is a lower bound for the $\tau_\varphi(s_0)$ function. For real membranes with a small but finite bending stiffness E_B, the lower bound is a small negative value $\tau_{\varphi,c} \sim -\sqrt{E_B \tau_s / L_w^2}$, with τ_s the (positive) meridional stress and L_w the wrinkle length. This formula is taken from eq. (3.37) and was derived for flat plates,

but we show in the next section that the behaviour of pendant capsules is the same if the wrinkle wavelength is small compared to the radius of curvature. As τ_s is of the order of γ and the bending stiffness scales like $E_B \sim E_{2\mathrm{D}} H_0^2$, see eq. (2.9), the dimensionless critical value reads $\tilde{\tau}_{\varphi,c} \sim -\sqrt{\tilde{E}_{2\mathrm{D}}} H_0/L_w$. Whereas the membrane thickness H_0 is of the order of micro- to nanometres, the wrinkle length is around one millimetre in typical experiments. Thus the nondimensionalised critical compression is only of the order 10^{-6} to 10^{-3}. Setting it to zero is, thus, a good approximation.

A way to respect this lower bound for $\tau_\varphi(s_0)$ is to allow the real midsurface of the capsule to oscillate around an axisymmetric *pseudo-surface*, see fig. 5.2 c). We denote quantities referring to this pseudo-surface and differing from the real midsurface with an overbar, so $(\bar{r}(s_0), z(s_0))$ is its shape which we are seeking. The shape equations for the axisymmetric pseudo-surface are determined by setting $\tau_\varphi = 0$ in areas where the original model would yield $\tau_\varphi < 0$ [89].

According to Hooke's law (5.6), the wrinkling condition $\tau_\varphi < 0$ is equivalent to

$$\lambda_\varphi < 1 - \gamma \frac{1-\nu^2}{E_{2\mathrm{D}}} \lambda_s - \nu(\lambda_s - 1). \tag{5.11}$$

At the point where λ_φ falls below this threshold during the numeric integration of the normal shape equations (5.7), we switch to a modified system of shape equations to continue the integration. This system describes the pseudo-surface and is mainly determined by setting $\tau_\varphi = 0$ in the wrinkling domain, i.e.

$$\lambda_\varphi = 1 - \gamma \frac{1-\nu^2}{E_{2\mathrm{D}}} \lambda_s - \nu(\lambda_s - 1). \tag{5.12}$$

Note that λ_φ is the hoop stretch of the real, wrinkled midsurface and is not to be confused with the stretch $\bar{\lambda}_\varphi = \bar{r}/r_0$ of the pseudo-surface.

In order to eliminate the hoop stretch of the real midsurface from our system of equations, we insert this expression (5.12) into the constitutive relation (5.6) for the meridional tension,

$$\tau_s = E_{2\mathrm{D}} \frac{1}{\lambda_\varphi} \left[(\lambda_s - 1) - \frac{\nu\gamma}{E_{2\mathrm{D}}} \lambda_s \right] + \gamma. \tag{5.13}$$

However, this tension is not suitable for considering the force balance of the pseudo-surface since it is measured per unit length of the wrinkled, non-axisymmetric midsurface. In order to adopt the simple axisymmetric force balance for the pseudo-surface, we have to measure the tension per unit length of the pseudo-surface [89], $\bar{\tau}_s = \tau_s \lambda_\varphi / \bar{\lambda}_\varphi$, resulting in

$$\bar{\tau}_s = \frac{1}{\bar{\lambda}_\varphi} \Big[\lambda_s \Big(E_{2\mathrm{D}} - 2\nu\gamma - \gamma^2 \frac{1-\nu^2}{E_{2\mathrm{D}}} \Big) - E_{2\mathrm{D}} + \gamma(1+\nu) \Big]. \tag{5.14}$$

The shape equations for the pseudo-surface are obtained by modifying the original shape equations (5.7) and (5.8). The necessary changes are to mark r, λ_φ and τ_s with an overbar, because they are different for the real midsurface and pseudo-surface, and to replace the constitutive relations for the stresses by (5.14) and $\tau_\varphi = 0$, which results in

$$\begin{aligned} \bar{r}'(s_0) &= \lambda_s \cos\psi, & \psi'(s_0) &= \frac{\lambda_s}{\bar{\tau}_s} (p - \Delta\rho\, g\, z), \\ z'(s_0) &= \lambda_s \sin\psi, & \bar{\tau}_s'(s_0) &= -\lambda_s \frac{\bar{\tau}_s}{\bar{r}} \cos\psi \end{aligned} \tag{5.15}$$

for the system of differential equations, and for the relations that close this system

$$\bar{\lambda}_\varphi = \frac{\bar{r}}{r_0} \quad \text{and} \quad \lambda_s = \frac{\bar{\tau}_s \bar{\lambda}_\varphi + E_{2\mathrm{D}} - \gamma(1+\nu)}{E_{2\mathrm{D}} - 2\nu\gamma - \gamma^2(1-\nu^2)/E_{2\mathrm{D}}}. \tag{5.16}$$

Finding a numerical solution for the shape of a deflated pendant capsule involves both the original and modified systems of the shape equations. We use a shooting method with $\tau_s(0)$ as the free shooting parameter, which is adjusted until the boundary condition $r(L_0) = a/2$ is satisfied. The integration starts at the apex, using the original shape equations (5.7). In each integration step, the wrinkling condition (5.11) is checked. When λ_φ falls below this threshold, at $s_0 = s_A$, the integration is stopped. From this point on, the wrinkled shape equations (5.15) are integrated, using continuity conditions for all functions as starting conditions. The integration goes on until the point $s_0 = s_B$, where the wrinkling condition is not met any more, i.e. where

$$\frac{\bar{r}}{r_0} > 1 - \gamma \frac{1-\nu^2}{E_{2\mathrm{D}}} \lambda_s - \nu(\lambda_s - 1). \tag{5.17}$$

Then we switch back to the original shape equations (5.7), again using continuity conditions for all functions. This last part should run up to the end $s_0 = L_0$, where the boundary deviation $r(L_0) - a/2$ can be calculated. The initial guess of $\tau_s(0)$ at the very beginning of the integration is then adjusted, and after some iterations the boundary deviation should approach to zero. The wrinkle length L_w, necessary for the wrinkling analysis, can be obtained as $L_w = s_B - s_A$.

In some cases, especially for high values of $E_{2\mathrm{D}}$, a simple shooting method fails to converge. It turned out that these cases are reliably handled by a multiple shooting method [122].

5.2.4. Wavelength of the wrinkles

We have not included a bending energy in the model described above, because for thin membranes with a small bending modulus ($E_B \sim E_{2\mathrm{D}} H_0^2$ in the case of isotropic materials) the bending moments give only small corrections in the equilibrium equations (2.16). These corrections are controlled by the dimensionless parameter $E_B/\gamma a^2$. For the experimental systems analysed below, this parameter is only of the order 10^{-6} to 10^{-10}. Therefore, E_B cannot be inferred directly from an analysis of the capsule's shape, and we use the wrinkle analysis developed in the following instead.

The shape equations can predict the regions where wrinkles occur, but not their amplitude and wavelength. These characteristics are mainly determined by the bending modulus E_B of the membrane. In chapter 3, we saw that a flat plate with simply supported edges wrinkles with the wavelength $\lambda_c \sim (E_B L_y^2/\tau_y)^{1/4}$. Furthermore, we saw that this formula stays valid if the wrinkles are not confined by edges, but by the locality of the compressive stress, as it is the case with wrinkled pendant capsules. Finally, we found that a weak initial plate curvature only influences the numerical prefactor of this relation (if the curvature is along the wrinkles, i.e. in s-direction in the case of pendant capsules).

In the case of pendant capsules we have a membrane that is initially curved in both directions (κ_s and κ_φ are nonzero, see fig. 5.3) and wrinkles in a region determined by the location of the compressive hoop stress. We will not solve this wrinkling problem in full detail as in chapter 3, where stability equations of shallow shells were solved. Instead, we present energy arguments in the following which show that the flat plate result for the relation between wavelength and bending stiffness can still be used as long as the curvatures are weak, and we will quantify this condition of weakness. These energy arguments are based on an educated guess for the wrinkling pattern and constitute therefore no complete, exact solution; however, our experience of chapter 3 suggests that it captures the correct behaviour.

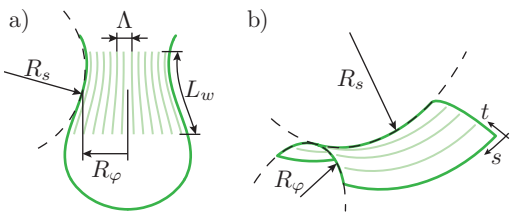

Figure 5.3.: a) The wrinkled region of a pendant capsule is curved in the meridional and circumferential directions. b) Geometry for the analytic calculation of the deformation energies: The membrane patch has two radii of curvature, R_s and R_φ and is parametrised via the arc lengths s (in meridional direction) and $t = \varphi R_\varphi$ (in circumferential direction).

For the analytical calculation, we assume that the curvatures $\kappa_s = 1/R_s$ and $\kappa_\varphi = 1/R_\varphi$ are constant in the wrinkling region and that the stresses are homogeneous, with tensional $\tau_s > 0$ and compressive $\tau_\varphi < 0$. The membrane patch is parametrised by the arc lengths s and $t = \varphi R_\varphi$, see fig. 5.3. Upon wrinkling, the main contributions to the deformation energy are bending in the circumferential direction and stretching in both circumferential and meridional directions. Changes in the gravitational potential energy caused by wrinkling are neglected since the wrinkles are largely parallel to the z-axis.

We first calculate the length change of a fibre that is oriented along the s or t direction upon wrinkling. With an initial radius of curvature R, corresponding to either R_s or R_φ, the wrinkled fibre can be parametrised in polar coordinates by $\rho(\theta) = R + C\sin(kR\theta)$, where C is the wrinkle amplitude and k the wave number. The length change caused by the wrinkling can be calculated from the arc-length element of this curve [19],

$$\mathrm{d}s = \sqrt{\rho(\theta)^2 + \rho'(\theta)^2}\,\mathrm{d}\theta = \left[R + C\sin(kR\theta) + \frac{1}{2}C^2k^2R\cos^2(kR\theta) + \mathcal{O}\big(C^3\big)\right]\mathrm{d}\theta. \tag{5.18}$$

For a fibre in meridional direction, we assume that the wrinkles have an effective length L_w and hence wave vector $k = \pi/L_w$ in s-direction. We take $R = R_s$ in (5.18) to obtain the length change up to quadratic order in C,

$$\Delta l_s = \int_0^{\frac{L_w}{R_s}} \left[C\sin(\pi R_S\theta/L_w) + \frac{1}{2}\pi^2\frac{C^2R_s}{L_w}\cos^2(\pi R_S\theta/L_w)\right]\mathrm{d}\theta = 2\frac{CL_w}{\pi R_s} + \frac{\pi^2C^2}{4L_w}. \tag{5.19}$$

A fibre positioned at the circumferential coordinate t contributes $\tau_s\Delta l_s\,\mathrm{d}t$ to the deformation energy when it is stretched against the tension τ_s. The amplitude of the wrinkles depends on the position along the circumferential direction by $C(t) = C_0\sin(2\pi t/\Lambda)$ where Λ is the wrinkle wavelength. Thus, the total energy caused by the stretch in meridional direction is

$$U_s = \int_0^{2\pi R_\varphi} \tau_s\Delta l_s\,\mathrm{d}t = \frac{\pi^3}{4}\frac{C_0^2R_\varphi}{L_w}\tau_s \quad \text{and analogously} \quad U_\varphi = \pi^3\frac{C_0^2L_wR_\varphi}{\Lambda^2}\tau_\varphi \tag{5.20}$$

for the stretching energy in circumferential direction. Since $\tau_\varphi < 0$, the contribution U_φ is negative, that is, it is the energy gain which drives the wrinkling. Note that the term linear in C in the length change (5.19) vanishes in the integrals, because the sinusoidally oscillating amplitude $C(t)$ is integrated over full periods.

The bending is strongest in φ-direction, and its energy cost depends on the curvature change of a circumferential fibre. For a curve given in polar coordinates, $\rho(\varphi) = R_\varphi + C\sin(2\pi\varphi R_\varphi/\Lambda)$, the curvature can be approximated to first order in the amplitude C as [19]

$$\kappa_\varphi = \frac{\rho^2 + 2\rho'^2 - \rho\rho''}{(\rho^2+\rho'^2)^{3/2}} \approx \frac{1}{R_\varphi} + C\left(-\frac{1}{R_\varphi^2} + \frac{4\pi^2}{\Lambda^2}\right)\sin(2\pi t/\Lambda) \tag{5.21}$$

with $t = \varphi R_\varphi$. Considering that the wrinkle amplitude depends on the position along the meridional direction via $C(s) = C_0 \sin \pi s/L_w$, the bending energy reads

$$U_B = \iint \mathrm{d}s\,\mathrm{d}t \left\{ \frac{1}{2} E_B \left(\kappa_\varphi - \frac{1}{R_\varphi} \right)^2 \right\} = \frac{1}{4} \pi E_B C_0^2 L_w R_\varphi \left(\frac{4\pi^2}{\Lambda^2} - \frac{1}{R_\varphi^2} \right)^2 . \tag{5.22}$$

Now the argumentation is the same as in section 3.3.1. For the wrinkled state to become preferable to the unwrinkled state, the total deformation energy must be negative, $U_s + U_\varphi + U_B < 0$, which is equivalent to

$$\tau_\varphi < \tau_{\varphi,c}(\Lambda) \equiv -\tau_s \frac{\Lambda^2}{4L_w^2} - E_B \frac{\Lambda^2}{4\pi^2} \left(\frac{4\pi^2}{\Lambda^2} - \frac{1}{R_\varphi^2} \right)^2 . \tag{5.23}$$

The wrinkling will first occur with a wavelength that renders the critical stress $|\tau_{\varphi,c}(\Lambda)|$ minimal, which is

$$\Lambda = \left(\frac{16\pi^2 E_B L_w^2}{\tau_s + E_B L_w^2/\pi^2 R_\varphi^4} \right)^{1/4} \quad \text{or equivalently} \quad E_B = \frac{\tau_s \Lambda^4}{16\pi^2 L_w^2 \left(1 - \Lambda^4/16\pi^4 R_\varphi^4\right)} . \tag{5.24}$$

The latter form can be used to determine the bending modulus from measurements of the wrinkle wavelength.

If the wrinkle wavelength is much smaller than the radius of curvature, $\Lambda \ll R_\varphi$, the term $1/R_\varphi^2$ in (5.23) can be neglected and the critical wavelength is exactly the result (3.36) for flat plates with fixed edges derived above. Note that the small ratio Λ/R_φ enters the formula for E_B (5.24) in the fourth power, so that the initial curvature of the membrane has only little influence on the wavelength analysis, and can therefore be neglected.

5.3. Analysis of theoretically generated shapes

The basic idea of our elastometry method is to fit solutions of the elastic shape equations (including wrinkling) to contours extracted from experimental images of deflated pendant capsules. The elastic moduli and the pressure serve as the fit parameters, where the pressure is mainly used to control the capsule volume, and the elastic parameters to adjust its shape. Before applying this core module to real experiments, we need to test it in cases with known results. To this end we take a solution of the Laplace-Young equation with an interfacial tension $\gamma = 49.8\,\mathrm{mN/m}$, density difference $\Delta\rho = 1000\,\mathrm{kg/m^3}$ and volume $V_0 = 8.23\,\mathrm{mm^3}$ as the initial shape of a pendant capsule – these values are taken from the HFBII experiment presented below. We then use our shape equations with fixed elastic moduli ($K_\mathrm{orig} = 600\,\mathrm{mN/m}$, $\nu_\mathrm{orig} = 0.3$) to compute deflated configurations. The area compression modulus $K_\mathrm{2D} = E_\mathrm{2D}/2(1-\nu)$ defined above in eq. (3.14) is used instead of the Young modulus to characterise the membrane because the fits work better when K_2D and ν are used as fit parameters: The fit error minimum has a "nicer shape" and is easier to locate in the (K_2D, ν)-plane than in the (E_2D, ν)-plane. From each theoretically generated contour, we calculate a set of approximately 150 sampling points $\boldsymbol{x}_i = (r_i, z_i)$, exactly as one would obtain from an image analysis. We optionally add some noise to simulate an imperfect contour analysis, and pass the sampling points to the fitting procedure to see whether it finds the correct solution.

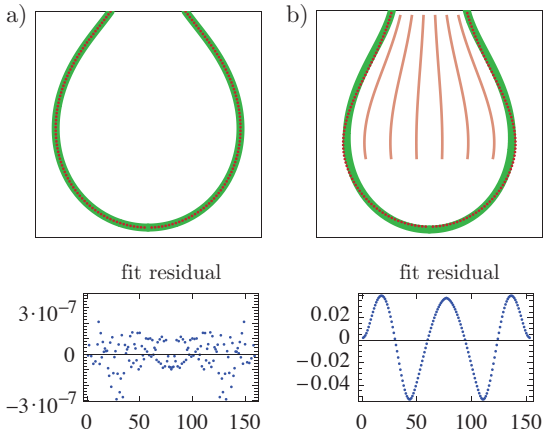

Figure 5.4.: Laplace-Young fits of deflated elastic capsules. a) $V = V_0$, fitted surface tension $\gamma_{\text{app}} = 49.8\,\text{mN/m}$ and b) $V = 0.9V_0$, fitted surface tension $\gamma_{\text{app}} = 28.7\,\text{mN/m}$. In the top row, the red dots are the elastic shape to which the solution of the Laplace-Young equation (green line) is fitted. Light red lines indicate the wrinkled region according to the elastic shape equations. In the bottom row, the fit residual (in reduced units) is plotted versus the number of the sampling point; the numbering starts at the left attachment to the capillary and goes counter-clockwise around the capsule.

5.3.1. Fitting elastic shapes with the Laplace-Young equation

Many experiments on elastic capsules attached to a capillary have been analysed using the standard software of pendant drop tensiometers [1, 42, 68, 119]. In this analysis, the Laplace-Young equation is fitted to the captured capsule shape, although the Laplace-Young equation is not the correct model if the capsule has an elastic membrane. The result of this process is a "measured" *apparent surface tension* γ_{app} as a function of how much the capsule is deformed. Since the Laplace-Young fits also provide the current capsule surface A, one can subsequently calculate the *Gibbs elasticity*

$$E_{\text{Gibbs}} = A \frac{\mathrm{d}\gamma_{\text{app}}}{\mathrm{d}A} \tag{5.25}$$

by finite differences. This is essentially the same definition as used for the area compression modulus in eq. (3.14), which is based on $K_{\text{2D}} = A_0 \cdot \tau/\Delta A$ for isotropic deformations.

We investigate the performance of this analysis applied to the theoretically generated shapes of deflated elastic capsules, see appendix D.2 for a description of the least-squares fitting procedure. In fig. 5.4, two fit results are plotted, one for the undeformed shape and one for a deflated shape. The first case is actually a fit to a drop shape, so that the Laplace-Young equation is the appropriate model. It finds the correct value of the surface tension, $\gamma_{\text{app}} = \gamma = 49.8\,\text{mN/m}$, and the fit residual is very small and randomly distributed, which indicates that this is just numerical noise. The fit in fig. 5.4 b), however, fails. There are visible deviations between the fitted Laplace-Young shape and the original elastic shape, and the fit residual is large and shows systematic deviations. The fitted surface tension $\gamma_{\text{app}} = 28.7\,\text{mN/m}$ is smaller, which is qualitatively correct because the initial surface tension is lowered by the elastic stresses, which are negative when the membrane is compressed by deflation, see the constitutive relation (5.6). Figure 5.4 b) shows a fit to an extremely deflated capsule, with well developed wrinkles. However, the same effects in weaker form can be seen for smaller deformations, even before the onset of wrinkling.

For the Gibbs elasticity, we find that E_{Gibbs} is significantly lower than the actual area compression modulus $K_{\text{orig}} = 600\,\text{mN/m}$ used for the theoretical shape generation, see fig. 5.5, red dots. It appears that for elastic capsules, the intricate interplay between membrane geometry and elastic tensions renders the Laplace-Young analysis more erroneous than intuitively expected: Not even for small deformation does the Gibbs elastic modulus approach the real area compression modulus. A precise theory of this effect is lacking so far, but in some way, the capsule geometry and the non-constant and anisotropic stress distribution must affect the

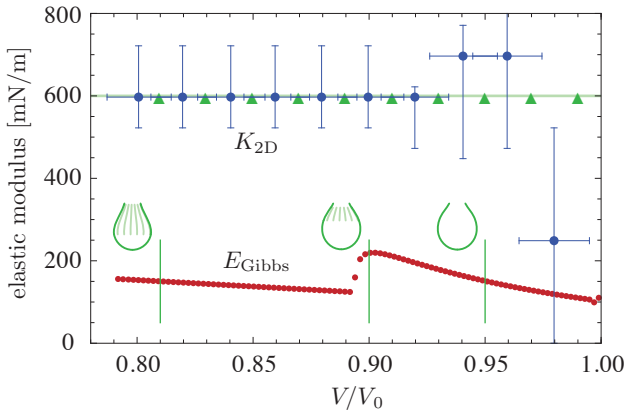

Figure 5.5.: Fit results for theoretically generated capsule shapes with $K_{orig} = 600\,\mathrm{mN/m}$ (green line). Green triangles represent the fits of the elastic shape equations to the clean contour, blue dots the elastic fits to the noisy contour, and red dots the Gibbs elasticity calculated from Laplace-Young fits. Vertical green lines indicate the positions of the capsule pictograms shown in green.

Laplace-Young fits so that the apparent surface tension obtained from them is not a suitable average value of the stress distribution in the membrane. This explains the observations of Stanimirova et. al. that pendant drop tensiometry gives wrong results if applied to capsules with high surface elasticity [119].

5.3.2. Fitting with the elastic shape equations and sensitivity to noise

The fitting procedure where solutions of the elastic shape equations are fitted to given sampling points is described in appendix D.2. Applying the procedure to the theoretically generated shapes (without noise) works very well, and it recovers the correct values for the elastic moduli, that is, $K_{2D} = K_{orig}$ and $\nu = \nu_{orig}$ in our test. Some example results for the fit residual distribution over the (K_{2D}, ν)-plane are shown in appendix D.4, see figs. D.4 and D.5. The results for K_{2D} over a range of reduced volumes are represented by green triangles in fig. 5.5.

In a further test, a small noise is added to the sampling points before fitting. Each sampling point is shifted by a random number drawn from the interval $[-0.0045, 0.0045]$ in r- and z-direction. A deviation of ± 0.0045 in reduced units corresponds to nearly 1 pixel in typical images, and so this is a reasonable noise amplitude to simulate imperfections of the contour detection. Figure 5.5 shows the fits to the noisy contour as blue dots. The error bars of the fits have been generated as described in appendix D.3: The basic idea is to construct worst-case systematic error estimates by displacing the sampling points by ± 1 pixel. Here, where the sampling points are given directly in reduced units, a displacement of ± 0.007 (corresponding to ± 1 px at usual image resolutions) has been used to generate the error bars.

For small deformations, the fits to the noisy contour do not succeed. Especially for $V = 0.98 V_0$ the fit fails, and the correct value of $K_{orig} = 600\,\mathrm{mN/m}$ is not even included in the range of error bars. The fits at $V/V_0 = 0.94$ and 0.96 are better and reasonably close to the correct value. But only for $V \leq 0.92 V_0$, the results lie perfectly in the diagram (fig. 5.5). It is not astonishing that the fit did not work for the smallest deformation: The root mean square deviation between the initial shape and the shape at $V/V_0 = 0.98$ is about 0.01 length units, the noise amplitude is 0.0045 and the offset used for the error bars is 0.007 – so the sampling points passed to the fitting procedure have an offset from their original place which is of the same order as the deformation. Only for deformations that are considerably larger than the noise we can expect successful fits. In appendix D.4, two fit results for the noisy contour are shown in figs. D.6 and D.7. The plots of the fit residual over the K_{2D}-ν-grid in these figures demonstrate that the minimum is better localised and easier to find for large deformations than for small ones.

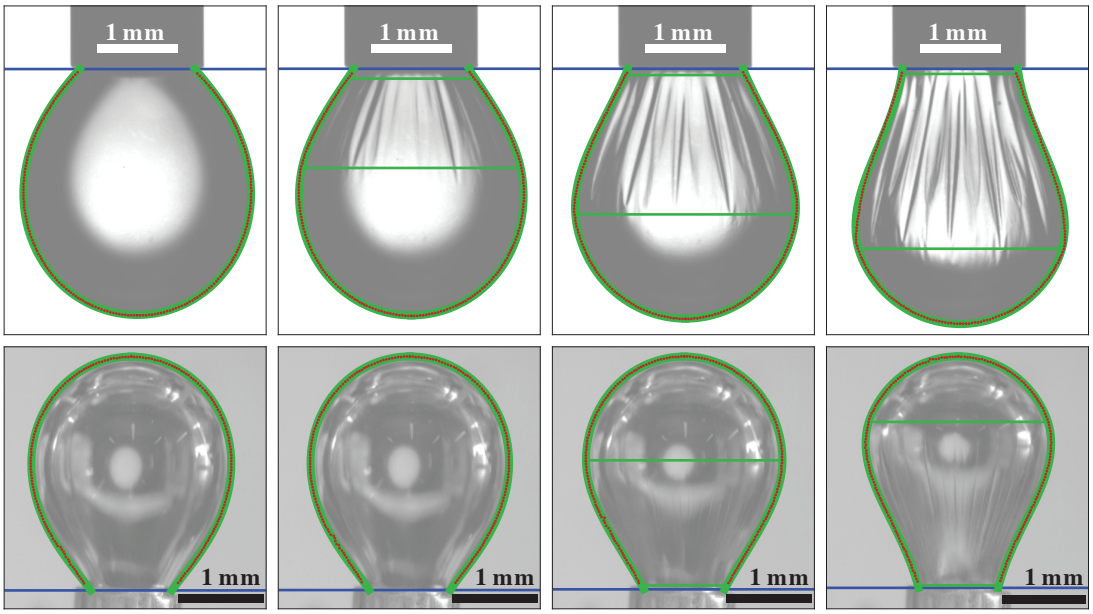

Figure 5.6.: Fitted images of OTS (upper row) and HFBII (lower row) capsules. The first image shows the equilibrated capsule, fitted with the Laplace-Young equation, while the next three show deflated shapes, fitted with the elastic model. The red dots are the sampling points extracted from the image, the blue line is the end of the capillary, the green line is the fitted solution of the shape equations, and the horizontal green lines indicate the wrinkled region according to the fit.

5.4. Analysis of experiments

The elastometry method sketched in the introduction of the present chapter shall now be applied to real capsules. Experimental data on two different systems, polysiloxane capsules and hydrophobin coated bubbles, is available through collaborations with the group of Prof. Heinz Rehage, TU Dortmund, and the group of Dr. Pietro Cicuta, University of Cambridge.

To prepare a pendant polysiloxane capsule, a glass cell is filled with p-xylene containing octadecyltrichlorosilane (OTS). Then a drop of water is placed into this phase using a syringe. The polymerisation process starts immediately after the oil/water-interface is formed [36]. Hydrophobin coated bubbles are prepared in a very similar fashion. As described in previous work [5], an air bubble is placed into a solution of class II hydrophobin (HFBII) in water using a J-shaped needle; and HFBII proteins adsorb at the interface over the course of 20 minutes. Although the proteins do not crosslink, a hydrophobin layer exhibits elasticity [6, 7].

After equilibration, the capsules are deflated slowly (i.e. quasi-statically, on a timescale of $\sim 10\,\mathrm{s}$ for a deflation of OTS capsules and even slower for HFBII capsules) by sucking the enclosed medium back into the syringe. The OTS capsule is subsequently re-inflated to check whether the deformation is reversible.

The whole experiment is recorded with a digital camera. From each movie, a set of frames is selected, and each image is analysed using a contour detection algorithm described in appendix D.1. Then, a three step fitting procedure can be used to determine the elastic moduli of the capsule membrane:

1) Reference configuration: The undeformed capsule shape is fitted using the Laplace-Young

equation with the interfacial tension γ and pressure p_0 inside the capsule as free parameters, see appendix D.2 for technical details.

2) Shape analysis: At each stage of deflation, solutions of the shape equations (including wrinkling) are fitted to the extracted contours with pressure p, Poisson ratio ν and area compression modulus $K_{2D} = E_{2D}/2(1-\nu)$ as free parameters, see also appendix D.2.

3) Wrinkle analysis: The wavelength Λ in the centre of the wrinkled region is measured from images. The length L_w of the wrinkles and a mean value of τ_s over this region are obtained from the fitted solution. Then, the bending modulus E_B is determined from eq. (5.24). Using the relationship $E_B = E_{2D}H_0^2/12(1-\nu^2)$, see eq. (2.9), an effective membrane thickness H_0 can also be estimated. This is, however, a rough estimate, since this relation applies only to thin sheets of isotropic material, but the membranes at hand are evidently anisotropic.

Note that the position and length L_w of the wrinkled region are *not* fit parameters but can be used as an independent check of the accuracy of the fit. L_w is determined from the fitted numerical solution as the arc length over which the modified shape equations (5.15) were integrated. In the following, the fit results are presented, see fig. 5.6 for some examples.

5.4.1. Results for polysiloxane capsules

In step one of the fitting procedure, four images of the reference configuration are fitted with the Laplace-Young equation to obtain an average surface tension $\gamma = 11.2\,\mathrm{mN/m}$. This value is lower than the surface tension of the clean p-xylene/water-interface because the OTS molecules are surface active agents which lower the interfacial tension during the polymerisation. Scaling factors that relate lengths measured in reduced units, pixels, and millimetres are also obtained from the Laplace-Young fits, see appendix D.4.2 for a full documentation; in the present discussion only the length unit $a = 1.44\,\mathrm{mm}$ is required.

In the experiment, the OTS capsule is deflated and subsequently re-inflated. In the second step of the analysis, images from both processes are fitted using the elastic model, see fig. 5.6 (upper row) for some example images. All data points in fig. 5.7 represent wrinkled shapes, because even the slightest deformation gives rise to wrinkles due to the low initial surface tension and high compression modulus. We find an area compression modulus K_{2D} which starts at approximately $K_{2D} \approx 500\,\mathrm{mN/m}$ and decreases with decreasing V/V_0. The Poisson

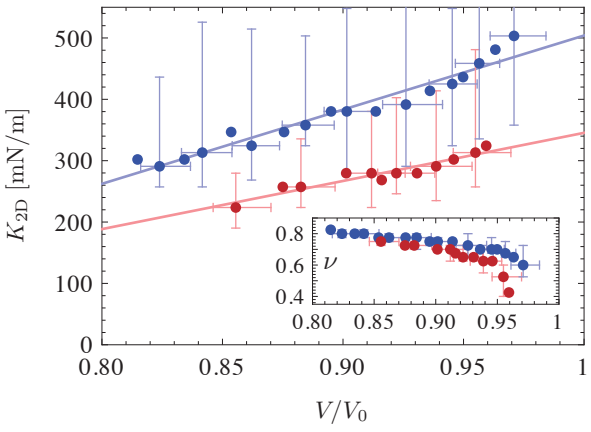

Figure 5.7.: Fit results for the area compression modulus K_{2D} and Poisson ratio ν (inset) for OTS capsules. The blue dots are for deflation, the red dots for re-inflation, all shapes are wrinkled. Both curves do not meet within the plotted range because the deflation was driven to even smaller volumes than shown, but for these the contour analysis failed. Error bars were generated by displacing the sampling points about ±1 pixel, see appendix D.3. Lines are drawn to guide the eye.

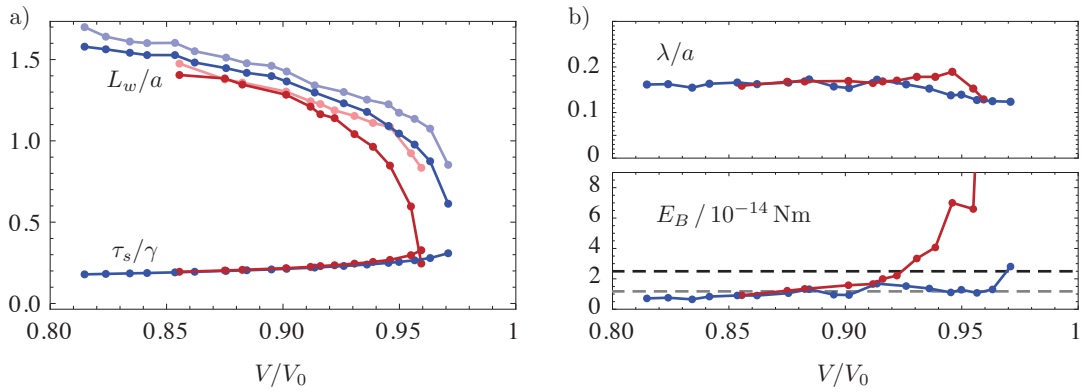

Figure 5.8.: Wrinkle analysis for the OTS capsule; blue colour is used for the deflation and red for the re-inflation. a) Wrinkle length L_w (upper curves) and mean tension τ_s (lower curves), both in reduced units with length unit $a = 1.44\,\text{mm}$ and tension unit $\gamma = 11.2\,\text{mN/m}$. Dark blue and dark red represent results taken from the fitted shape equations, light blue and light red represent direct measurements from the images. b) Measured wavelength (upper panel) and resulting bending stiffness (lower panel, both panels share their horizontal axis). The averaged bending stiffness $E_B = 2.5 \cdot 10^{-14}\,\text{Nm}$ is represented by the dashed black line; taking the average only over the deflation data (blue dots) results in $E_B = 1.2 \cdot 10^{-14}\,\text{Nm}$, see dashed grey line.

ratio increases at the same time from around $\nu = 0.6$ to 0.8. The resulting surface shear modulus for the initial values is $G_{2D} = K_{2D}(1-\nu)/(1+\nu) \approx 125\,\text{mN/m}$. In ref. [114], larger values of $200 - 300\,\text{mN/m}$ (obtained by interfacial shear rheology) are reported for similar OTS membranes.

Although the error bars in fig. 5.7 are overlapping, this result is reliable because the error bars represent worst case systematic errors (see appendix D.3). An analysis of the noise in the contour, see appendix D.5, also suggests that the fits are reliable because the noise is very small compared to the deformation. Further indications of the good accuracy of the fits are the coincidence of the wrinkled region obtained in the fits with the experimental observations, see fig. 5.8 a), and the visual agreement between fitted contour and experimental image, see fig. 5.6.

The deformation is not perfectly reversible, and we observe hysteresis: The area compression modulus obtained for re-inflated capsules is smaller than for the first deflation (compare lower red and upper blue data points in fig. 5.7). The presence of hysteresis indicates that the decreasing modulus is not a pure artifact of the method but a result of creep, for example by plastic effects, i.e. breakage or rearrangement of bonds in the OTS network, or by the formation of micro-defects such as shear cracks. Further investigations of experiments with several deflation/inflation-cycles have shown that the hysteresis diminishes after several cycles [61].

Finally, the wrinkling pattern is related to the bending stiffness in the third step of the analysis. Wrinkle wavelengths Λ can be measured from the images, and values for τ_s in the wrinkled region and L_w are obtained from the fitted solutions, see fig. 5.8 (dark blue and dark red dots). This results with eq. (5.24) in a bending stiffness shown in the lower panel of fig. 5.8 b). The average over all determined values is $E_B = (2.5 \pm 0.7) \cdot 10^{-14}\,\text{Nm}$. As the plot shows, the values obtained at the end of the re-inflation might be erroneous (possibly because of the non-reversibility of the deformation), and so it might be more appropriate to average the bending stiffness only over the deflation results (blue dots), which gives $E_B = (1.2 \pm 0.1) \cdot 10^{-14}\,\text{Nm}$. In any case, the determined bending stiffness is 3 orders of magnitude larger than previous estimates [26, 48] which used an experiment with a smaller capsule of the same material in shear

flow, resulting in wrinkles with a much shorter wavelength [139]. Moreover, the OTS capsules in ref. [139] were prepared in a different aqueous solution (glycerol and NaOH) and using longer polymerisation times. These deviations can give rise to distinct membrane thicknesses and crosslink densities, which can explain the differences in the bending modulus: The bending modulus varies with the third power of the membrane thickness and Cerda and Mahadevan estimated in ref. [26] a thickness around 20 times smaller than that of the capsules used here.

Combining the values for E_B with measurements of E_{2D} from the shape analysis we estimate the effective membrane thickness $H_{\text{eff}} \approx (0.77 \pm 0.07)\,\mu\text{m}$ (for the average over all data points) or $H_{\text{eff}} \approx (0.56 \pm 0.02)\,\mu\text{m}$ (for the average over the deflation). This is in approximate agreement with the actual capsule thickness $0.86\,\mu\text{m} < H_0 < 1.4\,\mu\text{m}$ measured by electron microscopy, see fig. D.10 in appendix D.4.

5.4.2. Results for hydrophobin coated bubbles

Hydrophobin coated bubbles do not *hang* but *rise* from a capillary because of buoyancy. Since the physics of rising and pendant capsules is the same, the experimental images are simply rotated by 180° and fed to the usual shape analysis. In the first step of the analysis, four images of the reference shape are fitted to obtain the interfacial tension $\gamma = 49.8\,\text{mN/m}$ and unit length $a = 0.95\,\text{mm}$.

In the second step, the number of fit parameters can be reduced by constraining $\nu = 0.6$ because this value has been determined in an independent experiment [5]. Then, only the area compression modulus K_{2D} must be determined, which is shown in fig. 5.9 a). The area compression modulus increases for small deformations, where the capsule does not wrinkle (blue squares in fig. 5.9 a)), to values around 500 mN/m. The onset of wrinkling coincides with a sharp increase of the modulus to a maximum value of $K_{2D} \approx 2000\,\text{mN/m}$. This sharp increase is consistent with the molecular structure of HFBII [60], which contains a rigid core consisting of four β-strands and is stabilised by disulfide bridges. The modulus K_{2D} increases sharply when compression of this rigid protein core sets in, while at small deformations only contacts between hydrophobin proteins or a soft shell consisting of coil and loop structures surrounding the rigid β-barrel are compressed. The sharp rise of the compression modulus triggers wrinkling. Subsequently, the compression modulus decreases again (blue circles in fig. 5.9 a)) likely signalling creep as also observed for the OTS capsules. Possible explanations for the creep behaviour are the formation of micro-defects such as shear cracks or localised bulges into the subphase, which weaken the hydrophobin layer.

The choice of the fixed value for ν influences the absolute values obtained for K_{2D} and the size of its jump when wrinkling sets in, while the characteristic course described above is robust. Taking the Poisson ratio as a fit parameter also results in a similar course of the elastic modulus, see fig. 5.9 b). However, the results for ν differ substantially from the previously assumed value of $\nu = 0.6$; and the results for K_{2D} are larger for small deformations. An analysis of the noise in the extracted contour, see appendix D.5, raises the question if the shapes in the pre-wrinkling regime are sufficiently deflated to be fitted at all. The fact that the fit results do not scatter too much and exhibit clearly visible trends, however, suggests that there is some significance to the results and that the interesting non-linear behaviour is at least qualitatively correct.

The values $K_{2D} < 500\,\text{mN/m}$ for the compression modulus for small deformations and prior to wrinkling are in good agreement with values reported previously for HFBII [1, 17, 29]. The large values around $K_{2D} = 2000\,\text{mN/m}$ at the onset of wrinkling have not been reported before, since the experimental methods used in the literature are not reliable in the presence of wrinkles. However, a comparison to viral capsids consisting of densely packed proteins is possible. In ref. [70], the bulk Young modulus of a viral capsid is measured as 1.8 GPa, which is comparable

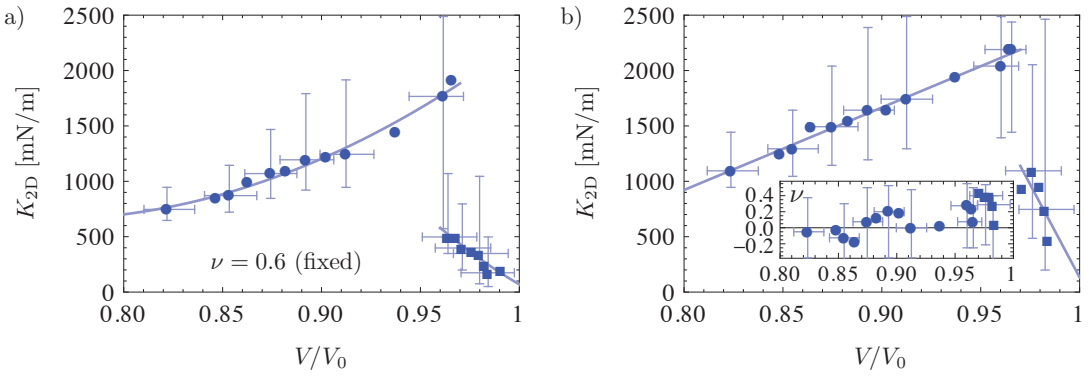

Figure 5.9.: Fit results for HFBII capsules, with wrinkled (•) and non-wrinkled (■) shapes. Lines are drawn to guide the eye. a) In these fits, the Poisson ratio is fixed to $\nu = 0.6$. b) The same experiment fitted with free Poisson ratio, see inset for the results.

to our result for the bulk modulus $E = E_{2D}/H_0 \approx 1\,\mathrm{GPa}$, where $H_0 \approx 2\,\mathrm{nm}$ is the hydrophobin layer thickness [76].

Step three of the procedure, the wrinkle wavelength analysis, cannot be performed for HFBII capsules: Because of the small bending stiffness, the wavelength is too small to be resolved in the experimental images. The observable folds in fig. 5.6 (lower row) are not primary, sinusoidal wrinkles, but rather secondary or higher order structures. Using eq. (5.24) with L_w, τ_s and $E_B = E_{2D}H_0^2/12(1-\nu^2)$ obtained from the elastic fits, we expect wavelengths between 7.6 and 11 µm, which is sub-pixel dimension in the available images. In the literature, similarly small or even smaller wrinkle wavelengths for compressed HFBII films in a Langmuir trough have been reported [5, 13, 17].

5.5. Outlook: a custom elasticity model for protein layers

In the previous section we found that hydrophobin layers exhibit a very peculiar, non-linear elastic behaviour. Based on the assumption that this behaviour can be attributed to the molecular structure of HFBII proteins, we now develop an elastic law that is supposed to explain the above results.

The microscopic view of the proposed model for a hydrophobin layer at an air/water-interface is shown in fig. 5.10: Globular proteins interact by soft springs (corresponding to an outer soft shell) and steric interactions (corresponding to hard cores). From this microscopic view we will derive continuum elastic laws that can be used in the shape equations of pendant/rising capsules. Because the bead-spring network and hard cores are quite generic, our model could apply much more widely. Further applications may include Pickering emulsions [16] or interacting particle rafts [133, 134] in colloidal systems.

To test if the model can explain the above fit results of the hydrophobin capsules, we will use the modified shape equations to generate deflated shapes obeying our custom elasticity model, and fit them using the standard shape equations (with Hookean elasticity) described above. The aim is to reproduce the characteristic course of K_{2D} as a function of the deflated volume, see fig. 5.9, with an initial increase, sharp jump and final decrease. As shown below, this succeeds in part. This is work in progress, and further research will be necessary for a full explanation of the hydrophobin layer elasticity.

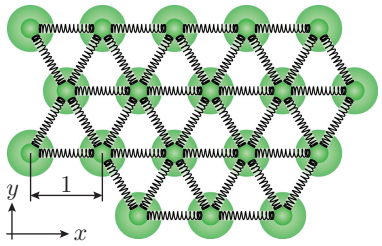

Figure 5.10.: Bead-spring model with hard cores to mimic the behaviour of HFBII molecules at the air/water-interface. The springs give the network a Hookean elasticity, and the hard cores (green disks) impose limits on the maximal admissible compression. The lattice constant is normalised to 1.

5.5.1. Continuum description of a bead-spring model with hard cores

The spring interactions between the beads in fig. (5.10) give the network its elasticity. We assume that the beads are arranged in the (x, y)-plane in a hexagonal crystal with a lattice constant normalised to 1. Such an arrangement is the closest packing of spheres and it behaves isotropically [84], so that the continuum elasticity of the membrane can be characterised by two elastic moduli, for example the (surface) Poisson ratio and (surface) Young modulus. On the microscopic level, the elastic response of the membrane is governed by the spring constant k. By evaluation of the deformation energy within one unit cell, it can be shown that the continuum elastic moduli are determined by [99, 118]

$$E_{2\mathrm{D}} = \frac{2}{\sqrt{3}}\,k \quad \text{and} \quad \nu = \frac{1}{3}. \tag{5.26}$$

Without the hard-core interactions, the membrane can thus be described with the usual Hookean elasticity as specified by eqs. (5.5) and (5.6), with the Poisson ratio confined to $\nu = 1/3$. We repeat the constitutive relations here, with a superscript $^{(\mathrm{s})}$ indicating that it is the contribution of the springs:

$$\tau_x^{(\mathrm{s})}(\lambda_x, \lambda_y) = \frac{E_{2\mathrm{D}}}{1-\nu^2}\frac{1}{\lambda_y}\left[(\lambda_x - 1) + \nu(\lambda_y - 1)\right] + \gamma, \tag{5.27}$$

and with indices x and y interchanged for $\tau_y^{(\mathrm{s})}$. The interfacial tension γ has been incorporated here, although it cannot be attributed to the springs, but to the air/water-interface in the meshes of the network.

Now comes the most important part of the model: Evaluating the influence of the steric interactions between the hard cores. The springs in the lattice have a rest length of 1 and can be oriented along three different directions i, which we characterise by the angle φ_i to the x-axis. This angle can take the values $\varphi_i = \varphi_0 + i\pi/3$, with $i \in \{-1, 0, 1\}$, where φ_0 determines the overall orientation of the lattice in the (x, y)-plane.

We consider a deformation in the principal axes system that is characterised by the stretches λ_x and λ_y. The length of a spring along direction i changes from 1 to

$$d_i = \left|\begin{pmatrix}\lambda_x \cos\varphi_i \\ \lambda_y \sin\varphi_i\end{pmatrix}\right| = \sqrt{\lambda_x^2 \cos^2\varphi_i + \lambda_y^2 \sin^2\varphi_i} \tag{5.28}$$

by this deformation. The steric interactions enforce that the springs of the lattice can be compressed at maximum to a minimal length of L (with $L < 1$, of course). Thus, we have three conditions $d_i \geq L$ to be satisfied, or equivalently

$$\begin{aligned}
\lambda_x^2 \cos^2(\varphi_0 - \pi/3) + \lambda_y^2 \sin^2(\varphi_0 - \pi/3) &\geq L^2 \\
\lambda_x^2 \cos^2(\varphi_0) + \lambda_y^2 \sin^2(\varphi_0) &\geq L^2 \\
\lambda_x^2 \cos^2(\varphi_0 + \pi/3) + \lambda_y^2 \sin^2(\varphi_0 + \pi/3) &\geq L^2.
\end{aligned} \tag{5.29}$$

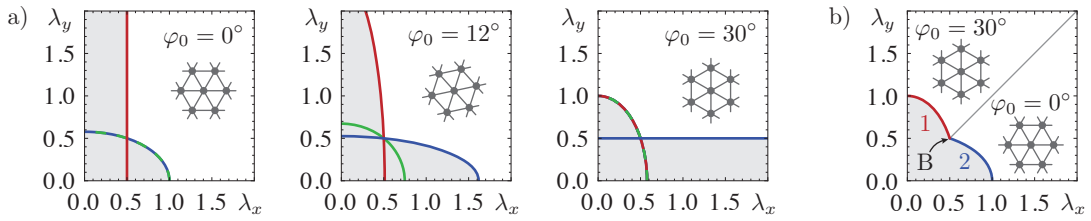

Figure 5.11.: Forbidden domains (light grey) in the (λ_x, λ_y)-plane limited by ellipses, for $L = 0.5$. a) Different orientations φ_0 produce different forbidden domains. Straight lines are degenerate ellipses with infinite major axis, and dashed lines with alternating colour indicate if two of the three ellipses are identical. The pictograms show the lattice orientation. b) Choice of φ_0 that minimises the area of the forbidden domain. For easy identification, the boundaries are labelled 1 and 2; and the point on both lines is termed B.

In the (λ_x, λ_y)-plane, these conditions specify three ellipses to be excluded from the admissible domain for the stretches, see fig. 5.11 a). All three ellipses go through the point (L, L). The hard-core length L corresponds to the diameter of the hard cores, measured in units of the lattice constant.

The forbidden domain, shaded light grey in this figure, depends on the orientation φ_0 of the lattice. For the remainder of this chapter we choose this parameter according to the following rule: If $\lambda_x < \lambda_y$, then $\varphi_0 = 30°$; otherwise $\varphi_0 = 0°$. With this choice, the forbidden domain becomes as small as possible, see fig. 5.11 b). Choosing φ_0 in dependence of the stress state means that it may change during a deformation – for hydrophobin rafts this seems plausible because the proteins are not rigidly crosslinked, but may change their neighbours to get from a 0° state to a 30° state (see pictograms in fig. 5.11). In case of a rising capsule, the stress state varies as a function of the arc length s_0, and so we may encounter regions of 0° and 30° orientation within a single capsule. Problems might arise at the boundary separating two regions of different orientation, because the lattices cannot be joined properly. This could give rise to a line energy; however, we neglect these complications in the following.

With this choice of φ_0, the boundary line between the forbidden and admissible domain of the stretches simplifies to $3\lambda_x^2/4 + \lambda_y^2/4 = L^2$ for $\lambda_x < \lambda_y$ and $\lambda_x^2/4 + 3\lambda_y^2/4 = L^2$ for $\lambda_x > \lambda_y$. Written as an explicit function, the boundary line reads

$$\lambda_x^{(\mathrm{b})}(\lambda_y) = \begin{cases} \sqrt{4L^2/3 - \lambda_y^2/3} & \text{if } \lambda_y > L \text{ (boundary 1)} \\ \sqrt{4L^2 - 3\lambda_y^2} & \text{if } \lambda_y < L \text{ (boundary 2)} \end{cases} . \tag{5.30}$$

Here we have introduced the terms boundary 1 and 2, which have to be distinguished in most of the following calculations. They are plotted in red and blue, respectively, in fig. 5.11 b). The point $(\lambda_x, \lambda_y) = (L, L)$ which is on both boundary lines is termed point B.

If the external loads try to push the membrane into the forbidden domain, the hard-core interactions keep it on the boundary of the forbidden domain by providing additional contributions to the stresses τ_x and τ_y. These hard-core contributions are denoted by $\tau_x^{(\mathrm{c})}$ and $\tau_y^{(\mathrm{c})}$. The complete stresses then read

$$\tau_x = \tau_x^{(\mathrm{s})}(\lambda_x, \lambda_y) + \tau_x^{(\mathrm{c})} \quad \text{and} \quad \tau_y = \tau_y^{(\mathrm{s})}(\lambda_x, \lambda_y) + \tau_y^{(\mathrm{c})} \tag{5.31}$$

with (λ_x, λ_y) a point on the boundary of the forbidden domain (5.30). Since $\tau_x^{(\mathrm{c})}$ and $\tau_y^{(\mathrm{c})}$ are transmitted through the "skeleton" of hard cores, they must satisfy certain conditions that can

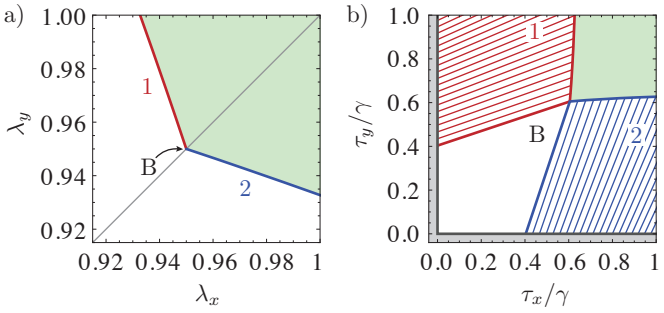

Figure 5.12.: Admissible domains (light green) and hard-core interaction domains for a) the stretches and b) the stresses, for $L = 0.95$. In b), the straight lines indicate the stresses that can be reached from a point on the boundary by adding the hard-core contributions to the elastic stresses. The wrinkling region is shaded in grey.

be derived from the geometry of the lattice. In appendix E.1 it is shown that the ratio of the hard-core stresses is confined to

$$\frac{\tau_y^{(\mathrm{c})}}{\tau_x^{(\mathrm{c})}} = \begin{cases} \lambda_y^2/3\lambda_x^2 & \text{if } \lambda_y > L \text{ (boundary 1)} \\ 3\lambda_y^2/\lambda_x^2 & \text{if } \lambda_y < L \text{ (boundary 2)} \end{cases} \quad \text{and} \quad \frac{1}{3} \le \frac{\tau_y^{(\mathrm{c})}}{\tau_x^{(\mathrm{c})}} \le 3 \quad \text{if } \lambda_x = \lambda_y = L \text{ (point B).} \tag{5.32}$$

Note that (λ_x, λ_y) must always be a point on the boundary of the forbidden domain when these equations are applied to calculate the hard-core contributions to the stresses.

The above results for our custom elasticity model for hydrophobin particle rafts are summarised and illustrated in fig. 5.12. Different regions in the stretch plane and stress plane are shown, with focus on the regime relevant for compressed membranes: $\lambda_i \le 1$ and $0 < \tau_i \le \gamma$. The light green regions are the admissible regions, where the hard cores are not in contact. Here, the usual Hookean elasticity (5.27) is valid, and there is a bijective mapping between (λ_x, λ_y) points in the stretch plane and (τ_x, τ_y) points in the stress plane.

On boundaries 1 and 2, the hard cores come into contact. In the stretch plane, this boundary cannot be trespassed: Even if the external forces try to push the lattice beyond this line, the lattice will get stuck on the boundary of the forbidden domain. In the stress plane, however, the points beyond boundaries 1 and 2 can be accessed by including the hard-core contributions $\tau_x^{(\mathrm{c})}$ and $\tau_y^{(\mathrm{c})}$ in the stresses.

A point $\left(\lambda_x^{(\mathrm{b})}, \lambda_y^{(\mathrm{b})}\right)$ on the boundary in the stretch space is mapped by Hooke's law to a point $\left(\tau_x^{(\mathrm{b})}, \tau_y^{(\mathrm{b})}\right)$ on the boundary in the stress space. From this point on, stresses $(\tau_x, \tau_y) = \left(\tau_x^{(\mathrm{b})}, \tau_y^{(\mathrm{b})}\right) + \left(\tau_x^{(\mathrm{c})}, \tau_y^{(\mathrm{c})}\right)$ can be reached, where the hard-core contributions $\tau_x^{(\mathrm{c})}$ and $\tau_y^{(\mathrm{c})}$ must be negative (because the skeleton can only support compressive stresses) and must obey the ratio constraint (5.32). The submanifold of stresses which is accessible from the point on the boundary is, thus, a straight line with a slope $\left(\lambda_y^2/\lambda_x^2\right)^2/3$ starting from boundary 1 or $3\left(\lambda_y^2/\lambda_x^2\right)^2$ starting from boundary 2 in fig. 5.12 b), see the thin red and blue lines.

For point B, with $\lambda_x = \lambda_y = L$, the ratio of the hard-core stresses is not fixed to a certain value. Instead, in can range from 1/3 to 3. In the plot of the stress plane, fig. 5.12 b), this means that the whole white region is accessible from point B.

5.5.2. Shape equations in the pendant/rising capsule geometry

We now apply the previously developed elasticity model to the shape equations in the pendant/rising capsule geometry. We identify the x-direction of the planar model with the (meridional) s-direction of the shell, and the y-direction with the (circumferential) φ-direction. To evaluate the right-hand side of the shape equations (5.7), we must be able to calculate λ_s

and τ_φ from given $\lambda_\varphi = r/r_0$ and τ_s. With the help of the plots of the stretch and stress planes in fig. 5.12, we can figure out the suitable algorithm:

- We check if the point is in the admissible domain or on the boundary by calculating $\lambda_s^{(\mathrm{b})}(\lambda_\varphi)$ with (5.30) and $\tau_s^{(\mathrm{s})}\big(\lambda_s^{(\mathrm{b})}, \lambda_\varphi\big)$ using (5.27), which is the smallest possible stress in the admissible domain. If the given τ_s is larger than this value, the point is in the admissible domain, if it is smaller then the point is on the boundary to the forbidden domain.

- If the point is in the admissible domain, everything is as before and eqs. (5.8) can be used to calculate λ_s and τ_φ.

- If the point is on the boundary, then we know that $\lambda_s = \lambda_s^{(\mathrm{b})}(\lambda_\varphi)$ according to eq. (5.30). In addition, we can calculate the spring contributions $\tau_s^{(\mathrm{s})}\big(\lambda_s^{(\mathrm{b})}, \lambda_\varphi\big)$ from Hooke's law (5.27). The hard-core contribution can then be obtained as the difference between the given τ_s and the spring contribution, $\tau_s^{(\mathrm{c})} = \tau_s - \tau_s^{(\mathrm{s})}\big(\lambda_s^{(\mathrm{b})}, \lambda_\varphi\big)$. This value should be negative. The sought stress τ_φ can then be calculated from the Hookean contribution $\tau_\varphi^{(\mathrm{s})}$ according to (5.27) and the hard-core contribution $\tau_\varphi^{(\mathrm{c})}$ according to (5.32), so that $\tau_\varphi = \tau_\varphi^{(\mathrm{s})}\big(\lambda_s^{(\mathrm{b})}, \lambda_\varphi\big) + \tau_\varphi^{(\mathrm{c})}$.

Thus we can use the usual shape equations (5.7) for the integration when the lattice is on boundary 1 or 2. Just the closing relations (5.8) that are necessary to compute the right-hand side must be replaced by the above procedure.

This method does not work when the lattice is stuck in point B, which must be handled separately in the shape equations. The reason is that the confinement to $\lambda_s = \lambda_\varphi = L$ already determines the shape of the capsule: It is uniformly compressed. The circumferential stretch $r/r_0 = L$ directly implies $r(s_0) = Lr_0(s_0)$. Inserting this solution into the differential equation for r in the system of shape equations (5.7) then yields $\psi(s_0) = \psi_0(s_0)$. The differential equation for z then becomes $z'(s_0) = L\sin\psi_0$ and has the solution $z(s_0) = Lz_0(s_0) + c$ with some constant c depending on the starting value. From the differential equation for ψ in the shape equations (5.7) we can then deduce

$$\tau_\varphi = \left(-\frac{\kappa_{s_0}}{L}\tau_s + p - \Delta\rho\, g\, z\right)/\kappa_\varphi \tag{5.33}$$

by inserting the known solutions. So in principle, only τ_s must be determined by solving its differential equation. In order to keep the code of the numerical implementation consistent, however, we solve the full system of shape equations (5.7) with the closing relations (5.8) modified to contain the explicit result (5.33) just derived. This produces the correct numerical solutions in the same "data format" as in all other parts, at the cost of having wasted some computation time.

When the lattice is in the jammed state B already at the start point of integration (at the apex), we need to evaluate the limits of the explicit solutions for $s_0 \to 0$. At the apex, the meridional and circumferential curvatures coincide, $\kappa_s(0) = \kappa_\varphi(0) = \kappa_{s_0}/L = p_0/2\gamma L$. From the force balance, the meridional and circumferential tensions follow as $\tau_s(0) = \tau_\varphi(0) = pL\gamma/p_0$. This finding has a remarkable impact: $\tau_s(0)$ is fixed by the external parameters, and cannot serve as a shooting parameter! The problem of having lost the only shooting parameter is resolved below in the discussion of continuity conditions.

Wrinkling can occur when the lattice is jammed on boundary 2 or point B. Like in section 5.2.3, we handle wrinkling by introducing a pseudo-surface (indicated with an overbar) and setting the hoop stress to zero. On boundary 2, we have $\lambda_\varphi = \sqrt{4L^2/3 - \lambda_s^2/3}$ (note that λ_φ

refers to the hoop stretch of the real, wrinkle surface and is to be distinguished from the pseudo hoop stretch $\bar{\lambda}_\varphi = \bar{r}/r_0$). The condition $\tau_\varphi = 0$ is equivalent to

$$\tau_\varphi^{(\mathrm{c})} = -\gamma - \frac{E_{2\mathrm{D}}}{1-\nu^2}\frac{1}{\lambda_s}\left[\left(\lambda_\varphi - 1\right) + \nu(\lambda_s - 1)\right]. \tag{5.34}$$

We further have $\tau_s^{(\mathrm{c})} = \tau_\varphi^{(\mathrm{c})} \cdot \lambda_s^2/3\lambda_\varphi^2$. So the complete meridional tension, measured per unit length of the pseudo-surface, is determined by

$$\bar{\tau}_s = \frac{\lambda_\varphi}{\bar{\lambda}_\varphi}\left[\tau_s^{(\mathrm{s})}(\lambda_s, \lambda_\varphi) + \frac{1}{3}\frac{\lambda_s^2}{\lambda_\varphi^2}\,\tau_\varphi^{(\mathrm{c})}\right]. \tag{5.35}$$

This is a quite complicated function of λ_s, because $\tau_\varphi^{(\mathrm{c})}$ and λ_φ herein also depend on λ_s. It must be solved for λ_s to evaluate the right-hand side of the wrinkled shape equations (5.15), which is done numerically in each integration step of the shape equations.

When wrinkling occurs in point B, the shape equations for the pseudo-surface (5.15) can also be used, and since $\lambda_s = \lambda_\varphi = L$, the inversion of a stress-strain relation to obtain λ_s is not necessary. In point B, the hard-core stresses $\tau_s^{(\mathrm{c})}$ and $\tau_\varphi^{(\mathrm{c})}$ are independent of each other, and the spring contributions $\tau_s^{(\mathrm{s})}$ and $\tau_\varphi^{(\mathrm{s})}$ are fixed because of $\lambda_s = \lambda_\varphi = L$. From the wrinkling condition $\tau_\varphi = 0$ we can, thus, calculate $\tau_\varphi^{(\mathrm{c})}$. The meridional hard-core contribution $\tau_s^{(\mathrm{c})}$ must be calculated from the differential equation for τ_s. Note that the geometry of the pseudo-surface is not fixed by the condition $\lambda_s = \lambda_\varphi = L$ because the circumferential stretch $\bar{\lambda}_\varphi$ of the pseudo-surface is free. This is in contrast to the case of a lattice being stuck in point B without wrinkling as discussed above.

5.5.3. Numerical integration and switching between the shape equations

The modified shape equations are integrated from the apex, $s_0 = 0$ to the attachment point $s_0 = L_0$ to the capillary. On this way, the integration will run through different domains and must switch to the appropriate shape equations discussed in the previous section. Figure 5.13 shows typical trajectories of the integration in the stress plane, that is, parametric plots of $(\tau_s(s_0), \tau_\varphi(s_0))$ with $s_0 \in [0, L_0]$.

We name the different domains of the stress plane as follows: The admissible domain (light green in fig. 5.13) is abbreviated “A”, the red and blue ruled regions are termed “1” and “2” (because they come from boundary 1 and 2 in the stretch plane), and the white region is termed “B”. Regions 2 and B also appear in wrinkled form, we then call them “2W” and “BW”.

In the numerical integration, an event handler must be introduced which detects when the integration runs from one region into another. This is quite similar to our treatment of the wrinkled region, where an event handler was implemented that checks the wrinkling condition (5.11) and switches to the appropriate shape equations. Changes from region A to regions 1, 2 or B can be detected on the basis of strains, which are limited by the boundary (5.30). The other direction, a change from a hard-core region into the A domain, occurs when the hard-core stresses become positive.

Switching between the different hard-core regions is, however, a bit more complicated because the continuity conditions are less obvious. An elaborate variational calculation shows surprisingly that τ_φ may jump at transitions from B $\to$ BW, B $\to$ 2, 2 $\to$ 1 and BW $\to$ 1 see appendix E.2 and fig. 5.13. This jump is necessary, especially when starting in region B, where we have seen that the shooting parameter is eliminated: The jump, or rather its arc-length coordinate s_J, serves as an substitute shooting parameter. In the following discussion of each trajectory shown in fig. 5.13 this becomes clearer.

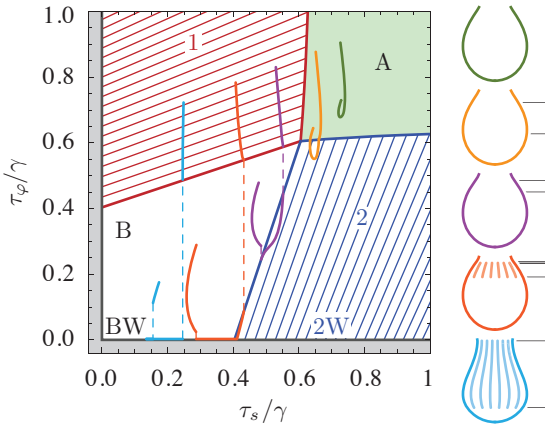

Figure 5.13.: Trajectories in the stress plane for integrations at different stages of deflation (see pictograms on the right), thin dashed parts of the trajectories are jumps in τ_φ. The integration always starts at the apex with $\tau_s = \tau_\varphi$, i.e. on the angle bisector, and runs through different domains of the stress plane. The parameters of the elastic model are $E_{2D}/\gamma = 5$, $\nu = 1/3$ and $L = 0.95$. In the pictograms, thin horizontal lines indicate the transitions between the regions.

B → BW → 1, light blue. The transition from B to BW occurs at s_J which can be chosen arbitrary (it just has to occur before the trajectory reaches the wrinkling region $\tau_\varphi = 0$). This is the shooting parameter that is adjusted to match the boundary condition $r(L_0) = a/2$ at the end of integration. The rest of the trajectory is "deterministic": The jump from BW to 1 occurs when the wrinkling condition $\bar{\lambda}_\varphi \leq \lambda_\varphi$ becomes false. As the stretches are fixed to L in B, BW and on the boundary of 1, the stretches are continuous at this transition, only the hoop stress jumps.

B → BW → 2W → 2 → 1, light red. The first transition occurs again at a free position s_J, and the remainder of the course is deterministic: BW → 2W is continuous and occurs when the ratio $\tau_\varphi^{(c)}/\tau_s^{(c)}$ becomes larger than 3; 2W → 2 is also continuous and happens when $\bar{\lambda}_\varphi$ becomes larger than λ_φ; and 2 → 1, which has a jump in τ_φ, is determined by λ_φ becoming larger than L.

B → 2 → 1, violet. Again, the transition out of region B happens at a shooting parameter s_J, and the second transition is deterministic as explained in the previous trajectory.

A → 2 → A, dark yellow. This trajectory is entirely deterministic, and the shooting parameter is $\tau_s(0)$ as usual because we are starting in region A. The integration switches from A to 2 when the boundary (5.30) in the stretch plane is reached; and back to A when the hard-core stresses become positive. Both transitions are continuous. A transition from A to 1 is also possible and obeys the same reasoning.

The dark green trajectory is trivial because it stays in region A for the whole integration. More paths are possible and have been worked out, but the presented ones were most commonly met in the numerical investigations.

5.5.4. Analysis of theoretically generated shapes with Hookean elasticity

With the newly developed shape equations we can compute deflated shapes of capsules obeying our custom elasticity model for bead-spring networks with hard cores. Starting with a Laplace-Young shape with $\tilde{\rho} = 0.25$ and $\tilde{p}_0 = 2$ (in the reduced units of tab. 5.1), the pressure is lowered from $p = p_0$ to $p = 0.1p_0$. Figure 5.14 shows the length of the wrinkled region as a function of the reduced volume for three such series of deflated shapes with different elastic parameters. The curves without hard-core interactions (red and blue, with $L = 0$) show that the onset of

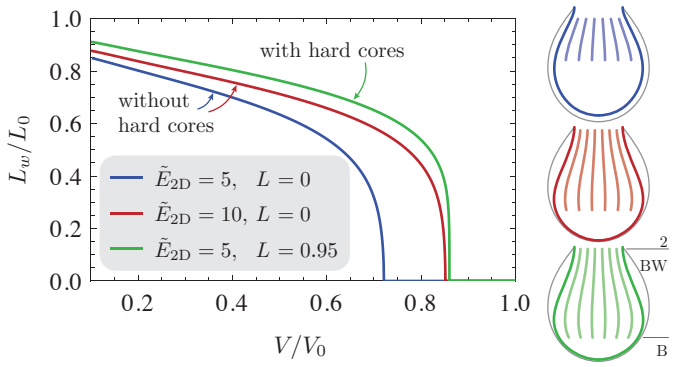

Figure 5.14.: Wrinkle length as a function of the reduced volume for deflated shells with and without hard-core interactions, for $\nu = 1/3$ and $\tilde{E}_{2D}$ as indicated in the legend. The shapes on the right for $V = 0.7V_0$ reveal differences not only in L_w but also in the overall shape (colours as in the legend, thin grey line is the undeformed shape, integration regions are indicated in the green contour).

wrinkling occurs earlier for higher elastic moduli. If hard-core interactions are included and occur already for small compressions (green curve, $L = 0.95$), the wrinkling sets in early, even though the elastic modulus is small.

Thus, if a shape analysis that judges only L_w and uses the usual Hookean elasticity without hard cores is applied to shapes that obey our custom elasticity model, it overestimates the elastic modulus considerably. Figure 5.14 illustrates this as the green line with $\tilde{E}_{2D} = 5$ and $L = 0.95$ is much closer to the red line with $\tilde{E}_{2D} = 10$ than to the blue line with $\tilde{E}_{2D} = 5$.

Our shape analysis does not rely on a measurement of L_w, but analyses the contour of the deflated shell. However, the wrinkled region is a very characteristic feature of the deflated shape, and has a large impact on the contour. In the wrinkled region, the contour typically appears rather straight and is relatively little curved [153]. We therefore expect similar results when our shape fitting procedure uses Hookean elasticity to fit deflated shapes in which hard-core interactions are important.

This hypothesis is tested in a fashion similar to that of section 5.3: Series of deflated shapes are computed using the modified shape equations, each theoretically generated shape is converted into a set of sampling points and fed to the usual shape analysis algorithm which uses Hookean elasticity without hard cores. As shown in fig. 5.15, the fitted area compression modulus $\tilde{K}_{2D}$ can differ substantially from the value $\tilde{K}_{orig}$ that has been used for the theoretical shape generation.

The analysis is concentrated to area compression moduli of $\tilde{K}_{orig} = 5$ to 20, hard-core lengths $L = 0.95$ to 0.99 and Poisson ratio $\nu = 1/3$ (which is fixed to this value also in the Hookean fits). When small hard-core lengths are combined with large area compression moduli, e.g. $L = 0.95$ with $\tilde{K}_{orig} = 20$, the hard-core interactions have no influence on the shape, because it starts to wrinkle before the hard-core domains are reached. The numerical integration then takes a path $\mathrm{A} \to \mathrm{AW} \to \mathrm{A}$, and produces a shape that can also be produced by the Hookean shape equations without hard-core interactions. This shape can be perfectly fitted with Hookean elasticity and reproduces the correct area compression modulus, and therefore these cases are omitted from fig. 5.15. There are some deflation series that are very close to the limit where the hard-core interactions cease to influence the shape (see $L = 0.96$ and $\tilde{K}_{orig} = 10$ in fig. 5.15, for example), where there are only small deviations between fit result and original modulus.

In deflation series where the hard-core interactions profoundly influence the shape, the course of the fitted area compression modulus is close to our expectations. For small deformations, where the hard cores are not yet in contact, the original value is reproduced, $\tilde{K}_{2D} = \tilde{K}_{orig}$. When the hard cores come into contact (which also triggers wrinkling), the fitted modulus can grow much larger than the original value. The peculiar dip in $\tilde{K}_{2D}$ shortly before the onset of

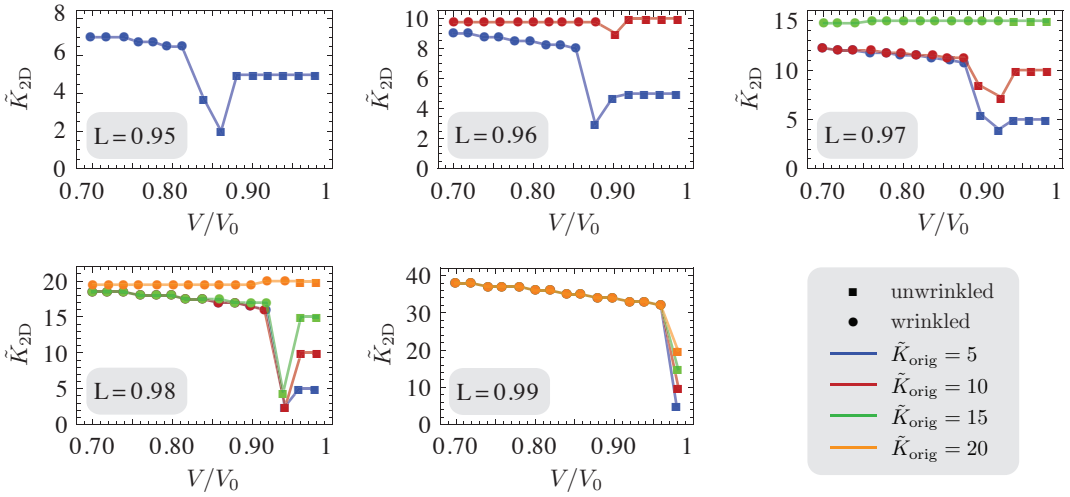

Figure 5.15.: Fit results for theoretically generated capsule shapes of various area compression moduli $\tilde{K}_{\text{orig}}$ and hard-core lengths L. The fits are performed using the usual Hookean elasticity (without hard cores) and come to differing results $\tilde{K}_{2D}$ for the fitted area compression modulus. In both shape generation and fits, the Poisson ratio is fixed to $\nu = 1/3$.

wrinkling is an artifact of holding $\nu = 1/3$ constant in the fits. Further tests with free ν showed that these points can also be fitted with $\tilde{K}_{2D}$ near $\tilde{K}_{\text{orig}}$ and ν dropping to negative values; a result which also lacks an intuitive explanation.

After the onset of wrinkling, the fitted values of $\tilde{K}_{2D}$ are on a plateau and increase only slightly for increasing deflation. The plateau value is independent of the original value $\tilde{K}_{\text{orig}}$, but it depends strongly on the hard-core length L: The larger L, the larger is the plateau value. Consequently, the fitted $\tilde{K}_{2D}$ can jump quite high at the onset of wrinkling if $\tilde{K}_{\text{orig}}$ is small and L is large; in fig. 5.15 it jumps to more than its six-fold value for $\tilde{K}_{\text{orig}} = 5$ and $L = 0.99$.

It was the aim of the newly developed elasticity model to explain the HFBII fit results (see fig. 5.9), to produce the same "signature" in the plots of fitted compression modulus versus reduced volume. Comparing fig. 5.15 to fig. 5.9, it becomes clear that this has only been achieved in part. It is possible to explain the hard jump at the onset of wrinkling, but not the initial increase of the compression modulus, nor its final decrease as obtained in the HFBII fits.

The initial increase of the compression modulus might be obtained if non-linear spring interactions are included in the elasticity model (springs that get stiffer for proceeding compression). The decrease after the jump, on the other hand, might be considered as a decreasing hard-core length L, because for smaller L, the plateau value is smaller. This could be modelled by "hard" cores which actually can be slightly compressed. Replacing the hard-core interactions by spring-interactions with relatively large spring constant could achieve this.

In summary, there are several indicators that the proposed elastic model is too "hard" in distinguishing easily compressible domains and purely incompressible ones. A softer transition might produce results closer to the HFBII elasticity, modelled for example by springs whose spring constant slightly increases with compression, and then sharply increases to a large but finite hard-core spring constant. Such a model could even be more tractable on the theoretical part because the resulting elastic law might come out as a bijective mapping between stretches and stresses if the spring constant is a continuous function of the compression. Then the tedious case-by-case analysis given above could be spared. In addition, the proposed model is

theoretically appealing because it can be easily verified by simulating the network of beads and springs directly. This gives a nice project for future research activities on this field.

Chapter 6

Conclusions and outlook

In this thesis, several new research results on the deformation of elastic shells have been reported. They are grouped in three divisions: The buckling transitions of deflated spherical shells, wrinkling and buckling of plates and shallow shells under in-plane loads and the deflation of capsules that are attached to a capillary. Special emphasis was put on the applications of the theoretical results in shape analyses to determine the elastic moduli of shells from simple experimental observations.

6.1. Buckling transitions of spherical shells

We first considered spherical shells that are deflated, and completed the theoretical understanding of the generic deformation behaviour. The deflation starts with a spherical shape for small volume changes, and jumps to an axisymmetric buckled shape in a primary buckling transition. If the shell is thick enough, it remains axisymmetric, and deflates completely until opposite sides are in contact. Thin shells, however, undergo a secondary buckling transition in which the dimple acquires a polygonal shape and loses its axisymmetry.

Two approaches to compute buckled axisymmetric shapes have been introduced in chapter 2. The first approach is based on non-linear shell theory with Hookean elasticity, i.e. with a quadratic strain-energy density function. Equilibrium equations have been derived by a variational calculation, and they coincide with the force and moment equilibrium conditions found in the literature. It is beneficial to have an energy functional at hand from which the shape equations follow by minimisation, because it provides a least energy criterion for competing shapes to decide which one is the physical ground state. A special case, where opposite sides of a strongly deflated shell are in contact, has also been considered. The second approach is an analytical model proposed by Pogorelov, which is specially designed for buckled shapes with a finite dimple. It is based on the observation that the buckled shape is close to an isometric deformation of the sphere, with a mirror-inverted spherical cap. We have seen that this approximate model agrees very well with the numerical solutions of the non-linear shape equations.

The first buckling, from a spherical to an axisymmetric indented shape, has been investigated under three different load cases, see section 2.5. We have seen that the stability of buckled shapes (with respect to further growth of the dimple) depends decisively on the load case.

When a simple mechanical pressure difference between the inside and outside is prescribed, the shell collapses completely after the buckling has set in, so that opposite sides of the shell are in contact. In the shell theory literature, this phenomenon is termed snap-through buckling. The onset of buckling is somewhere between the critical pressure $p_c \sim -\tilde{E}_B^{3/4}$ and the classical buckling pressure $p_{\mathrm{cb}} \sim -\tilde{E}_B^{1/2}$, see eqs. (2.58) and (2.46), where the imperfections inherent to real shells prevent the theoretical limit of p_{cb} to be reached in reality. The dimensionless bending stiffness that occurs in these relations is proportional to the ratio of bending stiffness and surface Young modulus, $\tilde{E}_B = E_B/E_{2\mathrm{D}}R_0^2$, see eq. (2.22).

On the other hand, when the system is constructed so that the shell must have a given volume, the first stable shapes after buckling have a small, but finite dimple. Buckling then occurs between the critical volume difference $\Delta V_{1\mathrm{st}}/V_0 \sim \tilde{E}_B^{3/5}$ and the classical threshold $\Delta V_{\mathrm{cb}}/V_0 \sim \tilde{E}_B^{1/2}$, see eqs. (2.50) and (2.49), respectively. Between these thresholds, the buckled shape is the energetically favourable ground state, and the spherical shape is metastable; the metastability is lost at ΔV_{cb} where the spherical shape becomes unstable.

In most experiments, there will be a feedback between the deformation and the pressure difference exerted on the shell, for example if the shell encloses a gas and for osmotic pressures. The feedback by an internal medium stops the snap-through buckling known from pressure control at a finite volume, thus stabilising buckled shapes with medium volume. Our findings explain why these are the shapes that are usually observed in osmosis driven microcapsule experiments, although they are unstable from the simple viewpoint of pressure control. This requires, however, that the initial osmolyte concentration in the capsule interior is sufficiently large. Buckling under osmotic pressure is indeed intermediate between buckling under volume control and buckling under mechanical pressure: In the limit of a small number N_{in} of osmotically active molecules in the capsule interior, buckling under mechanical pressure control is recovered; for increasing N_{in}, the behaviour effectively approaches buckling under volume control. The stabilising effect of an internal medium, such as an enclosed gas or osmotically active particles, is quite generic as long as the force density exerted on the shell is still a normal pressure that is spatially constant. We checked that the same qualitative results could be obtained by including a compressible fluid in the shell, with a free energy contribution $F \sim (V - V_0)^2$.

Two shape analyses for axisymmetric buckled shells have been developed. In section 2.4.2 we saw that the curvature at the dimple edge depends strongly on the dimensionless bending stiffness, with smaller bending stiffnesses leading to sharper bends. A power law $\kappa_{\mathrm{edge}} \sim \tilde{E}_B^{1/4}$ describes this dependence for sufficiently small bending stiffnesses and sufficiently small volume changes. This relation can be used to extract the reduced bending stiffness of a shell by analysing an image of its buckled shape. An experimental verification of this method has recently been done by Jose et al. [71].

The second shape analysis, see section 2.5.5, is intended to use spherical microcapsules as osmotic pressure sensors. An accurate analytic formula (2.69) has been derived that allows to deduce the osmotic pressure from the observed volume of buckled capsules when their elastic moduli are known. This relation can also be used to obtain the elastic moduli of a capsule from the measured volume if the external osmotic pressure is known from an independent measurement. When this shape analysis is combined with the first one, the absolute values of the surface Young modulus and bending stiffness can be determined (and not only the ratio between them). We applied the second shape analysis to published experimental data on polyelectrolyte capsules [51]. Our findings are also relevant for stabilising buckled shapes of a desired volume in applications by choosing the osmolyte concentrations according to eq. (2.71).

In chapter 4, we explained the mechanism behind the secondary buckling transition where the dimple loses its axisymmetry. So far, the secondary buckling transition has only been observed in experiments or simulations but lacked a physical explanation. The key ingredient underlying the secondary buckling is a locally compressive hoop stress, with a characteristic negative peak near the edge of the axisymmetric dimple. In a quantitative analysis, we approximated the profile of the compressive hoop stress τ_φ by a parabola. This led to a derivation of a critical compressive stress, the "curved plate criterion" in the auxiliary chapter 3. This threshold is quite analogous to the critical force in the Euler buckling of bars: When the critical stress is reached, the membrane cannot support the compression anymore and buckles out of its symmetric shape in order to release the compressive stress. Our analysis also showed that the secondary buckling transition is continuous as opposed to the primary buckling transition, which is discontinuous.

We found the critical volume reduction at the onset of secondary buckling by applying the curved plate criterion to solutions of the shape equations and the Pogorelov model of axisymmetric buckled shapes. The results have been verified by a linear stability analysis in the framework of non-linear DMV shell theory, where the full geometry and stress state has been taken into account. All three approaches produce consistent results for the critical volume reduction of secondary buckling, which is proportional to $\Delta V_{2\mathrm{nd}}/V_0 \sim \tilde{E}_B$. This result is also in agreement with existing simulation data in the literature.

Furthermore, we have obtained results for the wrinkle number n at the onset of secondary buckling and beyond. Scaling arguments give $n \sim \tilde{E}_B^{-1/4}\Delta V^{1/4}$, see eq. (4.24), for the number of wrinkles. At the onset of secondary buckling, where $\Delta V_{2\mathrm{nd}} \sim \tilde{E}_B$, the wrinkle number becomes approximately independent of the reduced bending stiffness in accordance with our more detailed analysis, see fig. 4.7. Beyond the onset of secondary buckling, the wrinkle number increases like $n \sim \Delta V^{1/4}$ in accordance with numerical simulations in the literature. Small discrepancies between our three approaches concerning the number of wrinkles at the onset of secondary buckling show that the number is very sensitive to the "ingredients" of the theoretical analysis.

Finally, a phase diagram for deflated spherical shells under volume control has been created, see fig. 4.5. It presents the stability regimes of all three relevant shapes (spherical, axisymmetric buckled, polygonal buckled), which are separated by the thresholds $\Delta V_{1\mathrm{st}}$, ΔV_{cb} and $\Delta V_{2\mathrm{nd}}$ summarised above. The phase diagram is certainly one of the central results of this thesis.

6.2. Wrinkling and buckling of shallow shells

The aim of chapter 3 was to establish a secondary buckling criterion based on our observation that axisymmetric buckled shapes have a negative peak in the hoop stress in the region where wrinkles appear according to numerical simulations. In the theoretical framework of small-strain elasticity theory for plates and shallow shells, stability equations have been derived from an energy functional by considering small normal deflections of the reference state. Stability equations (not to be confused with equilibrium equations) can predict emerging buckling patterns. The critical load at which the amplitude of the buckling pattern begins to grow is an important quantity that is to be determined, as well as the geometrical properties of the pattern like its wavelength.

A rectangular plate with simply supported edges served as a first example and reference case. It is compressed in x- direction and stretched in y-direction by spatially constant stresses $\tau_x < 0$ and τ_y. We used the stability equations to calculate the critical compressive stress $\tau_{x,c} \sim -E_B/\lambda_c^2$ at which the first mode becomes unstable. This unstable mode is a sinusoidal

pattern with wavelength λ_c, which is of the order of the plate width $\lambda_c \sim L_y$ for vanishing lateral tension $\tau_y = 0$, or determined by $\lambda_c \sim (E_B L_y^2/\tau_y)^{1/4}$ if the lateral tension τ_y is large, see eq. (3.65). The first case, with relatively large wavelength, is traditionally called buckling, and the second case, where the wavelength is much shorter, wrinkling.

The buckling problem of a rectangular plate under compression is, of course not new, and has been investigated extensively before. However, the phenomena of buckling and wrinkling have mostly been considered separately and with different tools. Buckling is usually investigated as done here, using stability equations to calculate a critical stress and the wavelength, see for example Timoshenko's books [124, 125]. Wrinkling, on the other hand, is typically investigated using energy arguments, in which an elastic energy is minimised with respect to the wrinkle wavelength [26]. A threshold for the compressive stress cannot be calculated in this framework, instead, it is assumed that the system is well beyond this threshold. Some authors refer to these different approaches as the NT (near threshold) analysis for buckling and the FFT (far from threshold) analysis for wrinkling [34]. Here, however, we have found a model system in which a crossover from buckling to wrinkling can be observed, all in a unified calculation based on the stability equations. The essential difference between buckling and wrinkling is not that buckling is near the onset and wrinkling far beyond the onset, it is the value of the lateral tension τ_y which is decisive. Wrinkling is obtained for $\tau_y \gg E_B/L_{\text{eff}}^2$, where L_{eff} is the length of the wrinkles. We were able to find these results because we imagined to control the compression τ_x and lateral tension τ_y independently from each other. In typical experiments with wrinkled thin sheets, however, there is only one parameter, for example the shear angle when a sheet is sheared. Then, τ_x and τ_y are not independent, but are ramped up simultaneously by increasing the single deformation parameter. The analysis of such setups offers thus only a limited view on the scaling laws that govern buckling and wrinkling.

As a second example problem, we studied the buckling and wrinkling of an infinite plate under localised compression in form of a parabolic stress profile $\tau_x(y)$. This system is already close to a portion of an axisymmetric buckled shell, where a negative peak in the hoop stress $\tau_\varphi(s_0)$ occurs that can be approximated by a parabola around its minimum. We have seen, for example in fig. 3.10, that the results for the critical compression $\tau_{x,c}$ and critical wavelength λ_c can be mapped onto the previous results for fixed plate edges by choosing an effective plate width L_{eff} that roughly coincides with the length of the wrinkles.

Finally, an initial small curvature in y-direction was incorporated into the model. The curvature $\kappa_y(y)$ was chosen to increase linearly with y, because the same behaviour is observed for the meridional curvature of axisymmetric buckled shapes in the region where the secondary buckling starts. Our analysis for $\tau_y = 0$ showed that the curvature has an impact on the numerical prefactors in the results for $\tau_{x,c}$ and λ_c. With eqs. (3.57) and (3.58), the "curved plate criterion" was written down, to be used in the analysis of the secondary buckling of spherical shells.

6.3. Deflation of capsules attached to a capillary

In the last part of this thesis, chapter 5, an elastometry method for capsules prepared from pendant drops or rising bubbles has been developed. The shape equations for shells of revolution as introduced for spherical shells can also be used to describe capsules with a reference configuration in form of a droplet shape, which is a solution of the Laplace-Young equation. For application to pendant capsules, the shape equations must be modified by setting the bending stiffness to zero (because the experimentally investigated capsules are typically very thin) and to introduce a pseudo-surface around which the real midsurface wrinkles in regions of compressive

hoop stress. This model describes the contours of deflated experimental polysiloxane capsules and hydrophobin coated bubbles accurately. A separate energy consideration gave a relation between the wavelength of the wrinkles and the bending stiffness of the capsule membrane.

A three step fitting procedure allows to completely characterise the mechanical properties of a capsule attached to a capillary: First, the undeformed shape is fitted with the Laplace-Young equation to obtain the interfacial tension γ. Then, a series of deflated shapes is fitted using our shape equations, which gives the Poisson ratio ν and area compression modulus $K_{2\mathrm{D}}$ of the capsule membrane. Finally, the bending stiffness E_B can be determined from a measurement of the wrinkle wavelength.

At first, the fitting procedure has been tested by fitting theoretically generated deflated shapes in order to check if the original moduli are reproduced by the fit. The fitting procedure works well as long as the noise in the set of sampling points, which is present in real applications due to the experimental images and the contour detection algorithm, is substantially smaller than the deformation. For comparison, we also analysed the theoretically generated shapes by fitting the Laplace-Young equation to them and calculating the Gibbs elasticity modulus from the obtained apparent interfacial tension. Surprisingly, the Laplace-Young analysis fails to produce reasonable results for the elastic modulus, even for very small deformations. This result is very important because this technique has been widely used by researchers working with pendant capsules [1, 68, 119].

Then, the procedure has been applied to two different systems of capsules, pendant polysiloxane (OTS) capsules and rising bubbles coated with the protein hydrophobin (HFBII). Applying this method to an OTS capsules gave reasonable values for all three elastic constants: $K_{2D} \approx 500\,\mathrm{mN/m}$, $\nu \approx 0.6$ and $E_B \approx 1.2 \cdot 10^{-14}\,\mathrm{Nm}$ for the small deformation behaviour. Furthermore, the analysed capsule shows softening or creep with decreasing volume, which can also be observed for the hydrophobin capsule (see figs. 5.7 and 5.9).

For the analysed HFBII capsule, the area compression modulus initially grows upon deflation, $K_{2\mathrm{D}} = 160\,\mathrm{mN/m}$ to $500\,\mathrm{mN/m}$ if we assume $\nu = 0.6$. At the onset of wrinkling, it jumps to $2000\,\mathrm{mN/m}$ because compression of the rigid protein core sets in (see fig. 5.9). Obviously, this complex behaviour cannot be explained by simple Hookean elasticity, and our measurement suggests that an appropriate elasticity model should include an immense strain stiffening upon compression.

We started to develop such a custom elasticity model for hydrophobin layers in the final section 5.5. This model is based on the microscopic view of particles with hard cores arranged in a two-dimensional lattice, crosslinked with soft compressible springs. While the springs contribute a Hookean elasticity to the network as used in the usual shape equations, the hard-core interactions impose constraints on the admissible strains. Hard-core contributions to the stresses enforce these constraints. An analysis of the shape equations constructed around this elasticity model revealed that wrinkling can be triggered by the onset of the hard-core interactions. This coincides with the observation that the analysed HFBII capsule starts to wrinkle after the measured jump in the area compression modulus.

As a further test whether the proposed elasticity model is a good approach to hydrophobin elasticity, we generated deflated shapes obeying our custom elasticity model and fitted them using the usual shape equations with Hookean elasticity without hard-core interactions. The signature obtained in these fits is not exactly the same as observed for HFBII capsules. Our elasticity model can explain the jump in the area compression modulus when the hard cores get in contact and trigger wrinkling. However, the other remarkable features of the apparent HFBII elasticity, namely the initial increase and final decrease of the area compression modulus, are not reproduced.

6.4. Outlook

During the research for this dissertation, new questions arose showing possible paths that could be worth an investigation. The following short discussion of open questions shall conclude this thesis.

Concerning the stability of buckled shapes after the first buckling transition of spherical shells, our investigation has drawn a fairly complete picture for volume control, pressure control and osmosis. However, even more experimental situations are possible which give rise to a feedback. When the shell material chemically reacts with an enclosed substance, there could be a feedback between the volume (or internal concentration of the substance) and the elastic moduli of the membrane. Deflation mechanisms such as slowly dissolving the interior liquid of the capsule by the external liquid [32, 113, 150] will involve a feedback if the exterior volume is not much larger than the internal capsule volume. Such feedbacks can either stabilise or destabilise non-collapsed buckled shapes. If reducing the capsule volume increases the internal pressure or stiffens the capsule material, non-collapsed shapes will be stabilised. However, if it is the other way around, complete collapse upon buckling will be the generic behaviour.

There are also open questions on the secondary buckling of spherical shells, which has been investigated only for volume control in this thesis. For pressure control and shapes with opposite sides in contact, the secondary buckling may also occur, but in modified form. Furthermore, our theory is only valid for shapes close to axisymmetry. Wrinkled shapes beyond the onset of secondary buckling cannot be calculated so far (except by numerical simulations). Thus, quantitative theoretical results for the evolution of the wrinkle amplitude and wrinkle number are still missing.

The analysis of pendant OTS and rising HFBII capsules has proved the concept of our elastometry method, which could be added to the features of pendant drop tensiometers in the future. The method is a convenient tool for physical chemists who seek to characterise the elastic properties of synthesised membranes. It can reveal changes in elastic constants with decreasing volume that are not accessible by other methods. This is an important feature for experimenters who try to design stable membranes that can be reversibly deformed. An immense improvement of the method could be achieved by a simultaneous measurement of the pressure inside the capsule, which should be possible with most commercially available pendant drop tensiometers as they already have built-in pressure sensors. This would eliminate one of the fit parameters and lead to a preciser determination of the area compression modulus.

Appendix A

Shape equations for shells of revolution

A.1. Derivation of the equilibrium equations

In section 2.2.3, the calculus of variations to derive the equilibrium equations from an energy functional was sketched. Between (2.12) and (2.15) lies a calculation in which the variations of the strains must be expressed in terms of the normal and tangential displacements δu and δv. To this end, we write the strains in terms of r, z and ψ by virtue of the geometric relations introduced in section 2.2.1,

$$\begin{aligned} e_s &= \lambda_s - 1 = \sqrt{r'^2 + z'^2} - 1, & e_\varphi &= \lambda_\varphi - 1 = r/r_0 - 1, \\ K_s &= \lambda_s \kappa_s - \kappa_{s_0} = \psi' - \kappa_{s_0}, & K_\varphi &= \lambda_\varphi \kappa_\varphi - \kappa_{\varphi_0} = \sin\psi/r_0 - \kappa_{\varphi_0}, \end{aligned} \tag{A.1}$$

where a prime denotes the derivative $\mathrm{d}/\mathrm{d}s_0 = \lambda_s \,\mathrm{d}/\mathrm{d}s$. The variations of the strains can thus be reduced to the variations of r, z and ψ (and their derivatives), which are related by (2.11) to the variations δu and δv,

$$\delta r = \sin(\psi)\,\delta u + \cos(\psi)\,\delta v \quad \text{and} \quad \delta z = -\cos(\psi)\,\delta u + \sin(\psi)\,\delta v \tag{A.2}$$

$$\Rightarrow \quad \begin{cases} \delta r' = \cos(\psi)\psi'\,\delta u + \sin(\psi)\,\delta u' - \sin(\psi)\psi'\,\delta v + \cos(\psi)\,\delta v' \\ \delta z' = \sin(\psi)\psi'\,\delta u - \cos(\psi)\,\delta u' + \cos(\psi)\psi'\,\delta v + \sin(\psi)\,\delta v' \end{cases} \tag{A.3}$$

so that we obtain for the stretching strains from (A.1)

$$\begin{aligned} \delta e_s &= \delta\lambda_s = (r'\,\delta r' + z'\,\delta z')/\lambda_s = \cos(\psi)\,\delta r' + \sin(\psi)\,\delta z' = \psi'\delta u + \delta v' \\ \delta e_\varphi &= \delta\lambda_\varphi = \frac{\delta r}{r_0} = \frac{\sin\psi}{r_0}\,\delta u + \frac{\cos\psi}{r_0}\,\delta v. \end{aligned} \tag{A.4}$$

For the bending strains, we need the variation of ψ, which can be obtained from

$$\begin{aligned} & r' = \lambda_s \cos\psi \\ \Rightarrow \quad & \delta r' = \cos(\psi)\,\delta\lambda_s - \lambda_s \sin(\psi)\,\delta\psi \\ \Rightarrow \quad & \delta\psi = \frac{\cos(\psi)\,\delta\lambda_s - \delta r'}{\lambda_s \sin\psi} = \frac{-\delta u' + \psi'\delta v}{\lambda_s} = -\frac{\delta u'}{\lambda_s} + \kappa_s\,\delta v \end{aligned} \tag{A.5}$$

$$\Rightarrow \quad \delta K_s = \left(-\frac{\delta u'}{\lambda_s} + \kappa_s \delta v\right)' \quad \text{and} \quad \delta K_\varphi = \frac{\cos\psi}{r_0}\left(-\frac{\delta u'}{\lambda_s} + \kappa_s \delta v\right). \tag{A.6}$$

Now we can expand (2.12) from the main text using the constitutive equations to replace the derivatives of the energy density w_S and (A.4) and (A.6) to replace the variations of the strains,

$$\delta U = \int_0^{L_0} \mathrm{d}s_0\, 2\pi r_0 \left\{ \underbrace{\frac{\partial w_S}{\partial e_s}}_{\lambda_\varphi \tau_s}\,\delta e_s + \underbrace{\frac{\partial w_S}{\partial e_\varphi}}_{\lambda_s \tau_\varphi}\,\delta e_\varphi + \underbrace{\frac{\partial w_S}{\partial K_s}}_{\lambda_\varphi m_s}\,\delta K_s + \underbrace{\frac{\partial w_S}{\partial K_\varphi}}_{\lambda_s m_\varphi}\,\delta K_\varphi \right\}$$

$$
\begin{aligned}
&= \int_0^{L_0} \mathrm{d}s_0\, 2\pi \Big\{ r\tau_s \left(\psi'\,\delta u + \delta v'\right) + \lambda_s \tau_\varphi (\sin(\psi)\,\delta u + \cos(\psi)\,\delta v) \\
&\qquad + r m_s \left(-\delta u'/\lambda_s + \kappa_s\,\delta v\right)' + \lambda_s m_\varphi \cos\psi \left(-\delta u'/\lambda_s + \kappa_s\,\delta v\right) \Big\} \\
&= 2\pi r m_s \left(-\delta u'/\lambda_s + \kappa_s\,\delta v\right)\Big|_0^{L_0} + \int_0^{L_0} \mathrm{d}s_0\, 2\pi \Big\{ \delta u \big[r\tau_s \psi' + \lambda_s \tau_\varphi \sin\psi \big] + \delta v' \big[r\tau_s \big] \\
&\qquad + \delta u' \big[\underbrace{(r m_s)'/\lambda_s - m_\varphi \cos\psi}_{\equiv -rq} \big] + \delta v \big[\lambda_s \tau_\varphi \cos\psi \underbrace{-(r m_s)'\kappa_s + \lambda_s m_\varphi \kappa_s \cos\psi}_{= \lambda_s \kappa_s r q} \big] \Big\} \\
&= 2\pi r m_s \left(-\delta u'/\lambda_s + \kappa_s\,\delta v\right)\Big|_0^{L_0} - 2\pi r q\,\delta u\Big|_0^{L_0} + 2\pi r \tau_s\,\delta v\Big|_0^{L_0} \\
&\qquad + \int_0^{L_0} \mathrm{d}s_0\, 2\pi r \lambda_s \left\{ \delta u \left[\tau_s \kappa_s + \tau_\varphi \kappa_\varphi + \frac{1}{r}\frac{\mathrm{d}(rq)}{\mathrm{d}s} \right] + \delta v \left[\frac{\cos\psi}{r}\tau_\varphi + \kappa_s q - \frac{1}{r}\frac{\mathrm{d}(r\tau_s)}{\mathrm{d}s} \right] \right\}.
\end{aligned}
\tag{A.7}
$$

In these steps, integration by parts has been used, and the transversal shear stress q was defined by $rq = m_\varphi \cos\psi - \mathrm{d}(r m_s)/\mathrm{d}s$. For closed shells, the boundary terms of the integration by parts vanish because $r(0) = r(L_0) = 0$; in other cases, these boundary terms will provide boundary conditions, depending on the allowed variations at the boundaries.

In the main text we also stated that the variation of the load potential $P = -pV$ for a uniform normal pressure is (2.13), which will be derived now. We have

$$
\begin{aligned}
\delta P = \delta \int_0^{L_0} \mathrm{d}s_0 \left\{ -p\pi r^2 z' \right\} &= \int_0^{L_0} \mathrm{d}s_0 \,(-p\pi) \left\{ 2rz'\,\delta r + r^2\,\delta z' \right\} \\
&= -p\pi r^2 \delta z\Big|_0^{L_0} + \int_0^{L_0} \mathrm{d}s_0 \,(-p\pi) \left\{ 2rz'\,\delta r - 2rr'\,\delta z \right\} \\
&= \int_0^{L_0} \mathrm{d}s_0 \,(-2p\pi r) \left\{ z'\,\delta r - r'\,\delta z \right\} = \int_0^{L_0} \mathrm{d}s_0 \left\{ -2\pi r \lambda_s p\,\delta u \right\},
\end{aligned}
\tag{A.8}
$$

which proves (2.13).

A more general load on a shell is described by (spatially varying) force densities $p_n(s)$ and $p_s(s)$ in normal and meridional direction, respectively. The hydrostatic case discussed above is the special case $p_n(s) = p$ and $p_s(s) = 0$. A tangential force density p_s can be exerted for example by hydrodynamic flow or by friction with solids like the elastic capsule membrane of the opposite side in self-contacting shapes. We cannot consider a tangential force in circumferential direction because it contradicts our assumption of torsionless, axisymmetric deformation. In the general case, a load potential P may not exist. Then, the derivation of equilibrium equations cannot be based on the minimisation of an energy functional, but on the principle of virtual work, which leads to the same mathematical formulation. The variation of the load potential is replaced by

$$
\delta P = -\int \mathrm{d}A \left\{ p_n\,\delta u + p_s\,\delta v \right\} = -\int_0^{L_0} \mathrm{d}s_0\, 2\pi r \lambda_s \left\{ p_n\,\delta u + p_s\,\delta v \right\},
\tag{A.9}
$$

the work done by the external load and the virtual displacements δu and δv.

In any case, the equilibrium equations are obtained from $\delta(U + P) = 0$. In the hydrostatic case, adding (A.7) and (A.8) gives (2.15) in the main text and the equilibrium equations (2.16). In the more general case, the p_s appears in the second of the equilibrium equations, which

represents the equilibrium in meridional direction. The general equilibrium equations are then

$$\begin{aligned} 0 &= \tau_s\kappa_s + \tau_\varphi\kappa_\varphi + \frac{1}{r}\frac{\mathrm{d}(rq)}{\mathrm{d}s} - p_n \\ 0 &= \frac{\cos\psi}{r}\tau_\varphi + \kappa_s q - \frac{1}{r}\frac{\mathrm{d}(r\tau_s)}{\mathrm{d}s} - p_s \\ 0 &= q + \frac{1}{r}\frac{\mathrm{d}(rm_s)}{\mathrm{d}s} - \frac{\cos\psi}{r}m_\varphi. \end{aligned} \tag{A.10}$$

A.2. Limits of the shape equations at the poles

In this section we will obtain the simplified expressions (2.19) which are necessary to evaluate the right-hand side of the shape equations at $s_0 = 0$ and $s_0 = L_0$, i.e. at the poles of the spherical shell.

We start with the circumferential stretch, which is defined as $\lambda_\varphi = r/r_0$ with $r = r_0 = 0$ at $s_0 = 0$. With L'Hôpital's rule we obtain for the limit

$$\lambda_\varphi(0) = \lim_{s_0\to 0}\frac{r}{r_0} = \lim_{s_0\to 0}\frac{r'(s_0)}{r_0'(s_0)} = \lim_{s_0\to 0}\frac{\lambda_s\cos\psi}{\cos\psi_0} = \lambda_s(0), \tag{A.11}$$

because $\cos\psi(0) = \cos\psi_0(0) = 1$; the same calculation holds for $s_0 \to L_0$. The strains and stresses are thus isotropic at the poles,

$$\tau_s = \tau_\varphi = \frac{E_{2\mathrm{D}}}{1-\nu}\frac{1}{\lambda_s}\big(\lambda_s - 1\big) \quad \text{and} \quad \lambda_s = \lambda_\varphi = \frac{E_{2\mathrm{D}}}{E_{2\mathrm{D}} - \tau_s(1-\nu)}. \tag{A.12}$$

With $\psi(0) = 0$, the circumferential curvature $\kappa_\varphi = \sin\psi/r$ is also ill-defined, which can be evaluated analytically as

$$\kappa_\varphi(0) = \lim_{s_0\to 0}\frac{\sin\psi}{r} = \lim_{s_0\to 0}\frac{\lambda_s\kappa_s\cos\psi}{\lambda_s\cos\psi} = \kappa_s(0). \tag{A.13}$$

Thus, the bending strains and moments are also isotropic at the poles,

$$m_s = m_\varphi = E_B(1+\nu)\frac{1}{\lambda_s}\big(\lambda_s\kappa_s - \kappa_{s_0}\big) \quad \text{and} \quad \kappa_s = \kappa_\varphi = \frac{m_s}{E_B(1+\nu)} + \frac{\kappa_{s_0}}{\lambda_s}. \tag{A.14}$$

The right hand sides of r', z' and ψ' of the shape equations (2.17) can be evaluated with these results at the poles. It remains to simplify the right-hand sides of τ_s', m_s' and q'. For τ_s' and m_s' we use a simple symmetry argument. A meridian on the shell is described by a coordinate range $s_0 \in [0, L_0]$. We can extend this meridian to a full circle by choosing $s_0 \in [-L_0, L_0]$. The functions m_s and τ_s are continuous and continuously differentiable on the extended meridian as they are solutions of a first-order system of differential equations. Moreover, due to the axisymmetry, they are symmetric with reference to $s_0 = 0$, i.e. they are either even functions, like $z(s_0)$, or odd functions, like $r(s_0)$. Since the function values $\tau_s(0)$ and $m_s(0)$ are, in general, not zero at the poles, these functions must be even, and so we have $\tau_s'(0) = m_s'(0) = 0$, as in (2.19) in the main text.

The transverse shear stress vanishes at the poles, $q(0) = 0$, because otherwise the term q/r in the last of the shape equations (2.17) would show a real divergence; and apart from that it can be shown by force balances that a nonzero shear stress at the poles can only be balanced by external point forces [151]. So, $q(s_0)$ can be an odd function with $q'(0) \neq 0$. This limit can

be evaluated directly from the last of the shape equations by using L'Hôpital's rule on the term q/r,

$$\begin{aligned} q'(0) &= \lim_{s_0 \to 0} \lambda_s \left(-\kappa_s \tau_s - \kappa_\varphi \tau_\varphi - \frac{q}{r} \cos\psi + p \right) \\ &= \lambda_s(0) \left(-2\kappa_s(0)\tau_s(0) + p - \cos\psi(0) \lim_{s_0 \to 0} \frac{q}{r} \right) \\ &= \lambda_s(0) \left(-2\kappa_s(0)\tau_s(0) + p - \frac{q'(0)}{\lambda_s(0)} \right) \\ \Rightarrow \qquad q'(0) &= \lambda_s(0) \left(-\kappa_s(0)\tau_s(0) + \frac{p}{2} \right) \end{aligned} \tag{A.15}$$

which is the remaining term of (2.19).

Appendix B

Minimisation of Pogorelov's energy functional

The analytic solution of Pogorelov's variational problem proceeds as follows. The coordinate range $[0,\infty)$ is divided into two parts $I_1 = [0,\sigma)$ and $I_2 = [\sigma,\infty)$. On the interval I_1, the function $\bar{w}$ is of the order of unity (since its starting value is 1) and it shall have a root at $\bar{s}_0 = \sigma$. From there on, $\bar{w}$ is assumed to stay small, that is, we can neglect $\bar{w}^2$ as compared to $\bar{w}$ on I_2, which will simplify the constraint (2.40). On I_1, Pogorelov argues that $\bar{w}'$ should be approximately constant because the curvature $\kappa_s \propto \bar{w}'$ has a maximum at the dimple edge and therefore varies only little in its vicinity. With this simplification and the boundary conditions (2.41) we have

$$\bar{w}_1(\bar{s}_0) = (\bar{s}_0 - \sigma)/\sigma, \tag{B.1}$$

and the constraint (2.40) and boundary conditions further dictate

$$\bar{u}_1(\bar{s}_0) = -\frac{1}{2\sigma}(\bar{s}_0 - \sigma)^2 - \frac{1}{6\sigma^2}(\bar{s}_0 - \sigma)^3 + \frac{\sigma}{3} \tag{B.2}$$

as the solution on I_1. On I_2, the constraint simplifies to $\bar{w}_2 = -\bar{u}_2'$, which can be inserted directly into the energy functional (2.39). The complete functional on I_1 and I_2 reduces with these two simplifications to

$$J = \int_0^\sigma \mathrm{d}\bar{s}_0 \left\{\bar{w}_1'^2 + \bar{u}_1^2\right\} + \int_\sigma^\infty \mathrm{d}\bar{s}_0 \left\{\bar{w}_2'^2 + \bar{u}_2^2\right\} = \frac{1}{\sigma} + \frac{17}{315}\sigma^3 + \int_\sigma^\infty \mathrm{d}\bar{s}_0 \left\{\bar{u}_2''^2 + \bar{u}_2^2\right\}. \tag{B.3}$$

With the ansatz on I_1, the functions $\bar{u}_1$ and $\bar{w}_1$ are fixed by (B.1) and (B.2), respectively. A variation is only possible by varying the parameter σ. On I_2, the function $\bar{u}_2$ can be subjected to arbitrary variations which respect the boundary conditions. At $\bar{s}_0 = \sigma$, the boundary condition is given by the continuity condition $\bar{u}_2(\sigma) = \bar{u}_1(\sigma) = \sigma/3$. To find the minimum of (B.3), we first keep σ fixed and variate with respect to $\bar{u}_2$. The solution will depend still on σ, and we then minimise with respect to σ.

Requiring a vanishing variation $\delta J[\bar{u}_2] = 0$ results in the differential equation

$$\bar{u}_2'''' + \bar{u}_2 = 0. \tag{B.4}$$

It can be solved with an exponential ansatz, and the solution which conforms the boundary conditions is given by

$$\bar{u}_2(\bar{s}_0) = -\frac{\sigma}{3\sqrt{2}}\left(\omega_1 e^{\omega_1(\bar{s}_0-\sigma)} + \omega_2 e^{\omega_2(\bar{s}_0-\sigma)}\right) \tag{B.5}$$

with $\omega_1 = -(1-i)/\sqrt{2}$ and $\omega_2 = -(1+i)/\sqrt{2}$. From the constraint $\bar{w}_2 = -\bar{u}'$, it follows immediately that

$$\bar{w}_2 = \frac{i\sigma}{3\sqrt{2}}\left(-e^{\omega_1(\bar{s}_0-\sigma)} + e^{\omega_2(\bar{s}_0-\sigma)}\right). \tag{B.6}$$

With eqs. (B.1), (B.2), (B.5) and (B.6), the complete solution is determined,

$$\bar{u}(\bar{s}_0) = \begin{cases} \bar{u}_1(\bar{s}_0), & 0 \leq \bar{s}_0 < \sigma \\ \bar{u}_2(\bar{s}_0), & \bar{s}_0 \geq \sigma \end{cases} \quad \text{and} \quad \bar{w}(\bar{s}_0) = \begin{cases} \bar{w}_1(\bar{s}_0), & 0 \leq \bar{s}_0 < \sigma \\ \bar{w}_2(\bar{s}_0), & \bar{s}_0 \geq \sigma \end{cases}. \tag{B.7}$$

Evaluating the functional J for this solution, we get

$$J(\sigma) = \frac{1}{\sigma} + \frac{\sqrt{2}}{9}\sigma^2 + \frac{17}{315}\sigma^3. \tag{B.8}$$

We can now perform the final minimisation with respect to σ, which gives a numerical value of

$$\sigma_{\min} = 1.24667 \quad \text{and} \quad J_{\min} = 1.15092. \tag{B.9}$$

Appendix C

Stability equations of axisymmetric shallow shells

C.1. Derivation of the stability equations

In this appendix, the derivation of the Cartesian stability equations of section 3.2.5 is transferred to axisymmetric shells. The procedure is analogous, but mathematically more involved.

The reference shape for our energy considerations is the axisymmetric buckled shape, characterised by its geometry (the functions r, z, ψ, κ_s and κ_φ, see section 2.2) and its stress state (τ_s, τ_φ, m_s and m_φ). This shape is perturbed by displacement fields $u(s,\varphi)$, $v(s,\varphi)$ and $w(s,\varphi)$ in meridional, circumferential and normal direction, respectively. The displacements induce strains and bending strains according to the strain-displacement relations of the DMV theory, which are given in ref. [96] in general coordinates in terms of covariant derivatives. They can be specialised to axisymmetric surfaces, parametrised by s and φ as in section 2.2.1, by going through the covariant derivatives, fundamental tensors and Christoffel symbols. This results in

$$\begin{aligned}
\varepsilon_s &= \partial_s u - \kappa_s w + \frac{1}{2}(\partial_s w)^2, & K_s &= \partial_s^2 w \equiv \mathrm{D}_{ss} w,\\
\varepsilon_\varphi &= \frac{\cos\psi}{r} u + \frac{1}{r}\partial_\varphi v - \kappa_\varphi w + \frac{1}{2r^2}(\partial_\varphi w)^2, & K_\varphi &= \frac{\cos\psi}{r}\partial_s w + \frac{1}{r^2}\partial_\varphi^2 w \equiv \mathrm{D}_{\varphi\varphi} w,\\
\varepsilon_{s\varphi} &= \frac{1}{2}\left(\frac{1}{r}\partial_\varphi u - \frac{\cos\psi}{r} v + \partial_s v + \frac{1}{r}(\partial_s w)(\partial_\varphi w)\right), & K_{s\varphi} &= \frac{1}{r}\partial_s\partial_\varphi w - \frac{\cos\psi}{r^2}\partial_\varphi w \equiv \mathrm{D}_{s\varphi} w,
\end{aligned} \tag{C.1}$$

which has been cross-checked with the general linear strains given in ref. [135]. Here, the differential operators D_{ss}, $\mathrm{D}_{s\varphi}$ and $\mathrm{D}_{\varphi\varphi}$ are defined to shorten the notation. These simplified strains and bending strains of the DMV theory are justified if the displacements are predominantly normal to the surface, i.e. if w is larger than u and v.

The energy change due to the strains is

$$\Delta W = \int \mathrm{d}A \left\{ w_{\text{stretch}} + w_{\text{bend}} + w_{\text{ext}} \right\} \tag{C.2}$$

with the energy densities

$$\begin{aligned}
w_{\text{stretch}} &= \tau_s\varepsilon_s + \tau_\varphi\varepsilon_\varphi + \frac{1}{2}\frac{EH_0}{1-\nu^2}\left(\varepsilon_s^2 + 2\nu\varepsilon_s\varepsilon_\varphi + \varepsilon_\varphi^2 + 2(1-\nu)\varepsilon_{s\varphi}^2\right)\\
w_{\text{bend}} &= m_s K_s + m_\varphi K_\varphi + \frac{1}{2}E_B\left(K_s^2 + 2\nu K_s K_\varphi + 2(1-\nu)K_{s\varphi}^2\right)\\
w_{\text{ext}} &= pw.
\end{aligned} \tag{C.3}$$

When integration by parts is used to rearrange the energy functional we must take the Jacobian determinant into account, $\mathrm{d}A = r\,\mathrm{d}s\mathrm{d}\varphi$. As a general rule for the integration by parts one obtains [4]

$$\int f\cdot(\partial_s g)\,\mathrm{d}A = -\int \frac{1}{r}\,\partial_s(rf)\cdot g\,\mathrm{d}A, \tag{C.4}$$

where boundary terms are omitted.

Collecting the first order terms (in u, v, w) and requiring them to vanish for arbitrary displacement fields reproduces the equilibrium equations of the DMV theory,

$$\frac{\partial(r\tau_s)}{\partial s} = \tau_\varphi \cos\psi, \qquad \kappa_s\tau_s + \kappa_\varphi\tau_\varphi + \frac{1}{r}\frac{\partial(rq)}{\partial s} = p, \qquad rq = -\frac{\partial(rm_s)}{\partial s} - m_\varphi\cos\psi. \tag{C.5}$$

They coincide with the equilibrium equations (2.16) of the nonlinear theory of shells of revolution, except that the effect of the transverse shearing force q is neglected in the meridional force balance, which is typical for the DMV theory [96].

The main concern of this appendix is the second order energy change, from which the stability equations are derived. This functional is given by

$$\begin{aligned}\Delta W^{(2)} = \int \mathrm{d}A \Bigg\{ &\frac{1}{2}\tau_s(\partial_s w)^2 + \frac{1}{2}\tau_\varphi\frac{1}{r^2}(\partial_\varphi w)^2 \\ &+ \frac{1}{2}\frac{E_{2\mathrm{D}}}{1-\nu^2}\Bigg[(\partial_s u - \kappa_s w)^2 + 2\nu(\partial_s u - \kappa_s w)\left(\frac{\cos\psi}{r}u + \frac{\partial_\varphi v}{r} - \kappa_\varphi w\right) \\ &\qquad + \left(\frac{\cos\psi}{r}u + \frac{\partial_\varphi v}{r} - \kappa_\varphi w\right)^2 + \frac{1}{2}(1-\nu)\left(\frac{\partial_\varphi u}{r} - \frac{\cos\psi}{r}v + \partial_s v\right)^2\Bigg] \\ &+ \frac{1}{2}E_B\left[(\mathrm{D}_{ss}w)^2 + 2\nu(\mathrm{D}_{ss}w)(\mathrm{D}_{\varphi\varphi}w) + (\mathrm{D}_{\varphi\varphi}w)^2 + 2(1-\nu)(\mathrm{D}_{s\varphi}w)^2\right]\Bigg\}.\end{aligned} \tag{C.6}$$

Just as in the derivation of the stability equations in Cartesian coordinates in section 3.2.5, this functional must be symmetrised and written in the form

$$\Delta W^{(2)} = \int \mathrm{d}A \left\{(u,v,w)\hat{H}(u,v,w)^T\right\}. \tag{C.7}$$

The symmetrisation involves extensive use of integration by parts (C.4). As a simplification, we assume that the angle ψ is varying slowly (in comparison to u, v, w and r), so that its derivative $\partial_s\psi \approx 0$ can be neglected. This limits our theory to the case where the typical length scale of the non-axisymmetric perturbation is much smaller than the radii of curvature of the axisymmetric buckled shape.

Following the rationale of section 3.2.5, the critical point for the loss of stability of the axisymmetric shape is when the lowest eigenvalue of $\hat{H}$ crosses zero. The three equations $0 = \hat{H}(u,v,w)^T$ can be rearranged with a lengthy calculation into the form

$$\begin{aligned} 0 &= E_B\Delta^2 w - \tau_s\mathrm{D}_{ss}w - \tau_\varphi\mathrm{D}_{\varphi\varphi}w - \kappa_s\tau_s^{(1)} - \kappa_\varphi\tau_\varphi^{(1)} \\ 0 &= \frac{1}{r}\frac{\partial\big(r\tau_s^{(1)}\big)}{\partial s} - \frac{\cos\psi}{r}\tau_\varphi^{(1)} + \frac{1}{r}\frac{\partial\tau_{s\varphi}^{(1)}}{\partial\varphi} \\ 0 &= \frac{1}{r}\frac{\partial\tau_\varphi^{(1)}}{\partial\varphi} + \frac{1}{r^2}\frac{\partial\big(r^2\tau_{s\varphi}^{(1)}\big)}{\partial s}. \end{aligned} \tag{C.8}$$

Here, the Laplacian $\Delta = \mathrm{D}_{ss} + \mathrm{D}_{\varphi\varphi}$ was introduced. The additional tensions $\tau_i^{(1)}$ appearing in these stability equations, which are functions the linearised versions $\varepsilon_i^{(1)}$ of the strains (C.1), are defined as

$$\begin{aligned} &\tau_s^{(1)} = \frac{E_{2\mathrm{D}}}{1-\nu^2}\big(\varepsilon_s^{(1)} + \nu\varepsilon_\varphi^{(1)}\big), \qquad \tau_{s\varphi}^{(1)} = \frac{E_{2\mathrm{D}}}{1+\nu}\varepsilon_{s\varphi}^{(1)}, \qquad \tau_\varphi^{(1)} = \frac{E_{2\mathrm{D}}}{1-\nu^2}\big(\varepsilon_\varphi^{(1)} + \nu\varepsilon_s^{(1)}\big), \\ &\varepsilon_s^{(1)} = \partial_s u - \kappa_s w, \quad \varepsilon_{s\varphi}^{(1)} = \frac{1}{2}\left(\frac{\partial_\varphi u}{r} - \frac{\cos\psi}{r}v + \partial_s v\right), \quad \varepsilon_\varphi^{(1)} = \frac{\cos\psi}{r}u + \frac{\partial_\varphi v}{r} - \kappa_\varphi w. \end{aligned} \tag{C.9}$$

The last two equations of (C.8) are the in-plane equilibrium equations of the general linear membrane theory of shells of revolution [135]. Analogous to the Cartesian case, they are satisfied automatically by using the stress potential ϕ, from which the tensions derive as $\tau_s^{(1)} = \mathrm{D}_{\varphi\varphi}\phi$, $\tau_\varphi^{(1)} = \mathrm{D}_{ss}\phi$ and $\tau_{s\varphi}^{(1)} = -\mathrm{D}_{s\varphi}\phi$. The governing equation for the stress potential is

$$\Delta^2\phi = E_{2\mathrm{D}}\left(-\kappa_\varphi \mathrm{D}_{ss}w - \kappa_s \mathrm{D}_{\varphi\varphi}w\right). \tag{C.10}$$

Introducing the stress potential into the first equation of (C.8), we get the full stability equations of shells of revolution,

$$\begin{aligned} E_B\Delta^2 w &= (\kappa_s \mathrm{D}_{\varphi\varphi} + \kappa_\varphi \mathrm{D}_{ss})\phi + (\tau_s \mathrm{D}_{ss} + \tau_\varphi \mathrm{D}_{\varphi\varphi})w \\ \frac{1}{E_{2\mathrm{D}}}\Delta^2\phi &= -(\kappa_s \mathrm{D}_{\varphi\varphi} + \kappa_\varphi \mathrm{D}_{ss})w, \end{aligned} \tag{C.11}$$

which is the system (4.12) in the main text.

C.2. Discretisation

For the numerical solution of the DMV stability equations, we discretise the differential equations (4.12) to obtain a system of linear equations. We use the same convention for the nondimensionalisation as in section 2.2, i.e. we take R_0 as the length unit and $E_{2\mathrm{D}}$ as the tension unit. A useful discretisation can be adopted from the literature on the numerical solution of the Poisson equation in polar coordinates [81, 82, 123] because the Poisson equation involves the same problems at $s = 0$ concerning divergences in the Laplacian. So we divide the domain $0 \le s \le s_{\max}$ into N intervals, separated by the points $s^{(i)} = i \cdot h$, with $0 \le i \le N$ and a step size $h = s_{\max}/N$. The functions $W(s)$ and $\Phi(s)$ are then represented by their values at these sampling points, $W^{(i)} = W\big(s^{(i)}\big)$ and $\Phi^{(i)} = \Phi\big(s^{(i)}\big)$.

In the stability equations (4.12), derivatives with respect to s up to fourth order occur. In the discretised equations they are approximated by central finite differences,

$$\begin{aligned} f'\big(s^{(i)}\big) &= \frac{-f^{(i-1)} + f^{(i+1)}}{2h} \\ f''\big(s^{(i)}\big) &= \frac{f^{(i-1)} - 2f^{(i)} + f^{(i+1)}}{h^2} \\ f'''\big(s^{(i)}\big) &= \frac{-f^{(i-2)} + 2f^{(i-1)} - 2f^{(i+1)} + f^{(i+2)}}{2h^3} \\ f''''\big(s^{(i)}\big) &= \frac{f^{(i-2)} - 4f^{(i-1)} + 6f^{(i)} - 4f^{(i+1)} + f^{(i+2)}}{h^4}. \end{aligned} \tag{C.12}$$

At the boundaries of the integration region, this involves problems since these formulae are "overlapping" the integration region, that is, they use function values of points outside the region. Thus, to evaluate the third and fourth derivatives at $i = N$, for example, we need to introduce two "phantom points" $i = N + 1$ and $i = N + 2$. That induces four further degrees of freedom in our equations, $W^{(N+1)}$, $W^{(N+2)}$, $\Phi^{(N+1)}$ and $\Phi^{(N+2)}$, and thus necessitates four extra equations: the boundary conditions. As discussed before, we impose a vanishing function value and derivative value at $s_{\max}$ for both functions W and Φ. In the discretised formulation, this means $W^{(N)} = 0$ and $W^{(N+1)} - W^{(N-1)} = 0$, and the same for Φ.

The boundary $i = 0$ is more difficult to handle, since some terms of the stability equations diverge. This problem can be circumvented by transforming the differential equations into

a weak form by integrating them over a disc of radius $\varepsilon \to 0$, i.e. integrating over the range $0 \leq s \leq \varepsilon$ and $0 \leq \varphi < 2\pi$. In the vicinity of $s = 0$, the axisymmetric solutions satisfy $\kappa_s = \kappa_\varphi \equiv \kappa$ and $\tau_s = \tau_\varphi \equiv \tau$, see (2.19). Furthermore, $\cos\psi \approx 1$ and thus $r \approx s$, so that the Laplacian reduces to $\Delta = \partial_s^2 + \frac{1}{s}\partial_s + \frac{1}{s^2}\partial_\varphi^2$, the usual Laplacian for flat polar coordinates. Thus, the second of the stability equations (4.12) reads

$$0 = \Delta^2\phi + E_{2\mathrm{D}}\kappa\Delta w. \tag{C.13}$$

Integrating the right hand side over the disk and using Gauss's divergence theorem to transform the surface integral into a contour integral, we obtain

$$\int \mathrm{d}A\, \boldsymbol{\nabla}\cdot(\boldsymbol{\nabla}\Delta\phi + E_{2\mathrm{D}}\kappa\boldsymbol{\nabla}w) = \oint \mathrm{d}t\, \boldsymbol{e}_s(\boldsymbol{\nabla}\Delta\phi + E_{2\mathrm{D}}\kappa\boldsymbol{\nabla}w) = \int_0^{2\pi} \mathrm{d}\varphi\, s(\partial_s\Delta\phi + E_{2\mathrm{D}}\kappa\partial_s w)\big|_{s=\varepsilon} \tag{C.14}$$

where $\boldsymbol{\nabla}$ is the nabla operator, $\oint \mathrm{d}t$ the contour integral over the circle of radius ε and $\boldsymbol{e}_s$ the unit normal vector to this contour. With the ansatz (4.14), $w = W(s)\cos(n\varphi)$ and $\phi = \Phi(s)\cos(n\varphi)$, we thus obtain from (C.13) and (C.14)

$$0 = \int_0^{2\pi} \mathrm{d}\varphi \cos(n\varphi) \left\{ s\Phi''' + \Phi'' - \frac{n^2+1}{s}\Phi' + \frac{2n^2}{s^2}\Phi + E_{2\mathrm{D}}\kappa W' \right\}\Big|_{s=\varepsilon}. \tag{C.15}$$

For the other stability equation, we obtain analogously

$$0 = \int_0^{2\pi} \mathrm{d}\varphi \cos(n\varphi) \left\{ E_B \left(sW''' + W'' - \frac{n^2+1}{s}W' + \frac{2n^2}{s^2}W \right) - \kappa\Phi' - \tau W' \right\}\Big|_{s=\varepsilon}. \tag{C.16}$$

As the integral over a full period of the cosine vanishes, these two equations are satisfied when the terms in curly braces do not diverge. This is, in the limit $\varepsilon \to 0$, the case if

$$W(0) = W'(0) = 0 \quad \text{and} \quad \Phi(0) = \Phi'(0) = 0. \tag{C.17}$$

This has the same form as the boundary conditions at the other end of the integration region; but in this case, it is the expression of the differential equations to be satisfied at $s^{(0)}$. Thus, the differential equations (4.12) must be imposed only at the points $s^{(1)}$, $s^{(2)}$, ..., where all terms of the Laplacian are regular; at $s^{(0)}$ we impose (C.17). By that, we have avoided the problem of diverging terms in the Laplacian.

Hence, we only need one phantom point $s^{(-1)}$, at which the function values are fixed by the conditions (C.17) to $W^{(-1)} = W^{(1)}$ and $\Phi^{(-1)} = \Phi^{(1)}$. For the solution of the linear system, we can even spare this phantom point, because the differential equations at the other points do not use this point. We can see this by considering explicitly the squared Laplacian that occurs in the stability equations (4.12). According to our discretisation (C.12), only the third and fourth derivatives, evaluated at $s^{(1)}$, use function values at $s^{(-1)}$. The relevant terms of the squared Laplacian are, thus, $\Delta^2 = \partial_s^4 + \frac{2}{s}\partial_s^3 + \ldots$ when we use the Laplacian of flat polar coordinates, which is justified because we are close to the point $s = 0$. The discretisation at $s = s^{(1)} = h$ then reads

$$f''''(s^{(1)}) + \frac{2}{s^{(1)}}f'''(s^{(1)}) = \frac{f^{(-1)} + \ldots}{h^4} + \frac{2}{h}\cdot\frac{-f^{(-1)} + \ldots}{2h^3} \tag{C.18}$$

where the function value $f^{(-1)}$ at the phantom point cancels out. Hence, the problem is closed by the boundary conditions $W^{(0)} = \Phi^{(0)} = 0$.

The discretisation of the stability equations (4.12) proceeds as follows. When we include the phantom points, we need to solve the equations on the grid of s-values $(0, h, 2h, \ldots, [N+2]h)$. The function values of W and Φ at these positions are organised in one big vector,

$$\boldsymbol{f} = \big(-\boldsymbol{W}-, -\boldsymbol{\Phi}-\big) = \big(W^{(0)}, W^{(1)}, \ldots, W^{(N+2)}, \Phi^{(0)}, \Phi^{(1)}, \ldots, \Phi^{(N+2)}\big). \tag{C.19}$$

The differential operators can be written as matrices of dimension $(N+3)\times(N+3)$ that operate on the $\boldsymbol{W}$ or $\boldsymbol{\Phi}$ sub-vector. For example, the fourth derivative according to (C.12) can be written as

$$\boldsymbol{d}_4 = \frac{1}{h^4}\begin{bmatrix} 0 & 0 & 0 & 0 & 0 & 0 & 0 & 0 & 0 \\ -4 & 6 & -4 & 1 & & & & & \\ 1 & -4 & 6 & -4 & 1 & & & & \\ & 1 & -4 & 6 & -4 & 1 & & & \\ & & & & \ddots & & & & \\ & & & & 1 & -4 & 6 & -4 & 1 \\ 0 & 0 & 0 & 0 & 0 & 0 & 0 & 0 & 0 \\ 0 & 0 & 0 & 0 & 0 & 0 & 0 & 0 & 0 \end{bmatrix} \tag{C.20}$$

where the first row and last two rows account for the phantom points, at which the derivative does not need to be evaluated. In the second line, the missing 1 to the left of the -4 is due to our argument that the usage of $f^{(-1)}$ of the third and fourth derivatives in the squared Laplacian cancels out. Blank elements of this matrix are to be understood as zero.

Analogous differentiation matrices $\boldsymbol{d}_1$, $\boldsymbol{d}_2$ and $\boldsymbol{d}_3$ exist. When a differential operator in the stability equations is multiplied with an s-dependent function, e.g. $g(s)\partial_s$ with $g(s) = \cos\psi/r$, each row of the differentiation matrix must be multiplied with the appropriate function value. This can be achieved by a matrix multiplication from the left, in our example $\boldsymbol{m}_g\boldsymbol{d}_1$ with a matrix

$$\boldsymbol{m}_g = \begin{bmatrix} 0 & & & & & \\ & g_1 & & & & \\ & & g_2 & & & \\ & & & \ddots & & \\ & & & & g_{N+2} & \\ & & & & & 0 \\ & & & & & & 0 \end{bmatrix} \quad \text{with} \quad g_i = g\big(s^{(i)}\big). \tag{C.21}$$

The most complex derivative operator that must be translated to a matrix is the squared Laplacian $\Delta^2 = (\mathrm{D}_{ss} + \mathrm{D}_{\varphi\varphi})(\mathrm{D}_{ss} + \mathrm{D}_{\varphi\varphi})$. For completeness, we give it here in explicit form,

$$\begin{aligned} \Delta^2 = {} & \underbrace{\frac{n^4}{r^4} - \frac{2n^2\kappa_s\kappa_\varphi}{r^2} - \frac{4n^2\cos^2\psi}{r^4}}_{=g_0(s)} \\ & + \underbrace{\left(\frac{2n^2\cos\psi}{r^3} - \frac{\kappa_s^2\cos\psi}{r} + \frac{2\kappa_s\kappa_\varphi\cos\psi}{r} + \frac{\cos^3\psi}{r^3} - \kappa_\varphi\psi''(s)\right)}_{=g_1(s)}\partial_s \\ & + \underbrace{\left(-\frac{2n^2}{r^2} - 2\kappa_s\kappa_\varphi - \frac{\cos^2\psi}{r^2}\right)}_{=g_2(s)}\partial_s^2 + \underbrace{\frac{2\cos\psi}{r}}_{=g_3(s)}\partial_s^3 + \partial_s^4. \end{aligned} \tag{C.22}$$

On matrix level, the first row of this equation is represented by a matrix $\boldsymbol{m}_{g_0}$ with a function $g_0(s)$ corresponding to the terms in the first row; and the other matrices can be obtained as $\boldsymbol{m}_{g_i}\boldsymbol{d}_i$ as explained above. All these matrices are summed up to give the matrix of the discretised squared Laplacian, $\boldsymbol{d}_{\Delta^2} = \boldsymbol{m}_{g_0} + \boldsymbol{m}_{g_1}\boldsymbol{d}_1 + \boldsymbol{m}_{g_2}\boldsymbol{d}_2 + \boldsymbol{m}_{g_3}\boldsymbol{d}_3 + \boldsymbol{d}_4$. All other operators in the stability equations (4.12) can be analogously transformed into matrices.

Finally, the whole set of stability equations is represented by a linear system that can be sketched as

$$\left[\begin{array}{cc} \boxed{\begin{array}{c} 1\ 0\ 0\ 0\ 0\ 0\ 0\ 0 \\ E_B\Delta^2 \\ -\tau_s \mathrm{D}_{ss} - \tau_\varphi \mathrm{D}_{\varphi\varphi} \\ 0\ 0\ 0\ 0\ 0\ 1\ 0\ 0 \\ 0\ 0\ 0\ 0\ 1\ 0\ \text{-}1\ 0 \end{array}} & \boxed{\begin{array}{c} 0\ 0\ 0\ 0\ 0\ 0\ 0\ 0 \\ -\kappa_s \mathrm{D}_{\varphi\varphi} - \kappa_\varphi \mathrm{D}_{ss} \\ 0\ 0\ 0\ 0\ 0\ 0\ 0\ 0 \\ 0\ 0\ 0\ 0\ 0\ 0\ 0\ 0 \end{array}} \\ \boxed{\begin{array}{c} 0\ 0\ 0\ 0\ 0\ 0\ 0\ 0 \\ \kappa_s \mathrm{D}_{\varphi\varphi} + \kappa_\varphi \mathrm{D}_{ss} \\ 0\ 0\ 0\ 0\ 0\ 0\ 0\ 0 \\ 0\ 0\ 0\ 0\ 0\ 0\ 0\ 0 \end{array}} & \boxed{\begin{array}{c} 1\ 0\ 0\ 0\ 0\ 0\ 0\ 0 \\ \frac{1}{E_{2\mathrm{D}}}\Delta^2 \\ 0\ 0\ 0\ 0\ 0\ 1\ 0\ 0 \\ 0\ 0\ 0\ 0\ 1\ 0\ \text{-}1\ 0 \end{array}} \end{array}\right] \cdot \left[\begin{array}{c} \\ \boldsymbol{W} \\ \\ \\ \boldsymbol{\Phi} \\ \\ \end{array}\right] = \mathbf{0} \tag{C.23}$$

Each block of the matrix represents a differential operator of the stability equations as indicated. The ones in the left column are acting on W, and those of the right column on Φ. The rows of the differentiation matrices that were full of zeroes can be used to implement the six boundary conditions as shown in the equation: $W(0) = W(s_{\max}) = W'(s_{\max}) = 0$ are implemented in the upper left block and $\Phi(0) = \Phi(s_{\max}) = \Phi'(s_{\max}) = 0$ in the lower right block. Note that the first column of each block is associated to the point $s^{(0)}$ and the last two to the phantom points $s^{(N)}$ and $s^{(N+1)}$.

Appendix D

Contour analysis and fitting procedure

Consider an image of a pendant capsule which has to be compared to a theoretical contour given by a parametrisation $r(s_0)$, $z(s_0)$ with $s_0 \in [0, L_0]$ – this may either be a solution of the Laplace-Young equation (5.2) or the elastic shape equations (5.7) and (5.15). The length unit of the theoretical contour is chosen as the capsule diameter a at its upper rim, which coincides with the inner diameter of the capillary.

D.1. Contour analysis

The steps to find sampling points on the contour in an image are visualised in fig. D.1 and can be described as follows:

1. The images are imported as png files into the software Mathematica and converted into a matrix of greyscale values, which range from 0 (dark) to 1 (bright).

2. An edge detection algorithm (Canny's method, which is implemented in Mathematica) is used to find edges in the image.

3. The position of the end of the capillary is found by searching a horizontal jump in the upper part of the outermost edge (horizontal blue line).

4. All outermost points are detected. At the capillary (blue), they are used to determine the length scale of the image: The outer capillary diameter $b^{(px)}$ is measured in pixels. Its real dimensions (in mm) are known. At the capsule, the points (yellow) capture the contour.

5. Sampling points (red) are distributed equidistantly (each 5 pixels) along the contour.

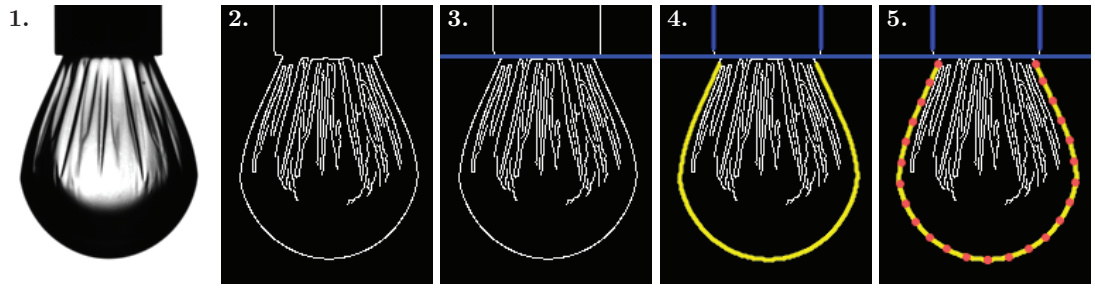

Figure D.1.: The five stages of the contour detection as described in the enumeration, using the example of an OTS capsule.

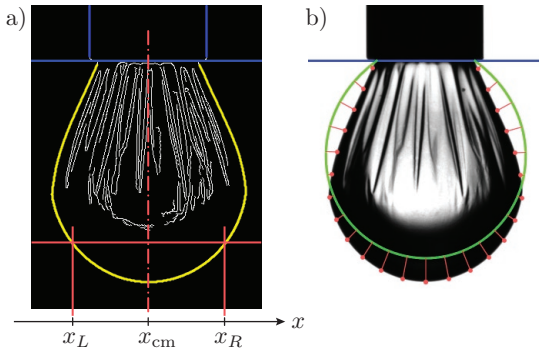

Figure D.2.: a) Principle for calculating the deviation from perfect axisymmetry. b) Measure of deviation between the theoretical contour (green line) and the sampling points (red). The shortest connections of the sampling points to the theory line (red lines) are squared and summed up.

In some cases, the capsule in the image is inclined, because of a maladjusted camera or tilted table. Thus it does not seem to be axisymmetric with respect to the vertical axis. To compensate for this, the image has to be rotated by a certain angle which is determined by minimising the deviation from axisymmetry defined as follows (see fig. D.2 a):

For each pixel row, the difference between the centre $(x_L + x_R)/2$ in this row and the x-coordinate x_{cm} of the centre of mass of all contour points (yellow) is squared and added to the error,

$$\delta_{\mathrm{axi}} = \frac{1}{n} \sum_{\text{all rows}} \left(x_{\mathrm{cm}} - \frac{x_L + x_R}{2} \right)^2 . \tag{D.1}$$

If necessary, each image is rotated by the angle that minimises this error before performing the five step contour extraction described above.

D.2. Least-squares fitting

All computed contours are nondimensionalised, specifically, the length unit is given as the diameter of the capsule's upper rim. In order to compare a computed contour to the sampling points, we have to determine a conversion factor $a^{(\mathrm{px})}$ measuring the diameter in pixels. The contour measured in pixels is then given by

$$\begin{pmatrix} r^{(\mathrm{px})} \\ z^{(\mathrm{px})} \end{pmatrix} = a^{(\mathrm{px})} \begin{pmatrix} r(s_0) \\ z(s_0) \end{pmatrix} . \tag{D.2}$$

Now, we can define a measure of how much a given theoretical curve $r^{(\mathrm{px})}$, $z^{(\mathrm{px})}$ deviates from the set of sampling points $\boldsymbol{x}_i^{(\mathrm{px})}$. In a geometrical language, the procedure can be described as follows (see fig. D.2 b):

- Lay the theoretical contour over the image, aligning its upper rim with the end of the capillary and the origin of the r-axis with the centre of mass of the sampling points.
- Sum up the squares of the distances d_i between $\boldsymbol{x}_i^{(\mathrm{px})}$ and the theoretical contour and calculate the *root mean square deviation* (RMS deviation) over all n sampling points:

$$\mathrm{RMS} \equiv \sqrt{\frac{1}{n} \sum_{i=1}^{n} d_i^2}. \tag{D.3}$$

Unfortunately, $a^{(\mathrm{px})}$ cannot be measured directly from the images because the point of attachment between capillary and capsule frequently accumulates dirt like patches of the polymerised material. So we decide to determine $a^{(\mathrm{px})}$ indirectly with the Laplace Young fits: We adjust $a^{(\mathrm{px})}$ so that the Laplace-Young fits have the lowest remaining RMS deviation, i.e. we use the scaling factor as an additional fit parameter. The mean value $\left\langle a^{(\mathrm{px})} \right\rangle$ of all Laplace-Young fits is then kept for all following fits of the elastic shape equations.

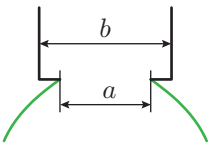

Figure D.3.: Capillary measures

In addition to the conversion factor $a^{(\mathrm{px})}$ between theory length unit and pixels, we need to know the diameter a in real length units, e.g. in millimetres. Since the outer diameter b (see fig. D.3) of the capillary is specified by the manufacturer, we can calculate the inner diameter as

$$a = \left\langle a^{(\mathrm{px})} / b^{(\mathrm{px})} \right\rangle \cdot b, \tag{D.4}$$

where the average $\langle \cdot \rangle$ is taken over all pictures that are used for the Laplace-Young fits.

The actual fitting process now involves a minimisation of the RMS deviation (D.3) by adjusting the fit parameters. In case of the Laplace-Young fits, the dimensionless density difference $\tilde{\rho}$ and pressure $\tilde{p}_0$ are the fit parameters that influence the shape, and $a^{(\mathrm{px})}$ is the fit parameter finding the correct scale of the image. The RMS deviation is implicitly a function of all three fit parameters, and is minimised using Mathematica's `FindMinimum` routine in three dimensions. Suitable starting values must be provided. From the fitted density difference $\tilde{\rho}$, the value of the surface tension can be calculated, see tab. 5.1,

$$\gamma = a^2 \, \Delta\rho \, g / \tilde{\rho}, \tag{D.5}$$

since the actual density difference $\Delta\rho$ is known and a is determined by eq. (D.4). In effect, the interfacial tension γ is the fitting parameter we are interested in, not the density difference.

In case of the elastic fits, the fit parameters are the pressure $\tilde{p}$ (which controls the volume) and the elastic moduli $\tilde{K}_{2\mathrm{D}}$ and ν (which influence the shape). Of interest are only the elastic moduli. While ν is a dimensionless number anyway, the dimensionless area compression modulus can be converted to the real area compression modulus (in SI units) by

$$K_{2\mathrm{D}} = \gamma \tilde{K}_{2\mathrm{D}}, \tag{D.6}$$

where γ is already known from the Laplace-Young fits.

As the numerical solution of the elastic shape equations is much more prone to numerical issues than the solution of the Laplace-Young equation and takes much longer time, Mathematica's `FindMinimum` routine cannot be directly used to adjust all three fit parameters simultaneously. Instead, we construct a grid in the $(K_{2\mathrm{D}}, \nu)$-plane. For each place on this grid, the pressure $\tilde{p}$ is adjusted using Mathematica's `FindMinimum` routine while keeping the other fit parameters fixed. The smallest fit residual obtained this way indicates the place on the grid which is closest to the actual elastic moduli of the capsule. In its vicinity, a refined grid is constructed and the procedure is repeated in order to better localise the true fit minimum. This method has the advantage that we have more control over the numerics. Unlike Mathematica's `FindMinimum`, our method cannot run into parameter domains outside the reasonable range, where the solutions of the shape equations cannot converge any more. Additionally, we can use parameter tracing for the initial values of the shooting parameters, and by plotting the fit residual over the grid, numerical issues and outliers can be registered. Examples of such plots are given below in section D.4.

D.3. Estimating error bars

Our contour detection has a resolution of ±1 pixel. The worst case would be that the sampling points $\boldsymbol{x}_i$ are shifted systematically. In order to estimate how strong this worst-case error in the contour detection influences the fit results, we repeat the elastic fits with displaced sampling points. The displacements are done in four different modes:

- Shift all contour points by 1 pixel outward.
- Shift all contour points by 1 pixel inward.
- Shift the points on the side inward, and the points at the bottom downward (so that the capsule appears more slender).
- Shift the points on the side outward, and the points at the bottom upward (so that the capsule appears more chubby).

The error bars for the points in the K_{2D}-V- and ν-V-diagrams (figs. 5.5, 5.7 and 5.9) are generated by taking the maximum deviation from the original results. If the maximum deviation is still smaller than the grid spacing on the K_{2D} or ν axes, we take the grid spacing as the smallest possible error bar. Hence, they are worst-case estimates. Typically, the inward/outward modes produce the largest deviations in V/V_0, whereas the slender/chubby modes produce the largest errors in the elastic constants.

We expect the modes described above to reveal the worst-case systematic errors of the method. Since they describe a possible systematic mistake of the camera, for example caused by lighting effects, we expect that all images are affected by the same mode. It follows that each point in the K_{2D}-V-diagrams has to be shifted in the same direction when correcting them. Thus, the positions of the points relative to each other are mainly conserved. This ensures that the trends observed in the diagrams are well resolved; only the overall scale of the plot may vary within the error bars.

Another systematic error comes from the fact that the pseudo-surface deviates from the detected outermost contour by about 1 wrinkle amplitude. Especially for OTS capsules, where the wrinkle amplitude grows larger than 1 pixel during deflation, it has to be checked that this error is smaller than the observed drift of the compression modulus.

For given wavelength Λ, the s_0-dependent wrinkle amplitude is determined by the consideration that a circumferential fibre of real length $w(s_0) = 2\pi r_0 \lambda_\varphi$ must be deposited on the perimeter $u(s_0) = 2\pi r_0 \bar{\lambda}_\varphi$ of the pseudo-surface. In the wrinkling region where $\bar{\lambda}_\varphi < \lambda_\varphi$, there is an excess length $w(s_0) - u(s_0) > 0$ which has to lie in the wrinkles. For sinusoidal wrinkles with small amplitude C and wavenumber $k = 2\pi/\Lambda$, the excess length is given according to (5.18) as

$$w - u = \int_0^{2\pi} \frac{1}{2} C^2 \, \bar{r} \, k^2 \cos^2(k\bar{r}\theta) \, \mathrm{d}\theta = 2\pi^3 \frac{C^2 \bar{r}}{\Lambda^2}, \tag{D.7}$$

where the integration was performed with the assumption that u is a multiple of Λ. This gives the relation

$$2\pi r_0 (\lambda_\varphi - \bar{\lambda}_\varphi) = 2\pi^3 \frac{C^2 \bar{\lambda}_\varphi r_0}{\Lambda^2} \tag{D.8}$$

so that the amplitude reads

$$C(s_0) = \frac{\Lambda}{\pi} \sqrt{\frac{\lambda_\varphi(s_0)}{\bar{\lambda}_\varphi(s_0)} - 1}. \tag{D.9}$$

Now, instead of measuring the RMS deviation between midsurface $(r(s_0), z(s_0))$ and sampling points, we measure it between the outermost surface $(r(s_0) + C(s_0), z(s_0))$ and sampling points.

Surprisingly, the influence on the resulting fit parameters is small compared to the four displacement modes discussed above, although the maximum amplitude is 5 pixels in the analysed OTS experiment. Only the capsule volume is affected significantly, so that the points in the K_{2D}-V-diagram would be shifted to the left. For clarity, this error mode is not presented in detail in the main text since it is less significant than the modes mentioned before. A possible reason for this small influence is that the displacement due to the amplitude is always much smaller than the deformation, because the wrinkle amplitude is only large when the deformation is extermely large.

D.4. Examples for fit results

In the following, some plots of fit results are shown (figs. D.4 to D.9). For each example, the upper left plot shows the fitted solution (green line) together with the experimental image (greyscale) and the sampling points (red). Horizontal green lines indicate the wrinkled region according to the fitted solution of the shape equations. The upper right plot shows the distribution of the fit residual in the (K_{2D}, ν)-plane, dark colours correspond to low RMS deviations; the best fit is indicated with a green dot. The bottom plot shows the residual for the best fit as a function of the sampling point number: The numbering starts at the left attachment to the capillary and goes counter-clockwise around the capsule.

D.4.1. Fits to theory shapes

Figures D.4 and D.5 show two fits to theoretically generated shapes, with $K_{\text{orig}} = 600\,\text{mN/m}$ and $\nu_{\text{orig}} = 0.3$ and zero noise. The reference shape has a surface tension of $\gamma = 49.8\,\text{mN/m}$, see section 5.3. Both fits are as perfect as they can be. They reproduce the correct volume and Poisson ratio and are as close as possible to the correct area compression modulus (the original value for the compression modulus in reduced units, $K_{\text{orig}}/\gamma = 12.06$, does not lie exactly on the fit grid, which has $K_{2D}/\gamma = 12$ as the closest value). This slight discrepancy explains the fit residual shown in the bottom plots, which is overall very small but shows a systematic deviation between fit and sampling points.

As explained in section 5.3.2, a noisy contour was prepared from the theoretically generated shapes by shifting each sampling by a random two-dimensional vector $\boldsymbol{\delta}$ whose components are random numbers drawn from the interval $[-0.0045, 0.0045]$. The fits to this noisy contour are shown in figs. D.6 and D.7. In the first case, where the capsule is only little deformed, the fit is close to the original moduli, but does not reproduce them exactly. In the second case, with larger deformation, the fit finds the correct values for K_{2D} and ν because the deformation is sufficiently larger than the noise, see appendix D.5. The fit residual, see the bottom plots of both figures, shows the inevitable deviations between the smooth solution of the shape equations and the noisy contour.

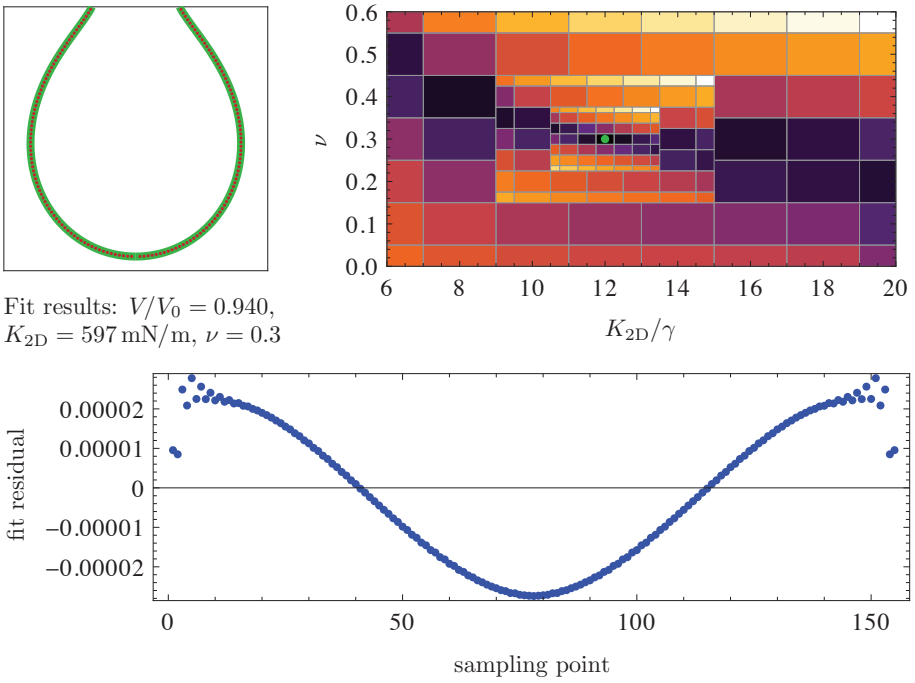

Figure D.4.: Fit to a theoretically generated shape with $V/V_0 = 0.94$, $K_{\mathrm{orig}} = 600\,\mathrm{mN/m}$ and $\nu_{\mathrm{orig}} = 0.3$, without noise.

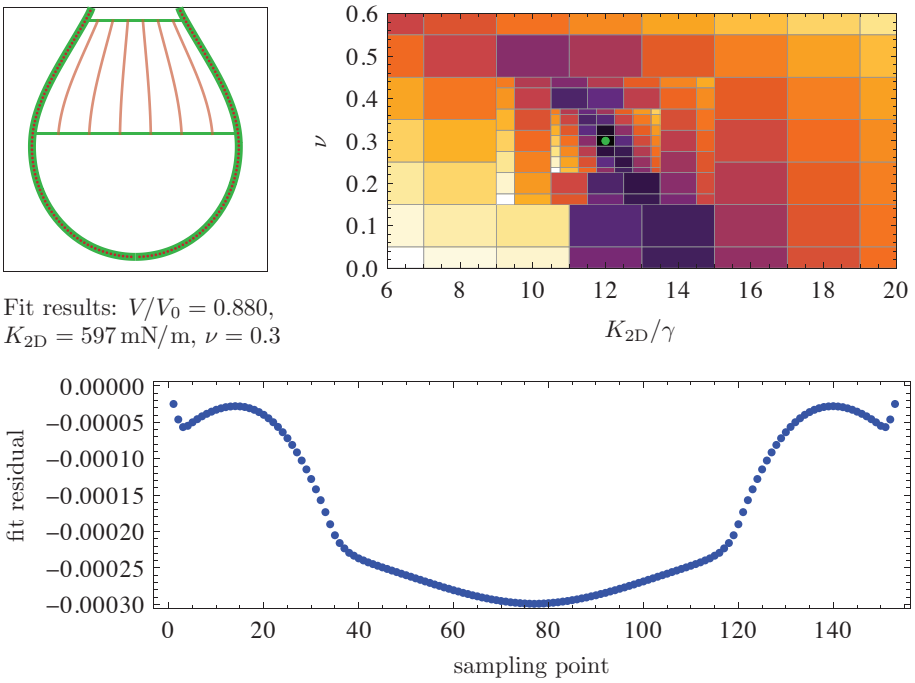

Figure D.5.: Fit to a theoretically generated shape with $V/V_0 = 0.88$, $K_{\mathrm{orig}} = 600\,\mathrm{mN/m}$ and $\nu_{\mathrm{orig}} = 0.3$, without noise.

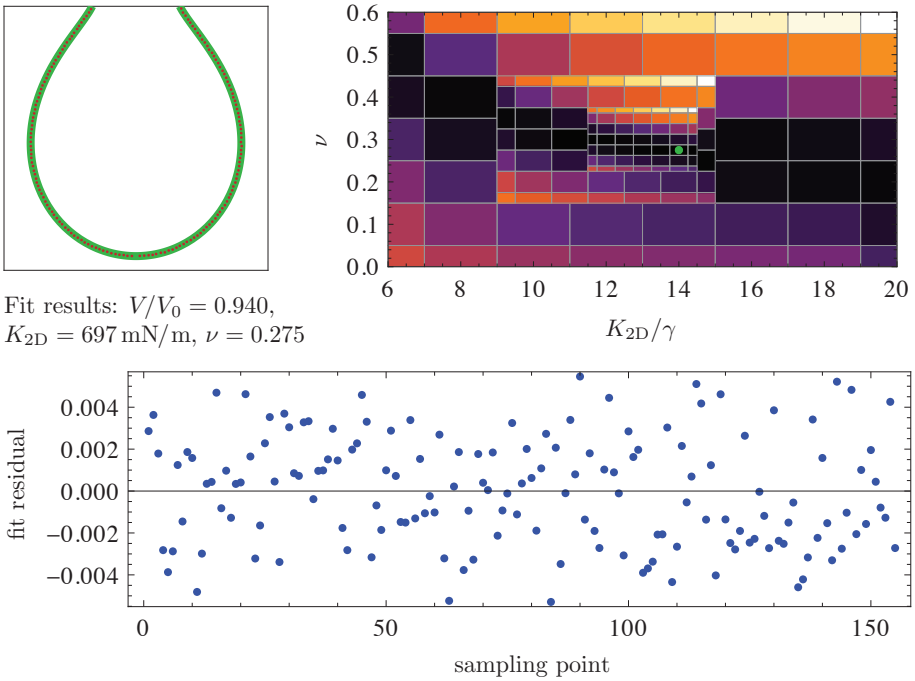

Figure D.6.: Fit to a theoretically generated shape with $V/V_0 = 0.94$, $K_{\mathrm{orig}} = 600\,\mathrm{mN/m}$ and $\nu_{\mathrm{orig}} = 0.3$, with noise amplitude 0.0045.

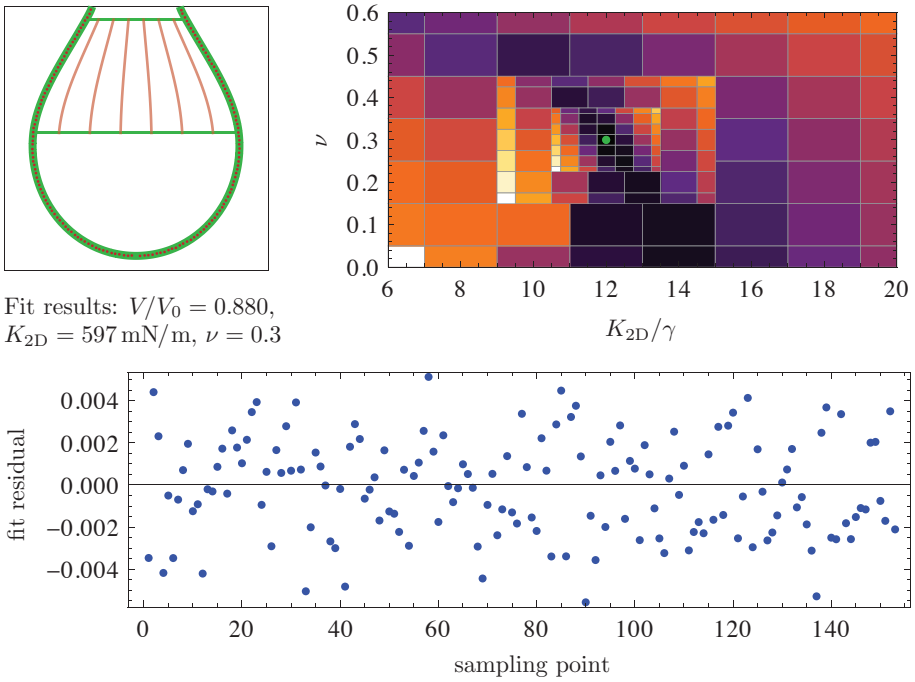

Figure D.7.: Fit to a theoretically generated shape with $V/V_0 = 0.88$, $K_{\mathrm{orig}} = 600\,\mathrm{mN/m}$ and $\nu_{\mathrm{orig}} = 0.3$, with noise amplitude 0.0045.

D.4.2. Fits of experiments with OTS and HFBII capsules

Step 1: Laplace-Young fits and conversion factors. In both OTS and HFBII measurements, four images of the undeformed capsule were fitted with the Laplace-Young equation with the interfacial tension γ, internal pressure p_0 and scaling factor $a^{(\mathrm{px})}$ as fit parameters. The averaged surface tensions and conversion factors are listed in the following table.

	γ	mm $\leftrightarrow$ px	theor. length unit $\leftrightarrow$ px
OTS	11.2 mN/m	1 mm$\hat{=}$135 px	1$\hat{=}$194 px
HFBII	49.8 mN/m	1 mm$\hat{=}$146 px	1$\hat{=}$139 px

Whereas the Laplace-Young fits for HFBII match the detected contour nearly perfectly, small systematic deviations (± 1 px) can be observed for the Laplace-Young fits to the initial OTS capsule. These deviations may be caused by the polymerisation process and might affect the results of the following elastic fits, especially for small deformation.

Step 2: Shape Analysis. Two representative fit results for OTS and HFBII capsules are shown in figs. D.8 and D.9. Evidently, the capsule shapes are reproduced very well. For the OTS capsule, even the boundary of the wrinkled region predicted by the theory (horizontal green lines) matches the experimental result, although the position of the horizontal green lines was *not* incorporated in the RMS deviation. The fact that they coincide with the experimental observations proves that the elastic model captures the wrinkling behaviour accurately.

The plots of the RMS deviation distribution in the (K_{2D}, ν)-plane (upper right plot in each figure) show that the minima are nicely located inside the refined area of the parameter space. That was facilitated by choosing the area compression modulus $K_{2\mathrm{D}}$ instead of the surface Young modulus $E_{2\mathrm{D}}$ on the horizontal axis. The reverse mapping $E_{2\mathrm{D}} = 2(1-\nu)K_{2\mathrm{D}}$ would stretch the circular minimum to a long and narrow ellipse, which would be harder to analyse with our rudimentary grid based minimisation method.

Finally, the fit residual along the contour (bottom plots of each figure) reveals whether there are systematic deviations between fitted contour and sampling points. In both cases, the systematic deviations are relatively small, though visible. For the OTS capsule, the largest deviations are at the right attachment point to the capillary, and other maxima at the point where the wrinkles end (around the $50^{\mathrm{t}h}$ sampling point). At this point, the experimental capsule shape even seems to have a small kink, which cannot be reproduced by the model according to the continuity conditions of the slope angle. In case of the HFBII capsule, this effect is much smaller since the wrinkle amplitude is smaller. Consequently, the fit residual shows a less systematic behaviour.

Step 3: Wrinkle analysis. As described in the main text, the wrinkle analysis is only possible for the OTS capsule since the wrinkles on the HFBII capsule cannot be resolved without microscopy. For OTS, the resulting bending stiffness is $E_B \approx (1.2 \text{ to } 2.5) \cdot 10^{-14}$ Nm, see the main text. The corresponding membrane thickness $H_0 \approx 0.56\,\mu$m to $0.77\,\mu$m obtained from equation (2.9) should rather be considered as an *effective* thickness, because this formula is only valid for shells composed of a thin sheet of isotropic material. Evidently, this is not the case because the obtained Poisson ratio $\nu \approx 0.6$ is outside the admissible range $[-1, 1/2]$ for three-dimensional Poisson ratios.

The results for the effective membrane thickness can be confirmed by raster electron microscopy measurements with another OTS capsule produced according to the same protocol (fig. D.10). During the preparation for the raster electron microscopy, the membrane was dried and teared in

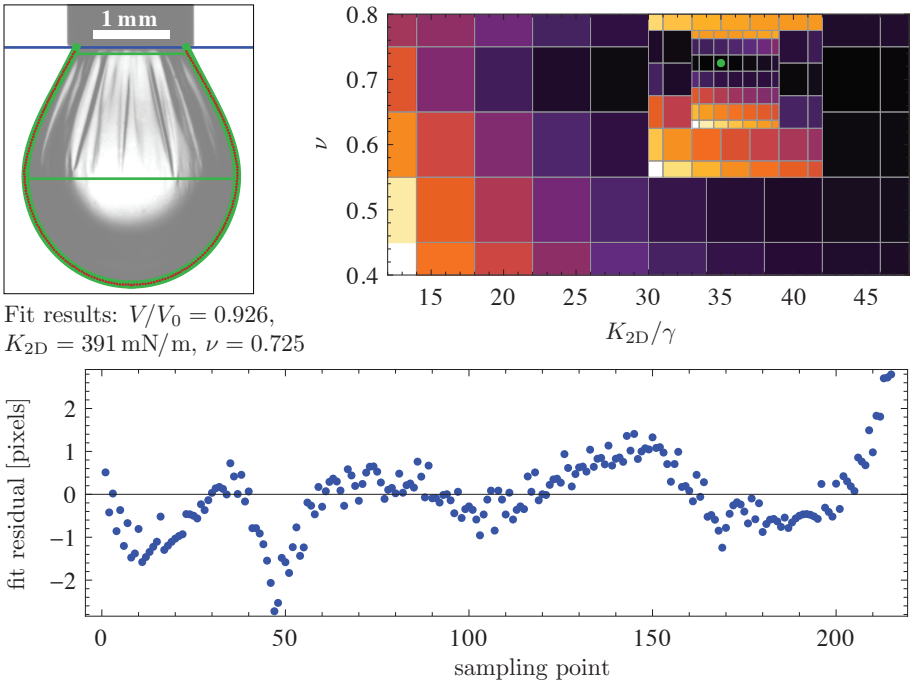

Fit results: $V/V_0 = 0.926$,
$K_{2D} = 391\,\mathrm{mN/m}$, $\nu = 0.725$

Figure D.8.: Fit to an experimental image of an OTS capsule.

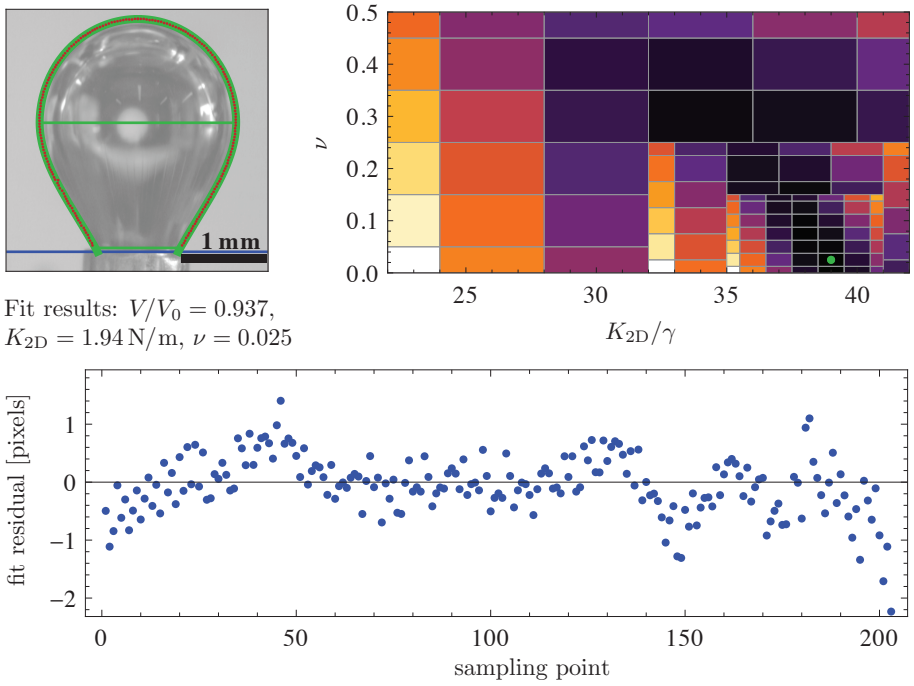

Fit results: $V/V_0 = 0.937$,
$K_{2D} = 1.94\,\mathrm{N/m}$, $\nu = 0.025$

Figure D.9.: Fit to an experimental image of a HFBII coated bubble.

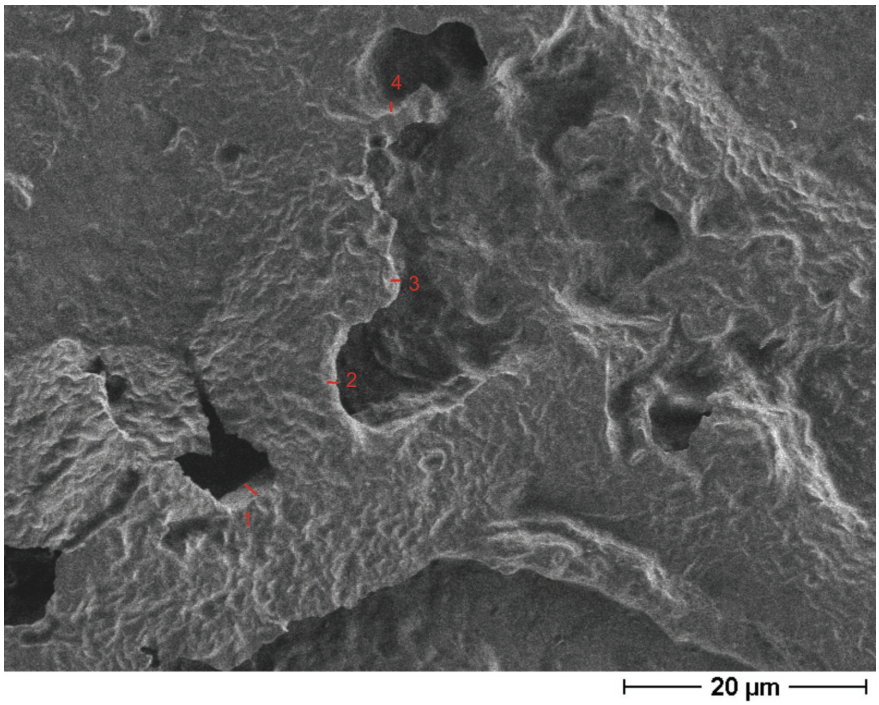

Figure D.10.: Raster electron microscopy image of a dried and torn OTS membrane. The numbered red lines indicate thickness measurements.

consequence. At some gaps (numbered 1-4 in fig. D.10), values of 1.4 µm, 0.98 µm, 0.83 µm and 0.86 µm were obtained for the thickness. This agreement of the fitted and measured membrane thickness suggests that our method works accurately.

D.5. Quantification of noise in the capsule contours

To transfer the above results from the fitting of theory shapes to the fitting of contours captured from images, we need to measure the amount of noise in a given set of sampling points. In the above case, this was obsolete since the noise was added manually and with known amplitude. Contours extracted from images are likely to be noisy too, but with unknown amplitude.

The set of sampling points $\boldsymbol{x}_i = (r_i, z_i)$ to be analysed is supposed to be ordered, with $i = 1$ corresponding to the first point at the left attachment point to the capillary, and $i = n$ to the last point before the right attachment point. In the results presented below, we assume that they are given in the reduced units of tab. 5.1, that is, with the capillary diameter a as unit length.

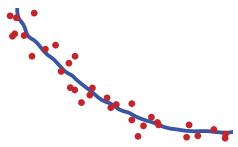

Figure D.11.: Noisy sampling points with smoothed mid-line.

As a first transformation, we form the moving average (over four successive sampling points) of the lists r_i and z_i, which results in two lists $\bar{r}_i$ and $\bar{z}_i$ representing smoothed sampling points. We interpolate between these smoothed points to obtain a parametrisation $(\bar{r}(t), \bar{z}(t))$ representing the mid-line of the band of noisy sampling points (see fig. D.11, blue continuous line). The root mean square deviation between the sampling points and smoothed mid-line is suitable to measure the

magnitude of the noise. We define the noise measure as

$$N = \sqrt{3} \cdot \left(\frac{1}{n} \sum_{i=1}^{n} \min_{t} \left\| \begin{pmatrix} r_i \\ z_i \end{pmatrix} - \begin{pmatrix} \bar{r}(t) \\ \bar{z}(t) \end{pmatrix} \right\|^2 \right)^{1/2} \tag{D.10}$$

where the prefactor $\sqrt{3}$ is motivated as follows.

In section D.4.1, noise was added manually to a contour by drawing a random number $\delta \in [-\Delta, \Delta]$ from a uniform distribution (actually, there were two displacements, in horizontal and vertical direction, but since tangential displacements do not produce noise, we only need to consider the displacement in normal direction). The probability density function of δ has a variance of $\sigma_\delta^2 = \Delta^2/3$. From this equation, the noise amplitude can be obtained as $\Delta = \sqrt{3}\,\sigma_\delta$, and σ_δ can be roughly estimated as the root mean square deviation between the smoothed mid-line and the sampling points. Thus, definition (D.10) should give the noise amplitude of the contour. Applying this definition to the theoretically generated noisy contour indeed gives with $N = 0.0041$ a value close to the original noise amplitude $\Delta = 0.0045$.

The magnitude of the noise has to be compared to the deformation out of the initial shape, which can be measured simply by the root mean square distance between sampling points and Laplace-Young shape (r_0, z_0),

$$D = \left(\frac{1}{n} \sum_{i=1}^{n} \min_{s_0} \left\| \begin{pmatrix} r_i \\ z_i \end{pmatrix} - \begin{pmatrix} r_0(s_0) \\ z_0(s_0) \end{pmatrix} \right\|^2 \right)^{1/2} . \tag{D.11}$$

As a test case with known results, we analyse the noisy contours of the theoretically generated shapes, see fig. D.12. In subfigure a), the noise and deformation measures N and D are plotted against the reduced volume. Averaged over all points, we find $N = 0.0041$. Multiples of this value are plotted in orange and green. The blue line is a quadratic fit to the data points for the deformation measure D. This blue lines intersects the N-, $2N$- and $4N$-lines at certain volumes $V_1 = 0.996V_0$, $V_2 = 0.984V_0$ and $V_4 = 0.963V_0$, respectively. Subfigure b) shows a simplified version of the fit results, which were already presented in fig. 5.5 in the main text. The volumes V_1, V_2 and V_4 are marked by the vertical red, orange and green lines and indicate some kind of "reliability level" of the fits: Around the red line, the deformation is of the same size as the noise amplitude, and thus a fit is not possible. The orange and green lines indicate the volumes where the deformation is twice the noise and four times the noise, respectively. As we can see from the fit results, the fit in the vicinity of the orange line fails, but the fits beyond the green line are satisfactorily close to the exact result $K_{\mathrm{orig}} = 600\,\mathrm{mN/m}$.

The same procedure was applied to the images of OTS and HFBII capsules that have been analysed in section 5.4, and the results are presented in a similar manner in figs. D.13 and D.14, respectively. For the OTS capsules we find that all analysed images are in the "safe region" beyond the green line, which suggests that all OTS fits are quite reliable. Note that the noise level $N = 0.002$, which is also measured with the capillary diameter a as the length unit, is very small for the OTS images because they are of high contrast and good quality.

In case of the HFBII images, a noise level very similar to the theory shapes is found, see fig. D.14 a). The noise levels shown in the $K_{2\mathrm{D}}$-V-diagram, fig. D.14 b), indicate that the reliability of the fits in the pre-wrinkling regime (the ascending branch, cf. fig. 5.9) is doubtful: In the pre-wrinkling regime, the deformation is not much larger than the noise. However, the clear trend of these data points and their small fluctuations around their linear fit suggest that there is a certain significance to these results. For a definite answer, however, more experimental data is needed, preferably with better image quality and less noise.

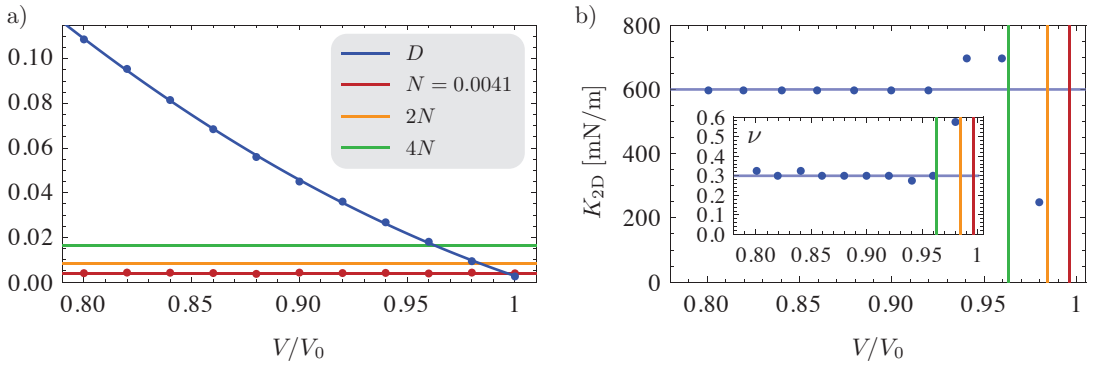

Figure D.12.: Noise quantification and fit results for the theoretical shapes, with known elastic moduli $K_{\mathrm{orig}} = 600\,\mathrm{mN/m}$ and $\nu_{\mathrm{orig}} = 0.3$. a) The measured noise N and deformation D (in length units of a, see tab. 5.1) are plotted against the reduced volume. The lines $2N$ and $4N$ indicate multiples of the measured noise. b) Fit results, as plotted in fig. 5.5 in the main text, with additionally indicated noise levels in red, orange and blue as in subfigure a). The inset shows the fitted Poisson ratio, which has not been shown in the main text for simplicity.

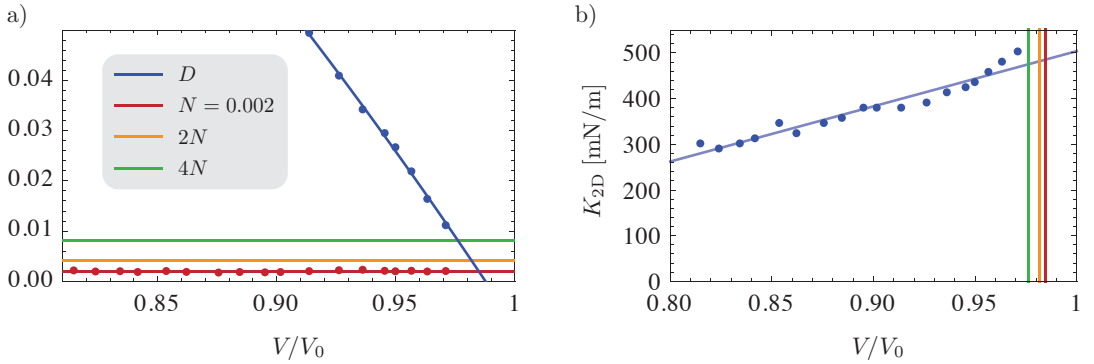

Figure D.13.: Noise quantification and fit results for the OTS images. a) The measured noise N and deformation D. b) Fit results, as plotted in fig. 5.7 in the main text (without re-inflation).

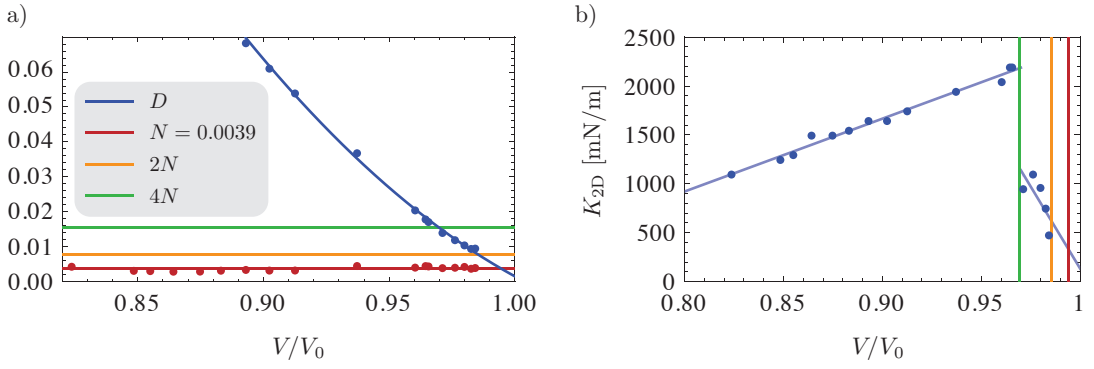

Figure D.14.: Noise quantification and fit results for the HFBII images. a) The measured noise N and deformation D. b) Fit results, as plotted in fig. 5.9 in the main text.

Appendix E

Derivation of the HFBII elasticity model

E.1. Ratios of the hard-core stresses

We consider a jammed state of the lattice, that is, when (λ_x, λ_y) is on the boundary of the admissible domain. Here, boundary 1 as specified by eq. (5.30) and fig. 5.11 b) is considered, where $3\lambda_x^2/4 + \lambda_y^2/4 = L^2$.

On this boundary, the lattice, see fig. E.1 a), is compressed predominantly in x-direction. Not all hard cores of neighbouring beads are in contact with each other, only those along the links that are drawn continuous in subfigure b). The dashed link in this figure is a spring interaction, not a hard-core interaction, and is therefore ignored in the following. Subfigure c) shows that the force F_x applied to a bead is split into components F_t tangential to the links. Trigonometric relations give $\cos\alpha = F_x/2F_t$. Analogous considerations give $\sin\alpha = F_y/2F_t$ for the splitting of F_y. Thus we have

$$\frac{F_x}{F_y} = \tan\alpha \tag{E.1}$$

as the condition that the skeleton is in static equilibrium.

With subfigure d) we can relate the geometric angle α to the lengths of the links. The hard-core links have, by definition, length L. The vertical (dashed) link has a rest length of 1, and is stretched (or compressed) by the deformation to a length $\lambda_y \cdot 1$. We thus obtain

$$\tan\alpha = \frac{\lambda_y}{\sqrt{4L^2 - \lambda_y^2}} \qquad \Rightarrow \qquad \frac{F_x}{F_y} = \frac{\lambda_y}{\sqrt{4L^2 - \lambda_y^2}}. \tag{E.2}$$

Finally, we have to relate the forces F_x and F_y to the stresses $\tau_x^{(c)}$ and $\tau_y^{(c)}$. Stresses are forces per length, and the investigated cell of the lattice has a height $l_y = \lambda_y$ and width $l_x = l_y/\tan\alpha = \sqrt{4L^2 - \lambda_y^2}$, see subfigure e). With $\tau_x^{(c)} = F_x/l_x$ and $\tau_y^{(c)} = F_y/l_y$, we thus arrive at

$$\frac{\tau_y^{(c)}}{\tau_x^{(c)}} = \frac{\lambda_y^2}{4L^2 - \lambda_y^2}. \tag{E.3}$$

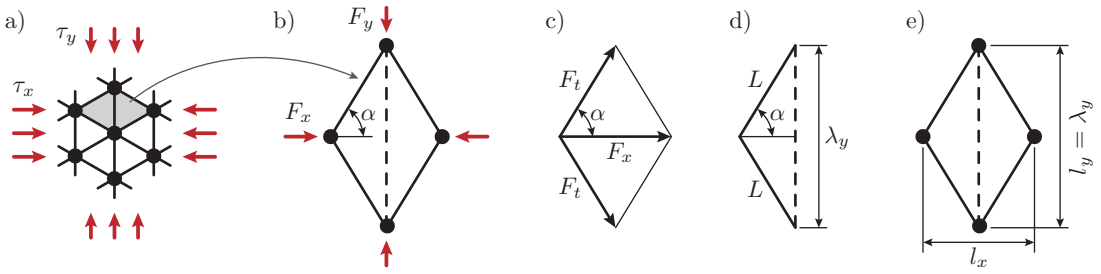

Figure E.1.: Sketches to calculate the ratio of the hard-core stresses

With the strain constraint (5.30) on boundary 1, this is equivalent to

$$\frac{\tau_y^{(\mathrm{c})}}{\tau_x^{(\mathrm{c})}} = \frac{1}{3}\frac{\lambda_y^2}{\lambda_x^2}. \tag{E.4}$$

Thus, only the ratio between the hard-core stresses is prescribed by the geometry of the lattice.

Analogous results can be obtained on boundary 2, with all indices x and y interchanged. The complete result is therefore

$$\frac{\tau_y^{(\mathrm{c})}}{\tau_x^{(\mathrm{c})}} = \begin{cases} \lambda_y^2/3\lambda_x^2 & \text{for } \lambda_y > L \text{ (boundary 1)} \\ 3\lambda_y^2/\lambda_x^2 & \text{for } \lambda_y < L \text{ (boundary 2)} \end{cases}. \tag{E.5}$$

In point B with $\lambda_x = \lambda_y = L$, which lies on both boundaries 1 and 2, the lattice is uniformly compressed and all neighbouring beads are in contact. Equation (E.5) then states that the ratio of the hard-core stresses is either 3 or 1/3. In fact, due to the close packing of spheres, any value in between can also be realised, so that

$$\frac{1}{3} \le \frac{\tau_y^{(\mathrm{c})}}{\tau_x^{(\mathrm{c})}} \le 3 \quad \text{for } \lambda_x = \lambda_y = L \text{ (boundary point B)}. \tag{E.6}$$

E.2. Variational calculation and continuity conditions

In section 2.2.3 and appendix A.1, the equilibrium equations for shells of revolution (including a bending stiffness) have been derived by a variational calculation. We now revisit this calculation and adopt it to our custom elasticity model with hard-core interactions and without bending stiffness. The aim is to determine the continuity conditions at the boundary of the different regions A, B, 1 and 2. As a byproduct, we will re-obtain the equilibrium equations, including the correct ratios between the hard-core stresses $\tau_s^{(\mathrm{c})}$ and $\tau_\varphi^{(\mathrm{c})}$ as developed in the previous appendix section.

We first collect the results of the previous variational calculation, setting $E_B = 0$ and using $p - \Delta\rho\, g\, z$ as the pressure. This corresponds to the variational calculation one would perform for region A. We need the variations of the elastic energy functional U and load potential P,

$$\begin{aligned} U &= \int_R w_S(\lambda_s, \lambda_\varphi)\, \mathrm{d}A_0 = \int_R 2\pi r_0 w_S\, \mathrm{d}s_0 \quad \text{and} \\ P &= -pV + \Delta\rho\, g\, z^{(\mathrm{cm})}\, V = \int_R \pi r^2 z'(-p + \Delta\rho\, g\, z)\, \mathrm{d}s_0, \end{aligned} \tag{E.7}$$

where the region R of integration is arbitrary and not necessarily $s_0 \in [0, L_0]$, and $z^{(\mathrm{cm})}$ is the z-coordinate of the centre of mass of the enclosed liquid. The variations have been obtained in (A.7) and (A.8) as

$$\begin{aligned} \delta U &= 2\pi r \tau_s^{(\mathrm{s})} \delta v\Big|_{\partial R} + \int_R \mathrm{d}s_0\, 2\pi r \lambda_s \left\{ \delta u \left[\tau_s^{(\mathrm{s})} \kappa_s + \tau_\varphi^{(\mathrm{s})} \kappa_\varphi \right] + \delta v \left[\frac{\cos\psi}{r} \tau_\varphi^{(\mathrm{s})} - \frac{1}{r} \frac{\mathrm{d}(r\tau_s^{(\mathrm{s})})}{\mathrm{d}s} \right] \right\}, \\ \delta P &= \pi r^2 (-p + \Delta\rho\, g\, z) \delta z\Big|_{\partial R} + \int_R \mathrm{d}s_0\, 2\pi r \lambda_s \Big\{ \delta u \left[-p + \Delta\rho\, g\, z \right] \Big\}. \end{aligned} \tag{E.8}$$

Here, δu and δv are the normal and tangential variation of the contour, see eq. (2.11) and fig. 2.3, and δz is the variation in z-direction. It is not very consistent to use these three variations, since only two of them are independent. This issue will be resolved later where

transversality conditions introduce even more dependencies of the variations at the boundary ∂R. The boundary terms in (E.8) are to be evaluated at the boundary of the integration region R: If it is limited by $s_0 = s_1$ and $s_0 = s_2$, then our notation is to be understood as $f|_{\partial R} = f|_{s_2} - f|_{s_1}$. We are especially careful in the notation of the stresses. Here we only have spring contributions, defined by $\tau_s^{(\mathrm{s})} = \frac{1}{\lambda_\varphi}\partial w_S/\partial\lambda_s$ and $\tau_\varphi^{(\mathrm{s})} = \frac{1}{\lambda_s}\partial w_S/\partial\lambda_\varphi$, see eq. (5.6). In the region A, these are identical to the complete stresses τ_s and τ_φ. Therefore, the equilibrium equations of membrane theory which follow from $\delta(U+P)=0$ can be written as

$$0 = \kappa_s\tau_s + \kappa_\varphi\tau_\varphi - p + \Delta\rho\, g\, z \quad \text{and} \quad 0 = \frac{\cos\psi}{r}\tau_\varphi - \frac{1}{r}\frac{\mathrm{d}r\tau_s}{\mathrm{d}s}. \tag{E.9}$$

They are a special case of the shell equilibrium equations (2.16) for vanishing bending stiffness.

In a second step, let us determine the equilibrium equations in region 2, where the strains are constrained by $\lambda_s^2 + 3\lambda_\varphi^2 - 4L^2 = 0$, see eq. (5.30). We can incorporate this constraint in the variational calculation by means of a Lagrange multiplier $t(s_0)$. From a physical point of view, the Lagrange multiplier takes care that the system remains on boundary 2 in the stretch space, and we can expect it to be related to the hard-core stresses, which fulfil the same function in the physical reality. The functional of this constraint that must be incorporated in the calculus of variations is $N = \int_R t(s_0)\left[\lambda_s^2 + 3\lambda_\varphi^2 - 4L^2\right]\mathrm{d}s_0$, and its variation can be obtained after some calculation as

$$\begin{aligned}\delta N &= \int_R t\left[2\lambda_s\,\delta\lambda_s + 6\lambda_\varphi\,\delta\lambda_\varphi\right]\mathrm{d}s_0 \qquad\qquad (\text{E.10})\\ &= 2\pi r\frac{\lambda_s t}{\pi r}\delta v\Big|_{\partial R} + \int_R \mathrm{d}s_0\, 2\pi r\lambda_s\left\{\delta u\left[\frac{\lambda_s t}{\pi r}\kappa_s + 3\frac{\lambda_\varphi^2}{\lambda_s^2}\frac{\lambda_s t}{\pi r}\kappa_\varphi\right] + \delta v\left[3\frac{\lambda_\varphi^2}{\lambda_s^2}\frac{\lambda_s t}{\pi r}\frac{\cos\psi}{r} - \frac{1}{r}\frac{\mathrm{d}(r\frac{\lambda_s t}{\pi r})}{\mathrm{d}s}\right]\right\}.\end{aligned}$$

This has the same form as δU, but with the hard-core stresses $\tau_s^{(\mathrm{c})}$ and $\tau_\varphi^{(\mathrm{c})}$ in place of τ_s and τ_φ when we identify

$$\tau_s^{(\mathrm{c})} = \frac{\lambda_s t}{\pi r} \quad \text{and} \quad \tau_\varphi^{(\mathrm{c})} = 3\frac{\lambda_\varphi^2}{\lambda_s^2}\frac{\lambda_s t}{\pi r}. \tag{E.11}$$

Thus, the variational calculation for region 2 has reproduced the correct ratio of the hard-core stresses determined in eq. (E.5). The equilibrium equations for region 2 follow from $\delta(U+P+N)=0$ and have the same form (E.9) as before, but with hard-core contributions included in the stresses ($\tau_s = \tau_s^{(\mathrm{s})} + \tau_s^{(\mathrm{c})}$ and analogous for τ_φ). An analogous calculation can be done for region 1.

In region B, we need to introduce two constraints $\lambda_s = L$ and $\lambda_\varphi = L$ with two separate Lagrange multipliers $t_s(s_0)$ and $t_\varphi(s_0)$ which will be related to the hard-core stresses. The functional of the constraints reads $N = \int_R \left\{[\lambda_s - L]t_s + [\lambda_\varphi - L]t_\varphi\right\}\mathrm{d}s_0$ and its variation can be written as

$$\begin{aligned}\delta N &= \int_R \left\{t_s\,\delta\lambda_s + t_\varphi\,\delta\lambda_\varphi\right\}\mathrm{d}s_0 \qquad\qquad (\text{E.12})\\ &= 2\pi r\tau_s^{(\mathrm{c})}\delta v\Big|_{\partial R} + \int_R \mathrm{d}s_0\, 2\pi r\lambda_s\left\{\delta u\left[\tau_s^{(\mathrm{c})}\kappa_s + \tau_\varphi^{(\mathrm{c})}\kappa_\varphi\right] + \delta v\left[\tau_\varphi^{(\mathrm{c})}\frac{\cos\psi}{r} - \frac{1}{r}\frac{\mathrm{d}(r\tau_s^{(\mathrm{c})})}{\mathrm{d}s}\right]\right\}\end{aligned}$$

with the hard-core stresses

$$\tau_s^{(\mathrm{c})} = \frac{t_s}{2\pi r} \quad \text{and} \quad \tau_\varphi^{(\mathrm{c})} = \frac{t_\varphi}{2\pi r_0\lambda_s}. \tag{E.13}$$

Again, the equilibrium equations that follow from $\delta(U+P+N)=0$ have the same form (E.9) as above, but now with two independent hard-core contributions $\tau_s^{(c)}$ and $\tau_\varphi^{(c)}$ included in the stresses.

So far, the equilibrium equations in regions A, 2 and B have been derived separately by using that the integrands of the variated functional must vanish for arbitrary δu and δv. From the boundary terms, we can now derive continuity conditions for the geometric quantities r, z, ψ, the stretches λ_s, λ_φ and the stresses τ_s, τ_φ at the boundary between two different regions.

Three continuity conditions can be derived from the requirement that the elastic energy density w_S stays finite. From this requirement follows that $\lambda_s<\infty$, and with $r'(s_0)^2+z'(s_0)^2=\lambda_s<\infty$ we conclude that r and z are continuous (a jump would imply an infinite derivative). As the hoop stretch $\lambda_\varphi=r/r_0$ is a function of two continuous functions, it is also continuous.

Further boundary conditions follow from the conditions that the boundary terms in the variational calculation must vanish. We consider the case that a region R_1 with $s_0\in[s_1,s_2]$ is in contact with a region R_2 with $s_0\in[s_2,s_3]$ (both regions can be chosen from A, 1, 2 and B). We mark all functions that are defined on $s_0>s_2$ (belonging to R_2) with a tilde to distinguish them from the functions defined on $s_0<s_2$.

The position s_2 of the transition is not fixed, it must also be variated. When the boundary of an integral $\int_{s_1}^{s_2} I(s_0)\,\mathrm{d}s_0$ is altered from s_2 to $s_2+\delta s_2$, then the value of the integral changes by $I(s_2)\delta s_2$. Collecting all boundary terms of the variation $\delta(U+P+N)$, see eqs. (E.8), (E.10) and (E.12), and setting them to zero gives

$$\begin{aligned}2\pi r\tau_s\delta v+\pi r^2(-p+\Delta\rho\, g\, z)\delta z+[2\pi r_0 w_S+\pi r^2 z'(-p+\Delta\rho\, g\, z)]\delta s_2\\ =2\pi\tilde r\tilde\tau_s\delta\tilde v+\pi\tilde r^2(-p+\Delta\rho\, g\,\tilde z)\delta\tilde z+[2\pi r_0\tilde w_S+\pi\tilde r^2\tilde z'(-p+\Delta\rho\, g\,\tilde z)]\delta s_2,\end{aligned}\quad\text{(E.14)}$$

where both sides are understood as being evaluated at s_2. The stresses τ_s and $\tilde\tau_s$ can contain hard-core contributions from δN, depending of what type regions R_1 and R_2 are, and the energy densities w_S and $\tilde w_S$ are distinguished because they are evaluated at different stretches, $w_S=w_S(\lambda_s,\lambda_\varphi)$ and $\tilde w_S=w_S(\tilde\lambda_s,\tilde\lambda_\varphi)$.

The variations δu, δv, δs_2, $\delta\tilde u$ and $\delta\tilde v$ are not independent from each other, but related by transversality conditions. Above we have derived that the shape $r(s_0)$ and $z(s_0)$ is continuous at any point s_0. Consequently, the shape variations must also produce a continuous variated shape, which implies $(r+\delta r)\big|_{s_2+\delta s_2}=(\tilde r+\delta\tilde r)\big|_{s_2+\delta s_2}$, or

$$\delta r(s_2)+r'(s_2)\delta s_2=\delta\tilde r(s_2)+\tilde r'(s_2)\delta s_2\quad\text{and}\quad\delta z(s_2)+z'(s_2)\delta s_2=\delta\tilde z(s_2)+\tilde z'(s_2)\delta s_2.\quad\text{(E.15)}$$

These transversality conditions can also be expressed in terms of the normal and tangential variations by use of eq. (2.11), which results in

$$\begin{aligned}\sin\psi\,\delta u+\cos\psi\,\delta v+r'\delta s_2&=\sin\tilde\psi\,\delta\tilde u+\cos\tilde\psi\,\delta\tilde v+\tilde r'\delta s_2\quad\text{and}\\ -\cos\psi\,\delta u+\sin\psi\,\delta v+z'\delta s_2&=-\cos\tilde\psi\,\delta\tilde u+\sin\tilde\psi\,\delta\tilde v+\tilde z'\delta s_2.\end{aligned}\quad\text{(E.16)}$$

Using the the second transversality condition (E.15) we see that the terms

$$\pi r^2(-p+\Delta\rho\, g\, z)[\delta z+z'\delta s_2]=\pi\tilde r^2(-p+\Delta\rho\, g\,\tilde z)[\delta\tilde z+\tilde z'\delta s_2]\quad\text{(E.17)}$$

cancel out in the boundary terms (E.14) because $r=\tilde r$ and $z=\tilde z$ at the point s_2. What remains from (E.14) is

$$r\tau_s\delta v+r_0 w_S\delta s_2=\tilde r\tilde\tau_s\delta\tilde v+r_0\tilde w_S\delta s_2.\quad\text{(E.18)}$$

From the five variations δu, δv, δs_2, $\delta\tilde u$ and $\delta\tilde v$, only three are independent because we have two transversality conditions (E.15). However, we cannot choose δv, $\delta\tilde v$ and δs_2 as the

three independent ones, because they are all related to a tangential shape variation. It is "safer" to consider δu, δv and δs_2 as independent, and then determine $\delta\tilde{u}$ and $\delta\tilde{v}$ from the transversality conditions to eliminate them from the boundary condition (E.18). Multiplying the first transversality condition (E.15) with $\cos\tilde{\psi}$, the second one with $\sin\tilde{\psi}$ and adding them results in

$$\delta\tilde{v} = (s\tilde{c} - c\tilde{s})\delta u + (c\tilde{c} + s\tilde{s})\delta v + [\tilde{c}(r' - \tilde{r}') + \tilde{s}(z' - \tilde{z}')]\delta s_2 \tag{E.19}$$

where the abbreviations $s = \sin\psi$ and $c = \cos\psi$ (and analogously with a tilde) have been introduced. With this we can eliminate $\delta\tilde{v}$ from the boundary terms (E.18), resulting in

$$\delta u\big[\tilde{r}\tilde{\tau}_s(s\tilde{c}-c\tilde{s})\big]+\delta v\big[\tilde{r}\tilde{\tau}_s(c\tilde{c}+s\tilde{s})-r\tau_s\big]+\delta s_2\big[r_0(\tilde{w}_S-w_S)+\tilde{r}\tilde{\tau}_s(\tilde{c}(r'-\tilde{r}')+\tilde{s}(z'-\tilde{z}'))\big] = 0. \tag{E.20}$$

Now we can argue that the variations δu, δv and δs_2 are independent and arbitrary, so that each term in this equations must vanish on its own.

Setting the term next to δu to zero results in $\sin\psi\,\cos\tilde{\psi} = \cos\psi\,\sin\tilde{\psi}$, which is equivalent to $\tan\psi = \tan\tilde{\psi}$ and we can conclude that

$$\psi(s_2) = \tilde{\psi}(s_2), \tag{E.21}$$

so the slope angle ψ is continuous at any region change. With this result and $r = \tilde{r}$ in mind, we can analyse the term next to δv and get

$$\tau_s(s_2) = \tilde{\tau}_s(s_2) \tag{E.22}$$

and thus, the meridional stress is also continuous. From the last term we obtain, using $r' = \lambda_s\cos\psi$ and $z' = \lambda_s\sin\psi$, the following condition:

$$w_S(\lambda_s,\lambda_\varphi) - \tau_s\lambda_s\lambda_\varphi = w_S(\tilde{\lambda}_s,\lambda_\varphi) - \tau_s\tilde{\lambda}_s\lambda_\varphi \tag{E.23}$$

(both sides evaluated at s_2).

After all, we have derived that most of the functions of interest r, z, ψ, λ_s, λ_φ, τ_s and τ_φ are continuous. However, λ_s and τ_φ may be discontinuous as long as the non-trivial continuity condition (E.23) is satisfied. A further investigation requires specification of regions R_1 and R_2 being in contact. As a first check of consistency, let us assume that both R_1 and R_2 are of type A, so that the transition at s_2 is purely artificial. The continuity of τ_s and λ_φ implies the continuity of τ_φ and λ_s by Hooke's law. Obviously, equation (E.23) is then also satisfied.

The transition from $R_1 = \mathrm{A}$ to $R_2 = 2$ is also entirely continuous, but the argumentation is far less trivial because Hooke's law only holds in the A region; in region 2 there are additional hard-core stresses. For the continuity of the meridional stress we need $\tau_s^{(\mathrm{s})}(\lambda_s,\lambda_\varphi) = \tau_s^{(\mathrm{s})}(\tilde{\lambda}_s,\lambda_\varphi)+\tau_s^{(\mathrm{c})}$. A jump in λ_s is thus possible when $\tau_s^{(\mathrm{c})}(s_2) \neq 0$. The non-trivial continuity condition (E.23), written as

$$w_S(\lambda_s,\lambda_\varphi) - \lambda_s\lambda_\varphi\tau_s^{(\mathrm{s})}(\lambda_s,\lambda_\varphi) = w_S(\tilde{\lambda}_s,\lambda_\varphi) - \tilde{\lambda}_s\lambda_\varphi\tau_s^{(\mathrm{s})}(\lambda_s,\lambda_\varphi), \tag{E.24}$$

is an equation to determine the relation between λ_s and $\tilde{\lambda}_s$. Inserting the functions for the energy density and Hookean stresses from eqs. (5.5) and (5.6) into this equation and rearranging it with Mathematica gives two solutions,

$$\lambda_s = \tilde{\lambda}_s \quad \text{or} \quad \lambda_s = \tilde{\lambda}_s + \nu(1-\lambda_\varphi). \tag{E.25}$$

In the first case, λ_s is continuous, thus $\tau_s^{(\mathrm{c})}(s_2) = 0$ as argued above, and because of the fixed ratio of the hard-core stresses, we have $\tau_\varphi^{(\mathrm{s})}(s_2) = 0$, too. So in this case, the hoop stress is

also continuous. The second case is more exciting because it might provide a possibility for a discontinuous transition. But when we calculate the hard-core stress in this case,

$$\tau_s^{(\mathrm{c})} = \tau_s^{(\mathrm{s})}(\lambda_s, \lambda_\varphi) - \tau_s^{(\mathrm{s})}(\tilde{\lambda}_s, \lambda_\varphi) = \frac{E_{2\mathrm{D}}}{1-\nu^2}\frac{1}{\lambda_\varphi}\nu(1-\lambda_\varphi), \tag{E.26}$$

we find that it is larger than zero because $\lambda_\varphi < L < 1$ in region 2. This is not allowed and rules out the second case. The only possibility to change between regions A and 2 is to do it continuously in all functions.

A discontinuous transition can be found between regions $R_1 = 2$ and $R_2 = \mathrm{B}$. At first we observe that the meridional stretch is confined by eq. (5.30) to $\lambda_s = \sqrt{4L^2 - 3\lambda_\varphi^2}$ in region 2, and to $\tilde{\lambda}_s = \lambda_\varphi = L$ in region B. As the hoop stretch is continuous, we conclude that $\lambda_s = \sqrt{4L^2 - 3L^2} = L$ is also continuous. The non-trivial continuity condition (E.23) is then obviously satisfied, and the continuity of the meridional stress guarantees that $\tau_s^{(\mathrm{c})}(s_2) = \tilde{\tau}_s^{(\mathrm{c})}(s_2)$. However, we cannot conclude that $\tau_\varphi^{(\mathrm{c})}$ is continuous, because it does not explicitly depend on $\tau_s^{(\mathrm{c})}$ in region B. There is no possibility to make any statements about $\tau_\varphi^{(\mathrm{c})}$ in region B because it is an independent parameter here. Thus, the meridional stress may be discontinuous at a transition between regions 2 and B (and analogously between 1 and B), and we see in the main text that this discontinuity is indeed necessary to be able to solve the shape equations numerically.

The transition between regions $R_1 = 1$ and $R_2 = 2$ is also discontinuous. Due to the confinement of the stretches to the boundary (5.30) of the admissible domain in the stretch plane, we can again conclude that $\lambda_s = \tilde{\lambda}_s = L$ is continuous. Therefore, the Hookean contributions $\tau_s^{(\mathrm{s})}$ and $\tau_\varphi^{(\mathrm{s})}$ are continuous, and so is $\tau_s^{(\mathrm{c})}$. The hard-core stress contribution in hoop direction, however, is discontinuous. We can even calculate the size of the jump with eq. (5.32): In region 1 we have $\tau_\varphi^{(\mathrm{c})}(s_2) = \tau_s^{(\mathrm{c})}(s_2)/3$, and it changes by a factor 9 to $\tilde{\tau}_\varphi^{(\mathrm{c})}(s_2) = 3\tau_s^{(\mathrm{c})}(s_2)$ in region 2.

In principle, jumps in the hoop stress are even possible in the artificial transition from region B to B, because $\tau_\varphi^{(\mathrm{c})}$ is constitutively undetermined. However, the shape is nearly entirely fixed by the constraint $\lambda_s = \lambda_\varphi = L$, and we have derived above a relation (5.33) between τ_φ and other quantities which enforces τ_φ to be continuous within region B. A discontinuity in the hoop stress within region B is only possible when the geometric constraints are removed by allowing the midsurface to wrinkle. Thus, the transition between regions B and BW can have a discontinuous τ_φ. On the other hand, the transition between region 2 and its wrinkling region 2W is continuous because it is equivalent to the artificial transition from 2 to 2, which must be continuous because the ratio of hard-core stresses is fixed and thus τ_φ is determined by the constitutive relations.

Bibliography

[1] N. A. Alexandrov, K. G. Marinova, T. D. Gurkov, K. D. Danov, P. A. Kralchevsky, S. D. Stoyanov, T. B. Blijdenstein, L. N. Arnaudov, E. G. Pelan, and A. Lips. Interfacial Layers from the Protein HFBII Hydrophobin: Dynamic Surface Tension, Dilatational Elasticity and Relaxation Times. *J. Colloid Interface Sci.*, 376(1):296–306, Mar. 2012.

[2] J. M. Andreas, E. A. Hauser, and W. B. Tucker. Boundary Tension by Pendant Drops. *J. Phys. Chem.*, 42:1001–1019, 1938.

[3] J. Arfsten, S. Leupold, C. Bradtmöller, I. Kampen, and A. Kwade. Atomic force microscopy studies on the nanomechanical properties of Saccharomyces cerevisiae. *Colloids Surf. B. Biointerfaces*, 79(1):284–90, Aug. 2010.

[4] B. Audoly and Y. Pomeau. *Elasticity and Geometry: From hair curls to the non-linear response of shells*. OUP Oxford, 2010.

[5] E. Aumaitre. *Viscoelastic properties of Hydrophobin layers*. PhD thesis, University of Cambridge, 2012.

[6] E. Aumaitre, D. Vella, and P. Cicuta. On the measurement of the surface pressure in Langmuir films with finite shear elasticity. *Soft Matter*, 7(6):2530, 2011.

[7] E. Aumaitre, S. Wongsuwarn, D. Rossetti, N. D. Hedges, A. R. Cox, D. Vella, and P. Cicuta. A viscoelastic regime in dilute hydrophobin monolayers. *Soft Matter*, 2011.

[8] D. Barthès-Biesel. Role of interfacial properties on the motion and deformation of capsules in shear flow. *Phys. A Stat. Mech. its Appl.*, 172(1-2):103–124, Mar. 1991.

[9] D. Barthès-Biesel. Mechanics of encapsulated droplets. *Progr Colloid Polym Sci*, 111:58–64, 1998.

[10] D. Barthès-Biesel. Modeling the motion of capsules in flow. *Curr. Opin. Colloid Interface Sci.*, 16(1):3–12, Feb. 2011.

[11] D. Barthès-Biesel, A. Diaz, and E. Dhenin. Effect of constitutive laws for two-dimensional membranes on flow-induced capsule deformation. *J. Fluid Mech.*, 460:211–222, June 2002.

[12] D. Barthès-Biesel and J. M. Rallison. The time-dependent deformation of a capsule freely suspended in a linear shear flow. *J. Fluid Mech.*, 113:251–267, Apr. 1981.

[13] E. S. Basheva, P. A. Kralchevsky, N. C. Christov, K. D. Danov, S. D. Stoyanov, T. B. J. Blijdenstein, H.-J. Kim, E. G. Pelan, and A. Lips. Unique Properties of Bubbles and Foam Films Stabilized by HFBII Hydrophobin. *Langmuir*, 27:2382–2392, Feb. 2011.

[14] L. Bauer, E. L. Reiss, and H. B. Keller. Axisymmetric buckling of hollow spheres and hemispheres. *Commun. Pure Appl. Math.*, 23(4):529–568, July 1970.

[15] L. Berke and R. L. Carlson. Experimental studies of the postbuckling behavior of complete spherical shells. *Exp. Mech.*, 8(12):548–553, Dec. 1968.

[16] B. P. Binks. Particles as surfactants - similarities and differences. *Curr. Opin. Colloid Interface Sci.*, 7:21–41, 2002.

[17] T. B. J. Blijdenstein, P. W. N. de Groot, and S. D. Stoyanov. On the link between foam coarsening and surface rheology: why hydrophobins are so different. *Soft Matter*, 6(8):1799, 2010.

[18] F. Boulogne, F. Giorgiutti-Dauphiné, and L. Pauchard. The buckling and invagination process during consolidation of colloidal droplets. *Soft Matter*, 9(3):750, 2013.

[19] I. N. Bronshtein, K. A. Semendyayev, G. Musiol, and H. Mühlig. *Handbook of Mathematics*. Springer, New York, 2007.

[20] M. Buenemann and P. Lenz. Mechanical limits of viral capsids. *Proc. Natl. Acad. Sci. USA*, 104(24):9925–30, June 2007.

[21] D. Bushnell. Symmetric and nonsymmetric buckling of finitely deformed eccentrically stiffened shells of revolution. *AIAA J.*, 5(8):1455–1462, Aug. 1967.

[22] H. B. Callen. *Thermodynamics*. John Wiley & Sons, New York, 1960.

[23] M. Carin, D. Barthès-Biesel, F. Edwards-Lévy, C. Postel, and D. C. Andrei. Compression of biocompatible liquid-filled HSA-alginate capsules: determination of the membrane mechanical properties. *Biotechnol. Bioeng.*, 82(2):207–12, Apr. 2003.

[24] R. L. Carlson, R. L. Sendelbeck, and N. J. Hoff. Experimental Studies of the Buckling of Complete Spherical Shells. *Exp. Mech.*, 7(7):281–288, 1967.

[25] D. Carvajal, E. J. Laprade, K. J. Henderson, and K. R. Shull. Mechanics of pendant drops and axisymmetric membranes. *Soft Matter*, 7(22):10508, 2011.

[26] E. Cerda and L. Mahadevan. Geometry and Physics of Wrinkling. *Phys. Rev. Lett.*, 90(7):074302, Feb. 2003.

[27] E. Cerda, K. Ravi-Chanar, and L. Mahadevan. Wrinkling of an elastic sheet under tension. *Nature*, 419(10):580, 2002.

[28] K. Chang and W. Olbricht. Experimental studies of the deformation and breakup of a synthetic capsule in steady and unsteady simple shear flow. *J. Fluid Mech.*, 250, 1993.

[29] A. R. Cox, F. Cagnol, A. B. Russell, and M. J. Izzard. Surface properties of class II hydrophobins from Trichoderma reesei and influence on bubble stability. *Langmuir*, 23(15):7995–8002, July 2007.

[30] K. D. Danov, P. A. Kralchevsky, and S. D. Stoyanov. Elastic Langmuir layers and membranes subjected to unidirectional compression: wrinkling and collapse. *Langmuir*, 26(1):143–55, Jan. 2010.

[31] S. S. Datta, S.-H. Kim, J. Paulose, A. Abbaspourrad, D. Nelson, and D. Weitz. Delayed Buckling and Guided Folding of Inhomogeneous Capsules. *Phys. Rev. Lett.*, 109(13):1–5, Sept. 2012.

[32] S. S. Datta, H. C. Shum, and D. A. Weitz. Controlled buckling and crumpling of nanoparticle-coated droplets. *Langmuir*, 26(24):18612–6, Dec. 2010.

[33] B. Davidovitch, R. D. Schroll, and E. A. Cerda. Nonperturbative model for wrinkling in highly bendable sheets. *Phys. Rev. E*, 85(6), June 2012.

[34] B. Davidovitch, R. D. Schroll, D. Vella, M. Adda-Bedia, and E. A. Cerda. Prototypical model for tensional wrinkling in thin sheets. *Proc. Natl. Acad. Sci. USA*, 108(45):18227–32, Nov. 2011.

[35] C. S. Davis and A. J. Crosby. Wrinkle morphologies with two distinct wavelengths. *J. Polym. Sci. Part B Polym. Phys.*, 50(17):1225–1232, Sept. 2012.

[36] P. Degen, Z. Chen, and H. Rehage. Stimulated Deformation of Polysiloxane Capsules in External Electric Fields. *Macromol. Chem. Phys.*, 211(4):434–442, Feb. 2010.

[37] P. Degen, D. C. F. Wieland, S. Leick, M. Paulus, H. Rehage, and M. Tolan. Effect of magnetic nanoparticles on the surface rheology of surfactant films at the water surface. *Soft Matter*, 7(17):7655, 2011.

[38] N. R. Demarquette and M. R. Kamal. Interfacial Tension in Polymer Melts. I: An Improved Pendant Drop Apparatus. *Polym. Eng. Sci.*, 34(24):1823–1833, 1994.

[39] M. Dias, L. Dudte, L. Mahadevan, and C. Santangelo. Geometric Mechanics of Curved Crease Origami. *Phys. Rev. Lett.*, 109(11):1–5, Sept. 2012.

[40] D. E. Discher, D. H. Boal, and S. K. Boey. Simulations of the erythrocyte cytoskeleton at large deformation. II. Micropipette aspiration. *Biophys. J.*, 75(3):1584–97, Sept. 1998.

[41] E. Donath, G. B. Sukhorukov, F. Caruso, S. A. Davis, and H. Möhwald. Novel Hollow Polymer Shells by Colloid-Templated Assembly of Polyelectrolytes. *Angew. Chem. Int. Ed.*, 37(16):2201–2205, 1998.

[42] P. Erni, H. A. Jerri, K. Wong, and A. Parker. Interfacial viscoelasticity controls buckling, wrinkling and arrest in emulsion drops undergoing mass transfer. *Soft Matter*, 8(26):6958, 2012.

[43] L. Euler. *Methodus inveniendi lineas curvas maximi minimive proprietate gaudentes, sive solutio problematis isoperimetrici lattissimo sensu accepti.* 1744.

[44] J. K. Ferri, P. A. L. Fernandes, J. T. McRuiz, and F. Gambinossi. Elastic nanomembrane metrology at fluid–fluid interfaces using axisymmetric drop shape analysis with anisotropic surface tensions: deviations from Young–Laplace equation. *Soft Matter*, 8(40):10352, 2012.

[45] A. Fery, F. Dubreuil, and H. Möhwald. Mechanics of artificial microcapsules. *New J. Phys.*, 6:18, Feb. 2004.

[46] A. Fery and R. Weinkamer. Mechanical properties of micro- and nanocapsules: Single-capsule measurements. *Polymer*, 48(25):7221–7235, Nov. 2007.

[47] R. Finken, S. Kessler, and U. Seifert. Micro-capsules in shear flow. *J. Phys. Condens. Matter*, 23(18):184113, May 2011.

[48] R. Finken and U. Seifert. Wrinkling of microcapsules in shear flow. *J. Phys. Condens. Matter*, 18(15):L185–L191, Apr. 2006.

[49] Y. C. Fung. On Pseudo-elasticity of Living Tissues. In S. Nemat-Nasser, editor, *Mechanics today Vol. 5*, pages 49–66. Pergamon Press, 1980.

[50] Y. C. Fung. *Biomechanics. Mechanical Properties of Living Tissues.* Springer, New York, 1981.

[51] C. Gao, E. Donath, S. Moya, V. Dudnik, and H. Möhwald. Elasticity of hollow polyelectrolyte capsules prepared by the layer-by-layer technique. *Eur. Phys. J. E*, 5(1):21–27, May 2001.

[52] B. F. Gibbs, S. Kermasha, I. Alli, and C. N. Mulligan. Encapsulation in the food industry: a review. *Int. J. Food Sci. Nutr.*, 50(3):213–24, May 1999.

[53] H. Giesekus. *Phänomenologische Rheologie.* Springer, 1994.

[54] V. D. Gordon, X. Chen, J. W. Hutchinson, A. R. Bausch, M. Marquez, and D. A. Weitz. Self-assembled polymer membrane capsules inflated by osmotic pressure. *J. Am. Chem. Soc.*, 126(43):14117–22, Nov. 2004.

[55] P. Graf. *Modellierung der Adhäsion und Deformation von Mikrokapseln.* Phd thesis, Universität Stuttgart, 2007.

[56] P. Graf, R. Finken, and U. Seifert. Adhesion of Microcapsules. *Langmuir*, (22):7117–7119, 2006.

[57] G. N. Greaves, A. L. Greer, R. S. Lakes, and T. Rouxel. Poisson's ratio and modern materials. *Nat. Mater.*, 10(11):823–837, Oct. 2011.

[58] A. E. Green and J. E. Adkins. *Large Elastic Deformations.* Oxford University Press, Oxford, 2nd edition, 1970.

[59] B. Gurmessa and A. Croll. Onset of Plasticity in Thin Polystyrene Films. *Phys. Rev. Lett.*, 110(7):074301, Feb. 2013.

[60] J. Hakanpää, A. Paananen, S. Askolin, T. Nakari-Setälä, T. Parkkinen, M. Penttilä, M. B. Linder, and J. Rouvinen. Atomic resolution structure of the HFBII hydrophobin, a self-assembling amphiphile. *J. Biol. Chem.*, 279(1):534–9, Jan. 2004.

[61] J. Hegemann. *Numerische Analyse von Formgleichungen elastischer Kapseln.* Master's thesis, Technische Universität Dortmund, 2013.

[62] M. Hermann, T. Ullmann, and K. Ullrich. The Nonlinear Buckling Problem of a spherical shell: Bifurcation Phenomena in a BVP with Regular Singularity. *Tech. Mech.*, 12(3):177–184, 1991.

[63] J. Hohage. *Modellierung des Deformationsverhaltens elastischer Membranen mittels triangulierter Oberflächen.* Master's thesis, Technische Universität Dortmund, 2012.

[64] D. Holmes and A. Crosby. Draping Films: A Wrinkle to Fold Transition. *Phys. Rev. Lett.*, 105(3):1–4, July 2010.

[65] J. Huang, M. Juszkiewicz, W. H. de Jeu, E. A. Cerda, T. Emrick, N. Menon, and T. P. Russell. Capillary wrinkling of floating thin polymer films. *Science*, 317(5838):650–3, Aug. 2007.

[66] N.-C. Huang. Unsymmetrical buckling of thin shallow spherical shells. *J. Appl. Mech.*, 31(3):447–457, 1964.

[67] J. Hure, B. Roman, and J. Bico. Stamping and Wrinkling of Elastic Plates. *Phys. Rev. Lett.*, 109(5):1–5, Aug. 2012.

[68] M. Husmann. *Polyorganosiloxan-Filme zwischen fluiden Phasen*. Phd thesis, Universität Essen, 2001.

[69] J. W. Hutchinson. Imperfection sensitivity of externally pressurized spherical shells. *J. Appl. Mech.*, 34:49, 1967.

[70] I. L. Ivanovska, P. J. de Pablo, B. Ibarra, G. Sgalari, F. C. MacKintosh, J. L. Carrascosa, C. F. Schmidt, and G. J. L. Wuite. Bacteriophage capsids: tough nanoshells with complex elastic properties. *Proc. Natl. Acad. Sci. USA*, 101(20):7600–5, May 2004.

[71] J. Jose, M. Kamp, A. van Blaaderen, and A. Imhof. Unloading and reloading colloidal microcapsules with apolar solutions by controlled and reversible buckling. *Langmuir*, 30(9):2385–93, Mar. 2014.

[72] E. Katifori, S. Alben, E. Cerda, D. R. Nelson, and J. Dumais. Foldable structures and the natural design of pollen grains. *Proc. Natl. Acad. Sci. USA*, 107(17):7635–9, Apr. 2010.

[73] S. Kessler, R. Finken, and U. Seifert. Elastic capsules in shear flow: analytical solutions for constant and time-dependent shear rates. *Eur. Phys. J. E. Soft Matter*, 29(4):399–413, Aug. 2009.

[74] S.-H. Kim, T. Y. Lee, and S. S. Lee. Osmocapsules for Direct Measurement of Osmotic Strength. *Small*, 10(6):1155–1162, 2014.

[75] H. King, R. D. Schroll, B. Davidovitch, and N. Menon. Elastic sheet on a liquid drop reveals wrinkling and crumpling as distinct symmetry-breaking instabilities. *Proc. Natl. Acad. Sci. USA*, 109(25):9716–20, June 2012.

[76] K. Kisko, G. R. Szilvay, E. Vuorimaa, H. Lemmetyinen, M. B. Linder, M. Torkkeli, and R. Serimaa. Self-assembled films of hydrophobin proteins HFBI and HFBII studied in situ at the air/water interface. *Langmuir*, 25(3):1612–9, Mar. 2009.

[77] Y. Klein, E. Efrati, and E. Sharon. Shaping of elastic sheets by prescription of non-Euclidean metrics. *Science*, 315(5815):1116–20, Mar. 2007.

[78] G. H. Knightly and D. Sather. Buckled states of a spherical shell under uniform external pressure. *Arch. Ration. Mech. Anal.*, 72(4):315–380, 1980.

[79] W. Koiter. The nonlinear buckling problem of a complete spherical shell under uniform external pressure I - IV. *Proc. Kon. Nederl. Akad. Wet. Amsterdam B*, 72:40, 1969.

[80] S. Komura, K. Tamura, and T. Kato. Buckling of spherical shells adhering onto a rigid substrate. *Eur. Phys. J. E*, 18(3):343–58, Nov. 2005.

[81] M.-C. Lai. A note on finite difference discretizations for Poisson equation on a disk. *Numer. Methods Partial Differ. Equ.*, 17(3):199–203, May 2001.

[82] M.-C. Lai and W.-C. Wang. Fast direct solvers for Poisson equation on 2D polar and spherical geometries. *Numer. Methods Partial Differ. Equ.*, 18(1):56–68, Jan. 2002.

[83] L. Landau and E. Lifshitz. *Theory of Elasticity*. Course of Theoretical Physics. Pergamon Press, Oxford, 2nd edition, 1970.

[84] L. Landau and E. Lifshitz. *Fluid Mechanics*. Course of Theoretical Physics. Butterworth-Heinemann, Oxford, 2nd edition, 1987.

[85] A. Lazarus, H. Florijn, and P. Reis. Geometry-Induced Rigidity in Nonspherical Pressurized Elastic Shells. *Phys. Rev. Lett.*, 109(14):1–5, Oct. 2012.

[86] B. Li, Y.-P. Cao, X.-Q. Feng, and H. Gao. Mechanics of morphological instabilities and surface wrinkling in soft materials: a review. *Soft Matter*, 8(21):5728, May 2012.

[87] B. Li, F. Jia, Y.-P. Cao, X.-Q. Feng, and H. Gao. Surface Wrinkling Patterns on a Core-Shell Soft Sphere. *Phys. Rev. Lett.*, 106(23):2–5, June 2011.

[88] H. Liang and L. Mahadevan. The shape of a long leaf. *Proc. Natl. Acad. Sci. USA*, 106(52):22049–54, Dec. 2009.

[89] A. Libai and J. G. Simmonds. *The Nonlinear Theory of Elastic Shells*. Cambridge University Press, 1998.

[90] R. Lipowsky, M. Brinkmann, R. Dimova, T. Franke, J. Kierfeld, and X. Zhang. Droplets, bubbles, and vesicles at chemically structured surfaces. *J. Phys. Condens. Matter*, 17(9):S537–S558, Mar. 2005.

[91] A. Lytra and N. Pelekasis. Static response and stability of coated microbubbles – multiplicity of solutions and parameter estimation. *Fluid Dyn. Res.*, 46(4):041422, Aug. 2014.

[92] J. H. Maddocks. Stability and Folds. *Arch. Rat. Mech. Anal.*, 99:301, 1987.

[93] W. Meier. Polymer nanocapsules. *Chem. Soc. Rev.*, 29(5):295–303, 2000.

[94] J. P. Michel, I. L. Ivanovska, M. M. Gibbons, W. S. Klug, C. M. Knobler, G. J. L. Wuite, and C. F. Schmidt. Nanoindentation studies of full and empty viral capsids and the effects of capsid protein mutations on elasticity and strength. *Proc. Natl. Acad. Sci. USA*, 103(16):6184–9, Apr. 2006.

[95] M. P. Neubauer, M. Poehlmann, and A. Fery. Microcapsule mechanics: From stability to function. *Adv. Colloid Interface Sci.*, Dec. 2013.

[96] F. I. Niordson. *Shell Theory*. Elsevier Science Publishers B.V., Amsterdam, 1985.

[97] M. Okubo, H. Minami, and K. Morikawa. Production of micron-sized, monodisperse, transformable rugby-ball-like-shaped polymer particles. *Colloid Polym. Sci.*, 279(9):931–935, Sept. 2001.

[98] M. Okubo, H. Minami, and K. Morikawa. Influence of shell strength on shape transformation of micron-sized, monodisperse, hollow polymer particles. *Colloid Polym. Sci.*, 281(3):214–219, Mar. 2003.

[99] M. Ostoja-Starzewski. Lattice models in micromechanics. *Appl. Mech. Rev.*, 55(1):35, 2002.

[100] L. Pauchard and Y. Couder. Invagination during the collapse of an inhomogeneous spheroidal shell. *Europhys. Lett.*, 66(5):667–673, June 2004.

[101] L. Pauchard, Y. Pomeau, and S. Rica. Déformation des coques élastiques. *C. R. Acad. Sci. Paris*, 324(7):411–418, Apr. 1997.

[102] L. Pauchard and S. Rica. Contact and compression of elastic spherical shells: The physics of a 'ping-pong' ball. *Philos. Mag. Part B*, 78(2):225–233, Aug. 1998.

[103] J. Paulose and D. R. Nelson. Buckling pathways in spherical shells with soft spots. *Soft Matter*, 9(34):8227, 2013.

[104] J. Paulose, G. A. Vliegenthart, G. Gompper, and D. R. Nelson. Fluctuating shells under pressure. *Proc. Natl. Acad. Sci. USA*, 109(48):19551–6, Nov. 2012.

[105] J. T. Petkov and T. D. Gurkov. Dilatational and Shear Elasticity of Gel-like Protein Layers on Air / Water Interface. *Langmuir*, 16(8):3703–3711, 2000.

[106] G. Pieper, H. Rehage, and D. Barthès-Biesel. Deformation of a Capsule in a Spinning Drop Apparatus. *J. Colloid Interface Sci.*, 202(2):293–300, June 1998.

[107] A. V. Pogorelov. Bendings of Surfaces and Stability of Shells. In *Translations of Mathematical Monographs Vol. 72*. American Mathematical Society, 1988.

[108] C. Pozrikidis. *Modeling and Simulation of Capsules and Biological Cells*. Chapman and Hall/CRC, 2003.

[109] W. H. Press, S. A. Teukolsky, W. T. Vetterling, and B. P. Flannery. *Numerical Recipes*. Cambridge University Press, 2007.

[110] M. Pretzl, M. Neubauer, M. Tekaat, C. Kunert, C. Kuttner, G. Leon, D. Berthier, P. Erni, L. Ouali, and A. Fery. Formation and mechanical characterization of aminoplast core/shell microcapsules. *ACS Appl. Mater. Interfaces*, 4(6):2940–8, June 2012.

[111] F. Quemeneur, C. Quilliet, M. Faivre, A. Viallat, and B. Pépin-Donat. Gel Phase Vesicles Buckle into Specific Shapes. *Phys. Rev. Lett.*, 108(10):1–5, Mar. 2012.

[112] C. Quilliet. Numerical deflation of beach balls with various Poisson's ratios: from sphere to bowl's shape. *Eur. Phys. J. E. Soft Matter*, 35(6):48, June 2012.

[113] C. Quilliet, C. Zoldesi, C. Riera, A. van Blaaderen, and A. Imhof. Anisotropic colloids through non-trivial buckling. *Eur. Phys. J. E*, 27(1):13–20, Sept. 2008. Erratum: ibid., 32(4): 419-420, Aug. 2010.

[114] H. Rehage, M. Husmann, and A. Walter. From two-dimensional model networks to microcapsules. *Rheol. Acta*, 41(4):292–306, Jan. 2002.

[115] Y. Rotenberg, L. Boruvka, and A. Neumann. Determination of Surface Tension and Contact Angle from the Shapes of Axisymmetric Fluid Interfaces. *J. Colloid Interface Sci.*, 93(1):169–183, 1983.

[116] S. Sacanna, W. T. M. Irvine, L. Rossi, and D. J. Pine. Lock and key colloids through polymerization-induced buckling of monodisperse silicon oil droplets. *Soft Matter*, 7(5):1631, 2011.

[117] U. Seifert. Configurations of fluid membranes and vesicles. *Adv. Phys.*, 46(1):13–137, Feb. 1997.

[118] H. S. Seung and D. R. Nelson. Defects in flexible membranes with crystalline order. *Phys. Rev. A*, 38(2):1005–1018, 1988.

[119] R. Stanimirova, K. Marinova, S. Tcholakova, N. D. Denkov, S. D. Stoyanov, and E. Pelan. Surface rheology of saponin adsorption layers. *Langmuir*, 27(20):12486–98, Oct. 2011.

[120] C. E. Stauffer. The Measurement of Surface Tension by the Pendant Drop Technique. *J. Phys. Chem.*, 69(6):1933–1938, 1965.

[121] M. Stein and J. M. Hedgepeth. Analysis of partly wrinkled membranes. *NASA Tech. Note D-813*, 1961.

[122] J. Stoer and R. Bulirsch. *Introduction to Numerical Analysis*. Springer, New York, 2010.

[123] P. Swarztrauber and R. Sweet. The direct solution of the discrete Poisson equation on a disk. *SIAM J. Numer. Anal.*, 10(5):900–907, 1973.

[124] S. P. Timoshenko and J. M. Gere. *Theory of elastic stability*. McGraw-Hill, New York, 2nd edition, 1961.

[125] S. P. Timoshenko and S. Woinowsky-Krieger. *Theory of Plates and Shells*. McGraw-Hill, New York, 2nd edition, 1959.

[126] C. Truesdell and W. Noll. *The Non-Linear Field Theories of Mechanics*. Encyclopedia of Physics. Springer, 1965.

[127] N. Tsapis, E. Dufresne, S. Sinha, C. Riera, J. Hutchinson, L. Mahadevan, and D. Weitz. Onset of Buckling in Drying Droplets of Colloidal Suspensions. *Phys. Rev. Lett.*, 94(1):018302, Jan. 2005.

[128] A. Vaziri. Mechanics of highly deformed elastic shells. *Thin-Walled Struct.*, 47(6-7):692–700, June 2009.

[129] A. Vaziri and L. Mahadevan. Localized and extended deformations of elastic shells. *Proc. Natl. Acad. Sci. USA*, 105(23):7913–8, June 2008.

[130] D. Vella, A. Ajdari, A. Vaziri, and A. Boudaoud. Wrinkling of Pressurized Elastic Shells. *Phys. Rev. Lett.*, 107(17):174301, Oct. 2011.

[131] D. Vella, A. Ajdari, A. Vaziri, and A. Boudaoud. Indentation of Ellipsoidal and Cylindrical Elastic Shells. *Phys. Rev. Lett.*, 109(14):1–5, Oct. 2012.

[132] D. Vella, A. Ajdari, A. Vaziri, and A. Boudaoud. The indentation of pressurized elastic shells: from polymeric capsules to yeast cells. *J. R. Soc. Interface*, 9(68):448–55, Mar. 2012.

[133] D. Vella, P. Aussillous, and L. Mahadevan. Elasticity of an interfacial particle raft. *Europhys. Lett.*, 68(2):212–218, Oct. 2004.

[134] D. Vella and L. Mahadevan. The "Cheerios effect". *Am. J. Phys.*, 73(9):817, 2005.

[135] E. Ventsel and T. Krauthammer. *Thin Plates and Shells*. CRC Press, Aug. 2001.

[136] S. Vidon and R. M. Leblanc. Langmuir Study of Octadecyltrimethoxysilane Behavior at the Air-Water Interface. *J. Phys. Chem. B*, 102(7):1279–1286, Feb. 1998.

[137] G. A. Vliegenthart and G. Gompper. Forced crumpling of self-avoiding elastic sheets. *Nat. Mater.*, 5(3):216–21, Mar. 2006.

[138] G. A. Vliegenthart and G. Gompper. Compression, crumpling and collapse of spherical shells and capsules. *New J. Phys.*, 13(4):045020, Apr. 2011.

[139] A. Walter, H. Rehage, and H. Leonhard. Shear induced deformation of microcapsules: shape oscillations and membrane folding. *Colloids Surfaces A Physicochem. Eng. Asp.*, 183-185:123–132, July 2001.

[140] C. J. Wischnewski. *Numerische Untersuchung triangulierter Modelle elastischer Kapseln.* Bachelor thesis, Technische Universität Dortmund, 2013.

[141] T. Witten. Stress focusing in elastic sheets. *Rev. Mod. Phys.*, 79(2):643–675, Apr. 2007.

[142] T. Witten and H. Li. Asymptotic shape of a fullerene ball. *EPL*, 51, 1993.

[143] Y. W. Wong and S. Pellegrino. Wrinkled Membranes Part I: Experiments. *J. Mech. Mater. Struct*, 1(1):1–23, 2006.

[144] Y. W. Wong and S. Pellegrino. Wrinkled Membranes Part II: Analytical Models. *J. Mech. Mater. Struct.*, 1(1):27–61, 2006.

[145] Y. W. Wong and S. Pellegrino. Wrinkled Membranes Part III: Numerical Simulations. *J. Mech. Mater. Struct*, 1(1):61–93, 2006.

[146] E. H. Yong, D. R. Nelson, and L. Mahadevan. Elastic Platonic Shells. *Phys. Rev. Lett.*, 111(17):177801, Oct. 2013.

[147] H. N. Yow and A. F. Routh. Formation of liquid core-polymer shell microcapsules. *Soft Matter*, 2(11):940, 2006.

[148] Y. Zhang, H. Chan, and K. Leong. Advanced materials and processing for drug delivery: the past and the future. *Adv. Drug Deliv. Rev.*, 65(1):104–120, 2013.

[149] O.-Y. Zhong-can and W. Helfrich. Bending energy of vesicle membranes: General expressions for the first, second, and third variation of the shape energy and applications to spheres and cylinders. *Phys. Rev. A*, 39(10):5280–5288, 1989.

[150] C. I. Zoldesi, I. L. Ivanovska, C. Quilliet, G. J. L. Wuite, and A. Imhof. Elastic properties of hollow colloidal particles. *Phys. Rev. E*, 78(5):1–8, Nov. 2008.

Publications of the author

[151] S. Knoche. *Deformation and Buckling of Elastic Capsules*. Diploma thesis, Technische Universität Dortmund, Mar. 2011.

[152] S. Knoche and J. Kierfeld. Buckling of spherical capsules. *Phys. Rev. E*, 84(4):046608, Oct. 2011.

[153] E. Aumaitre, S. Knoche, P. Cicuta, and D. Vella. Wrinkling in the deflation of elastic bubbles. *Eur. Phys. J. E*, 36(3):22, Mar. 2013.

[154] S. Knoche, D. Vella, E. Aumaitre, P. Degen, H. Rehage, P. Cicuta, and J. Kierfeld. Elastometry of deflated capsules: elastic moduli from shape and wrinkle analysis. *Langmuir*, 29(40):12463–71, Oct. 2013.

[155] S. Knoche and J. Kierfeld. Secondary polygonal instability of buckled spherical shells. *EPL (Europhysics Lett.*, 106(2):24004, Apr. 2014.

[156] S. Knoche and J. Kierfeld. The secondary buckling transition: Wrinkling of buckled spherical shells. *Eur. Phys. J. E*, 37(7):18, July 2014.

[157] S. Knoche and J. Kierfeld. Osmotic buckling of spherical capsules. *Soft Matter*, 10:8358–8369, Aug. 2014.

Acknowledgements

This thesis has been written under the guidance of Prof. Jan Kierfeld, whose door stood always open to anyone who searched for advice. I want to thank him for the versatile assistance and encouragement from which I profited throughout the last years.

My thanks are extended to all the collaborators who contributed to my research on pendant and rising elastic capsules. First of all, I thank Prof. Heinz Rehage and Dr. Patrick Degen from the Chair of Physical Chemistry, whose experimental work on OTS capsules was an essential part from the very beginning of my work and triggered the idea of a shape analysis for pendant capsules.

A conference in Vienna was the starting point of a collaboration with a group of researchers from Cambridge and Oxford working on HFBII coated bubbles. I thank Dr. Pietro Cicuta and Dr. Elodie Aumaitre for providing the experimental data and their many suggestions for the improvement of our shape analysis method. Special thanks go out to Dr. Dominic Vella, who contributed the idea of incorporating wrinkles in the shape equations by setting the hoop stress to zero. This was a key point in the development of the shape analysis, and many further improvements followed.

I am also very grateful to all the people who were around and helped me at the university. In particular, I thank Susann, both Ninas, Kris, Björn and Matthias for proofreading this manuscript, and my former colleagues from room P1-O2-215 for all the help, discussions and distractions.